Dipole dipole interactions in dense alkali vapors confined in nano-scale cells.

Tom Peyrot

université PARIS-SACLAY

INSTITUT d'OPTIQUE GRADUATE SCHOOL ParisTech

NNT : 2019SACLO012

Thèse de doctorat

Dipole dipole interactions in dense alkali vapors confined in nano-scale cells

Thèse de doctorat de l'Université Paris-Saclay
préparée à l'Institut d'Optique Graduate School

École doctorale n°572 Ondes et Matières (EDOM)
Spécialité de doctorat: Physique

Thèse soutenue et présentée à Palaiseau, le 2 Octobre, par

Tom Peyrot

Composition du Jury :

Robert Löw Professeur associé, Université de Stuttgart	Rapporteur
Gabriel Dutier Maitre de conférences, Laboratoire de Physique des Lasers	Rapporteur
Nicolas Treps Professeur, Laboratoire Kastler Brossel	Président
Fabienne Goldfarb Maitre de conférences, Laboratoire Aimé Coton	Examinatrice
Ifan Hughes Professeur, Université de Durham	Examinateur
Antoine Browaeys Directeur de recherche, Laboratoire Charles Fabry	Directeur de thèse
Yvan Sortais Maitre de conférences, Laboratoire Charles Fabry	Invité
Philippe Adam Tuteur DGA	Invité

Contents

Acknowledgement

En rédigeant ses remerciements de thèse, on a un peu l'impression de mettre un point final à deux longues histoires... Premièrement, c'est évidemment la fin de la thèse, de trois ans d'une intensité sans précédent quant à l'investissement que l'on peut fournir sur un projet. Mais c'est aussi la fin des études, d'une formation scientifique qui se ponctue de la plus belle des manières. En réalité, rédiger ces remerciements c'est plutôt repartir trois ans en arrière et réaliser en écrivant les lignes, que les résultats obtenus sont le fruit d'un travail d'équipe impliquant de nombreuses personnes qu'il s'agit à présent de nommer expressément!

En premier lieu, rien de tout ceci n'aurait pu voir le jour sans l'extraordinaire encadrement que j'ai reçu de ta part Antoine. Tu as été pour moi un directeur de thèse admirable. Bien que je reste encore aujourd'hui pour toi le “P'tit Tom”, certains auraient pu douter du petit homme à qui tu as accordé ta confiance dès le départ. Le fait d'avoir été à la fois si proche pour me former correctement à ta passion quasi-névrotique pour la Science, mais également assez détaché pour laisser cours à mes propres initiatives, a été à mon sens l'élément déterminant de mon doctorat. Je pourrais certainement écrire un chapitre entier bourré d'anecdotes et de révérences, mais essayons de ne pas déroger au principe de concision que tu m'as inculqué.

The second person I would like to thank is obviously James Keaveney. When I arrived in Durham, I barely knew how to measure a current with an ammeter and was sincerely afraid of any computer code with more than five lines... These are two examples amongst many others to prove that the experimental job presented in this manuscript is nothing but thanks to the inestimable hours you spent with me in the laboratory showing how computer and measurement devices talk together... Physics aside, these years in Durham would have been much more complicated for me without your presence. I can tell it now: I have one British friend. Who could be boasting about it?

Ensuite, bien évidemment, j'aimerais dire un grand merci à Yvan. Comme je l'ai déjà dit, cest grâce à toi que j'ai pu faire cette thèse, mais c'est également grâce à toi que j'ai pu la mener à bien. Je pense que tu m'as transmis la persévérance scientifique;

cette rigueur qui consiste à ne jamais laisser le moindre doute persister sur les résultats que l'on obtient. C'est grâce à cela que nous avons pu avancer tous ensemble au cours de ces trois années pour produire ces solides résultats. Enfin, avec ton départ, je pense que le groupe perd un élément fondateur de l'originalité de sa recherche et les conséquences se verront dans les prochaines années. Je te souhaite toute la réussite possible pour ton nouveau projet.

Let us switch back to english to thank both Ifan and Charles for their supervision and welcoming at Durham University. Having the opportunity to see the ideas popping out from Charles'mind has been really enlightening! I can tell I had the chance to be there for our unforgettable weekly meeting or when I was annoyingly knocking on the door asking precisions about your new theories! Those who think that we can summarize Ifan with two words, *Measurements* and *Uncertainties*, are simple-minded. Ifan is first a great professor and this is thanks to you that I had the unique chance to give courses at Durham University. Not only being a formidable project leader able to focus on a particular project to get the job done, our exchange in Durham and Florence leave so many good memories for the future. Keep Swanning!

Certains voient dans l'ordre des remerciements un classement. Il ne faut pas. Le chaos s'organise de lui-même. Cette thèse, c'est donc aussi la rencontre de personnes aussi brillantes que fascinantes. Ce sont des relations qui ne s'arrêteront pas à la fin de ces remerciements, en tout cas j'en suis bien convaincu. Il y a ceux qui sont déjà partis vers d'autres horizons...Sylvain, j'espère que tu te plais au Japon et que vous y trouvez votre bonheur avec Akané. Votre venue à Durham a été une excellente idée que je te remercie d'avoir sortie du chapeau. Avec l'idée, Vincent est également sorti du chapeau...Une fois l'euphorie de la cathédrale passée, et même si malgré le prénom et tous tes efforts je doute de tes capacités d'impressioniste, je pense que jamais tu ne cesseras de m'impressioner ;)

Many thanks Will for the "easy side" of Physics. Merci Thierry pour tous tes conseils pour rendre la physique ludique. Thanks Nikola for the last impetus you gave to my PhD. Et un bon courage à toi mon Ludo pour terminer cette thèse! Merci Igor, Hannes, Pascal, Paul, Theodora, Nick, Kai, Marius, Tony et les autres membres du groupe. Merci au service des TPs, particulièrement Fabienne, Lionel, Thierry et Cédric. Merci pour tout et surtout pour les formidables conditions dans lesquelles j'ai pu enseigner les travaux pratiques. Il y a tellement de gens...Je remercie toutes

les personnes de l'Institut qui ont pu contribuer de près ou de loin à m'aider ou simplement faire un sourire tout au long de ces trois dernières années.

Last but not least, il convient de rendre à César ses lauriers. Je voudrais remercier chaleureusement ma famille. La Mère, le Père et surtout le Saint Esprit. Salutations. Paro, good luck et Nina, espérons que la collapsologie collapsera! Enfin, s'il n'y a pas d'ordre dans les remerciements, on finit tout de même par le plus important. Le Chea kho (c'est du Khmer, faut pas chercher). T'avoir à mes côtés est la plus belle chose au monde! Tout simplement parce que ce qu'il faut deux partenaires hors-normes pour former un couple hors-norme! Peu importe de quoi est fait demain: un champ de permaculture, deux gosses et les emmerdements associés, un gros chien bl...Non... Tant que tu es là pour m'aimer au retour de nos voyages, nous pourrons cultiver notre jardin!

The author

Introduction

Light scattering from polarizable objects is an effect which manifests itself in a multitude of everyday life situations [Feynman, 1965; Jackson, 1999]. For instance, light is expected to propagate in straight line. Yet, we can see sunlight beams because airborne particles scatter it in every directions. Keeping eyes up, the sky is blue due to Rayleigh scattering by nitrogen or oxygen molecules. Going beyond our atmosphere, the brightness of the solar corona results from Thomson scattering of light on free electrons close to the sun. Light therefore gives information about the structure of the matter through which it passes. Particularly, this matters is composed of particles that have their own resonant frequency, and the latter is responsible for the different colors belonging to objects around us. When the light frequency coincides with this resonant frequency, the scattering is strongly enhanced and we say that the light-matter interaction is *resonant*. Besides, as we will see, when many particles are subjected to an electromagnetic field, they may interact and react collectively to the field [Gross and Haroche, 1982]. The purpose of this manuscript is to study how a resonant light interacts with a system composed of many light-induced dipoles in interaction. The purpose of this introduction is to explain why this subject is of current interest and why we used dense alkali vapors confined in nano-scale cells to study it.

Light scattering in dense ensembles: motivations

The scattering of light with a wavelength λ, resonant with a single polarizable object, is well understood nowadays: the electromagnetic field polarizes the object, leading to a driven dipole that emits light in turn. This dipole is characterized by a resonant frequency ω_0 and a spectral width Γ_0. The situation involving two emitters is still under control: they interact via resonant interaction between light-induced dipoles if the separation distance between them is smaller than $\lambda\!\!\!^{-} = \lambda/(2\pi)$. There, modifications of the spectral properties of the two-body system have analytical expressions. To date, there is nevertheless no general theory describing the scattering of many dipoles interacting in a small volume $\lambda\!\!\!^{-3}$. As a result, systems composed of emitters with a spatial density $\mathcal{N}$ such that $\mathcal{C} = \mathcal{N}\lambda\!\!\!^{-3} \geq 1$ have led to fundamental researches in various domains of physics.

The current trend is towards shrinking the dimensions of light-matter based devices.

Thus, nano-physics is certainly one of the fields most immediately concerned by this interaction. For example, the emissivity of a system composed of many antennas placed in a small volume [Huang *et al.*, 2010] ($\mathcal{C} > 10$) can suffer from the coupling between the different emission modes due to dipole-dipole interactions. The latter could also be handle in order to use nano-plasmonic oscillators as transducers or sensors [Thijssen *et al.*, 2013]. Another current area of research concerns the promising atomic-like properties of systems based on semicondutor quantum dots [Awschalom, Loss, and Samarth, 2002]. To enhance their coupling to light, such systems are often placed in micro-cavities, and similarly, their scattering properties could then be altered due to dipole-dipole interactions [Solomon, Pelton, and Yamamoto, 2001].

Although interesting for many applications, artificial atoms, such as the one described above, are more complex than "real atoms". In particular, it is hard to make them identical (leading to inhomogeneous broadening). They also interact strongly with their environment through non-radiative processes. On the contrary, real atoms are the simplest polarizable objects. In particular, the expression for the polarizability of alkali atoms – having only one valence electron in their electronic core – is well-known. The complexity of manipulating atoms is one of the counterparts of using them over artificial atoms. We will show that this difficulty can be overcome to a certain extent. However, their very low non-radiative decay and high reproducibility (every atom is the same) make them ideal candidates to study the modification of the light scattering due to dipole-dipole interaction in dense ensembles.

Collective effects in light scattering from *atomic* ensembles have gained a renewed interest recently with the recognition that they can degrade the accuracy of atom-based sensors such as optical clocks by introducing unwanted energy level shifts [Chang, Ye, and Lukin, 2004; Bromley *et al.*, 2016; Campbell *et al.*, 2017]. These probe-induced shifts can generate biases in the reference frequency of the clock that can reach the 10^{-18} level in relative uncertainties: the order of magnitude is comparable to the limits of the current best performing atomic clocks [Riehle, 2017]. Alternatively, the collective response can be an asset if properly handled, and several recent works suggest how it can be used to enhance light-matter interfaces [Bettles, Gardiner, and Adams, 2015, 2016; Shahmoon *et al.*, 2017; Perczel *et al.*, 2017]. These works suggest placing the atoms in lattice geometries. The lattice configuration could then be tailored in such way that constructive or destructive interferences between the field radiated by the emitters allow to tune the dipole-dipole interaction at will.

All systems presented in the above paragraph deal with cold atoms (temperature below the milli-Kelvin range) apparatuses. In these experiments, the atomic motion

is essentially frozen, which is very convenient to study their properties by only considering the internal degrees of freedom of the atoms. In this manuscript, we use high-temperature alkali vapors instead: we now explain why this is not just contradictory.

Thermal atomic vapors in nano-scale geometries

This Thesis work was carried out – with the support of the DGA-DSTL program – between the University of Durham (United Kingdom) and the Laboratoire Charles Fabry of the Institut d'Optique at Palaiseau (France). In the group of Palaiseau, the research line is the study of mesoscopic systems of atoms in interactions using cold atoms experiments [de Léséleuc *et al.*, 2017; Pellegrino *et al.*, 2014]. In the group of Durham, a similar thematic is studied with cold atoms [Busche *et al.*, 2006], but they also have a longstanding experience with the manipulation of hot atomic vapor systems [Siddons *et al.*, 2008; Zentile *et al.*, 2015a]. This manuscript results from the will to study the scattering of light in dense ensembles sharing the experience of the two groups. This will grew out of the desire to compare the modification of light scattering in dense atomic ensemble using cold and hot gases. The triggering element of this Thesis was the work of James Keaveney [Keaveney *et al.*, 2012b]. In this paper, the group of Durham measured strong modifications of the resonant frequency ω_0 and decay rate Γ_0 as a function of the density in a thin and hot atomic vapor slab. Few years later, the group of Palaiseau realized an experiment with a dense microscopic atomic sample but reported negligible shifts and spectral widths as a function of the atomic density [Jennewein *et al.*, 2016], indicating that cold and hot atoms do not behave in the same way. To understand the origin of this difference, a collaboration between the two groups led to undertake new experiments with the hot thermal vapor system.

First of all, working with thermal vapor is an almost ideal situation to study light scattering in dense ensembles: the density of atoms scaling exponentially with temperature, very dense atomic samples can be produced with a relative ease[1] [Keaveney, 2014]. Furthermore, from an experimental point of view, hot vapor set-ups are much simpler than laser-cooled experiments. As a consequence, practical applications using these systems are numerous, particularly concerning their potential as future atomic

[1] Consider a cesium vapor at 300 °C, the corresponding density is $\mathcal{N} = 4 \times 10^{22}$ at·m^{-3}. In comparison, Bose-Einstein condensates, involving demanding experimental conditions, reach at most few 10^{20} at·m^{-3}.

sensors. For instance, vapor cells has been used as brain sensor [Sander *et al.*, 2012], to build a Faraday filter [Zentile *et al.*, 2015b], for terahertz imaging [Wade *et al.*, 2016] or as microwave electrometers [Sedlacek *et al.*, 2012]. In addition, Refs. [Griffith *et al.*, 2009; Sheng *et al.*, 2013] also reported that these vapor cells could serve as very-high sensitive magnetometers. Finally, recent works proved that the storage of light information up to one second in a thermal vapor is possible [Katz and Firstenberg, 2018] and robust to atomic motion [Cherroret *et al.*, 2019]: this time scale is very promising to consider thermal vapor as quantum memory for future communication networks [Sangouard *et al.*, 2011].

Reducing the size of these cells to the millimeter scale, there has been a vast interest in harnessing their potential as miniaturized atomic-clocks [Kitching, Knappe, and Hollberg, 2002; Knappe *et al.*, 2005]. The strong interaction between two Rydberg atoms in the blockade regime[2] led to study the coherent excitation of Rydberg atoms in micrometer-sized atomic vapor cells. Based on that technology, researchers from the the University of Stuttgart (Germany) recently succeeded in producing a room-temperature single-photon source [Ripka *et al.*, 2018]. All these examples show that miniaturization of thermal vapor system is a burgeoning area of research with up-and-coming applications.

The system used in this Thesis is a vapor cell with sub-micrometer thickness. The results presented in this manuscript therefore builds on a long experience acquired in the Laboratoire de Physique des Lasers located in Villetaneuse (France) and the Institute for Physical Research at Ashtarak (Armenia). As we will see in the first chapter, the nano-geometry is first an asset to study resonant dipole-dipole interactions. However, with the growing in the number of platforms using miniaturized light-matter interfaces, characterizing the modifications that the cell itself possibly induces on the optical response of a vapor confined inside, naturally emerges as a second main impetus of the PhD project.

The two main motivations for this manuscript are therefore:

1. The study of the resonant dipole-dipole interaction in dense ensembles.

2. The characterization of systems composed of a vapor confined in a miniaturized geometry.

[2]Rydberg atoms are highly excited atoms that particularly interact very strongly with each other via the dipole-dipole interaction. The Rydberg blockade regime corresponds to the inhibition of the excitation of ground-state atoms to the Rydberg state by the presence of another nearby Rydberg atom [Browaeys, Barredo, and Lahaye, 2016].

When this is done, we will have a good understanding of the optical response of a vapor confined in a nano-cell and hence of the biases when using them as sensors. In order to deal with the two above subjects, the manuscript is structured as follows:

Thesis summary

- In **Chapter 1**, we recall the main equations governing the interaction of light with a dense atomic ensemble and present explicitly the advantages and drawbacks of using thermal vapor confined in a nano-cell. We also derive the equations describing the transmission of light through the vapor: this will be in this manuscript the main observable to characterize the atomic optical response.
- In thermal vapors, atoms move. We show in **Chapter 2** that this motion leads to a non-local response of the atomic vapor. When the distance characterizing this non-local response is larger than the cell size, we enter what we will call the *mesoscopic regime*.
- We will show in **Chapter 3** that when the atomic density increases, the medium becomes local again. We will use this fact to clarify to a certain extent the origin of the atomic spectral shifts due to the resonant dipole-dipole interaction.
- When atoms are close to a surface, as is the case in a nano-cell, the van der Waals interaction can alter the atomic properties. The purpose of **Chapter 4** is to introduce a new versatile method to characterize as precisely as possible the influence of this interaction on the optical response of the system.
- In **Chapter 5**, we present the fabrication and characterization of a new generation of all-glass super-polished nano-cells. These cells could be used to test the influence of the surface roughness on the spectra.
- In most of the Thesis, we used transmission spectroscopy to gain information on the optical response of the vapor confined in the nano-cell. In the (final) **Chapter 6**, we collect the off-axis light scattering and compare this method with the results obtained throughout the manuscript.

Publications

The following papers have come out of the work described in this Thesis:

- T. Peyrot, Y. R. P. Sortais, A. Browaeys, A. Sargsyan, D. Sarkisyan, J. Keaveney, I. G. Hughes and C. S. Adams, *Collective Lamb Shift of a Nanoscale Atomic Vapor Layer within a Sapphire Cavity*, Phys. Rev. Lett. **120**, 243401 (2018).
- T. Peyrot, Y. R. P. Sortais,J.-J. Greffet, A. Browaeys, A. Sargsyan, J. Keaveney, I. G. Hughes and C. S. Adams, *Optical Transmission of an Atomic Vapor in the Mesoscopic Regime*, Phys. Rev. Lett. **122**, 113401 (2019).
- T. Peyrot, Ch. Beurthe, S. Coumar, M. Roulliay, K. Perronet, P. Bonnay, C. S. Adams, A. Browaeys, and Y. R. P. Sortais *Fabrication and characterization of super-polished wedged borosilicate nano-cells* , Opt. Lett. **44**, 1940 (2019).
- T. Peyrot,N. Sibalik, Y. R. P. Sortais, A. Browaeys, A. Sargsyan, D. Sarkisyan, I. G. Hughes and C. S. Adams, *Measurement of the atom-surface van der Waals interaction by transmission spectroscopy in a wedged nano-cell*, To appear in Phys. Rev. A.

Chapter 1

Light induced dipole-dipole interactions

Contents

Introduction

In this first chapter, we introduce the concepts and theoretical formalism used throughout this Thesis to describe the interaction of a light with a wavelength λ and a collection of interacting particles. Generally speaking, the theory should rely on a fully quantum description of both the atoms and light. However, we will show that under some approximations, both of them can be treated classically.

We will start the discussion with a single two-level system and show that its behavior is similar to the one of a classically driven damped harmonic oscillator. Then, considering two atoms, it will turn out that they strongly interact via dipole-dipole interactions as soon as their inter-atomic distance is smaller than the reduced

wavelength $\lambda\!\!\!^{-} = \lambda/2\pi = 1/k_\ell$, where k_ℓ is the light wave-vector. Further increasing the number of particles, we will consider a many-body system with a volume density $\mathcal{N}$. A collective parameter $\mathcal{N}/k_\ell^3$ will emerge as a figure of merit for quantifying the interactions. It indicates that dipole-dipole interaction becomes important as soon as many atoms are confined in a small volume $\lambda\!\!\!^{-3}$.

As we have seen in the general introduction, one of the purposes of this manuscript is to study the interaction between a dense atomic sample ($\mathcal{N}/k_\ell^3 \gg 1$) and light nearly resonant ($k_\ell = \omega_\ell/c \sim \omega_0/c$ where ω_0 and ω_ℓ are the resonant frequency and the laser frequency respectively) with this ensemble. Previous experiments that investigated the dense regime (*i.e.* $\mathcal{N}/k_\ell^3 \geq 1$) can be grouped into two categories. We make a distinction between experiments where the size L of the atomic sample is (i) much larger than λ or (ii) on the order of λ. We will show that the second approach is more appropriate to perform direct measurement of the near-resonant dipole-dipole interaction. For this last purpose, numerous studies were conducted using small and cold atomic clouds (temperature $\Theta \sim \mu$K) and we are going to report the main results obtained in these experiments. However, the system we have opted for in this manuscript is different. It consists of thermal vapors of alkali-metal atoms ($\Theta > 300$K) confined in a nano-scale cell: we will explain the motivations that led us to choose such a system to study the interactions.

In order to reveal the latter experimentally, we will mainly observe the *transmission* of light through the nano-cell. We will derive this observable starting from a microscopic approach and give an analytical expression in the simplest case possible of a cold, dilute and large atomic ensemble. It will pave the way for the following experimental chapters.

Using dense thermal vapors confined in a nano-scale system raises a series of open questions. First of all, interactions in dense atomic clouds is currently a hot topic of research: it is fair to say that going from one or two single emitters to a large number of particles is a theoretical problem with no general settled solution. In thermal vapors, atomic motion is responsible for the Doppler effect that significantly complicates the static case. The collisions between atoms can also modify their spectral properties. In addition, the nano-metric geometry leads to several complications presented here as a non-exhaustive list: (i) when the atomic medium thickness is on the order of the wavelength of the light, dipole-dipole interactions have been predicted to be medium-size dependent [Friedberg, Hartmann, and Manassah, 1973], (ii) when the thickness of the cell becomes smaller than the distance characterizing the relaxation of the dipoles (due to a radiative decay or thermalization with other

atoms), collisions with the surfaces of the cell are playing an important role in the response of the system [Schuurmans, 1976]. (iii) When the cell thickness becomes smaller than $\lambda\!\!\!^{-}$, the van der Waals interaction between a dipole and a nearby surface becomes significant [M. Ducloy and M. Fichet, 1991]. We introduce in this first chapter the prerequisites to help addressing all these issues.

1.1 Theory of light induced dipole-dipole interactions

We begin the discussion by considering a single two-level atom interacting with an electromagnetic field. We will show that the dipole induced by the field can be described fully classically if the latter is weak enough. In response to the light excitation, the dipole emits a field that can excite another dipole: this is the *dipole-dipole interaction*. Finally, we explain the difficulties arising when the number of particles increases.

1.1.1 Single two-level atomic system

Two-level atomic system We first consider the simplest possible case of a two-level atom with ground state $|1\rangle$ and excited state $|2\rangle$. The level spacing corresponds here to a π optical transition along the x-axis and we set, without loss of generality, the ground (respectively excited) state energy to 0 (respectively $\hbar\omega_0 \simeq h \times 380$ THz). The Hamiltonian in the $\{|1\rangle, |2\rangle\}$ basis is given by

$$\hat{H}_0 = \hbar\omega_0 |2\rangle \langle 2| . \tag{1.1}$$

A convenient tool to study the evolution of a state $|\psi\rangle$ is the density matrix operator $\hat{\rho} = |\psi\rangle \langle\psi|$. In the same basis, the density matrix can be written as:

$$\hat{\rho} = \begin{pmatrix} \rho_{11} & \rho_{12} \\ \rho_{21} & \rho_{22} \end{pmatrix} . \tag{1.2}$$

Diagonal terms ρ_{11} and ρ_{22} correspond respectively to the ground and excited state populations and the crossed terms $\rho_{21} = \rho_{12}^*$ are the atomic coherences.

Coupling to light: atomic dipole When light impinges on an atom, an electron can be promoted to the excited state. This interaction is represented by the dipole operator that couples the states $|1\rangle$ and $|2\rangle$. It can be written $D = d_{12} |1\rangle \langle 2| + d_{21} |2\rangle \langle 1|$, with d_{ij} the only non-zero dipole matrix coefficients, and its average value is given by:

$$\langle D \rangle = \mathrm{Tr}(\rho D) = d_{12}\rho_{21} + d_{21}\rho_{12}. \tag{1.3}$$

When the average is non-zero, we commonly say that light induces a dipole.

The light inducing the dipoles in our case comes from a monochromatic and linearly polarized laser used in continuous wave (cw) mode. We work in the framework of the semi-classical approximation: when the number of photons in the coherent mode of the laser is large, the electromagnetic field behaves like a classical wave [Gardiner and Zoller, 2014]. We assume that the laser light is polarized along the x axis (*i.e.* $\boldsymbol{E}(\boldsymbol{r},t) = E(r,t)\boldsymbol{e_x}$) and we write

$$E(r,t) = E_0(r)\cos(\omega_\ell t) = \frac{1}{2}E_0(r)e^{i\omega_\ell t} + c.c.\ . \tag{1.4}$$

The equations that govern the coupling between the laser light and the atoms are the optical Bloch equations (OBE).

Optical Bloch equations These equations are a set of coupled linear equations that describe the time dependence of the density matrix elements. They are textbook material and we write them using the rotating wave approximation[1] as in Ref. [Grynberg *et al.*, 2010]:

$$\dot{\rho}_{22} = -\frac{id_{12}E_0(r)}{2\hbar}\left(e^{i\omega_\ell t}\rho_{21} - e^{-i\omega_\ell t}\rho_{12}\right) - \Gamma_0\rho_{22}, \tag{1.5}$$

$$\dot{\rho}_{11} = -\dot{\rho_{22}}, \tag{1.6}$$

$$\dot{\rho}_{21} = -i\omega_0\rho_{21} + \frac{iE_0(r)e^{-i\omega_\ell t}}{2\hbar}\left(\rho_{11} - \rho_{22}\right) - \frac{\Gamma_0}{2}\rho_{21}, \tag{1.7}$$

$$\dot{\rho}_{12} = \dot{\rho_{21}}^*. \tag{1.8}$$

The decay rate Γ_0 describes spontaneous emission and originates from the coupling to the vacuum fluctuations.

In the rotating frame we can rewrite Eq. (1.3) as:

$$\langle D \rangle = \overbrace{\left(d_{12}\rho_{21}e^{i\omega_\ell t}\right)}^{d} e^{-i\omega_\ell t} + \overbrace{\left(d_{21}\rho_{12}e^{-i\omega_\ell t}\right)}^{d^*} e^{+i\omega_\ell t} = de^{-i\omega_\ell t} + d^*e^{i\omega_\ell t} \tag{1.9}$$

and using the OBE, we derive the two following equations that govern the evolution of the dipole and populations, with $\Delta = \omega_\ell - \omega_0$:

[1] In the rotating wave approximation, the terms which oscillate rapidly in the equations have been neglected.

$$\dot{d} = \left(i\Delta - \frac{\Gamma_0}{2}\right) d - i\frac{|d_{12}|^2}{2\hbar}\left(\rho_{22} - \rho_{11}\right) E_0(r), \tag{1.10}$$

$$\dot{\rho_{22}} = -\dot{\rho_{11}} = -\frac{i}{\hbar}\mathrm{Im}\left(dE_0^*(r)\right) - \rho_{22}\Gamma_0. \tag{1.11}$$

We solve numerically this coupled system and display in Fig. 1.1(a-c) the on-resonance ($\Delta \sim 0$) steady-state amplitude solutions for populations and d when the driving field varies. For low driving, $\rho_{22} \simeq 0$ and $\rho_{11} \simeq 1$ (see also Fig. 1.1(b)) and the dipole moment strength is proportional to the field amplitude: this is the *weak driving field regime*. We will use this approximation in all this work and ignore any power saturation. It is valid for $|E_0(r)|^2 \ll (\hbar^2\Gamma_0^2)/|d_{12}|^2$ and generally requires laser intensities smaller than some $\mathrm{mW.cm^{-2}}$ for alkali-atom in the low-lying states[2]. In this weak regime, we display the dipole evolution as a function of time after switching on the laser in Fig. 1.1(d). The dipole moment reaches steady-state after a transient regime of several $1/\Gamma_0$.

Weakly driven quantum dipole In the weak driving approximation, Eq. (1.10) becomes

$$\dot{d} = \left(i\Delta - \frac{\Gamma_0}{2}\right) d + i\frac{|d_{12}|^2}{2\hbar} E_0(r) \tag{1.12}$$

and its solution is given by:

$$d(t) = d_{\mathrm{st}}\left(1 - e^{\left(i\Delta - \frac{\Gamma_0}{2}\right)t}\right), \tag{1.13}$$

with

$$d_{\mathrm{st}} = \frac{1}{2}\epsilon_0\alpha(\omega_\ell)E_0(r). \tag{1.14}$$

In the above equation, we have introduced the frequency-dependent atomic polarizability

$$\alpha(\omega_\ell) = \frac{-3\pi i\Gamma_0/k_\ell^3}{i\Delta - \Gamma_0/2}, \tag{1.15}$$

which is basically the optical response of a single particle.

From the solutions of the OBE, two important characteristics of the coupling between the laser and the atom appear:

[2]It turns out that in thermal vapors, the condition is less strict due to various broadening. In Appendix B, we show the limit of the weak-driving limit.

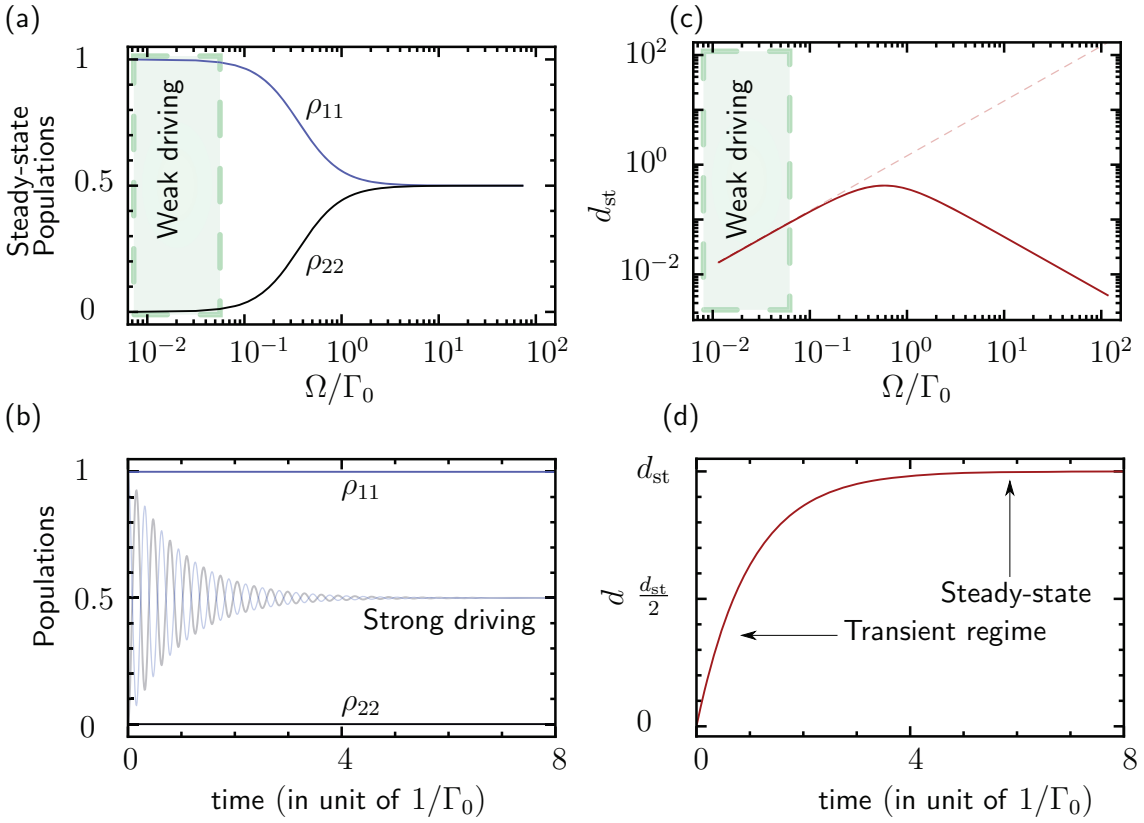

Figure 1.1: Weak probe approximation (a) Steady-state populations with respect to the Rabi-frequency $\Omega = d_{12}E_0/\hbar$ normalized by the natural line-width Γ_0 and (b) populations as a function of time in unit of $1/\Gamma_0$. Thick lines: $\Omega/\Gamma_0 = 0.01$, transparent lines: $\Omega/\Gamma_0 = 20$. (c) steady-state dipole moment at resonance as a function of the normalized Rabi-frequency. In transparent dotted line: result in the weak probe regime (*i.e.* imposing $\rho_{22} \simeq 0$ in the simulation). In red full line: result with no approximation. (d) Evolution of the dipole moment at resonance in the weak probe approximation ($\Omega/\Gamma_0 = 0.01$). The dipole experiences a transient evolution and reaches steady state $d_{\rm st}$ after several relaxing times $1/\Gamma_0$.

- In the the weak driving limit, the induced dipole is proportional to the driving field.

- The proportionality constant α is the polarizability which is a Lorentzian function of the driving frequency ω_ℓ that is centred on the resonance of the dipole ω_0.

The classical harmonic oscillator We show now that this light-matter coupling can be retrieved with a fully classical approach. For this purpose, we consider the classical model introduced by Lorentz for the electron. The equation of motion for the particle of mass m and charge q, elastically bound to the nucleus, and driven by an electric

field is given by:

$$m\ddot{x} = qE(r, \omega_\ell) - \Gamma\dot{x} - m\omega_0^2 x. \tag{1.16}$$

Here, Γ is a dissipation term responsible for the damping and ω_0 is the resonant frequency of the system related to its spring force strength. In the near resonant limit, $\omega_\ell \sim \omega_0$ and the dipole moment $d(t) = qx(t)$ can be rewritten in the same form as Eq. (1.13) with:

$$d_{\text{st}} = -i\frac{q^2 E/(2m\omega_0)}{i\Delta - \Gamma/2}. \tag{1.17}$$

We therefore showed that in the weak driving field regime, a quantum two-level system behaves like a one-dimensional (1D) classical harmonic oscillator provided that the damping rate is assimilated to the spontaneous decay Γ_0 and that the transition dipole moment d_{12} is $q\sqrt{\hbar/(m\omega_0)}$. As a consequence, systems composed of many atoms are expected to behave as an ensemble of classical coupled radiators. We now show how two dipoles in interaction is different from the individual case.

1.1.2 Resonant dipole-dipole interaction between two atoms

Dipole-dipole interactions is a term often used in the literature to describe different physical situations. We make here a distinction between the resonant and non-resonant dipole-dipole interactions. In the non-resonant case, also called the van der Waals regime, two dipoles in the same state can interact. It is usually associated with a virtual exchange of photons through the vacuum field and can only be understood quantum-mechanically [Cohen-Tannoudji, Diu, and Laloe, 2018]. This is not the subject of this manuscript[3]. We rather concentrate on the resonant dipole-dipole interaction which, mediated by the dipole field, can be completely described classically.

The dipole field A dipole $\boldsymbol{d_1}$ placed in $\boldsymbol{r_1}$ emits a field at a position $r = |\boldsymbol{r}|$ given by [Jackson, 1999; Feynman, 1965]:

[3]Note however that in Chapter 4, we will study the van der Waals interaction of an atom with a surface.

$$\boldsymbol{E_1}(r) = \frac{k_\ell^3}{4\pi\epsilon_0}\left\{[3(\boldsymbol{d_1}.\hat{\mathbf{n}})\hat{\mathbf{n}} - \boldsymbol{d_1}]\left(\frac{1}{(k_\ell R)^3} - \frac{i}{(k_\ell R)^2}\right) + [(\boldsymbol{d_1}.\hat{\mathbf{n}})\hat{\mathbf{n}} - \boldsymbol{d_1}]\frac{1}{k_\ell R}\right\} \times e^{ik_\ell R} \tag{1.18}$$

$$= [G]\,\boldsymbol{d_1},$$

where $\hat{\mathbf{n}}$ is the unit vector in the direction of $\boldsymbol{r} - \boldsymbol{r_1}$, $R = |\boldsymbol{r} - \boldsymbol{r_1}|$ and $[G]$ the vacuum green tensor. This field can drive other dipoles and this is at the origin of the *dipole-dipole interaction*. Namely, the field felt by an atom at a position r' is now the sum of the external field $\boldsymbol{E_0}$ and the field radiated by other particles at this position r'. We call this resulting field the local field $\boldsymbol{E}_{\text{loc}}(r')$.

It can be seen from Eq. (1.18) that the field emitted by a dipole depends on its orientation. To simplify the discussion we consider now two atomic dipoles that can only oscillate along one direction, let us say the x-axis[4]. In this case, Eq. (1.14) is still valid since:

$$\boldsymbol{d_1} = \epsilon_0\,[\alpha]\,\boldsymbol{E}_{\text{loc}}, \tag{1.19}$$

with

$$[\alpha] = \begin{bmatrix} \alpha(\omega_\ell) & 0 & 0 \\ 0 & 0 & 0 \\ 0 & 0 & 0 \end{bmatrix}, \tag{1.20}$$

where $[\alpha]$ is the polarizability tensor that reduces to a scalar quantity. Indeed, because the dipoles are solely allowed to oscillate along the $x-$axis, only the component of the field in that particular direction can drive another dipole (see Fig. 1.2(a)).

We now place another atom at a position r_2 and denote by θ the angle between the $x-$axis and the inter-atomic direction. The situation is illustrated in Fig. 1.2(a). The second atom can now be driven by the projection on $\boldsymbol{e_x}$ of the field emitted by the first atom:

$$E_{1x}(r) = \frac{k_\ell^3}{4\pi\epsilon_0}\left[\left(\frac{1}{(k_\ell r_{12})^3} - \frac{i}{(k_\ell r_{12})^2}\right)\left(3\cos^2\theta - 1\right) + \frac{1}{k_\ell r}\sin^2\theta\right] e^{ik_\ell r_{12}} d_1 = G_x d_1, \tag{1.21}$$

where $r_{12} = r_1 - r_2$. In the following, we show that the dipole-dipole interaction that

[4] In the quantum mechanical picture, this is equivalent to a two-level system connected by a π transition. We could allow the dipole to oscillate in 3D, as in the case of a multilevel atom, at the price of unnecessary cumbersome equations that add nothing new to the discussion.

originates from the term $G_x(|r_{12}|) \equiv G$, is responsible for the modification of the resonant frequencies and decay rates of the two dipoles.

Dipole-dipole shift and broadening The total field impinging on each dipole is now the sum of the laser field and the field radiated by the other dipole. Using Eq. (1.12) for the two dipoles, we find the coupled system:

$$\begin{cases} \dot{d_1} = & \left(i\Delta - \frac{\Gamma_0}{2}\right) d_1 + i\frac{|d_{12}|^2}{2\hbar} \left(E_0(r_1) + d_2 G\right), \\ \dot{d_2} = & \left(i\Delta - \frac{\Gamma_0}{2}\right) d_2 + i\frac{|d_{12}|^2}{2\hbar} \left(E_0(r_2) + d_1 G\right). \end{cases} \tag{1.22}$$

In the coupled basis, we form $d_\pm = (d_1 \pm d_2)/\sqrt{2}$ and we get the two equations:

$$\dot{d_\pm} = \left(i\Delta - \Gamma_0/2 \pm i\frac{|d_{12}|^2}{2\hbar} G\right) d_\pm + \frac{E_0(r_1) \pm E_0(r_2)}{\sqrt{2}} \tag{1.23}$$

$$= \left(i(\Delta - \omega_\pm) + \Gamma_\pm\right) d_\pm + \frac{E_0(r_1) \pm E_0(r_2)}{\sqrt{2}}. \tag{1.24}$$

These equations are similar to Eq. (1.12) and we see that the coupled dipoles solutions $d_\pm$ are shifted and broadened by the quantities $\omega_\pm$ and $\Gamma_\pm$ given by:

$$\omega_\pm = \mp\frac{|d_{12}|^2}{2\hbar} \mathbb{R}\mathrm{e}(G), \tag{1.25}$$

$$\Gamma_\pm = \Gamma_0 \pm \frac{|d_{12}|^2}{2\hbar} \mathbb{I}\mathrm{m}(G). \tag{1.26}$$

Equations (1.25) and (1.26) show that the dipole-dipole shift and broadening directly originates from the real and imaginary part of the vacuum green's function G. It is worthwhile pointing out that these quantities do not depend on the average of the dipole moment: the eigen-energies of the coupled system do not rely on the state in which it is prepared, but are rather an intrinsic property of the dipolar transition.

In Fig. 1.2(b), we represent the dependence Γ_+ and ω_+ in units of Γ_0 according to r_{12} in the case of $\theta = 0$. Importantly, the shift in the near-field regime ($k_\ell r_{12} \ll 1$) is proportional to $1/(k_\ell r_{12})^3$. We are going to come back to this result in the next section where we will study the case of many atoms in interaction. When $k_\ell r_{12} > 1$, the shift and broadening display an oscillating behavior with a period λ. When $k_\ell r_{12} \ll 1$, the broadening converges to $2\Gamma_0$. We would find 0 for Γ_- and these changes in the dipole lifetime give rise to the so-called sub and super-radiant states [Bettles, Gardiner, and Adams, 2016].

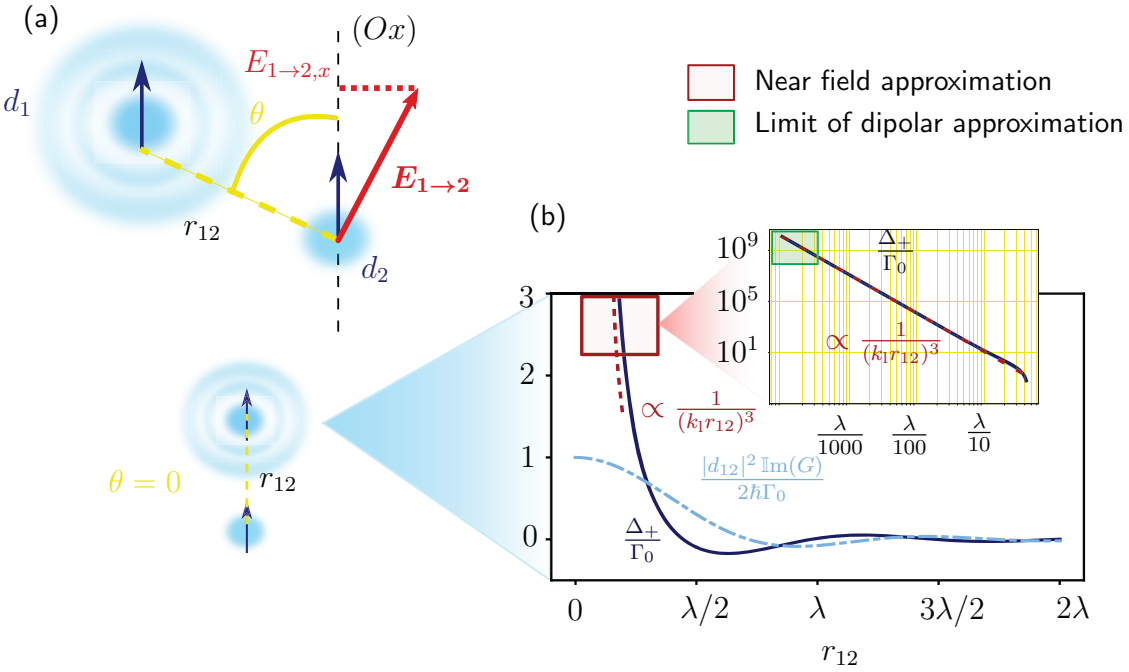

Figure 1.2: Two interacting dipoles (a) The angle between the atomic dipole moment and the inter-atomic distance is denoted by θ. Dipoles are only allowed to oscillate along (Ox) such that only the component $E_{1\to 2,x}$ along (Ox) of the dipole field $\boldsymbol{E_{1\to 2}}$ emitted by the first dipole induces the second dipole. (b) In the (arbitrary) case of $\theta = 0$, dipole dipole shift ω_+ and broadening Γ_+ are represented in unit of Γ_0 as a function of the inter-atomic distance r_{12}. In the near field region ($r_{12} \ll \lambda$), the inset panel (red square) shows the $1/(k_\ell r_{12})^3$ dependence of the shift. At really short distances (green square), even dipole approximation is expected to fail: quadrupole, octupole, *etc*... contributions should be included. In the far field, an oscillatory behavior with a period λ is observed.

1.1.3 Interaction in dense atomic systems

We have just seen that two coupled oscillators feature two eigen-modes with different eigen-frequencies and damping rates. We now present the difficulties encountered in the case of an ensemble constituted of many atomic dipoles in interaction.

Coupled dipole model A way to treat this problem is to consider the many-body system as an ensemble of coupled radiators [Javanainen *et al.*, 1999; Svidzinsky, Chang, and Scully, 2010]. In this approach, an ensemble of closed equations describes the total external field driving each atom. In what follows, we adopt two simplified notations for the dipole field: (a) $E_{r_j\to r_i}(r_i)$ is the field emitted by a dipole d_j placed at a position r_j, that is acting at a position r_i on a dipole d_i. (b) $E_{r_i}(r)$ represents the field emitted

by a dipole d_i placed in r_i calculated at a position r in the space. The idea of the coupled dipole approach is that a dipole d_i feels the external driving field $E_0(r_i)$ and the sum of fields from all other dipoles:

$$E(r_i) = E_0(r_i) + \sum_{j \neq i} E_{r_j \to r_i}(r_i). \tag{1.27}$$

The coupled system ($E_{r_j \to r_i}(r_i) \propto d_j$) is usually solved numerically and the resulting field everywhere in space is given by the superposition principle:

$$E(r) = E_0(r) + \sum_{i} E_{r_i}(r). \tag{1.28}$$

However, in our study, at least two major complications prevent us from using this coupled-dipole method:

- The computer time for a simulation grows as the cube of the atom number [Javanainen *et al.*, 2014] and current atomic numbers in simulations (10000 at most) is significantly smaller than in usual atomic vapors[5].

- The coupled dipole approach including room-temperature atomic motion has not been solved to date: neglecting this motion for thermal vapors is not conceivable.

We consequently rather use a "standard" electrodynamics approach describing the vapor as a continuous polarizable medium.

The continuous polarizable medium. In this approach the medium is described by a continuous distribution of atoms with a volume density $\mathcal{N}$. We therefore convert sums to integrals in Eqs. (1.27) and (1.28). Concerning the expression governing the driving field, summation over $j \neq i$ requires to exclude a small volume $\mathcal{V}'$ of the total volume of interest $\mathcal{V}$:

$$\sum_{j \neq i} E_{r_j \to r_i}(r_i) \to \int_{\mathcal{V}-\mathcal{V}'} \mathrm{d}^3 r'' \mathcal{N} E_{r'' \to r'}(r'). \tag{1.29}$$

In the heuristic approach introduced by Lorentz, the volume $\mathcal{V}'$ is a small sphere that radiates a field $-P/(3\epsilon_0)$ [Lorentz, 2011]. The polarization $P = \mathcal{N}d$ stands for the volume density of dipoles. The local field at a position r' can therefore be written as:

[5] Take for example a usual density of 10^{20} at·m^{-3} and the volume of a cylinder $\pi\omega_0^2 L$ with a waist $\omega_0 = 100$ µm and $L = 100$ nm. The number of atoms is about 3×10^5.

$$E_{\mathrm{loc}}(r') = \underbrace{E_0(r') + \int_{\mathcal{V}} \mathrm{d}^3 r'' \mathcal{N} E_{r''\to r'}(r')}_{\text{Mean field}} + \underbrace{\frac{P(r')}{3\epsilon_0}}_{\text{Polarization field}} . \tag{1.30}$$

The field everywhere space, outside of the volume $\mathcal{V}'$ then becomes:

$$E(r) = \underbrace{E_0(r)}_{\substack{\text{External laser}\\ \text{field}}} + \underbrace{\int_{\mathcal{V}} \mathrm{d}^3 r'' \mathcal{N} E_{r'}(r)}_{\substack{\text{total dipole}\\ \text{field } E_{\mathrm{d}}(r)}} . \tag{1.31}$$

The two last equations constitute the *major result* of this part. On the one hand, expression (1.30) gives the (local) field inducing atomic dipoles at a position r'. On the other hand, expression (1.31) provides the total field everywhere in space resulting from the superposition of the external laser field $E_0(r)$ and total dipole field $E_{\mathrm{d}}(r)$ at a position r.

In the two-atom case we have seen that the shift of the resonance due to the dipole-dipole interaction could be estimated via the green tensor. Similarly here, the shift of the resonances in the many-body system is expected to be related to the strength of the local field. To find an order of magnitude of the interaction we can assume that dipoles only interact by pairs and we neglect three-body interactions. In the near field regime (if we neglect retardation effects), we see from Eq. (1.21) that the dipole-field is proportional to $1/(k_\ell \langle r_{12} \rangle)^3$ where $\langle r_{12} \rangle$ is a mean distance between the atoms in a given pair. Since the density of atoms is roughly $\mathcal{N} \sim 1/\langle r_{12}^3 \rangle$, we expect as of now the shift of the resonance to be related to

$$\Delta\omega \simeq \Gamma_0 \mathcal{C}, \tag{1.32}$$

where the collective parameter

$$\mathcal{C} = \mathcal{N} \lambda\!\!\!^{-3} = \frac{\mathcal{N}}{k_\ell^3}. \tag{1.33}$$

This parameter indicates that the dipole-dipole interaction should be important when the density is such that many atoms lie in a small sphere of volume $\lambda\!\!\!^{-3}$.

1.2 Experiments in the dense regime

Collective interaction in dense samples ($\mathcal{C} > 1$) is a current burgeoning field of research relying on recent technological advances [Davis *et al.*, 1995]. In this section we first

focus on a non-exhaustive list of recent experiments using atoms. It helps understanding the reasons for working with an alkali atomic vapor confined in a nano-cell. Advantages and drawbacks of using such a device also naturally emerge. Particularly, we will see that the use of a small system ($L < \lambda$) is appropriate to perform direct measurement of the near-resonant dipole-dipole interaction. For instance, transmission spectroscopy is an available quantity to probe the interactions and we will finally derive this physical quantity starting from a microscopic approach.

1.2.1 Cold atoms versus thermal vapors

Experiments with cold atoms With the advances in laser cooling techniques [Aspect *et al.*, 1988] of the 90's, the manipulation of motion-frozen atomic ensembles of adjustable density has been made possible. Cold atom experiments (100 nK $< \Theta <$ few μK) therefore emerged as an obvious platform to study collective scattering in the dense regime of interaction. A collection of spectroscopic experiments were undertaken and can be grouped in two categories:

- Large and optically thick ensembles of cold atoms [Bender *et al.*, 2010; Bienaimé *et al.*, 2010; Chalony *et al.*, 2011; Balik *et al.*, 2013] (see top left part of Fig. 1.3)
- Small (typically with sub-wavelength size) and optically thin atomic clouds [Pellegrino *et al.*, 2014; Jennewein *et al.*, 2016; Corman *et al.*, 2017](see top right part of Fig. 1.3)

Experiments in the first category mainly studied macroscopic collective effects such as Mie scattering [Bender *et al.*, 2010], the average radiation force acting on a large cloud of atoms [Bienaimé *et al.*, 2010] or the coherent collective flash in the forward direction [Chalony *et al.*, 2011]. Due to large optical depths[6] (OD), these experiments were conducted either at intermediate densities [Balik *et al.*, 2013] ($\mathcal{C} \sim 0.01$) or far detuned [Bender *et al.*, 2010]. A way to access resonant features even for dense atomic samples consists in probing thinner systems to reduce the optical depth. One method to produce small and dense samples is to load microscopic dipole traps ($L \sim 1$ μm) with randomly positioned resonant scatterers thanks to a high-aperture aspherical lens. In these experiments [Jennewein *et al.*, 2016; Corman *et al.*, 2017] where $\mathcal{C} \sim 1$, the failure of the continuous medium theory has been observed. The microscopic

[6]The optical depth is define as the neperian logarithm of the transmission through a material $-\ln(T)$. Typically, OD=1 means that the transmission factor is $1/e \sim 0.3$.

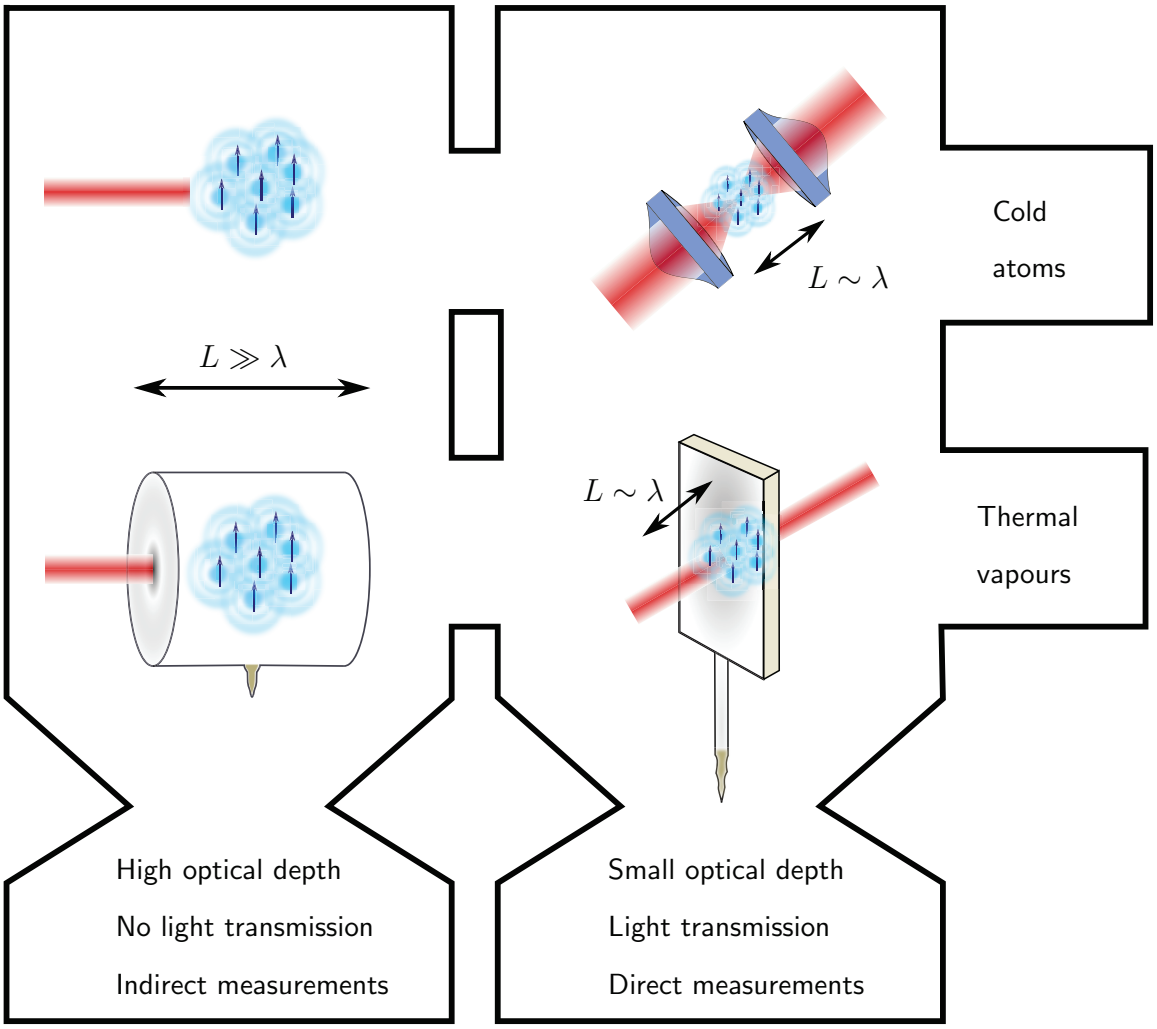

Figure 1.3: Cold and large vs hot and small ensembles Left column: large ensembles ($L \gg \lambda$). Right column: thin ensembles ($L \sim \lambda$). Top line: cold atomic clouds. Bottom line: hot thermal vapors.

approach based on the coupled dipole theory, though closer to experiments, presents no quantitative agreement with the data either. This unexplained disagreement was one of the key motivations that triggered my Thesis project. However we decided to approach the dense regime in a somewhat different configuration.

Experiment with vapor cells Another angle to study resonant dipole dipole interactions with atoms is to use thermal vapors confined in spectroscopic cells. In these systems, atoms are not cold any more and the density of atoms is related to the temperature-dependent (typically $20°\text{C} < \Theta < 400°\text{C}$) vapor pressure via the ideal gas law. This temperature is the one of a reservoir of atoms connected to a spectroscopic

transparent enclosure together constituting a vapor cell. In macroscopic cells (mm to cm thick such as in bottom left part of Fig. 1.3), density dependent ($\mathcal{C} \sim 10$) shifts and widths were observed. The importance of atom-atom collisions due to motion was also reported [Maki *et al.*, 1991; Weller *et al.*, 2011]. As in the case of cold atoms, the optical depth reached in these dense and large systems is very large (OD ≥ 10). These experiments were therefore conducted either far-detuned [Weller *et al.*, 2011] or using elaborate techniques such as selective reflection [Maki *et al.*, 1991]. This last technique consists in exploiting the modification of a reflected beam at a dielectric-vapor interface. In the early 2000s, sub-micrometer cells (see bottom right part of Fig. 1.3) were developped in Armenia in the group of D. Sarkisyan [Sarkisyan *et al.*, 2001]. Density-dependent collective shifts were observed [Keaveney *et al.*, 2012b] at really high density ($\mathcal{C} \sim 50$) with these nano-cells. *This is the experimental system used in this Thesis.* It is described in more details in the next experimental chapters.

In comparison to cold atoms, the use of thermal vapors features strengths and weaknesses. From a theoretical point of view, the task appears much harder since thermal atoms move. As we saw in the previous section, it first makes the coupled dipole model very challenging to use. Phenomena such as atom-atom collisions also lead to difficulties in the modelling of the system. Finally, atom-wall collisions and interactions, coming from the necessity of confining the atoms, also take place. From an experimental perspective however, spectroscopic investigations are much simpler once the nano-cell is built: (i) high collective parameters are simply reached by just turning up the reservoir temperature, (ii) the system-size can be measured much more accurately using optical techniques. Finally, (iii) the compactness of the system allows to change easily the method to probe the interaction, switching for example, from transmission to fluorescence techniques.

1.2.2 From microscopic radiators to macroscopic observables

In this Thesis, the main observable used to probe dipole-dipole interactions is the optical transmission[7] through the nano-cell. As compared to reflection, a technique widely used hitherto with nano-cells [M. Ducloy and M. Fichet, 1991], transmission spectroscopy presents at least two main advantages:

1. By inspection with the far-detuned signal, the transmission dip at resonance gives information about the atomic density $\mathcal{N}$ in the nano-cell.

[7] In Chapter 4, we perform fluorescence spectroscopy and compare the results to the transmission case. We derive the associated equations there.

2. The interpretation of spectral features arising from any expected or unexpected phenomenon is significantly easier starting from a Lorentzian profile rather than a dispersive signal.

Because we do not intend to solve all problems at once, we start by deriving the transmission through a motion-frozen atomic slab closely following the derivation made in Ref. [Fearn, James, and W Milonni, 1996] to solve Eq. (1.31). We use the local relation (1.19) into Eq. (1.18) to find the dipole field radiated at a given point r in space by a small volume d^3r' around r', polarized along the $x-$axis:

$$\begin{aligned}\boldsymbol{\delta E}_{\mathrm{d}}(r) =&\frac{k_\ell^3}{4\pi}\left\{[3(\hat{\mathbf{e}}_x.\hat{\mathbf{n}})\mathbf{n}-\hat{\mathbf{e}}_x]\left(\frac{1}{(k_\ell R)^3}-\frac{i}{(k_\ell R)^2}\right)-[(\hat{\mathbf{e}}_x.\hat{\mathbf{n}})\mathbf{n}-\hat{\mathbf{e}}_x]\frac{1}{k_\ell R}\right\}\\ &\times e^{ik_\ell R}\alpha(\omega_\ell)E_{\mathrm{loc}}(r')\mathrm{d}^3r'\end{aligned} \tag{1.34}$$

and we recall that R=$|\boldsymbol{r}-\boldsymbol{r'}|$, $\hat{\mathbf{n}}=(\boldsymbol{r}-\boldsymbol{r'})/R$ and $\hat{\mathbf{e}}_x$ is the unit vector for the x-axis. For a continuous medium of atomic volume density $\mathcal{N}$, infinite extension in x', y' directions[8]and of thickness L along z' axis, the total dipole field is written as:

$$\begin{aligned}\boldsymbol{E}_{\mathrm{d}}(r) =&\frac{k_\ell^3}{4\pi}\int_{-\infty}^{\infty}\mathrm{d}x'\int_{-\infty}^{\infty}\mathrm{d}y'\int_0^L\mathrm{d}z'\mathcal{N}\\ &\left\{[3(\hat{\mathbf{e}}_x.\hat{\mathbf{n}})\hat{\mathbf{n}}-\hat{\mathbf{e}}_x]\left(\frac{1}{(k_\ell R)^3}-\frac{i}{(k_\ell R)^2}\right)-[(\hat{\mathbf{e}}_x.\hat{\mathbf{n}})\hat{\mathbf{n}}-\hat{\mathbf{e}}_x]\frac{1}{k_\ell R}\right\}\\ &\times e^{ik_\ell R}\alpha(\omega_\ell)E_{\mathrm{loc}}(r').\end{aligned} \tag{1.35}$$

Performing the integrals over x' and y' in the far field regime (*i.e.* ignoring $1/R^3$ and $1/R^2$ terms) is a standard textbook result. It can be shown (Appendix A.1 or [Fearn, James, and W Milonni, 1996]) that the same results survives the near field corrections and that the dipole field projected along the $x-$axis only depends on z and stands for:

$$E_{\mathrm{d}}(z)=\frac{ik_\ell\mathcal{N}\alpha(\omega_\ell)}{2}\int_0^L\mathrm{d}z'E_{\mathrm{loc}}(z')e^{ik_\ell|z-z'|}, \tag{1.36}$$

where by translation invariance in the system, the local field only depends on z'. Finally using Eq. (1.31), the field transmitted at a position z after the slab can be written on its final form:

[8]The laser beam waist used in the manuscript is on the order of 100 µm and therefore much larger than L. It justifies the use of a 1D model.

$$E_{\mathrm{t}}(z) = E_0(z) + E_{\mathrm{d}}(z). \tag{1.37}$$

In the laboratory, we measure transmission spectra defined as the squared ratio of the total transmitted field to the one out of resonance:

$$T(\omega_\ell) = \left| \frac{E_{\mathrm{t}}(z)}{E_0(z)} \right|^2 . \tag{1.38}$$

We have derived from a microscopic approach the transmission through an atomic slab of thickness L. This is an important achievement because we will use it extensively in the following chapters. Note that, within this formalism, the term *absorption* stands for destructive interferences between the incident laser field and the induced dipole field appearing in the numerator. Quite often in the literature, the term *extinction* is mentioned to describe this effect. In the next section, we use this last formula to give insights on our experimental investigation of the interactions.

1.2.3 A transmission model to probe interactions

The transmission coefficient that we just derived depends on the laser frequency through the atomic polarizability $\alpha(\omega_\ell)$. To illustrate this transmission model, we present in this part a theoretical transmission spectrum in the simplest case of a cold, non-interacting and large atomic ensemble. It gives an overview of the way we plan to reveal experimentally the dipole-dipole interactions.

Transmission without interaction In a large and dilute atomic ensemble, the response function of the medium often called susceptibility can be written $\chi = N\alpha$. Besides, the local field reduces to $E_0 e^{ik_\ell z'}$ and using Eq. (1.37), we get for $z > L$:

$$E_{\mathrm{t}} = E_0 \left(1 + ik_\ell \chi L/2\right). \tag{1.39}$$

In Fig. 1.4(a-b), we display the real and imaginary parts of χ respectively associated with the dispersive and absorptive properties of the gas. For a cold, dilute, large slab of atoms (see Fig. 1.4(c)), the resulting transmission spectrum for a collectivity of $\mathcal{C} = 10^{-5}$ and a slab of $L = 1$ mm has a Lorentzian symmetric shape centred around the zero-detuning axis (see Fig. 1.4(d)).

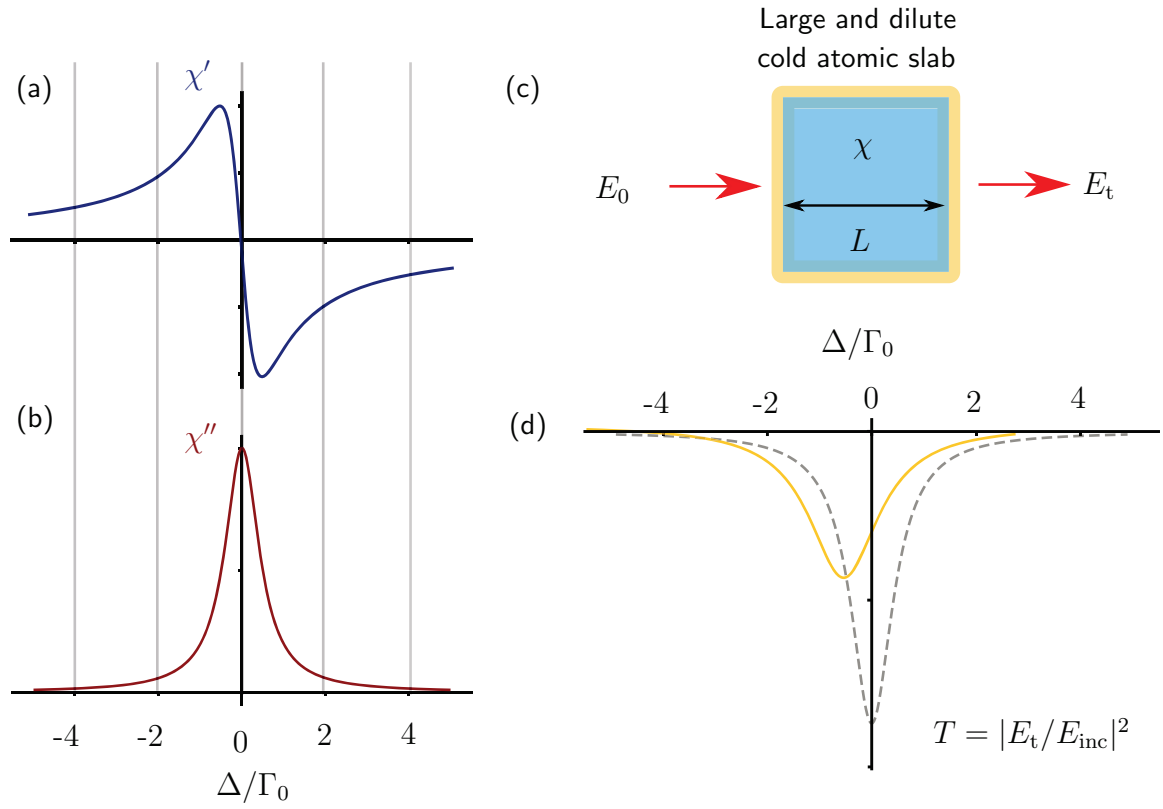

Figure 1.4: Spectroscopic transmission model (a) Normalized real part of the susceptibility χ' associated with the dispersion properties of the gas. (b) Normalized imaginary part of the susceptibility χ'' associated with absorption. (c) Scheme of principle: transmission through a cold dilute and large atomic slab of size L and density $\mathcal{N}$. (d) Transmission spectrum when the laser detuning $\Delta = \omega_\ell - \omega_0$ varies for a collective parameter $\mathcal{C} = 10^{-5}$ and $L = 1$ mm. In dashed grey (respectively yellow), width and shift are Γ_0 and 0 (respectively $2\Gamma_0$ and $-\Gamma_0$).

Experimental investigation of the interactions We present in Fig. 1.4(d), a broadened, and shifted spectrum for comparison (shift of χ: $-\Gamma_0$, and width of χ: $2\Gamma_0$). The experimental work in this Thesis consists in collecting many experimental spectra in a given situation (density N and cell thickness L) and fitting it with the transmission model letting the density of atoms, an extra shift and width as free parameters. We expect these parameters to provide information on the nature of the interaction (dependence with $\mathcal{N}$ for example).

1.3 Using dense thermal vapors in nano-cells: open questions

Obviously, our experimental situation differs from the case of a dilute, large slab of atoms fixed in vacuum. Working with a dense, thermal vapor confined in a nano-cell provides a series of opens questions that will require all along this manuscript to refine the transmission model introduced above.

1.3.1 Atomic motion in thermal vapors

Non-local effects Atomic motion in thermal vapors is one of the most obvious modifications of the spectral properties[9]. How to include it starting from the microscopic approach is not trivial. Reducing motional effects to Doppler shifts [Javanainen *et al.*, 2014; Bromley *et al.*, 2016] is not valid when atoms moves over a distance larger than a wavelength before they relax (*i.e.* $v/\Gamma_0 > \lambda$). This is because the relation between a dipole and the driving field is non-local. In the intermediate case ($\Theta = 100$ µK $\rightarrow v \sim 10$ m.s^{-1}), $v/\Gamma_0 \sim$10 nm, some works are under way to include the motion in a cleaner way [Zhu *et al.*, 2016; Bromley *et al.*, 2016]. For dilute thermal vapors ($\Theta = 300$ K $\rightarrow v \sim 200$ m.s^{-1}), $v/\Gamma_0 \gg \lambda$ and non-local effects are expected to be predominant. How do these effects modify the line-shapes? How should the theoretical model be revised to account for this motion? Are non-local effects layer thickness or density dependent? We will answer these questions in Chapter 2.

Collisions Due to their motion, atoms collide with the cell walls. When the relaxation distance v/Γ_0 is larger than the cell thickness, most of the atoms experience transient dynamics. In this case, the atom-field relation is still more subtle and whether or not the bulk atomic response χ holds is an open-ended question. Simultaneously, atom-atom collisions may happen. Regardless of collision nature approximations, it can be shown [Lewis, 1980] that it produces Lorentzian homogeneous line broadening and shift. In practice, the line-width Γ_0 has to be be corrected to include these effects. Do we see the effect of the collisions in the experimental data? Does it modify the non-local relation between the dipoles and field? How does it scale with the atomic density? Can collisional shift be distinguished from the static Lorentz shift? Answering these questions will link Chapter 2 and 3 together.

[9] It is common knowledge in macroscopic spectroscopic cells that inhomogeneous broadening due to Doppler shift results in Gaussian line-shapes.

1.3.2 Atomic vapor in a nano-cell

Density shifts While previous experiments with vapors reported the presence of density shifts [Keaveney *et al.*, 2012b; Maki *et al.*, 1991], the situation is more confusing in the cold-atoms community where experiments reported the presence of the shift [Roof *et al.*, 2016] or not [Jennewein *et al.*, 2016; Corman *et al.*, 2017]. Besides, theoretical works showed that these shifts should depend on the medium geometry (slab [Friedberg, Hartmann, and Manassah, 1973; Friedberg and T. Manassah, 2009], ellipse [Friedberg and Manassah, 2010],...). The origin and condition of validity of these shifts are also actual sources of debate [Javanainen *et al.*, 2014; Keaveney *et al.*, 2012b]. It is first worth to clarify the situation. How is the local field expression in Eq. (1.36) refined to account for dipole dipole interaction? Is the geometry dependence of quantum nature or can it be explained classically? What is the role of the Fabry-Perot nature of the cavity in this affair? Chapter 3 clarifies to a certain extent this long-standing debate.

Cavity effects The cells used in this manuscript are either made in sapphire (refractive index $n_s = 1.76$) or borofloat ($n_s = 1.46$) leading to very low finesse cavities $\mathcal{F} \sim 1$. This leads to a variety of complications to account for. First, the field driving the dipoles is modified inside the cavity. Then, the field radiated by the atoms can be multiply reflected hence leading to strong line-shape asymmetries that need to be understood for fitting purposes. Bypassing a complete line-shape model is an approach often used by many authors that could be misleading as we will see in Chapter 3. How to account for the physical environment surrounding the atoms is clarified along the different chapters.

Interaction with a surface Close to a surface, the van der Waals potential scales as $1/z^3$ in the non-retarded regime where z is the atom-surface distance. The order of magnitude of this effect is comparable to the resonant dipole-dipole interaction. The atoms experience a spatially varying potential that produces inhomogeneous shifts: it is another source of non-Lorentzian line-shapes. In Chapter 4, we incorporate this potential into the transmission model and we try to find a method to extract in a precise way the interaction strength C_3. It raises a panel of questions such as: (i) Does C_3 depends on the surface material? (ii) May surface roughness have a significant impact on the spectra? (iii) Can a repulsive potential close to the surface induce an atom-surface bound state? Does it even exist? We will try to answer this question in Chapter 5.

1.3.3 Coherent and incoherent light scattering

Last but not least, there are not less than two reasons for addressing all these previous questions using off-axis fluorescence spectroscopy. As compared to transmission spectroscopy, off-axis light scattering do not follow the Helmholtz equation where the emitters can be described with an effective dielectric constant. This scattering rather originates from the random positions of the scatterers in the ensemble [Schilder *et al.*, 2017]. It is therefore enlightening to investigate the presence or not of non-local, cavity, surface or density effects on an incoherent light spectrum. This will be the purpose of Chapter 6.

Chapter 2

Mesoscopic reponse of a dilute atomic vapor confined in a nano-cell

Contents

Introduction

In Chapter 1, we pointed out the importance of the atomic motion in the optical response of an ensemble of atoms. In this second chapter, we show that it leads to a mesoscopic response of a vapor confined in a nano-cell. One important characteristic of mesoscopic systems is the fact that their properties are not ruled by local quantities. The mesoscopic regime arises when the size of the system becomes smaller than a distance ξ characterizing the non-local response of the medium to an excitation.

Non-locality is thus a prerequisite to the observation of mesoscopic behaviors. For instance, the concept of local conductivity fails to describe the transport of electrons or phonons when the distance over which the phase of the carriers is lost exceeds the size of the system, as is the case in nano-wires [Agrat, Yeyati, and van Ruitenbeek, 2003; Schwab *et al.*, 2000]. In these systems the electrical potential (or the temperature) is undefined and one uses instead a global conductance. Also, non-local effects are at the origin of the low temperature anomalous conductivity of a metal at frequencies ranging from GHz to infra-red [Pippard and Bragg, 1947], as the skin depth over which the field varies near a surface is smaller than the mean-free path of the electrons in the metal [Wooten, 1972; Gilberd, 1982]. In this particular situation, only the electrons that move parallel to the surface of the metal can contribute significantly to the conduction process.

In optics, non-locality is often observed in *non-linear* bulk media [Boyd, 2009; C. Rotschild and Segev, 2006], in particular in the presence of long-range interactions between particles [Busche *et al.*, 2006]. In contrast, manifestations of non-local optical properties in *linear* media are scarce. They have been observed for molecules near metallic surfaces [Eagen *et al.*, 1980; Ford and Weber, 1984] and the mesoscopic regime was reached with nano-particles for which the electron mean-free path is on the order of the particle size [Kreibig and Genzel, 1985; Voisin *et al.*, 2001]. Also, the *selective reflection* at the interface between a glass and a bulk atomic vapor [Cojan, J. L. , 1954; Burgmans, Schuurmans, and Bölger, 1977; Briaudeau *et al.*, 1998] was interpreted as an indirect evidence of non-locality originating from the motion of the atoms and their transient response following a collision with the glass surface [Schuurmans, 1976; Nienhuis, Schuller, and Ducloy, 1988; Vartanyan and Trger, 1994; Vartanyan and Lin, 1995; Ritter *et al.*, 2018].

In any *homogeneous* medium, the relation between the polarization vector and the electric field at a frequency ω_ℓ is given by[1] (one-dimensional model) [Landau and Lifshitz, 1960]:

$$P(z,\omega_\ell) = \int_{-\infty}^{+\infty} \mathrm{d}z' \epsilon_0 \chi(z-z',\omega_\ell) E(z') \ , \tag{2.1}$$

where the susceptibility $\chi(z-z',\omega)$ describes the spatial response of the medium and typically decays over a distance ξ, the so-called range of non-locality. In an atomic vapor, the non-locality comes from the atomic motion and ξ is equal to their phase coherence length, *i.e.* the distance travelled by the atoms before the phase of the light excitation imprinted on them is lost. It is lost due to collisions with other particles or

[1] In contrast to Chapter 1, where we used the local relation $P(z') = \epsilon_0 \chi(z') E(z')$.

to radiative decay and $\xi = v/\Gamma_t$ with v the atom velocity and Γ_t the total homogeneous line-width [Schuurmans, 1976; Nienhuis, Schuller, and Ducloy, 1988; Vartanyan and Lin, 1995]. The total homogeneous line-width is the sum of the natural line-width Γ_0 and collisional effects. In a nano-cell, the presence of the walls separated by a distance L breaks the translational invariance and the mesoscopic regime is achieved as soon as $\xi \gtrsim L$. Confining vapors in nano-cells, the non-locality should give rise to a mesoscopic response, as the system size is now on the order of the phase coherence length ξ, as explained below. So far, the interplay between non-locality and system-finite size were barely studied in nano-cells [Dutier *et al.*, 2003b]. In particular, the question remains whether the concept of susceptibility itself holds in the mesoscopic regime. Another important issue to clarify is the range of experimental parameters for which the local transmission model introduced in Eq. (1.31) remains valid.

Structure of the chapter. We first show that including the atomic motion in the optical Bloch equations yields a non-local susceptibility with a spatial extension ξ. Then, we point out that if the cell thickness L is such that $\xi > L$, the atoms do not reach steady-state leading to a *mesoscopic regime*. With the initial aim of studying dipole-dipole interactions, we confined a Cs atomic vapor in a nano-cell and collected transmission spectra. In the dilute regime, we observed striking differences with respect to usual spectra gathered in bulk cells. To explain these differences, we then derive two transmission models that include the Fabry-Perot nature of the nano-cell. On the one hand, *Model 1* ignores the spatial extension ξ hence the non-local properties of the vapor. On the other hand, *Model 2* accounts for it and contains the mesoscopic properties of the system. We fit the experimental spectra with the two models for different cell thicknesses. A study of the fitted parameters reveals the mesoscopic characteristics of the vapor-cell system.

2.1 Mesoscopic response due to the atomic motion

In this section, we explain the origin of the mesoscopic response of a thermal atomic vapor confined in a nano-cell.

2.1.1 Hydrodynamic Maxwell-Bloch equations for the coherence field

We aim at describing the propagation of a laser field along the z axis through an atomic vapor. To this purpose, we decompose the linearly polarized, monochromatic field driving the atom inside the cavity formed by the sapphire plates:

$$E(z,t) = \frac{1}{2}\left[E(z)e^{-i\omega_\ell t} + E^*(z)e^{i\omega_\ell t}\right], \tag{2.2}$$

and the polarization of the atomic vapor:

$$P(z,t) = \frac{1}{2}\left[P(z)e^{-i\omega_\ell t} + P^*(z)e^{i\omega_\ell t}\right], \tag{2.3}$$

in their positive and negative frequency components. We first consider a given atomic transition between ground and excited states, with respective hyperfine states F and F'. The transition frequency is $\omega_{\mathrm{FF'}}$ and the dipole matrix element $d_{\mathrm{FF'}}$. For this transition, we introduce the classical coherence field $\rho_{21}(z,t,v) = \langle \rho_{21}^{(i)}(t,v)\rangle_{\mathrm{atoms}}$ where $\langle \ldots \rangle$ is the configuration average of the coherences $\rho_{21}^{(i)}$ of all atoms i located within the $(z, z+\delta z)$ slab and with velocities in the range $(v, v+\delta v)$ where $\delta z, \delta v \to 0$. The evolution of this field is given by the hydrodynamic equation:

$$\frac{\partial \rho_{21}(z,t,v)}{\partial t} = \overbrace{-i\omega_{\mathrm{FF'}}\rho_{21}(z,t,v) + i\frac{d_{\mathrm{FF'}}E(z,t)}{\hbar} - \frac{\Gamma_{\mathrm{t}}}{2}\rho_{21}(z,t,v)}^{\text{Internal atom evolution (Bloch equations)}} \overbrace{-v\frac{\partial \rho_{21}(z,t,v)}{\partial z}}^{\text{atoms flying into and off from the slab at position } z}. \tag{2.4}$$

The quantity $d_{\mathrm{FF'}}$ is the dipole matrix element of the transition at a pulsation $\omega_{\mathrm{FF'}}$ between states F and F'. In the following, we will use the notation $d_{\mathrm{FF'}} = dC_{\mathrm{FF'}}$ as[2] in Ref. [Siddons *et al.*, 2008]. The first part of the right hand side of the equation is the standard Bloch equations for the evolution of the coherence under weak driving (we explained this term in Chapter 1), when the population of the excited state can be neglected ($\rho_{22} \to 0$). In addition, since the field is defined as an average over many atoms at a given location z, it can also change due to atoms flying into and off the vapor slab at position z. It appears owing to the fact that we consider the coherence field rather than the coherence of a given atom. The corresponding term is written under the second brace. Using Eq. (2.2) and the rotating wave approximation, we

[2] We can find in Ref. [Siddons *et al.*, 2008] that $d = 3\sqrt{\frac{\epsilon_0 \hbar \Gamma_0 \lambda^3}{8\pi^2}}$ and $C_{\mathrm{FF'}}$ are the Clebsch-Gordan coefficients that depends on the hyperfine transition.

obtain the time-independent equation

$$v\frac{\partial\rho_{21}(z,v)}{\partial z} = -\left[\frac{\Gamma_{\mathrm{t}}}{2} - i\Delta_{\mathrm{FF'}}\right]\rho_{21}(z,v) + i\frac{dC_{\mathrm{FF'}}E(z)}{2\hbar}, \tag{2.5}$$

where $\Delta_{\mathrm{FF'}} = \omega_\ell - \omega_{\mathrm{FF'}}$ is the laser frequency detuning from the atomic transition.

2.1.2 Non-local susceptibility

To understand the origin of the non-locality, we take the Fourier transform of this last equation with respect to z and t, resulting in[3]:

$$\rho_{21}(k,\omega_\ell,v) = iC_{\mathrm{FF'}}\frac{dE(k,\omega_\ell)}{2\hbar}\frac{1}{\Gamma_t/2 - i(\Delta_{\mathrm{FF'}} - kv)}. \tag{2.6}$$

In the (k,ω) space and for an homogeneous medium, the relation between the polarization and the field is: $P(k,\omega_\ell) = \epsilon_0\chi(k,\omega_\ell)E(k,\omega_\ell)$. Besides, we have $P(k,\omega_\ell) = \langle 2\mathcal{N}\, d\, C_{\mathrm{FF'}}\rho_{21}(k,\omega_\ell,v)\rangle$, with $\mathcal{N}$ the vapor density and where $\langle\ldots\rangle$ is the average on the the Maxwell Boltzmann velocity distribution $M_{\mathrm{b}}(v)$. Consequently the susceptibility of the vapor in the (k,ω) space is $\left\langle\chi_v^{\mathrm{FF'}}(k,\omega_\ell,v)\right\rangle$ with:

$$\chi_v^{\mathrm{FF'}}(k,\omega_\ell,v) = i\mathcal{N}\frac{C_{\mathrm{FF'}}^2 d^2}{\hbar\epsilon_0}\frac{1}{\Gamma_t/2 - i(\Delta_{\mathrm{FF'}} - kv)}\ . \tag{2.7}$$

The k-dependence (not to be confused with k_ℓ, the wave-vector of the laser) resulting from the Doppler effect is at the origin of the non-locality and leads to spatial dispersion [Landau, Pitaevskii, and Lifshitz, 1960]. The inverse Fourier transform in k yields the susceptibility in the (z,ω) space:

$$\chi_v^{\mathrm{FF'}}(z-z',\omega_\ell,v) = i\mathcal{N}\frac{C_{\mathrm{FF'}}^2 d^2}{\hbar\epsilon_0}\frac{1}{2\pi}\int_{-\infty}^{\infty}\frac{e^{ik(z-z')}}{\Gamma_t/2 - i(\Delta_{\mathrm{FF'}} - kv)}\,\mathrm{d}k. \tag{2.8}$$

To calculate the integral, we integrate in the k-complex plane.

When applying the residue theorem, care must be taken, as the position of the pole

[3] The driving field is monochromatic here. We do not write the delta function in the ω space for sake of simplicity. The method can yet be generalized to more complex driving fields.

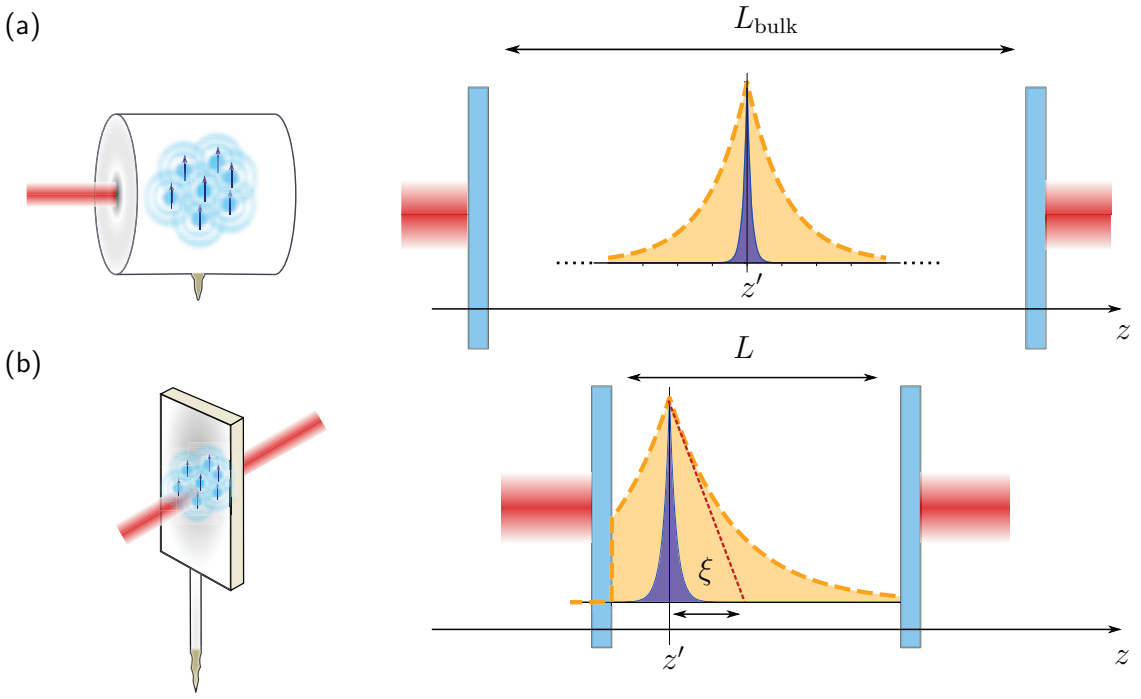

Figure 2.1: Non-local and mesoscopic effects Illustration of the non-local response in presence of an interface in a bulk cell (thickness L_{bulk}) and a nano-cell (thickness L). Light orange fill: non-local response χ for $\xi \sim \lambda$. Dark blue fill: local response χ for $\xi \ll \lambda$. (a) In a bulk cell, the response function is not affected by the walls. (b) In a nano-cell, the non-local response leads to mesoscopic effects: the atomic response is modified by the presence of the walls.

$k_0 = (\Delta_{\text{FF'}} + i\Gamma_t/2)/v$ in the plane depends on the sign of the velocity[4]. It leads to:

$$\chi_v^{\text{FF'}}(z-z',\omega_\ell,v) = 0 \quad \text{when} \quad \frac{z-z'}{v} < 0\ , \tag{2.9}$$

$$\chi_v^{\text{FF'}}(z-z',\omega_\ell,v) = i\mathcal{N}\frac{C_{\text{FF'}}^2 d^2}{\hbar\epsilon_0|v|}\exp\left[\left(-\frac{\Gamma_{\text{t}}}{2}+i\Delta_{\text{FF'}}\right)\frac{z-z'}{v}\right] \quad \text{when} \quad \frac{z-z'}{v} > 0\ . \tag{2.10}$$

The expression (2.10) shows that the distance ξ over which the polarization depends on the field (*i.e.* the range of non-locality) is $\xi = |v|/\Gamma_{\text{t}}$, thus confirming the qualitative discussion at the beginning of the chapter. For a typical vapor at room temperature (no collisional broadening), $v \simeq 200$ m.s^{-1} and $\Gamma_{\text{t}} = \Gamma_0 \simeq 2\pi \times 10$ MHz which leads to $\xi \simeq 3$ µm. This distance originates from the motion of the atoms and drastically

[4]The fact that $\chi_v(z-z',\omega_\ell,v)$ depends on the sign of $(z-z')/v$ indicates that the optical response at position z only depends on atoms located at position $z' < z$ moving with a positive velocity and on atoms at $z' > z$ having a negative velocity.

modifies the properties of the field transmitted by the system, as we will see below.

NOTE: Non-locality is not specific to nano-cells and the susceptibility in large cells is represented in Fig. 2.1(a). In this case, the distance ξ over which the atoms relax is much smaller than the cell thickness ($\xi \ll L$) and the atoms reach steady-state. In a nano-cell, the situation is different because atoms are closer to cell surfaces. Boundary conditions due to atom-wall collisions must be accounted for independently.

2.1.3 Mesoscopic response of the vapor-cell system

Quenching collisions We assume quenching collisions with the cell walls [Schuurmans, 1976], *i.e.* the phases of the atomic coherences are reset upon collisions. Velocity classes $\pm v$ become independent and the presence of the walls therefore breaks the translational invariance in the medium (in contrast with elastic collisions). We express this fact by multiplying $\chi_v(z-z',\omega_\ell)$ by a top-hat function ($\Pi_0^L(z')=1$ for $0<z'<L$ and is null elsewhere). When $\xi \gtrsim L$, the atoms mainly experience a transient flight inside the cell. The non-local response of the medium then depends on the size L of the entire system, and is not a characteristic of the bulk medium only (see Fig. 2.1(b)). This regime, called mesoscopic, is not reached either in bulk cells where the atomic response is not truncated ($\xi < L$), nor if the spatial extension ξ is neglected. Finally, the response of the system is obtained by summing over all the atomic transitions:

$$\chi_L(z,z',\omega_\ell) = \sum_{F,F'} \Pi_0^L(z') \times \left\langle \chi_v^{\mathrm{FF'}}(z-z',\omega_\ell,v) \right\rangle . \tag{2.11}$$

This final expression will be used later in the chapter.

Now that we have described the origin of the mesoscopic regime, we present our experimental work.

2.2 Measurement of the optical transmission of an atomic vapor in the dilute regime

In this section, we present in more details our experimental set-up to observe the optical transmission through the nano-cell. We particularly describe the methods used to measure the vapor properties such as density $\mathcal{N}$ and thickness L. Subsequently, we produce experimental transmission data and comment their spectral properties.

2.2.1 The experimental set-up

Details about the nano-cell The sapphire cells used in this manuscript are built in Armenia in the group of D. Sarkisyan [Sarkisyan *et al.*, 2001]. Prior to filling, the system is pumped to reach a vacuum level better than 10^{-3} mbar. The one used in this chapter is loaded with Cs atoms. Both windows are made of 1 mm thick sapphire (Al_2O_3) crystal with 20 mm×30 mm transverse dimensions. The crystal plates are cut such that the surface plane is perpendicular to their optical axis to avoid any birefringence issue. Their surface roughness is on the order of 3 nm rms. One of these plates is slightly curved, with a radius of curvature $R > 100$ m leading to a wedged shape (angle $\sim 10^{-4}$ rad). Both of them are connected together with a thermo-resistant glue handed with platinum spacers. The resulting space between them (*i.e.* the nano-cell), varies between 30 nm and 2 µm. We show a picture of the nano-cell in Fig. 2.2(b). The windows are connected[5] to the atomic reservoir whose temperature defines the density of atoms inside the nano-cell.

Measurement of the temperature At thermodynamic equilibrium, the saturation vapor pressure $\mathcal{P}$ at a temperature Θ is related to the atomic density with the ideal gas law $\mathcal{N} = \mathcal{P}/k_B\Theta$, where k_B is the Boltzmann constant. The vapor pressure dependence with temperature can be found in Ref. [Zentile *et al.*, 2015a] and differs from one alkali to another. The main reason for measuring the temperature is that the top part with the wedged sapphire windows must remain 30°C warmer than the reservoir to avoid vapor condensation. To this purpose, two alumina-chrome thermocouples (type K) are positioned to measure the temperature of the side-arm and windows heated by separated home-made ovens. The temperature measured by the reservoir thermocouple should provide an information on the density of atoms in the nano-cell. Due to possible temperature variations and because the reservoir thermocouple is not directly in contact with the atoms, we cannot estimate the *real* atomic temperature with a better precision than $\Delta\Theta = \pm 10$°C. We will rather deduce more accurately the atomic density directly from the spectral properties.

Measurement of the thickness A second important parameter in the system is the cell thickness. It is measured by an off-resonant interferometric technique initially described in [Jahier *et al.*, 2000]. The idea is to collect the laser intensity reflected

[5] From our collaboration with colleagues in Armenia, we receive cells (with no details as to how they are fabricated). Particularly, key points such as the use of glue or spacers and the connection of the sapphire side-arm to the Pyrex vacuum manifold are kept secret.

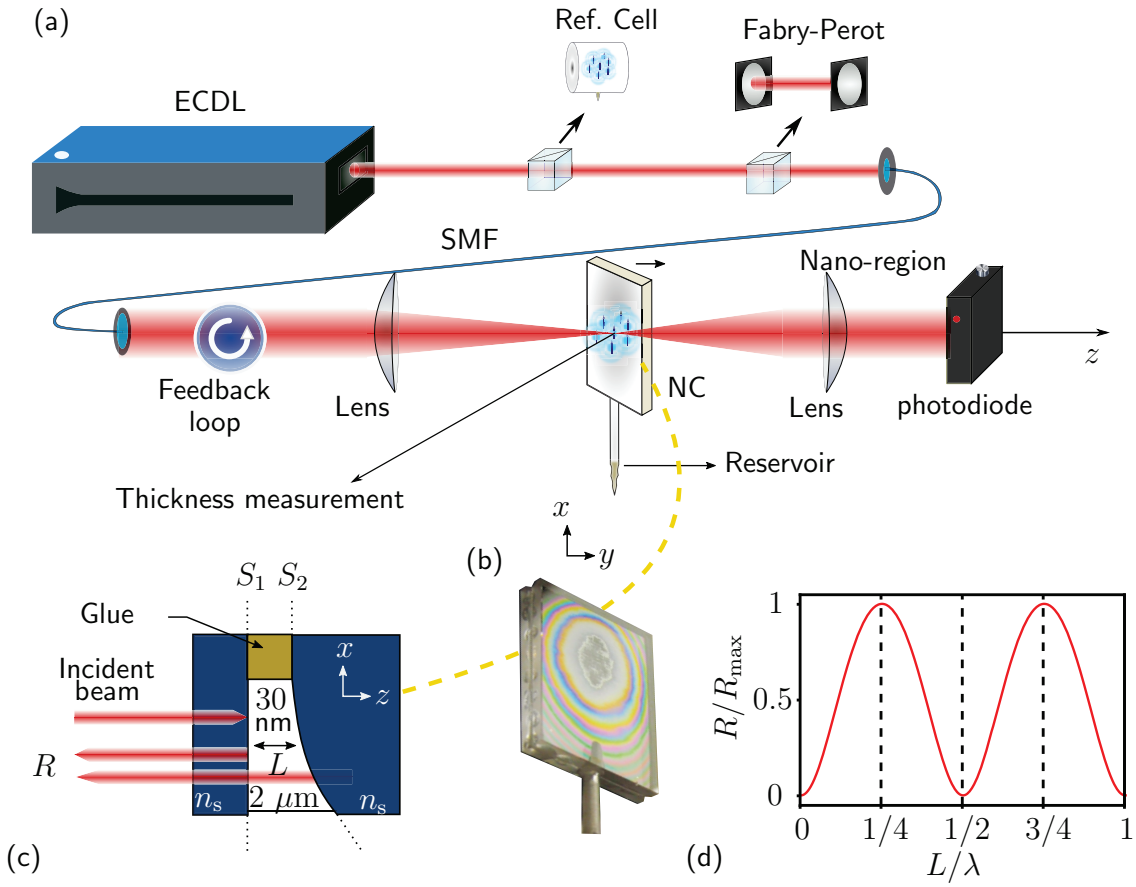

Figure 2.2: Experimental set-up (a) ECDL: DL-PRO external cavity diode laser from TOPTICA. Ref. Cell: 7-cm Cs filled vapor cell for reference spectroscopy. Fabry-Perot: home-made etalon for time-to-frequency laser scan linearization (see also Fig. 2.3(a-b)). SMF: single-mode fiber. Lens: focal lens with a 75-mm focal length. Feedback loop (see also Fig. 2.3(c)) NC: nano-cell. The transmitted light is collected on a photodiode placed after the nano-cell. (b) Photograph of the Cs nano-cell. Newton fringes indicate the wedged shape of the nano region. (c) Thickness measurement: the incident beam is reflected on the sapphire-vacuum (S_1) and vacuum-sapphire (S_2) interfaces. The angle of the wedge is exaggerated. The two reflections interfere to give the reflected signal R. (d) Normalized reflection power R according to the cell thickness. Knowing where the optical contact (here $L = 0$ correspond to the glued part) is, we deduce the cell thickness from the reflected power intensity.

from the interferences on the surfaces of the wedge of the cell (see Fig. 2.2(c)). Due to the Fabry-Perot nature of the nano-cell, the reflection intensity with respect to the cell thickness is proportional to:

$$R = 1 - \left| \frac{4n_s/(1+n_s)^2}{1 - \left(\frac{n_s-1}{n_s+1}\right)^2 \exp\left(2ik_\ell L\right)} \right|^2 . \tag{2.12}$$

We display in Fig. 2.2(d) the normalized interferometric signal as a function of the cell thickness. When we measure the cell thickness, the laser scan is stopped and its frequency is set far-off resonance. The laser is focused on the cell with a waist ($1/e^2$ in intensity) smaller than 100 µm. With this method, the precision on the cell thickness determination is mainly limited by the waist size and is typically between 5 and 10 nm. This is an important estimation because this parameter will be fixed in our fitting procedures.

Driving field properties One major asset of the experimental system is that the laser used for measuring the local cell size simultaneously drives an atomic slab of the very same thickness (See Fig. 2.2(a) for set-up details). The external-cavity diode laser (DL PRO from TOPTICA) has a spectral line-width better than tenths of kHz. It impinges on the nano-cell at almost normal incidence. When the laser drives the atoms, it is continuously scanned at a few Hertz rate around the alkali resonant line of interest. In this chapter $\lambda = 894$ nm for the D_1 line of Cs. The laser power is on the order of 1 µW (if not recalled later, this is the case in all the manuscript) such that the intensity of the laser incident on the atoms is way below the saturation threshold (saturation parameter $s < 0.1$ [Steck]). As a result, we comply with the weak probe approximation introduced in Chapter 1. The experimental limits of this regime are further studied in Appendix B. In order to produce an experimental transmission spectrum, *i.e.* a transmission according to the laser frequency, we need to calibrate the signal collected on the photodiode. This is the purpose of the next part.

2.2.2 Calibration of the detection system

The laser light is transmitted through the vapor filled nano-cell and the resulting atomic spectra are collected on a silicon-based low-noise Thorlabs photodiode (model DET36A/M). The raw data signal consists in a voltage as a function of time. Inspired by a previous work [Keaveney, 2014], I have developed two procedures to

normalize transmission spectra:

Time-to-frequency normalization. To observe a transmission spectrum, we scan the laser frequency over the atomic resonances. However, this scan is not linear with time. In other words, there is *a priori* no linear relation between the recorded time on the photodiode and the laser frequency. An home-made Fabry-Perot is initially used to correct the time non-linearity in the laser frequency scanning. The spacing between both mirrors of the cavity is about 10 cm leading to a free spectral range of about 1 GHz, but the exact value is not important. The calibration is done as follows:

- We first locate the arrival times corresponding to the transmission maxima of the Fabry-Perot represented in Fig. 2.3(a).
- We fit these time locations with a linear function. The difference between the experimental arrival times and the linear fit reveals the non-linearity in the laser scanning (see Fig. 2.3(b)).
- We fit the difference by a polynomial function of order 3. Then, we subtract from our experimental data this third-order correction. As a result, the relation between the corrected time and the frequency becomes linear.

A 7-cm commercial spectroscopic cell is finally used to do the time-to-frequency conversion [Steck]

Normalization of the transmission signal The intensity of the laser varies when the frequency scan is performed. Several techniques are possible to correct for this variation. The most simple method is to assume a linear variation and proceed to a division of the raw data by a ramp matching the off-resonant signal. However, due to Fabry-Perot effects on several elements of the set-up (lenses, cubes, wave-plates, fibers...), this linear variation is not an ideal approximation. We have therefore set-up a feedback loop to stabilize the laser intensity when it scans the frequency. The intensity feedback loop is represented in Fig. 2.3(c) associated with a scheme of principle of its operation. To adapt the optical intensity variation in real time, the corrector needs to be much faster than the laser scan rate. Initially, we have built an home-made proportional, integral, and differential controller (PID). It broke for unexplained reasons and we finally used a commercial one (the LB1005 Servo controller from Precision Photonics). In practice, we managed to correct intensity variations up to 0.5% of absorption, limited by residual Fabry-Perot effect after the controller. Thanks

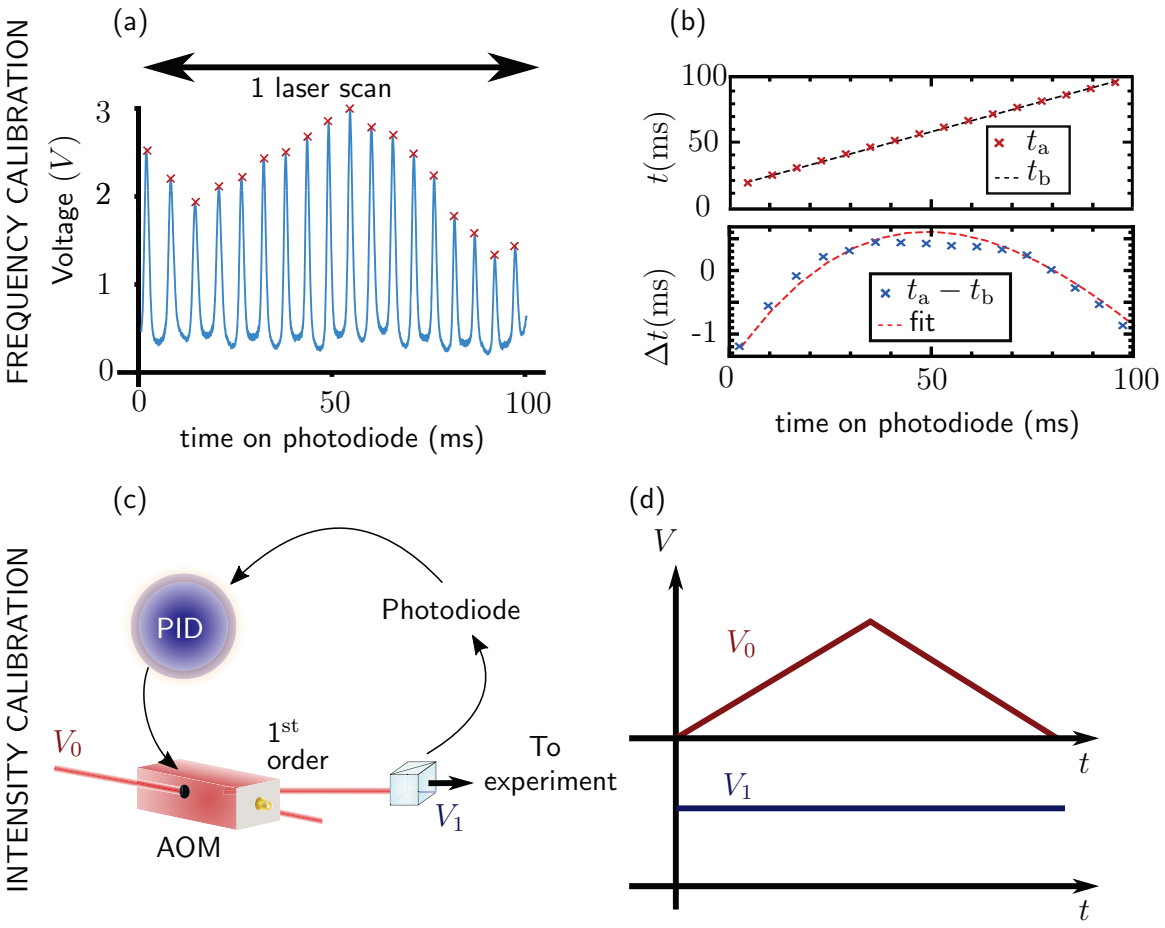

Figure 2.3: Calibration of the detection system (a) Transmission from a home-made Fabry-Perot as a function of the time recorded on the photodiode. The red crosses show the location of the peaks. (b) Top panel: Red crosses are the arrival time t_{a} of the transmission peaks as a function of the recorded time. The black dotted line is a linear fit to the data (t_{b}). Bottom panel: The subtraction of the arrival time by the linear fit show the non-linearity in the laser scan (blue crosses). Red dotted line: 3^{rd} order polynomial fit to the data which is finally used to correct the initial recorded time. (c) Feedback loop. Initial laser power before the loop: V_0. The first diffraction order from the acousto-optic modulator (AOM) is collected on a photodiode. The signal is sent on a proportional-integral-derivative controller (PID) that acts back on the AOM to correct the intensity variations. The corrected signal after the loop is V_1. (d) Signals V_0 and V_1 (ideal representation) with respect to time.

to this operation, we only have to divide the raw data by the transmission out of resonance, which is expected to be flat (*i.e.*independent of the frequency, see Fig. 2.3(d) for an ideal operation).

2.2.3 Experimental spectra in the dilute regime

Observation of the Dicke Narrowing We present in Fig. 2.4(b) spectra resulting from the above calibrations for a temperature of $\Theta = 170°C$ and different cell thicknesses. For the sake of comparison, we superimpose as a dashed line a spectrum obtained in a 7-cm reference spectroscopic cell. The scheme of the Cs D_1 line energy levels probed by the laser is represented in Fig. 2.4(a). The differences between the spectra in nano and bulk cells are striking. First, we observe out of resonances that the spectra collected in the nano-cell feature very long tails with respect to the large cell spectrum. Also, the line-shapes obtained with the nano-cell are more narrow on resonance and seem Lorentzian in comparison to the broad and Gaussian-like spectrum observed in the bulk cell. These spectral properties have already been reported in many studies [Briaudeau *et al.*, 1998; Dutier *et al.*, 2003a] and the phenomenon is commonly known as the Dicke narrowing. The main idea of this narrowing is the fact that only atoms flying parallel to the cell walls contribute significantly to the optical response (a situation reminiscent of the anomalous skin depth described in the introduction). The other atoms collide with the cell walls and do not reach steady-state: the cell acts like a velocity filter.

Oscillation of the transmission with L Another striking feature can be observed in Fig. 2.4(c), where we plot the value $T_{\min}$ of the minimum of the transmission for the hyperfine transition from $F = 4$ to $F' = 3$ according to the cell thickness. We see that $T_{\min}(L)$ does not decay exponentially as the Beer-Lambert law predict. This is expected for two reasons[6]. Firstly, the atoms being in a cavity, the transmitted field amplitude is not given by the Beer-Lambert law: a $\lambda/2$-periodic oscillation, originating from the multiple reflections in the cavity, modulates the exponential decay. Secondly, even without the cavity, the field inside the vapor cannot be exponential due to the mesoscopic character of the system, which leads to a λ-periodic oscillation. This λ-periodic oscillation, characteristic of the mesoscopic regime and commonly named

[6]The increase in transmission that we can see at $L \sim \lambda/4$ is probably due to a inaccurate measurement of the local thickness. Indeed, for L being a multiple of $\lambda/4$, we should use another laser to refine the precision on the measurement (see also [Dutier, 2003]).

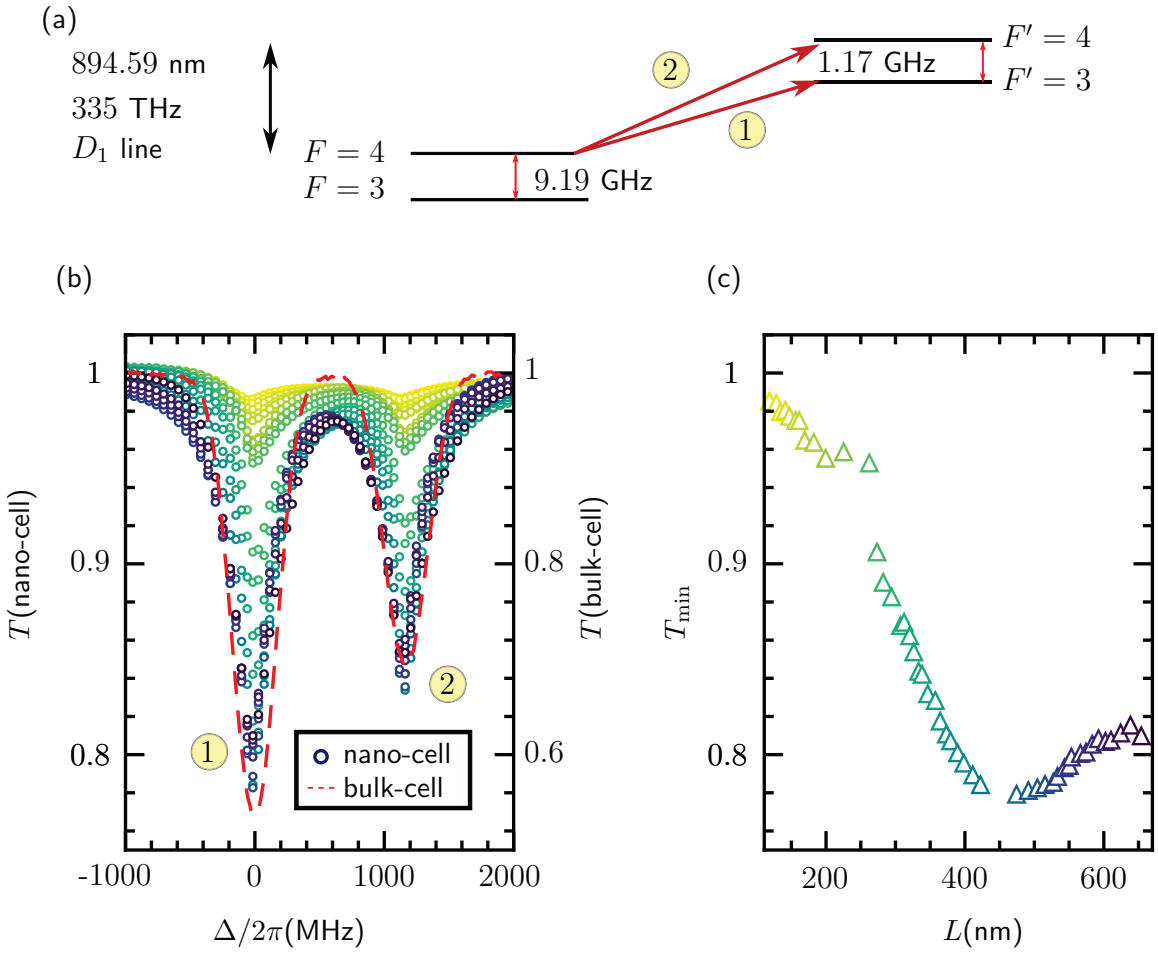

Figure 2.4: Oscillation of the minimum of transmission (a) Scheme of the Cs D_1 line energy levels. The laser scans $F = 4$ to $F' = [3, 4]$ denoted respectively by transition 1 and 2. (b) Experimental spectra of the Cs D_1 line with respect to the laser detuning. The zero detuning is defined with respect to the $F = 4$ to $F' = 3$ transition. The temperature is $\Theta = 170°$C and from yellow to purple: $L \in [110\ \text{nm}, 670\ \text{nm}]$. In dashed red line a spectrum in a 7-cm bulk cell is superimposed. (c) Minimum of transmission $T_{\min}$ directly extracted from the spectra.

the *collapse and revival* of the Dicke narrowing [Dutier *et al.*, 2003b] will be discussed in more details in Chapter 6.

Based on the results of section 2.1, we will develop two models to interpret the experimental data:

1. The *Model 1*, that incorrectly ignores the spatial extension ξ and therefore neglects the mesoscopic regime.

2. The *Model 2*, that correctly accounts for the atomic motion and incorporates the mesoscopic response.

2.3 Transmission through the nano-cell in the mesoscopic regime

In order to derive the field transmitted by the system, we first calculate the field radiated by the atoms ignoring the sapphire cell. We then provide more general expressions that account for the Fabry-Perot nature of the cell. We finally build *Model 1* and *Model 2* to interpret the experimental data.

2.3.1 Field emitted by a vacuum-immersed thin atomic layer

We first consider an atomic slab of thickness L placed under vacuum, *i.e.* we do not consider the sapphire windows of the nano-cell. As before, the slab is excited by a plane wave (frequency ω_ℓ) with complex amplitude $E_0 \exp[ik_\ell z]$ where $k_\ell = \omega_\ell/c$. We recall from Chapter 1 that the amplitude of the field transmitted after the slab is[7] [Fearn, James, and Milonni, 1996]:

$$E_{\mathrm{t}}(z > L) = E_0 e^{ik_\ell z} + \frac{ik_\ell}{2\epsilon_0} \int_0^L \mathrm{d}z' P(z', \omega_\ell) e^{ik_\ell (z - z')} \ . \tag{2.13}$$

In a non-local linear medium consisting of atoms moving with velocity v (distribution $M_{\mathrm{b}}(v)$) as considered here, the relation between the polarization vector and the field is:

$$P(z, \omega_\ell) = \int_{-\infty}^{\infty} \mathrm{d}z' \epsilon_0 \chi_L(z, z', \omega_\ell) E(z'), \tag{2.14}$$

[7] Note that it is equivalent to Eq. (1.31), regardless of the relation (local or not) between the polarization and the field.

leading to the following expression for the transmitted field:

$$E_{\rm t} = E_0 e^{ik_\ell z} + \sum_{F,F'} \frac{ik_\ell}{2\epsilon_0} \int_0^L {\rm d}z' e^{ik_\ell(z-z')} \underbrace{\left[\int_{-\infty}^{\infty} {\rm d}z'' \epsilon_0 \left\langle \Pi_0^L(z'')\, \chi_v^{\rm FF'}(z', z'', \omega_\ell, v) \right\rangle E(z'') \right]}_{I=I_1+I_2}. \tag{2.15}$$

The average $\langle ... \rangle$ on the Maxwell distribution is an integral over velocity $\int_{-\infty}^{\infty} {\rm d}v M_{\rm b}(v)$. It gives two integrals I_1 for positive and I_2 for negative velocity classes:

$$I_1 = \int_0^{z'} {\rm d}z'' \epsilon_0 \int_0^{\infty} {\rm d}v M_{\rm b}(v) \frac{i\mathcal{N} C_{\rm FF'}^2 d^2}{\hbar \epsilon_0 v} \exp\left(\frac{z'-z''}{v} (-\frac{\Gamma_{\rm t}}{2} + i\Delta_{\rm FF'}) \right) E(z''), \tag{2.16}$$

$$I_2 = \int_{z'}^{L} {\rm d}z'' \epsilon_0 \int_{-\infty}^{0} {\rm d}v M_{\rm b}(v) \frac{-i\mathcal{N} C_{\rm FF'}^2 d^2}{\hbar \epsilon_0 v} \exp\left(\frac{z'-z''}{v} (-\frac{\Gamma_{\rm t}}{2} + i\Delta_{\rm FF'}) \right) E(z''). \tag{2.17}$$

This separation into two integrals, one involving negative velocities, and the other positive ones, using Eqs. (2.9) and (2.10) for $\chi_v(z'-z'', \omega_\ell, v)$, also comes from the assumption that the atoms loose their coherence at the boundaries of the slab. Otherwise, an atom with a velocity $-v$ would bounce off the surface, switching its velocity to $+v$, and would contribute to the polarization even for $z' < z$.

In order to proceed further, we need the expression of the field inside the vapor. As we consider a dilute atomic medium placed in vacuum, we (i) neglect the reflection at the boundaries of the slab, (ii) consider no extinction of the driving field along the propagation[8] and take $E(z'') \approx E_0 \exp[ik_\ell z'']$. After some algebra, we end up with (See more detail in Appendix A.2):

$$E_{\rm t} = E_0 e^{ik_\ell z} \left[1 - \sum_{\rm FF'} \frac{\mathcal{N} C_{\rm FF'}^2 d^2}{2\hbar\epsilon_0} \int_{-\infty}^{\infty} {\rm d}v M_{\rm b}(v) \left(\frac{k_\ell L}{\Lambda} - \frac{k_\ell |v|}{\Lambda^2} + \frac{k_\ell |v| e^{-\frac{\Lambda L}{|v|}}}{\Lambda^2} \right) \right], \tag{2.18}$$

where we have introduced $\Lambda = \Gamma_{\rm t}/2 - i(\Delta_{\rm FF'} - k_\ell v)$. Equation (2.18) is equivalent to the one derived by several authors [Vartanyan and Lin, 1995; Briaudeau *et al.*, 1998] starting from a different point of view, which made the non-locality less explicit than the above derivation. We now discuss the contributions of the three integrals (labelled J_1, J_2 and J_3 respectively) in Eq. (2.18) (see also [Briaudeau *et al.*, 1998]).

1. The first term J_1 is the one we would have obtained had we simply taken for the susceptibility $\chi_v^{\rm FF'}(z, z', \omega_\ell, v)$ of atoms at velocity v, the local, Doppler-shifted

[8] The model is therefore expected to be valid for small absorptions only.

(and incorrect!) expression:

$$\chi_v^{\mathrm{FF'}}(z-z',\omega_\ell,v) = i\frac{\mathcal{N}C_{\mathrm{FF'}}^2 d^2}{\hbar\epsilon_0}\frac{1}{\Gamma_\mathrm{t}/2 - i(\Delta_{\mathrm{FF'}} - k_\ell v)}\,\delta(z-z'). \tag{2.19}$$

Although intuitive, this approach would have missed the contributions from the two remaining terms, which are important in the mesoscopic regime. The term J_1 dominates as soon as $L \gtrsim |v/\Lambda|$. Close to resonance and for $kv \lesssim \Gamma_\mathrm{t}$, this yields $L \gtrsim \xi$. This indicates that in large cells ($L \gtrsim$ few µm), J_1 is the dominant contribution and the conventional dispersion theory[9] applies.

2. The second and third terms J_2 and J_3 become important as soon as $|v|/(|\Lambda|L) \gtrsim 1$, *i.e.* $L \lesssim \xi$. These two terms are specific to the mesoscopic regime and are a consequence of the non-local character of the atomic response. They dominate for thin cells.

3. Finally, the third term $J_3 \sim J_2 \exp[-L/\xi]$ describes the fact that the atomic dipole stops emitting when it reaches the boundary of the slab. When $J_2 \gtrsim J_1$, we have seen that $L < \xi$ and $J_3 \sim J_2$, indicating that in the mesoscopic regime it is not possible that J_2 alone dominates.

2.3.2 Transmission through the nano-cell: Fabry-Perot effects

We now consider the more involved case where the atomic slab is confined between the two windows of the cell (index n_s), leading to a low-finesse cavity effect. This situation has already been discussed, in particular in Ref. [Dutier *et al.*, 2003a], starting from a different point of view. In order to include these low-finesse cavity effects, the amplitude coefficient in transmission $t_{10} = 2n_\mathrm{s}/(1+n_\mathrm{s})$ and reflection $r_{20} = (1-n_\mathrm{s})/(1+n_\mathrm{s})$ of the driving field E_0 on two closely spaced sapphire cell walls with refractive index n_s are taken into account. The driving field $E_\pm$ *inside the cavity* is still considered in the dilute regime and can therefore can be written as $E_+e^{ik_\ell z} + E_-e^{-ik\mathrm{l}z} \simeq t_{10}/[1 - r_{20}^2\exp(2ik_\ell L)]E_0\{\exp[ik_\ell z] + r_{20}\exp[ik_\ell(2L-z)]\}$. Similarly, the radiated fields from the atoms are reflected multiple times inside cavity. These fields, initially co- and counter propagating along $z-$axis inside the cavity respectively give rise to an atom induced field after the cavity $z > L$ of:

[9] The conventional dispersion theory is a common terminology that refers to the dispersion properties of a medium in the steady-state regime. In our case, we refer to this terminology for a model widely used for vapor cell, where the effects of the atomic motion on the optical response only appears through a Doppler shift.

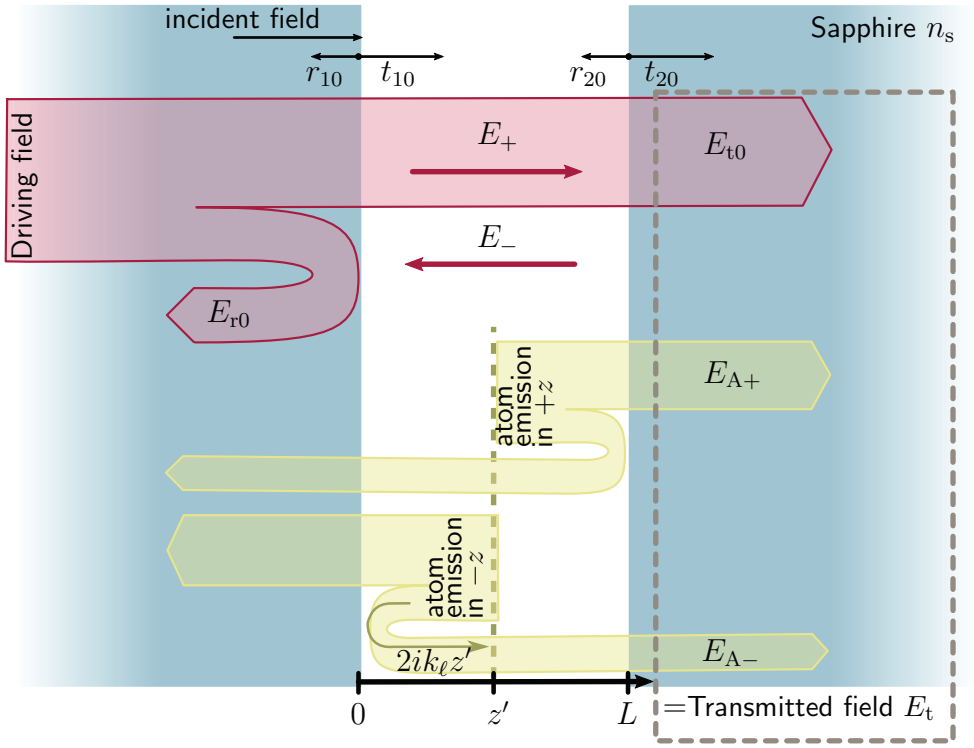

Figure 2.5: Reflection and transmission of fields on the sapphire-vapor and vapor-sapphire interfaces The incident driving field E_0 in red is split a the first interface. The resulting driving fields inside the low-finesse cavity is: E_+ propagating along z-axis direction and E_- in the counter-propagating direction. They induce dipoles that initially emit fields (in yellow) in the $+z$ (respectively $-z$) directions. These fields are multiply reflected by the cavity and give rise to a field E_{A+} (respectively E_{A-}) propagating in the $+z$ direction outside the cavity. Atomic signals propagating backwards ($z < 0$) and contributing to the reflection signal can be computed similarly.

$$E_{A_+}(z) = \sum_{F,F'} \frac{t_{20}\exp(ik_\ell z)}{1 - r_{20}^2 e^{2ik_\ell L}} \frac{ik_\ell}{2\varepsilon_0} \int_0^L \mathrm{d}z' P(z', \omega_\ell) \exp(-ik_\ell z') \ , \tag{2.20}$$

$$E_{A_-}(z) = \sum_{F,F'} \frac{r_{20}t_{20}\exp(ik_\ell z)}{1 - r_{20}^2 e^{2ik_\ell L}} \frac{ik_\ell}{2\varepsilon_0} \int_0^L \mathrm{d}z' P(z', \omega_\ell) \exp(ik_\ell z') \ . \tag{2.21}$$

Equations (2.20) and (2.21), where $t_{20} = 2/(1+n_s)$, are valid whether the polarization-field relation is local or not.

If the spatial extension of the susceptibility is neglected (*i.e.* $\chi_v^{\text{FF'}}$ takes the form of Eq. (2.19)), the relation is local, and the spatial integration is easy: it is *Model 1*. If the spatial extension of the susceptibility is kept (*i.e.* $\chi_v^{\text{FF'}}$ is given by Eq. (2.10)), the relation is non-local and spatial integrals are more involved: it is *Model 2*. Finally,

we obtain the transmission factor through the thin cell system $T = |E_t/E_{t0}|^2$, where $E_t = E_{t0} + E_{A+} + E_{A-}$ is a coherent superposition of the transmitted atom-induced field and transmitted driving field $E_{t0} = t_{10}t_{20}/[1 - r_{20}^2 \exp(2ik_\ell L)]E_0 \exp(ik_\ell z)$. A picture of the different fields involved to compute the transmission is represented in Fig. 2.5. All the models presented in this Thesis have been implemented with Python programs. Developing these programs for fitting purposes was also an important part of my work. In order to reach reasonable computing time, all the integrals presented above require analytical or semi-analytical forms that are detailed in Appendix A.3.

We now use these two models to interpret our experimental data.

2.3.3 The fitting procedure

In our models, we allow free parameters $\mathcal{N}$, Δ_P and Γ_P to vary such that from now on $\Delta_{FF'} = \omega_\ell - \omega_{FF'} - \Delta_p$ and $\Gamma_t = \Gamma_0 + \Gamma_p$. The key point of the analysis is that these parameters are constructed to describe bulk properties of the atomic vapor. As a consequence, they can only account for bulk properties of the homogeneous atomic ensemble such as collisions or the Lorentz field corrections. Crucially, they must therefore not vary with the cell thickness L. This motivates one to fit experimental data with *Model 1* and *Model 2* and compare the fitted parameters for different cell thicknesses.

Fit with Model 1 The result of *Model 1*, for which we have adjusted the values of $\mathcal{N}$, Δ_p and Γ_p to best fit an experimental spectrum obtained for $L = 360$ nm at $\Theta = 170°C$, is shown in Fig. 2.6(a). Strikingly, it does not agree with the data: the experimental line-width appears narrower than the calculated Doppler broadened width. This is again a signature of the coherent Dicke narrowing already observed by many authors [Dicke, 1953; Romer and Dicke, 1955; Dutier *et al.*, 2003b; Sargsyan *et al.*, 2016]. In nano-cells, this emphasises the failure of the conventional dispersion theory, which assumes the local susceptibility of the atomic gas given in Eq. (2.19) and a Maxwell-Boltzmann velocity distribution. To improve our model, we first account phenomenologically for the narrowing due to velocity selection caused by the surface. We therefore suppose that mainly the atoms flying parallel to the windows contribute to the signal [Briaudeau *et al.*, 1998]. In *Model 1* only, the Maxwell Boltzmann distribution is replaced by $M_b(v) = \delta(v)$. The result, shown in Fig. 2.6(b) for the same experimental spectrum, is in much better agreement with the data. Nonetheless, the residuals reveal that the model fails to reproduce the narrow feature near resonance,

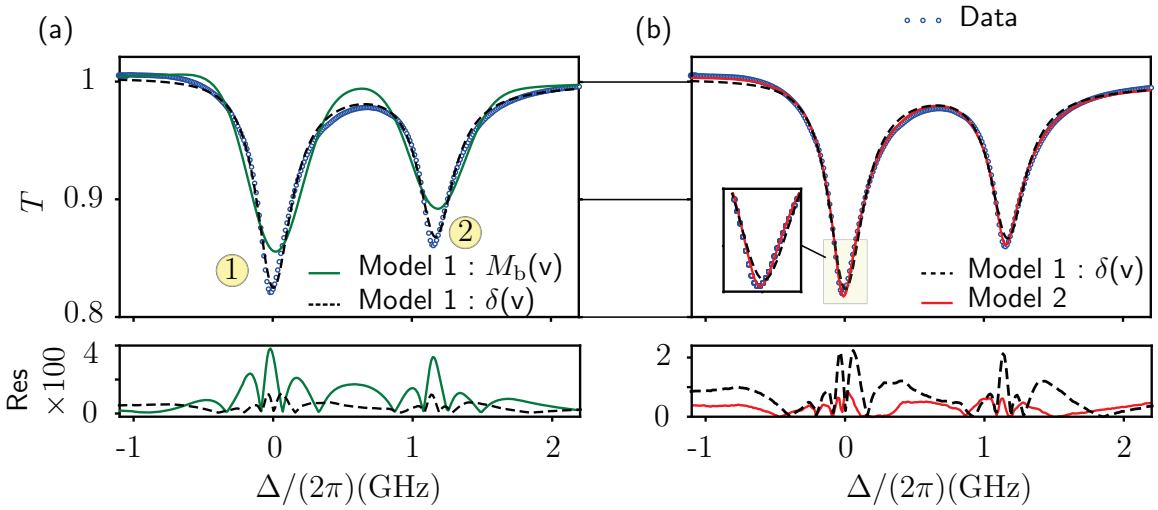

Figure 2.6: Fitting with different models (a) and (b) Comparison of different fitting models to an experimental transmission spectrum displayed in blue dots for $L = 360$ nm and $\Theta = 170°$C ($\mathcal{N} = 5.6 \times 10^{20}$ at·m^{-3}). The green full line is *Model 1* with a full Maxwell Boltzmann integration: it fails to reproduce the data. The black dotted line is *Model 1*, where the Maxwell Boltzmann distribution is replaced by δ(v) to account phenomenologically for the presence of the interface. The red full line is *Model 2*. Zoom on the optical transition 1 (see Fig. 2.4(a)) shows that only *Model 2* reproduces accurately the sharp features on resonance.

characteristic of the contribution from the slow atoms [Briaudeau *et al.*, 1998].

Fit with Model 2 The fit of the data by *Model 2* is presented in Fig. 2.6(b) for the best found parameters $\mathcal{N}$, Δ_p and Γ_p. The agreement is much better than with *Model 1*. In particular, the narrow feature near resonance is reproduced accurately: despite the fact that we keep the full Maxwell velocity distribution, the velocity selection imposed in *Model 1* and at the origin of the narrowing, is an automatic consequence of the mesoscopic nature of this model. The long tails, characteristic of the fast atoms contribution are also perfectly reproduced. The fitting procedure described on a single spectrum can be extended to a whole set of data, previously displayed in Fig. 2.4(a) for a temperature of $\Theta \simeq 170°$C and a range of thicknesses between 110 and 670 nm.

Even though residuals in Fig. 2.6(b) could discriminate between the two models [Hughes and Hase, 2010], the values of Δ_p and Γ_p returned by the fit will indicate more clearly that only the complete *Model 2* is correct, as we discuss below.

Assignment of error bars. Assigning error bars for the fitted parameters $\mathcal{N}$, Δ_p and Γ_p is a challenging part of the data analysis. This is so because it is extremely difficult to assess precisely the experimental error associated with each data point (corresponding to different laser detuning frequencies) of a single spectrum. As a consequence, no direct χ^2 analysis can provide a meaningful error on the fitted parameters. Nevertheless, the error on the extracted parameters can be of two origins: (i) statistical errors, (ii) systematic errors. The statistical error comes from the repetition of the measurement at a same temperature and cell thickness. The fitted results for a parameter spread around a mean value with a standard deviation Δ_{sta}. The larger the absorption, the better the signal to noise ratio and therefore the smaller the statistical error. The main systematic bias originates from the fact that we need to evaluate the cell thickness and let it fixed during the fitting procedure. We do so because if we let more than three parameters to float, the fitting routine either not converge or give meaningful results. We therefore propagate this error on the cell thickness (± 2.5 nm). Namely, we fit the spectra with two fixed values of the cell thickness: $L - 2.5$ nm and $L + 2.5$ nm. It gives two values for the parameter. The associated systematic error Δ_{sys} is half of the difference between these two values. The final error bar associated with each parameter is finally:

$$\Delta = \sqrt{\Delta_{sta}^2 + \Delta_{sys}^2}. \tag{2.22}$$

Experimental observation of the mesoscopic regime Both parameters Δ_p and Γ_p characterize the bulk properties of the vapor and may only depend on the density $\mathcal{N}$. They should therefore remain constant when L varies. Importantly, the Fabry-Perot nature of the cavity is already taken into account through the multiple reflections and therefore should not contribute either to Γ_p and Δ_p in the dilute regime. The evolution of Γ_p for both models is represented in Fig. 2.7. For $L \geq 200$ nm, only *Model 2* presents no clear dependence with L. Furthermore, Γ_p extracted from this model is in reasonable agreement with the expected self-broadening $\beta\mathcal{N}$ due to collisional dipole-dipole interactions at the density corresponding to $\Theta \approx 170°C$ [Weller *et al.*, 2011]. For more details about collisional effects, refer to section 3.3 of Chapter 3. Particular attention should be devoted to the different origins of Γ_p variations for lower thicknesses. The small increase in *Model 2* is due to the van der Waals interaction between an atom and the surface: for Cs, the theoretical atom-sapphire interaction coefficient C_3 is around a few kHz·μm^3 [Bloch and Ducloy, 2005; Whittaker *et al.*, 2014] and will be the subject of Chapter 4. *Model 1* by contrast, yields a strong dependence

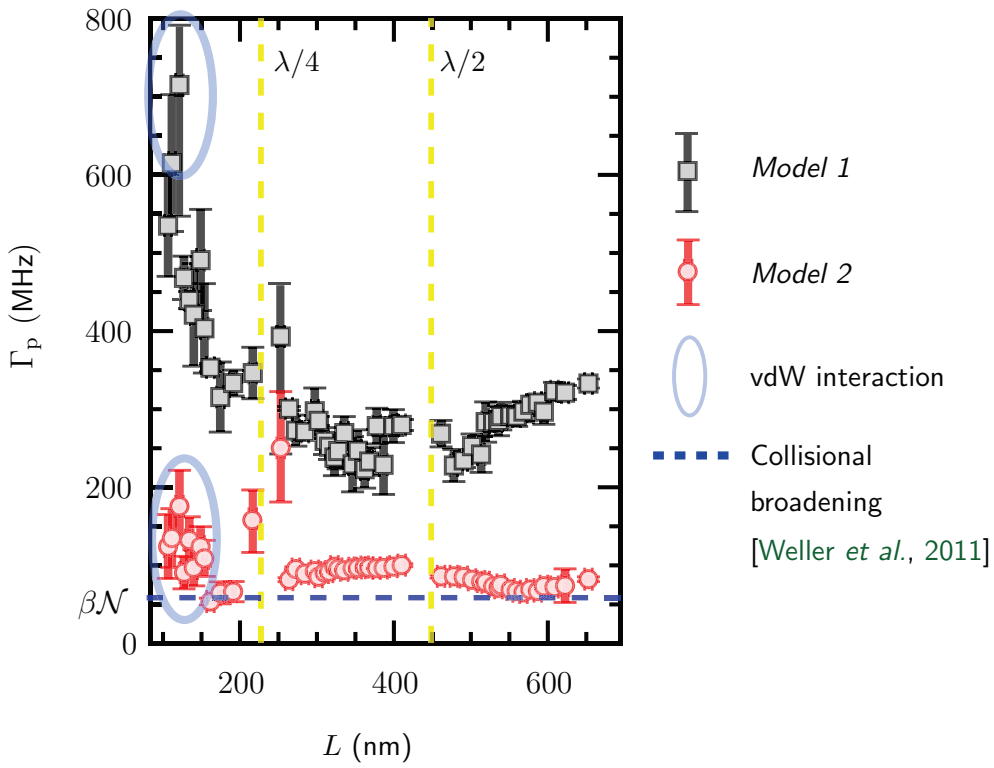

Figure 2.7: Observation of the mesoscopic regime The experimental data used for the fits are represented in Fig. 2.4(b). Fitted broadening parameter Γ_{P} with respect to the cell thickness L in black squares for the *Model 1* and in red circles for the *Model 2*. For thickness $L < 100$ nm, one observes the influence of the van der Waals interaction (blue oval). The blue dotted line represents the theoretical collisional self-broadening prediction.

of Γ_{p} with L, which is not acceptable based on the arguments presented above. The van der Waals effect is superimposed on a large variation from 250 to 550 MHz, incorporated in the non-local model and corresponding to a transient broadening. The agreement between *Model 2* and the transmission spectra is therefore an experimental report of the mesoscopic regime in the optical domain [Peyrot *et al.*, 2019c].

2.4 Conclusion

The situation studied in this chapter, of an atomic vapor where the phase coherence length exceeds the dimension of the system, is widely met in miniaturized atomic sensors. The optical response of mesoscopic systems is now understood globally using a transmission factor. This situation is evocative of the electrical conduction in nano-photonics devices where the concept of local conductivity is no longer valid and a global conductance has to be introduced. The analogy between our system and the anomalous skin depth in metal is also striking. The formalism used in both case to describe the propagation of the electric wave is similar. Particularly, we get inspiration from the hydrodynamic derivative commonly used in this domain, to derive the non-local susceptibility. It makes a strong parallel between these two communities.

We have shown that the propagation of light through nano-cells cannot be described by local properties, and even the concept of non-local system-size-independent susceptibility collapses. We have observed the transmission of light through a vapor confined in a nano-cell. When the vapor is dilute enough, a small collisional broadening results in a phase-coherence length $\xi = v/\Gamma_t$ comparable to the cell thickness, leading to the mesoscopic regime. In this regime, the non-local relation between P and E (Eq. (2.14)) also depends on L and the concept of size-independent susceptibility collapses, as is also the case in nano-photonic devices [Eagen *et al.*, 1980; Ford and Weber, 1984; Cocoletzi and Mochn, 2005; Churchill and Philbin, 2016; Tserkezis, Mortensen, and Wubs, 2017]. We have observed significant discrepancies between spectra obtained in nano-cell with respect to more standard one usually obtain in bulk cells. We have developed two models to interpret these differences. The theoretical *Model 2* features the mesoscopic properties of the system such as transient broadening or the collapse and revival of the Dicke Narrowing [Dutier *et al.*, 2003b]. As a consequence, it provides consistent fitted parameters evolution with the cell thickness. Importantly, it allows the extraction of meaningful quantities such as energy shift and line-width, hence providing a theoretical framework for characterizing future atomic sensors. Finally the excellent agreement with the data up to 20% light absorption is remarkable since extinction of the driving field in the forward direction is not considered in this chapter.

Chapter 3

Collective effects in a dense thin atomic vapor slab

Contents

Introduction

In the first chapter of this manuscript, we have seen that dipole-dipole interactions should start to play a significant role when light interacts with many emitters confined in a volume smaller than λ^3. Particularly, it should lead to a shift and broadening of the optical response of the atomic ensemble. We have then highlighted in Chapter 2 that when the atoms move with a velocity v, the response of the system to the light excitation is non-local. We introduced a distance $\xi = v/\Gamma_t$ characterizing the relaxation of the atoms. In a dense medium, the total homogeneous line-width Γ_t should therefore increase due to dipole-dipole interactions and non-local effects play a minor role as ξ can now be much smaller than the size of the system.

Simultaneously, the influence of dipole-dipole interactions in small geometries has resulted in a long-term debate about spectral energy shifts. Triggered in the early 1970s by Friedberg and Manassah [Friedberg, Hartmann, and Manassah, 1973], the *Cooperative Lamb Shift* (CLS) contention has generated as many interests as chaos. The origin of this frequency shift is confusing: for some it arises from virtual photon exchanges triggered by the quantum vacuum fluctuations of the electromagnetic field [Friedberg, Hartmann, and Manassah, 1973; Frucci *et al.*, 2017], for others it is a purely classical effect [Javanainen and Ruostekoski, 2016]. A clarification is therefore needed. Particularly, there is no unambiguous demonstration of the phenomenon in the literature. The conditions for validity of the CLS are also controversial. Can we measure it experimentally? Beyond the CLS, is it possible to extract atomic properties such as shift or broadening, not affected by the environment (cell walls for example)? This are the questions we try to elucidate in this chapter.

Structure of the chapter We first present in more details the CLS controversy and provide a hopefully clear demonstration in the slab geometry. In this context, we modify the transmission model, including as a perturbation, density effects in the dipolar field. We then explain the origin of the CLS and assess its domain of validity. Subsequently, we measure the transmission through the nano-cell in the dense regime and interpret the observed shifts. Extending our model to all perturbation orders in atomic density, we are able to measure density shifts and broadening, not influenced by their environment.

3.1 The Collective Lamb Shift

In this section, we first present the CLS controversy in more details. We then derive the CLS in two steps: (i) we give an expression for the local field inside the slab to find the field radiated by the dipoles, (ii) we expand the latter at second order in density to derive the shift observed in transmission.

3.1.1 Origin of the controversy

The resonant dipole-dipole interactions between atoms should lead to a collective frequency shift of the atomic lines. In the case of an atomic slab of thickness L and

density $\mathcal{N}$, it was predicted to be [Friedberg, Hartmann, and Manassah, 1973]:

$$\Delta_{\mathrm{CLS}} = \Delta_{\mathrm{LL}} - \frac{3}{4}\Delta_{\mathrm{LL}}\left(1 - \frac{\sin 2k_\ell L}{2k_\ell L}\right), \tag{3.1}$$

where $\Delta_{\mathrm{LL}} = -\pi(\mathcal{N}/k_\ell^3)\Gamma_0$ is the Lorentz-Lorenz shift, $k_\ell = 2\pi/\lambda$ is the wave-vector[1], Γ_0 is the natural line-width of the relevant atomic transition and $\mathcal{N}$ the volume density of atoms. This result was derived using second order energy perturbations in the dipole strength. The so-called *Cooperative Lamb Shift* was defined as:

$$\Delta_{\mathrm{CLS}} = \mathbb{R}\mathrm{e}\left(\langle\psi| V_{\mathrm{dd}} |\psi\rangle\right), \tag{3.2}$$

where V_{dd} is the dipole-dipole potential operator and $\langle\rangle$ the quantum average on a weakly-driven (only one excitation in the system) system $|\psi\rangle$ describing the ensemble of density $\mathcal{N}$. The derivation of Eq. (3.1) starting from Eq. (3.2) made by the authors involved intricate integrals, that have to be normalized in a quite obscure way to avoid divergences[2]. As a matter of fact, this complexity clouded the meaning of the shift which was furthermore not related to any observable quantity.

Four decades later, the first measurements of the CLS were reported using a layer of Fe atoms [Röhlsberger *et al.*, 2010] and a slab containing a hot alkali vapor [Keaveney *et al.*, 2012b]. Following these experiments, it was pointed out that Eq. (3.1) is valid only in the low density limit ($\mathcal{N}/k_\ell^3 \ll 1$ [Javanainen and Ruostekoski, 2016; Javanainen *et al.*, 2017]), a condition not met by the experiment of [Keaveney *et al.*, 2012b] for which $\mathcal{N}/k_\ell^3 \sim 100$. Reference [Javanainen *et al.*, 2014] suggested that this CLS should only be present when large inhomogeneous broadening is present, such as in a hot vapor. However, subsequent experiments on ultra-cold atoms (insignificant inhomogeneous broadening) either reported a shift consistent with the CLS prediction [Roof *et al.*, 2016], or a negligible shift [Corman *et al.*, 2017]. Recently, theoretical work highlighted that the CLS in a slab geometry [Javanainen and Ruostekoski, 2016] should merely arise from cavity interferences between the boundaries of the medium. In contrast to the original suggestion [Friedberg, Hartmann, and Manassah, 1973], in the cavity viewpoint, the CLS would not be related to the Lorentz local field. Clearly, the situation is confusing and further work is needed to clarify it. In order to do so, we provide below a new, simpler, demonstration of the CLS in the slab geometry.

[1] Note that we assimilate here the wave-vector of the light k_ℓ and the one of the atom because the laser is near-resonant.

[2] Despite many attempts of the authors for clarifying their demonstration (see for example [Friedberg and Manassah, 2010]), the origin of some integrals remains unclear (especially Eq. 4.1 of [Friedberg, Hartmann, and Manassah, 1973]).

3.1.2 Local field in dense media

To derive the above CLS formula, we compute the field transmitted by the slab given by Eq (1.37). It requires the expression of the dipole field appearing in Eq. (1.36) which is recalled below:

$$E_{\mathrm{d}}(z) = \frac{ik_\ell \mathcal{N}\alpha(\omega_\ell)}{2}\int_0^L \mathrm{d}z' E_{\mathrm{loc}}(z') e^{ik_\ell|z-z'|}\ .$$

In this last formula, α and E_{loc} are respectively the atomic polarizability and the local field defined in Chapter 1. In this chapter, we will assume a local relation between the driving field and the atomic slab because we expect large broadening. In this case, the relaxation distance ξ introduced in the previous chapter should be much smaller than λ and the thickness L of the vapor. Non-local and mesoscopic effects should therefore play no significant role in the atomic response. We will see below that this approximation is justified in the case of our experiment. We therefore use the local relations $P = \epsilon_0 \chi \langle E \rangle$ and $P = \epsilon_0 \mathcal{N}\alpha E_{\mathrm{loc}}$, to substitute the local field with the mean field $\langle E \rangle$:

$$E_{\mathrm{loc}}(z') = \frac{\chi \langle E(z') \rangle}{N\alpha}. \tag{3.3}$$

To find an expression for the mean field inside the slab ($z' \in [0, L]$), we adapt the work made in Ref. [Fearn, James, and W Milonni, 1996] to a finite-size medium. The mean field in the slab is the sum of the driving field and the dipole field (see Eq. (1.31)). A combination of Eqs. (1.36) and (3.3) yields:

$$\langle E(z') \rangle = E_0 e^{ik_\ell z'} + \frac{ik_\ell \chi}{2}\left[e^{ik_\ell z'}\int_0^{z'} \mathrm{d}z'' \langle E(z'') \rangle e^{-ik_\ell z''} + e^{-ik_\ell z'}\int_{z'}^{L} \mathrm{d}z'' \langle E(z'') \rangle e^{ik_\ell z''}\right]. \tag{3.4}$$

Because of the cavity-like geometry, we suggest a trial solution $\langle E(z') \rangle = E_{\mathrm{tr1}} e^{ik_{\mathrm{tr}} z'} + E_{\mathrm{tr2}} e^{-ik_{\mathrm{tr}} z'}$ with E_{tr1}, E_{tr2} and k_{tr} to be determined. Introducing it in the above Eq. (3.4), we perform the spatial integration. We then regroup terms on both sides of Eq. (3.4) for each wave vector class $(k_{\mathrm{tr}}, -k_{\mathrm{tr}}, +k_\ell, -k_\ell)$. We find a set of four equations with three unknowns:

$$E_{\mathrm{tr1}} = \frac{ik_\ell\chi}{2}\left[\frac{E_{\mathrm{tr1}}}{i(k_{\mathrm{tr}}-k_\ell)} - \frac{E_{\mathrm{tr1}}}{i(k_{\mathrm{tr}}+k_\ell)}\right], \tag{3.5}$$

$$E_{\mathrm{tr2}} = \frac{ik_\ell\chi}{2}\left[\frac{iE_{\mathrm{tr2}}}{(k_{\mathrm{tr}}+k_\ell)} + \frac{iE_{\mathrm{tr2}}}{(k_{\mathrm{tr}}-k_\ell)}\right], \tag{3.6}$$

$$0 = E_0 + \frac{ik_\ell\chi}{2}\left[\frac{iE_{\mathrm{tr1}}}{k_{\mathrm{tr1}}-k_\ell} - \frac{iE_{\mathrm{tr2}}}{k_{\mathrm{tr1}}+k_\ell}\right], \tag{3.7}$$

$$0 = \left[\frac{E_{\mathrm{tr1}}e^{i(k_{\mathrm{tr}}+k_\ell)L}}{i\,(k_{\mathrm{tr1}}+k_\ell)} + \frac{E_{\mathrm{tr2}}e^{i(k_\ell-k_{\mathrm{tr}})L}}{i\,(k_\ell-k_{\mathrm{tr}})}\right]. \tag{3.8}$$

Notably, Eqs. (3.7) and (3.8) give:

$$k_{\mathrm{tr}} = \sqrt{1+\chi}k_\ell \equiv nk_\ell. \tag{3.9}$$

We retrieve here, starting from a microscopic approach, that light travels in a medium with a refractive index $n \equiv \sqrt{1+\chi}$. In a similar way, we find:

$$E_{\mathrm{tr1}} = \frac{t_1 E_0}{1-r_2^2 e^{2ink_\ell L}}, \tag{3.10}$$

$$E_{\mathrm{tr2}} = r_2 e^{2ink_\ell L}E_{\mathrm{tr1}}, \tag{3.11}$$

with $t_1 = 2/(1+n)$ and $r_2 = (n-1)/(n+1)$. It is again exactly the field in a cavity of index n surrounded by a vacuum-like (unitary index) medium. Note that the refractive index notion is only valid when the atomic response to light is local.

We can now demonstrate the CLS.

3.1.3 The Collective Lamb Shift: a cavity-induced shift

The field that excite the atoms is the cavity field that we just derived. Consequently, the field transmitted after the slab ($z > L$) can now be written:

$$E_{\mathrm{t}}(z) = E_0 e^{ik_\ell z} + \frac{ik_\ell\chi}{2}\int_0^L \mathrm{d}z'\left(E_{\mathrm{tr1}}e^{ink_\ell z'} + E_{\mathrm{tr2}}e^{-ink_\ell z'}\right)e^{ik_\ell(z-z')}. \tag{3.12}$$

We Taylor-expand E_{t} at second order in χ. With $r_2 \simeq \chi/4$ and $t_1 \simeq 1-\chi/4$, we get:

$$E_{\mathrm{t}}(z) \simeq E_0 e^{ik_\ell z} + \frac{ik_\ell \chi E_0}{2} \int_0^L \mathrm{d}z' \left(t_1 e^{ink_\ell z'} + r_2 t_1 e^{-ink_\ell z'} \right) e^{ik_\ell (z-z')}. \tag{3.13}$$

Performing the integral over z', we find at second order in χ:

$$E_{\mathrm{t}} \simeq E_0 e^{ik_\ell z} \left[1 + i\frac{\chi k_\ell L}{2} \left(1 + \frac{i\chi k_\ell L}{4} - \frac{\chi}{4} + \frac{\chi}{4} \frac{e^{2ik_\ell L} - 1}{2ik_\ell L} \right) \right]. \tag{3.14}$$

As in Chapter 1, the susceptibility of the dilute slab consisting of atoms with polarizability $\alpha = i(6\pi\Gamma_0/k_\ell^3)/(\Gamma_{\mathrm{t}} - 2i\Delta)$ ($\Delta = \omega_\ell - \omega_0$ with ω_0 the resonant frequency, Γ_0 the radiative line-width and Γ_{t} the total homogeneous line-width) is $\chi = N\alpha$. Using $1 + x \approx 1/(1-x)$ for $|x| \ll 1$ in the parenthesis of Eq. (3.14), we obtain the transmission coefficient:

$$T(\Delta) = \left| \frac{E_{\mathrm{t}}}{E_0} \right|^2 = \left| 1 - \frac{3\pi \mathcal{N} L}{k_\ell^2} \frac{\Gamma_0}{\Gamma_{\mathrm{c}} - 2i(\Delta - \Delta_{\mathrm{c}})} \right|^2 , \tag{3.15}$$

with the thickness dependent shift

$$\Delta_{\mathrm{c}} = -\frac{3}{4}\Delta_{\mathrm{LL}} \left(1 - \frac{\sin 2k_\ell L}{2k_\ell L} \right) \tag{3.16}$$

and width

$$\Gamma_{\mathrm{c}} = \Gamma_{\mathrm{t}} - \frac{3}{2} \left(k_\ell L + \frac{\sin^2 k_\ell L}{k_\ell L} \right) \Delta_{\mathrm{LL}}. \tag{3.17}$$

The offset $-\frac{3}{4}\Delta_{\mathrm{LL}}$ for the shift appearing in Eq. (3.16) is traced back to the transmission through the first interface. To recover the extra offset Δ_{LL} in Eq. (3.1), we must use the Lorentz-Lorenz formula [Jackson, 1999] in Eq. (3.14): one sees in Fig. 3.1(a) that the only effect of the local field correction $\chi = N\alpha/(1 - N\alpha/3)$ is to translate Δ_{min} by a quantity Δ_{LL}. All details on the calculation steps can be found in Appendix A.4.

This derivation therefore helps clarifying what is the CLS and its range of application:

- for a dilute medium, the line-shape is Lorentzian and the CLS is a frequency shift of the position of the transmission minimum Δ_{min} and not a shift of the resonance ω_0 of the bulk medium characterized by χ;

- it is a consequence of the reflection of the field at the boundaries of an atomic slab *surrounded by vacuum* (medium with unitary index);

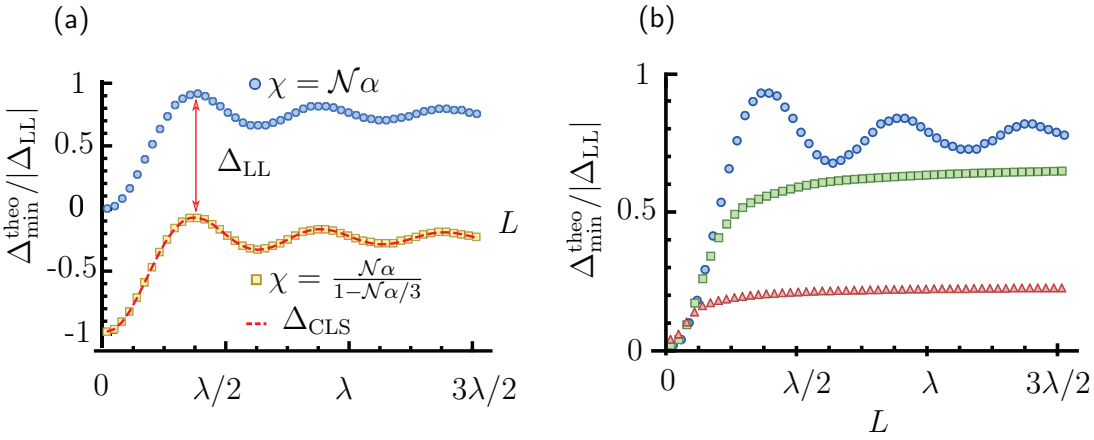

Figure 3.1: Collective Lamb Shift (a) Theoretical Δ_{min} normalized by the Lorentz-Lorenz shift according to the cell thickness. The parameter $\mathcal{N}/k_\ell^3\,(\Gamma_0/\Gamma_t) = 10^{-4}$. Blue dots: $\chi = \mathcal{N}\alpha$, yellow squares: $\chi = \mathcal{N}\alpha/\,(1 - \mathcal{N}\alpha/3)$. The CLS prediction from Ref. [Friedberg, Hartmann, and Manassah, 1973] is superimposed as a dashed red line. (b) The same quantity is plotted for $\chi = \mathcal{N}\alpha$. In blue dots, green squares and red triangles, the parameter $\mathcal{N}/k_\ell^3\,(\Gamma_0/\Gamma_t)$ is respectively equal to 10^{-4}, 0.03 and 0.2.

- it includes the dipole-dipole interactions in the propagation. Namely, the field that induces the dipoles propagates in a medium of index n;

- Eq. (3.1) is only valid in a medium for which $\chi \ll 1$ at resonance, *i.e.* $(\mathcal{N}/k_\ell^3)(\Gamma_0/\Gamma_t) \ll 1$ hence refining the condition $\mathcal{N}/k_\ell^3 \ll 1$ of Ref. [Javanainen and Ruostekoski, 2016; Javanainen *et al.*, 2017]. We see in Fig. 3.1(b) the contribution of higher orders in density when the transmission $T(\Delta)$ is calculated at all density order starting from Eq. (3.12).

In a nano-cell, the atomic slab is not surrounded by vacuum. Consequently, there is no reason to believe that the shift should be given by Eq. (3.1) as the boundary conditions are modified. In order to describe the situation when the medium surrounding the atoms is not vacuum, we now investigate experimentally the shifts in a dense vapor confined in a nano-cell.

3.2 Transmission through a dense atomic vapor slab

In this section, we first present our experimental set-up to study the dipole-dipole interactions. In particular, we investigate the evolution of Δ_{min} extracted from the experimental spectra when the density of atoms increases. We finally extend

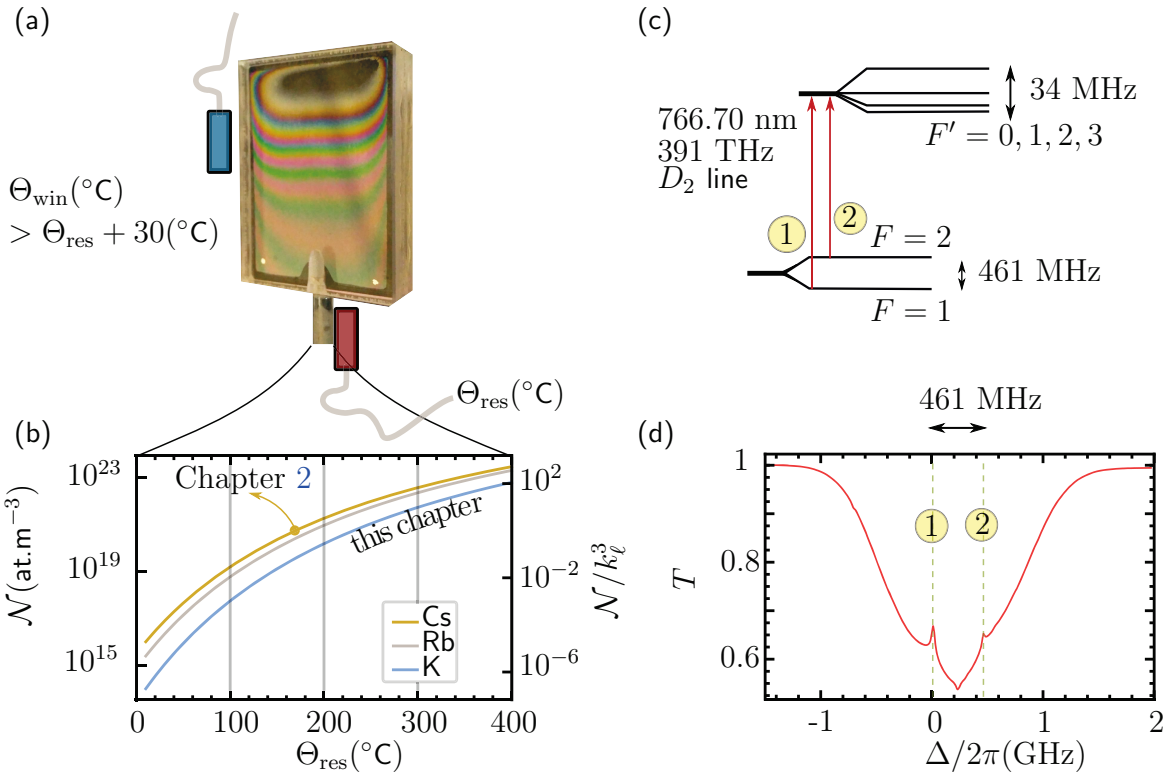

Figure 3.2: Experimental details (a) The potassium nano-cell. (b) Atomic density as a function of the reservoir temperature. (c) Energy diagram for the potassium D_2 line. (d) Saturated absorption spectrum used for frequency calibration in a 7-cm potassium reference cell.

our theoretical model to all perturbation orders in χ to interpret the data more quantitatively.

3.2.1 Preliminary experimental observations

Set-up details The experimental set-up to study density shifts is identical to the one used in Chapter 2 except that here, the nano-cell is filled with potassium and is represented in Fig. 3.2(a). Compared to earlier measurements performed with rubidium [Keaveney *et al.*, 2012b], or with cesium [Whittaker, 2017], potassium has the advantage of a smaller hyperfine splitting in the ground state, which results into a single atomic line at lower densities. The density curves represented in Fig. 3.2(b) for many alkalis, explain to a certain extent the use of a nano-cell to study the dipole-dipole interaction in the dense regime: we see that it is possible to change by orders of magnitude the atomic density simply by varying the reservoir temperature.

The laser is scanned across the resonance over a range of about 30 GHz. We measure the transmission of a laser beam nearly resonant with the D_2 transition of potassium[3] ($\lambda \approx 767$ nm, $\Gamma_0 \approx 2\pi \times 6$ MHz). The energy diagram is represented in Fig. 3.2(c). Due to the small hyperfine splitting, the different transitions of the D_2 line overlap at room temperature in a bulk cell. We therefore perform a saturated absorption spectroscopy in a reference cell for the frequency calibration (see Fig. 3.2(d)).

Observation of a blue to red transition of $\Delta_{\min}$ Figure 3.3(a) shows the measured optical density OD, extracted from the transmission T via $\mathrm{OD} = -\ln(T)$, according to the laser detuning Δ for three values of the atomic density $\mathcal{N}$. We plot $\Delta_{\min}$, defined as the detuning at which the OD is the largest, as a function of density for various thicknesses L in Fig. 3.3(b). At high density ($\mathcal{N}/k_\ell^3 \gtrsim 20$), we observe a red-shifted, linear variation of $\Delta_{\min}$ with $\mathcal{N}$ for all L. At low $\mathcal{N}$, for $L > \lambda/2$, $\Delta_{\min}$ exhibits a pronounced blue-shift, and turns into a red-shift at higher density. For thicknesses $L \lesssim \lambda/2$, $\Delta_{\min}$ features a plateau at low $\mathcal{N}$, as also seen in [Keaveney *et al.*, 2012b]. Similar blue-shifts of the minimal transmission were observed in a nano-cell of cesium [Maurin *et al.*, 2005], although much smaller than here, and recently in a slab of ultra-cold rubidium atoms [Corman *et al.*, 2017], where an evolution from the blue to the red side of the resonance was also measured.

3.2.2 The refractive index model

To explain the data, we now develop a model that deconvolves the effects of the cavity produced by the interface between the sapphire windows and the atomic medium, and the bulk properties of the atomic medium. This was also the approach used in Ref. [Keaveney *et al.*, 2012b]. However, the model used there to extract the shift took only partially the cavity effect into account (see details in the supplemental material of [Peyrot *et al.*, 2018]). Furthermore, as explained above, Eq. (3.1) is irrelevant for the experimental situation of a nano-cell: the atomic slab should be dilute and surrounded by vacuum for the formula to hold. The agreement between the measured shift with respect to the cell thickness and Eq. (3.1) in Ref. [Keaveney *et al.*, 2012b] must therefore be considered as fortuitous.

Our new model incorporates the multiple reflections in the cavity. The atomic slab is described by a continuous resonant medium with a refractive index n. Ascribing

[3] The natural isotopes of potassium are ^{39}K, ^{41}K and ^{40}K. Their proportion are respectively 93%, 7% and less than 1%. We account in our models for the two predominant isotopes.

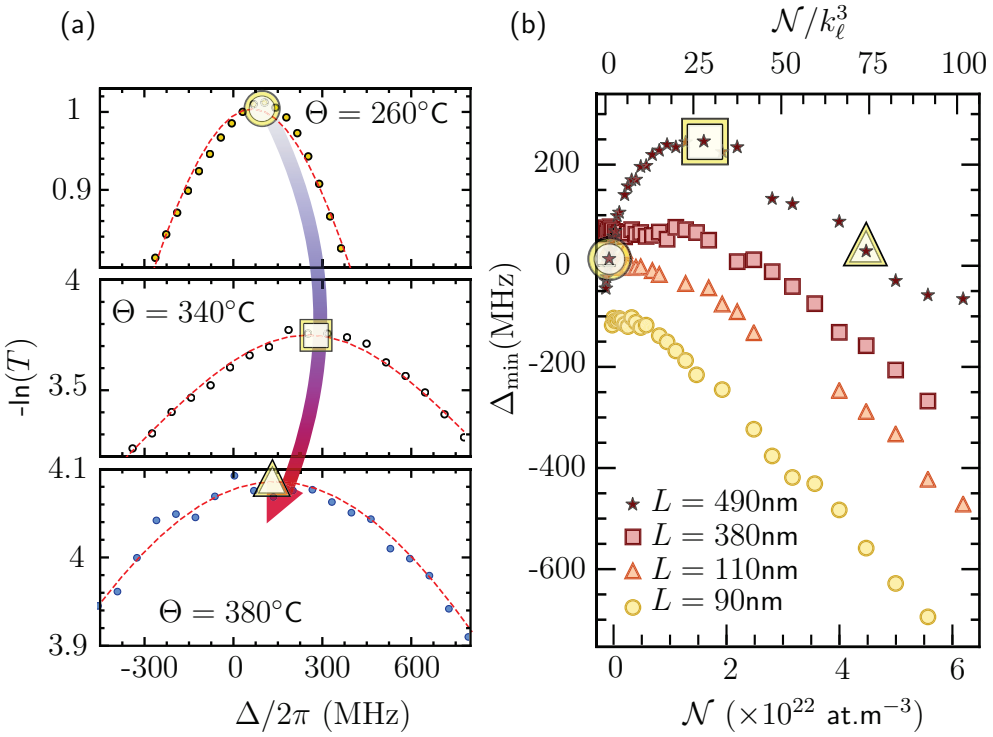

Figure 3.3: Blue-to-red transition of $\Delta_{\min}$ (a) Measured optical density for a slab of thickness $L = 490$ nm according to the detuning and for temperatures $\Theta = (260°\text{C}, 340°\text{C}, 380°\text{C})$ (top, middle, bottom). It corresponds respectively to $\mathcal{N}/k_\ell^3 = (3, 29, 74)$. The red dashed line are Gaussian fits to extract $\Delta_{\min}$. The frequency $\Delta_{\min}$ of the maximum of the optical depth are spotted by the yellow symbols and are reported on the right panel. (b) $\Delta_{\min}$ versus density $\mathcal{N}$ for $L = 90$ nm (yellow dots), $L = 110$ nm (orange triangles), $L = \lambda/2 = 380$ nm (red squares) and $L = 3\lambda/4 = 575$ nm (*bordeaux* stars).

a refractive index to a hot vapor confined in a nano-cell is far from being obvious, as studied in Chapter 2 and by several authors (*e.g.* [Schuurmans, 1976; Vartanyan and Lin, 1995; Zambon and Nienhuis, 1997; Dutier *et al.*, 2003a]). Indeed, we saw that the atomic motion is responsible for the non-local relation between the driving field and the induced polarization. Besides, it should lead to a mesoscopic response of the system if the spatial extension ξ is larger than the cell thickness L. For the potassium vapor, the Doppler width $\Delta\omega_{\text{D}} = k_\ell \langle v \rangle / (2\pi) \sim 500$ MHz where the most probable velocity is given by $\langle v \rangle = \sqrt{2k_{\text{B}}\Theta/m}$ with m the atomic mass and k_{B} the Boltzmann constant. When the density is as large as the ones used here, the collisional broadening of the line exceeds by far the Doppler width (see below and Fig. 3.5(d)). For a broadening of $\Gamma_{\text{t}} = 2$ GHz, the dipoles therefore reach their steady-state over a distance $\sim \Delta\omega_{\text{D}}/(k_\ell \Gamma_{\text{t}}) < 100$ nm, much smaller than L and λ. Equivalently, $\xi \ll [\lambda, L]$

and it then becomes possible to define a *steady-state, local* refractive index.

We adapt the derivation made previously in Subsection 3.1.2 to the case of a real cavity of index n_s. It can be shown that Eqs. (3.10) and (3.11) hold provided that transmission and reflection coefficients are replaced by $t_1 = 2n_\mathrm{s}/(n+n_\mathrm{s})$ and $r_2 = (n-n_\mathrm{s})/(n+n_\mathrm{s})$. Care must be taken for two reasons when using the superposition principle in Eq. (3.12) to compute the transmitted field. First, the field radiated by the atoms in the direction $-z$ should now be included as in Eq. (2.21). Second, the field radiated by the atoms is now multiply reflected by the *empty* cavity. The dipole field is therefore multiplied by a factor $F = t_{20}/(1-r_{20}^2\exp(2ik_\ell L))$, where $r_{20} = (1-n_\mathrm{s})/(1+n_\mathrm{s})$ and $t_{20} = 2/(1+n_\mathrm{s})$, before giving rise to the transmitted field:

$$E_t(z) = \overbrace{\frac{t_{10}t_{20}E_0}{1-r_{20}^2e^{2ik_\ell}}e^{ik_\ell z}}^{\substack{\text{Field } E_{\mathrm{t}0} \text{ transmitted}\\ \text{by the empty cavity}}} + \overbrace{\underbrace{\frac{iFE_0k_\ell\chi}{2}\int_0^L \mathrm{d}z'\left(E_{\mathrm{tr}1}e^{ink_\ell z'} + E_{\mathrm{tr}2}e^{-ink_\ell z'}\right)e^{ik_\ell(z-z')}}_{\substack{\text{Field radiated by the atoms initially in the}\\ +z \text{ direction and multiply reflected by the cavity}}} + \underbrace{\frac{iFE_0r_{20}k_\ell\chi}{2}\int_0^L \mathrm{d}z'\left(E_{\mathrm{tr}1}e^{ink_\ell z'} + E_{\mathrm{tr}2}e^{-ink_\ell z'}\right)e^{ik_\ell(z+z')}}_{\substack{\text{Field radiated by the atoms initially in the}\\ -z \text{ direction and multiply reflected by the cavity}}}}^{}, \tag{3.18}$$

with $t_{10} = 2n_\mathrm{s}/(1+n_\mathrm{s})$. Starting from Eq. (3.18), it is quite involved to find an analytical expression for the transmission coefficient defined by $t \equiv E_t/E_{\mathrm{t}0}$. However, it can easily be shown from an interferences textbook argument [Javanainen and Ruostekoski, 2016; Peyrot *et al.*, 2018] that the intensity transmission coefficient $T = |t|^2$ can be written as:

$$T = \left|\frac{t_1t_2/(1-r_2^2e^{2ink_\ell L})}{t_{10}t_{20}/(1-r_{20}^2e^{2ik_\ell L})}\right|^2. \tag{3.19}$$

Instead of performing the full calculation to show that Eq. (3.18) matches Eq. (3.19), we have checked it numerically. In other words, we retrieve again starting from the microscopic approach, a result predicted by a macroscopic reasoning. We relate the refractive index of the atomic slab to the electric susceptibility χ by $n(\Delta) = \sqrt{1+\chi(\Delta)}$. Here we take $\chi = \mathcal{N}\alpha(\Delta,\mathcal{N})$ with $\alpha(\Delta,\mathcal{N})$ the polarizability of the atoms, including the influence of the density at the single atom level through a broadening and a shift as in the previous chapter. It is calculated by summing the contribution of all hyperfine transitions of the potassium D_2 line with Lorentzian profiles, weighted by

the corresponding Clebsch-Gordan coefficients[4]:

$$\alpha(\Delta, \mathcal{N}) = \frac{i}{\hbar\epsilon_0} \sum_{F,F'} \frac{d^2 C^2_{\mathrm{FF'}}}{\Gamma_\mathrm{t}/2 - i\Delta_\mathrm{t}} \ . \tag{3.20}$$

In Eq. (3.20), $\Gamma_\mathrm{t} = \Gamma_0 + \Gamma_\mathrm{p}$ is still the sum of the radiative line-width Γ_0 and a width Γ_p that accounts in a phenomenological way for any broadening mechanism inside the gas beyond the cavity-induced broadening. In the same way, the total detuning $\Delta_\mathrm{t} = \Delta_{\mathrm{FF'}} - \Delta_\mathrm{p}$, with $\Delta_{\mathrm{FF'}}$ the hyperfine splitting and Δ_p a phenomenological shift inside the gas beyond the cavity-induced shift[5]. Whether the Doppler shift should be included here or not is not crucial because, as we will see later, the experimental collisional broadening exceeds by far the Doppler width.

The quantities $\Delta_\mathrm{p}(\mathcal{N}, L)$ and $\Gamma_\mathrm{p}(\mathcal{N}, L)$ therefore contain the physics not included in the model: (i) the interaction of the atoms with the cell walls (only dependent on the thickness L), (ii) the collisional dipole-dipole interactions between the light-induced dipoles (only dependent on the density $\mathcal{N}$), and (iii) any extra effects that may depend both on L and $\mathcal{N}$. We now compare our transmission model $T = |t(\Delta)|^2$ to the data.

Fitting experimental data Figures 3.4(a-b) show a comparison of the model's prediction and measured spectra. The agreement is very good. In particular, the model reproduces the observed asymmetric line-shapes. Importantly, this is partly this asymmetry that prevents from defining a meaningful shift based on the minimum transmission Δ_{min}. To demonstrate the importance of the sapphire layers in the optical response, we also plot in Fig. 3.4(a-b) the result of Eq. (3.19) for the case of an atomic layer immersed in vacuum ($n_\mathrm{s} = 1$): there, the asymmetry is nearly absent. The asymmetry of the line-shape should be interpreted as an interference effect between forwards and backwards waves in the cavity. When $n_\mathrm{s} \neq 1$, the dipole field on the red and blue side of the transition does not have the same phase. This phase is represented in Fig. 3.4(c-d). For example, in the case of $L = \lambda/4$ (Fig. 3.4(d)), we first see that far from resonance, the radiated field is not in quadrature with the driving field: it is more in phase on the red side and in opposition of phase on the blue side. It explains the strong asymmetry of the line[6] and why we can also observe transmission slightly above unity on experimental spectra without violating energy conservation.

[4]This leads exactly to the susceptibility in Eq. (2.7) ignoring velocity effects.
[5]Introducing a single parameter Δ_P for the shift, we assume that it does not depend on the hyperfine transition.
[6]See also Chapter 6 in the case of fluorescence.

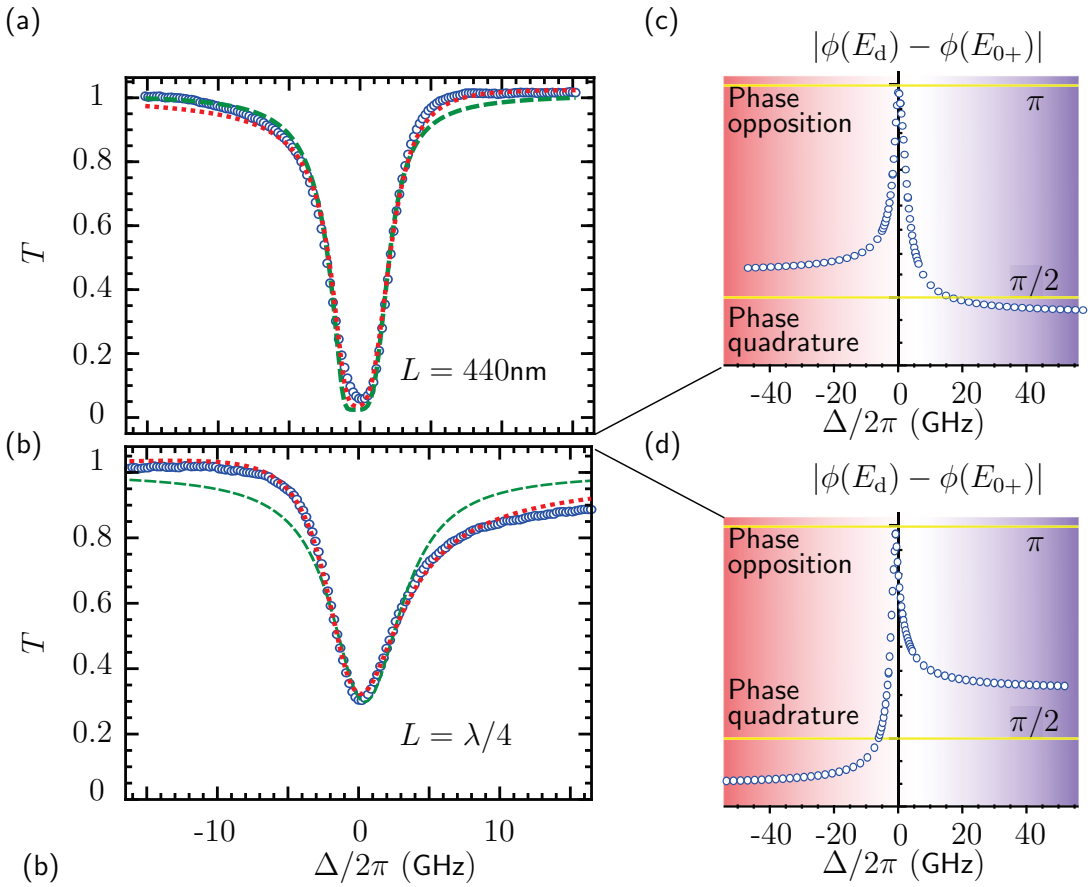

Figure 3.4: Fit of experimental spectra Left panels: transmission profiles for (a) $\Theta = 330°$C and $L = 440$ nm and (b) $\Theta = 365°$C and $L = \lambda/4$ where the asymmetry is the most pronounced. Blue dots: measured transmission. Green dashed line: transmission calculated with the model where $n_s = 1$. Red dotted line: transmission calculated by the cavity model where $n_s = 1.76$. (c-d) Absolute phase difference between the dipole and driving field for the corresponding spectra. It is obtained theoretically using the parameters extracted by the fits in (a) and (b) respectively.

3.3 Atomic properties in the dense regime

3.3.1 Density shifts and broadening

To fit the data with the model and obtain the good agreement shown in Figs. 3.4(a-b), we let the density $\mathcal{N}$ (or equivalently the temperature[7] Θ, the line shift Δ_p and the broadening Γ_p as free parameters. In Figs. 3.5(a-b) we plot the fitted values of Δ_p and

[7] Although the temperature is left as a free parameter here, the fitted values are very close to the values measured on the experiment by the thermocouple in contact with the reservoir.

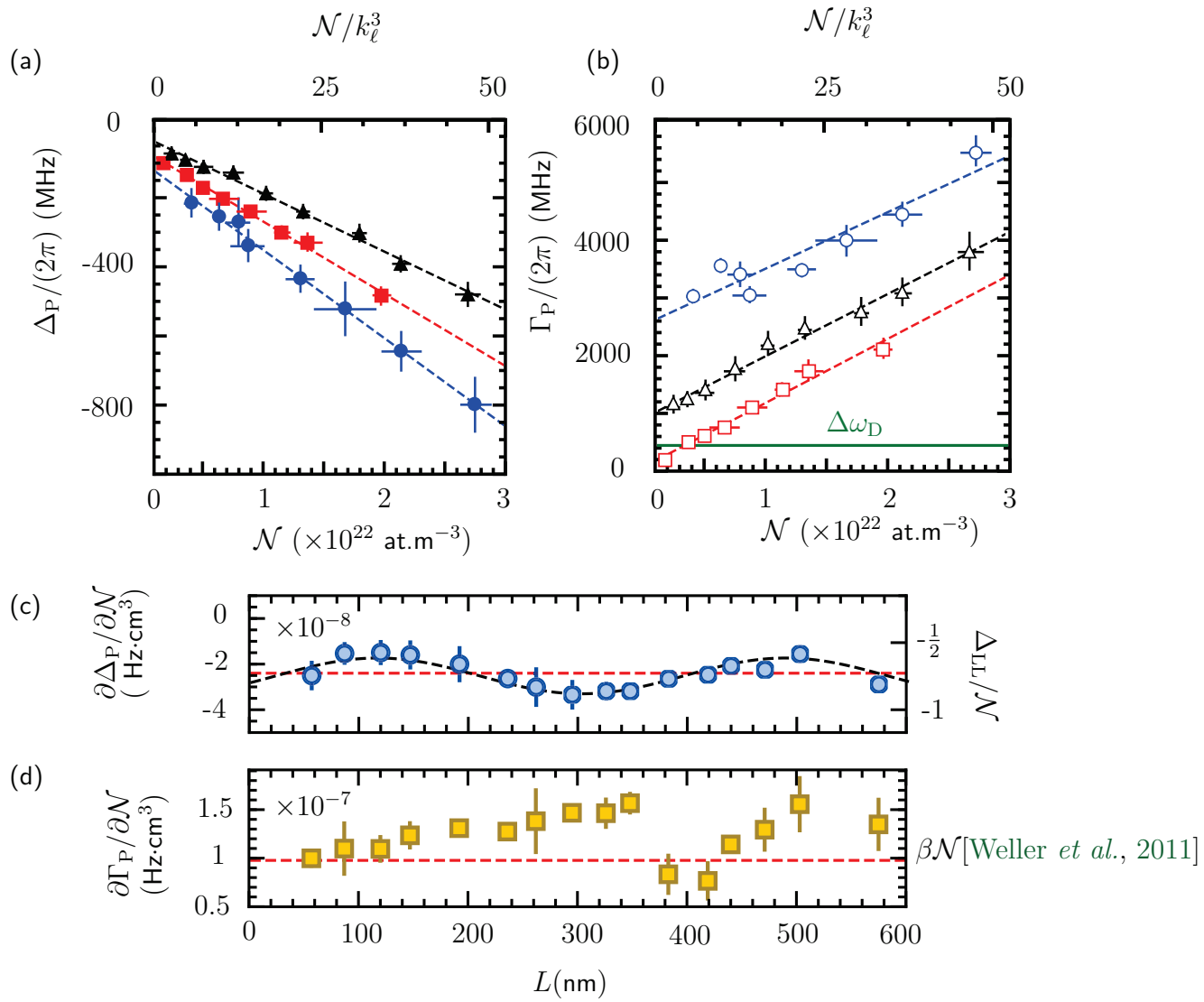

Figure 3.5: Shifts and broadening of atomic lines (a) Experimental shift Δ_p and (b) broadening Γ_p for various cell thicknesses L. Blue dots: $L = 85$ nm, black triangles: $L = 260$ nm and red squares: $L = 380$ nm. Green full line: Doppler width. The dashed lines are linear fits to the data. The error bars on both axes are extracted with the method described in Chapter 2. (c) Blue dots: slope $\partial\Delta_p/\partial N$ of the shift extracted from the model according to the cell thickness L, together with the fit by a sinusoidal function (dashed black line). The offset in dashed red line is interpreted in the main text. (d) Yellow squares: slope $\partial\Gamma_p/\partial N$ of the width extracted from the cavity model as a function of L. The red dashed line is the theoretical value of the self-broadening coefficient $\beta\mathcal{N}$ resulting from the collisional interactions between atoms.

Γ_p as a function of the fitted $\mathcal{N}$, for various thicknesses. To assign the error bars, three contributions must be accounted for: (i) statistical errors, that are not completely negligible here due to the fact that we repeated the measurement only few times. (ii) systematic effects due to the variation of L, which is fixed in the fitting procedure, in its uncertainty ± 2.5 nm range (this two contributions have already been discussed in section 2.3.3 of the previous chapter). (iii) Due to the large asymmetries observed even at large detuning, the normalization process is hard to carry out. Particularly, the transmission intensity is not completely flat out of resonance. It generates a third contribution to the error bar that we estimate by normalizing the data by two different methods: (1) normalization by a linear function interpolating the first and last points of the spectrum, (2) normalization by the first value of the transmission of the spectrum. We fit the data normalized by the two procedures and the systematic error associated is half the difference between the results for the two procedures. The final error bar is the quadratic sum of the three contributions.

We now analyse quantitatively the results obtained. We see that both Δ_p and Γ_p can be written as:

$$\Delta_\mathrm{P} = \Delta_\mathrm{Offset}(L) + \frac{\partial \Delta_\mathrm{P}}{\partial \mathcal{N}}(L)\mathcal{N}, \tag{3.21}$$

$$\Gamma_\mathrm{P} = \Gamma_\mathrm{Offset}(L) + \frac{\partial \Gamma_\mathrm{P}}{\partial \mathcal{N}}(L)\mathcal{N}. \tag{3.22}$$

The offsets on the two quantities originate from the interaction between the atoms and the cell walls. For the shift, it is due to van der Waals atom-surface interaction that we will study in chapter 4. The offset on Γ_P is mainly a transient broadening originating from atom-wall quenching collisions that dominate at low density. Figure 3.5(b) indicates that Γ_P is much larger than the Doppler width. The broadening is therefore dominated by the density-dependent contribution coming from the collisional dipole-dipole interactions. It validates *a posteriori* the local refractive index approach and the fact that we do not need to include the velocity distribution in the model.

The dependence of the extracted parameters Δ_P and Γ_P is also linear with the density. Particularly, the transition from blue-to-red that we observed with Δ_min in Fig. 3.3(b) has completely disappeared on Δ_P. It means that our model includes this phenomenon that we explain as a competition between two effects:

1. when the density increases, the real (respectively imaginary) part of the refractive index n is not purely associated with the real (respectively imaginary) part of

the susceptibility. Indeed, when χ is not small compared to unity, $n = \sqrt{1+\chi} \neq 1 + \chi/2$. The apparent blue shift is consequently not a shift of the resonance of χ but rather comes from a mixing of the real and imaginary part of χ due to the propagation of light in a medium of index n. We did not find a completely convincing physical reason that would rather distort the line-shape towards the blue rather than the red side of the resonance.

2. At large densities, the red shift of the resonance of χ, that we extract in Fig. 3.5(a) is larger than the blue shift due to the propagation. The position of the minimum of transmission therefore features the transition from the blue-to-red side of the resonance.

We finally note that the extracted parameters Δ_{p} and Γ_{p} accounts for all the cavity effects. This is one of the main achievements of this Thesis: we are now able to measure the properties of a medium deconvolved from an environment that alter its spectral properties. We now try to clarify the origin of the linear behavior observed in Figs. 3.5(a-b).

3.3.2 Collisional or collective effects?

To remove the influence of quenching collisions with the surface on the shift and broadening (an effect depending on L only), we fit the data presented in Figs. 3.5(a-b) by a linear function and extract the slopes $(\partial\Delta_{\mathrm{P}}/\partial\mathcal{N})(L)$ and $(\partial\Gamma_{\mathrm{P}}/\partial\mathcal{N})(L)$. We plot in Figs. 3.5(c-d) these slopes with respect to the cell thickness L. Both quantities feature an offset that we now try to interpret.

Collisional or collective shift? The linear dependence of the shift with density can originates from two *scenarii*. It could either be related to the local field corrections or to collisional effects. These two cases are respectively the static and dynamic version of the dipole-dipole interaction. We have shown in Appendix A.4 that using the Clausius-Mossoti relation for the susceptibility yields the thickness-independent Lorentz shift $\Delta_{\mathrm{LL}} = -\pi(\mathcal{N}/k_\ell)^3\Gamma_0$. The collisional shift is less well documented. A dimensional analysis suggests that it is proportional to density and independent of the velocity. Consider indeed an atom that moves around another atom at a distance $\lambda\!\!\!^{-} = 1/k_\ell$: the shift associated with one collision is about Γ_0, as predicted by the dipole-dipole potential at this distance[8]. During a time $\tau = \lambda\!\!\!^{-}/v$, the number of

[8] In the near field regime the dipole-dipole potential is $V_{\mathrm{dd}} \sim \hbar\Gamma_0/(k_\ell r)^3$.

collision is $\tau \times \gamma_c$ with $\gamma_c = \mathcal{N}\sigma_s v$ [Lewis, 1980] the collision rate and σ_s the cross section of the atom. Since the cross section $\sigma_s \propto 1/k_\ell^2$ for resonant processes, the total shift is therefore expected to vary as:

$$\Delta_{\text{coll}} \sim \Gamma_0 \tau \gamma_c = \frac{\mathcal{N}}{k_\ell^3}\Gamma_0. \tag{3.23}$$

Reference [Maki *et al.*, 1991] pointed out that experiments performed in the linear regime of interaction (*i.e.* the weak driving approximation) cannot distinguish between the static and dynamic contributions to the shift, both linear with density. As a consequence, the offset on the shift slope appearing in Fig. 3.5(c) (red dotted line) results from these two phenomena. In the strong driving limit, these two contributions should not scale identically with $\mathcal{N}$ [Maki *et al.*, 1991]. Going beyond the weak driving field approximation does not cause any particular experimental difficulty. However, deriving a full transmission model in this regime, which is absolutely required to interpret the data, would be a highly non-trivial undertaking.

We observe a residual oscillation of the shift slope with an approximate period of half a wavelength (black dotted line). This oscillation is unexpected: all known dependences of Δ_p with the cell thickness are included and it should result in a shift slope being a bulk property of the medium, *i.e.* independent of L. It is though not to exclude that we overlooked a systematic error in the data analysis. Residual biases, originating from non-local effects that are not included in this analysis, could also result in an apparent oscillation. Another final possibility that could explain this oscillation is the discrete nature of the atoms: their position correlations would introduce an effective shift and broadening that may depend on L. This interpretation is now supported by a work in progress that should appear in [Dobbertin, 2020]. In this work, the authors perform the following analysis:

1. They compute the numerical solution of the discrete scattering model with a Greens tensor including the effects of the cavity to generate transmission spectra.

2. They fit these profiles with Eq. (3.19), that do not include the correlations (this is exactly what we have done in our analysis).

3. They extract a similar oscillation of the slope of the shift versus density as a function of the cell thickness.

This surprising and unexpected matching certainly calls for new measurements with a systematic comparison to this new theoretical approach.

Collisional broadening A complete analysis of collisional processes is beyond the scope of this manuscript. However, according to the standard line-broadening theory [Lewis, 1980], the collisional broadening is Lorentzian and proportional to the density of atoms[9]: $\Gamma_{\text{col}} = \beta\mathcal{N}$. The coefficient of proportionality β depends on the atomic transition. It is given by [Weller *et al.*, 2011]:

$$\beta = \Gamma_0 \left(\frac{\lambda}{2\pi}\right)^3 \times \delta_{1,2}, \tag{3.24}$$

where $\delta_{1,2} = 1$ for the D_1 line and $\sqrt{2}$ for the D_2 line. For the D_2 line of potassium, $\Gamma_0 \simeq 2\pi \times 6$ MHz, $\lambda = 767$ nm and $\delta_{1,2} = \sqrt{2}$ leading to $\beta = 9.7 \times 10^{-8}$ Hz·cm^3. The slopes of the broadening with respect to density, presented in Fig. 3.5(d), are in very good agreement with this theoretical prediction superimposed on the graph in dashed line. Due to this collisional broadening, the larger the density, the broader the line: it leads to a saturation phenomenon that we finally discuss now.

3.3.3 Saturation of the susceptibility

In Fig. 3.6(a), we plot the value of the minimum of transmission T_{min} as a function of $\mathcal{N}$ for different cell thicknesses. We observe that although the density increases, the quantity of absorption clearly saturates. This phenomenon is a consequence of the self-collisional broadening. To see how this comes about, we recall that the susceptibility can be written as $\chi = \mathcal{N}\alpha$ with α given by Eq. (3.20). If the collisional broadening is proportional to the density of atoms, the susceptibility is no longer linear with density and the saturation occurs. To observe this saturation in the optical response χ, we fit the spectra associated with the data presented in Fig. 3.6(a) with our transmission model (Eq. (3.19)). From the fitted parameters $\Delta_{\text{p}}, \Gamma_{\text{p}}$ and $\mathcal{N}$, we can compute theoretically the susceptibility associated with these transmission spectra. We present in Fig. 3.6(b) the maximal value of the modulus of χ typically obtained on resonance. We see that in our case, the saturation occurs at a density of $\mathcal{N} > 10^{22}$ at·m^{-3}. Besides, we note that the susceptibility almost reach unity (see also Ref. [Keaveney *et al.*, 2012a], where such large susceptibility have also been observed.).

Reference [Javanainen *et al.*, 2014] pointed out that in presence of inhomogeneous broadening, the polarizability of each velocity class gets suppressed by a quantity $\Gamma_0/\Delta\omega_{\text{D}}$ where $\Delta\omega_{\text{D}}$ is the inhomogeneous Doppler width. It gives a ratio of approxi-

[9] This is valid in the binary approximation which does not break for the range of density studied in this manuscript.

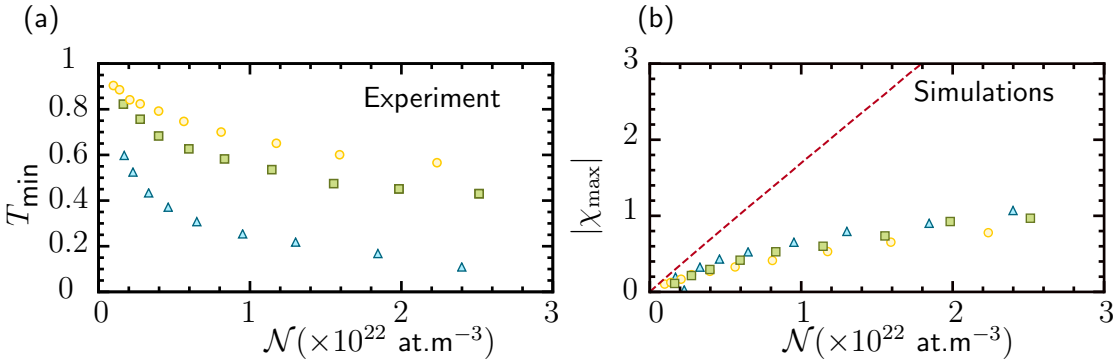

Figure 3.6: Saturation of the atomic susceptibility (a) Experiment. Minimum of transmission with respect to density. Yellow dots: $L = 87$ nm, green squares: $L = 120$ nm and blue triangles: $L = 147$ nm. (b) Simulation. Maximum of the modulus of χ as a function of density for the same cell thicknesses. The susceptibility is calculated with the parameters fitted with the model. Red dashed line: same quantity calculated without collisional broadening.

mately 0.01 between the total susceptibility and the one from each velocity class. It ultimately boils down to two conclusions:

- The saturation occurs whenever the medium becomes homogeneously broadened *i.e.* when $\beta\mathcal{N} \gg \Delta\omega_{\mathrm{D}}$.
- The effective susceptibility of each velocity class is much smaller than unity. This could be the reason why we still observe a linear behavior of spectral shifts and widths with respect to the density. Indeed, we saw at the beginning of the chapter that the condition to observe first-order shifts in density was $\mathcal{N}/k_\ell^3\,(\Gamma_0/\Gamma_{\mathrm{t}}) \ll 1$. In an inhomogeneously broadened medium, it is likely that this condition should be replaced by $\mathcal{N}/k_\ell^3\,(\Gamma_0/(\Delta\omega_{\mathrm{D}} + \Gamma_{\mathrm{t}})) \ll 1$.

3.4 Conclusion

In conclusion, we performed a new series of measurements of the transmission of near-resonant light through an alkali vapor with nano-meter scale thickness in order to investigate the origin and validity of the CLS. We found that the CLS, as initially predicted by [Friedberg, Hartmann, and Manassah, 1973], is valid for a dilute enough ($\mathcal{N}/k_\ell^3\,(\Gamma_0/\Gamma_{\mathrm{t}}) \ll 1$) slab of atoms surrounded by vacuum. In this case only, it corresponds to the displacement of the minimum of transmission. When the medium is not vacuum, we have observed asymmetric spectra: it prevents from defining a shift in

a meaningful way. A model, deconvolving the cavity effect from the atomic properties of the slab, accurately reproduced the observed strong asymmetries of the line-shapes. Using this model, we extracted from our data shifts and widths of the bulk atomic medium resonance. We found a linear dependence of these quantities with respect to the density that led to a saturation of the susceptibility of the atomic vapor.

Several questions have not been solved yet:

- First, we observed an oscillation of the slopes of the shift when the cell thickness varies (see Fig. 3.5)(c). This is unexpected! Besides, a recent theoretical prediction [Dobbertin, 2020] tends to show that it would originate from the atomic correlations between the atoms due to their discrete nature. This interpretation is still preliminary and calls for future in-depth investigations.

- Secondly, the role of the inhomogeneous broadening in the observation of density shifts is not fully clarified: when do the different velocity classes start to interact? Does it require that the homogeneous broadening exceeds the Doppler width? Is the presence of inhomogeneous broadening a necessary condition to observe the shifts, as suggested by Ref. [Javanainen *et al.*, 2014]?

- Finally, our experiment was done in the linear regime of interaction and as a result, we have not been able to distinguish between static and dynamic dipole-dipole shifts. Extending the model to strong driving, also including the cavity effects, is however a highly non-trivial work.

In this chapter, $\xi \ll L$ and the relaxation of the dipoles is mainly limited by collisions. When density effects are smaller, we have seen in Chapter 2 that the walls of the nano-cell play an important role in the optical response of the system. Another effect due to the nano-cell walls that we ignored so far is the long-range van der Waals interaction between an atom and a neighboring surface. This is the subject of the next chapter.

Chapter 4

Atom-surface interactions

Contents

Introduction

In the previous chapters, we have investigated the dependence of the line-shifts with respect to the density of atoms $\mathcal{N}$ and the thickness of the medium L. There, we have seen that the optical response of an atomic vapor in a nano-geometry can be affected by the presence of the cell walls. Particularly, it induces a thickness-dependent offset of the shift that needs to be characterized.

Placing atoms close to surfaces is not necessarily a drawback since it offers new possibilities for engineered atom-atom and atom-light interactions. In nano-photonic devices for example, light can be tightly confined in sub-wavelength geometries where atoms lie in the vicinity of surfaces [Mitsch *et al.*, 2014]. In this case, coupling to

matter depends on the direction of light propagation and this may have applications in quantum information science [Lodahl *et al.*, 2017]. This has stimulated a recent growth in the number of platforms where atoms are kept close to surfaces, ranging from nano-fibers [Le Kien, Balykin, and Hakuta, 2004; Vetsch *et al.*, 2010; Patterson *et al.*, 2018] and nano-cells [Sarkisyan *et al.*, 2001]; to waveguides [Ritter *et al.*, 2018] and microtoroidal optical resonators [J. Alton *et al.*, 2010]. Simultaneously, shrinking the dimensions of atom-based sensors [Knappe *et al.*, 2005; Wade *et al.*, 2017] increases the number of atoms close to a surface relative to atoms in the bulk. Atom-surface interactions are therefore becoming increasingly important: they may limit the ultimate achievable precision of atom vapor sensors and they are crucial in understanding the dynamics in each new platform. However, despite their significance, direct measurements of atom-surface interactions are scarce.

So far, we attributed the modification of the optical response caused by the surface to atomic collisions with a wall or cavity effects originating from the reflections of light on a dielectric interface. In this chapter, we study another effect due to the surface: the van der Waals (vdW) interaction. Measuring the vdW atom-surface interaction — which scales with the distance z to the surface as $1/z^3$ in the non-retarded regime— is challenging as it requires placing the atoms in a given internal state at a distance $z < \lambda/(2\pi)$ from the surface. Here λ is the wavelength of the strongest atomic transition from the considered state. Previous experiments on vdW atom-surface interactions often used sophisticated techniques like reflections of cold atoms on a surface [Landragin *et al.*, 1996; Mohapatra and Unnikrishnan, 2006] or high-lying atomic states [Fichet *et al.*, 2007]. High-lying states allow easier access to the vdW regime as: (i) transitions among higher-lying states correspond to longer wavelengths λ, relaxing the constrain on the atom-surface distance; and (ii) these transitions have larger dipole matrix elements, resulting in a stronger vdW C_3 coefficient in the atom-surface potential $V(z) = -C_3/z^3$. However, for many applications [Knappe *et al.*, 2005; Mitsch *et al.*, 2014], it is the properties of the atom-surface potential for the low-lying states that are of most interest because atoms naturally lie in the ground state.

Spectroscopy of thermal vapors contained in cells is an attractive method for the measurement of atom-surface interactions [M. Ducloy and M. Fichet, 1991; Failache *et al.*, 1999; Fichet *et al.*, 2007], since it can be used for a large range of vapors, atomic or molecular, and surfaces. However, measurements have low precision for weak vdW interaction strengths of ground state atoms, mainly limited by the uncertainty in estimating collisional processes in dense vapors [Fichet *et al.*, 2007; Laliotis *et al.*,

2008]. A recent method that measured the ground state vdW interaction based on *fluorescence* spectroscopy in low-density thermal vapors [Whittaker *et al.*, 2014] also raised debate [Bloch, 2015] about the absolute achievable precision of the measurements, since the theoretical model used neglected atomic motion in the spatially varying atom-surface potential. Finding simple and precise methods that would allow reliable extraction of the ground-state atom-surface potential parameters, and characterization of the atom dynamics in the proximity of surfaces in new platforms, remains an open goal.

Finally, the $1/z^3$ dependence of the shift is valid when the distance z to the surface verifies: (Few nm) $\leq z \leq \lambda$. On the one hand, retardation effects have to be taken into account at larger atom-surface distances, resulting in the Casimir-Polder regime: $V(z) \propto 1/z^4$ (See e.g. the review [Hinds, 1991]). On the other hand, a repulsive potential barrier has been predicted very close to the surface [Lima *et al.*, 2000]. We expect these effects to be of minor importance with respect to the vdW interaction in our set-up. Can we though see traces of their influence on experimental transmission spectra?

Structure of the chapter In a first section, we will review some elements of the vdW atom-surface theory in order to predict expectations for the C_3 coefficient in different atom-material configurations. Then, we shall study experimentally the atom-surface interaction looking at the optical response of the vapor in the extremely thin region of the nano-cell. In order to extract properly the effect of the surface and get the C_3 coefficient, we will refine our transmission model to account for the motion of the atoms in the spatially-varying potential. In a last brief section, we will present the limitations and perspectives of adapting the work presented in this chapter to other atom-surface potential dependences.

4.1 Theory of vdW atom-surface interaction

In this section, we first derive the spatial dependence of the vdW interaction starting from a classical analogy. We then give the expression of the potential when the atomic states considered lie far from any plasmonic resonance of the dielectric material. We finally compute the atom-surface coefficient strength C_3 for an atom of Cs close to a sapphire or a borosilicate wall.

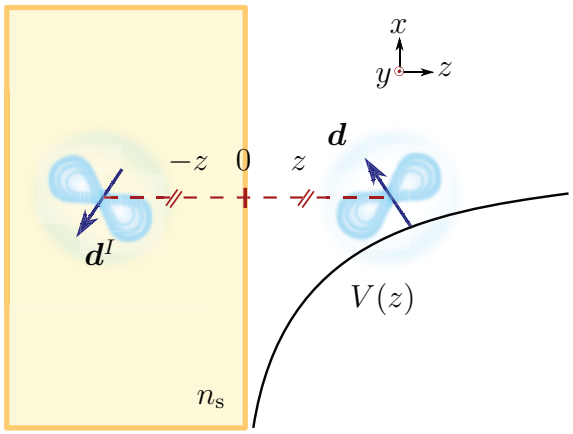

Figure 4.1: Atom-surface interaction Illustration of a surface of refractive index n_s acting on an atomic dipole $\boldsymbol{d}$. The effect is similar to the interaction with an image dipole $\boldsymbol{d^I}$ placed symmetrically with respect to the surface plane. The resulting dipole-dipole potential is $V(z) = -C_3/z^3$ with z the distance to the surface.

4.1.1 Atom-surface potential near a dielectric surface

The derivation of the atom-surface potential closely follows the work presented in Ref. [Fichet *et al.*, 1995].

The classical analogy From an electrostatic point of view, the effect of a dielectric wall (with refractive index[1] n_s) on a particle of charge q placed at a distance z from the surface, can be modelled assuming an image charge $-q\,(n_\mathrm{s}^2-1)\,/\,(n_\mathrm{s}^2+1)$, located at a position $-z$. In the same way, the effect of a dielectric surface on an electric dipole $\boldsymbol{d}$ is similar to the one of an image dipole $\boldsymbol{d^I}$ with spatial components given by:

$$d^I_{x,y} = -\frac{n_\mathrm{s}^2-1}{n_\mathrm{s}^2+1} d_{x,y}, \tag{4.1}$$

parallel to the surface and:

$$d^I_z = \frac{n_\mathrm{s}^2-1}{n_\mathrm{s}^2+1} d_z, \tag{4.2}$$

perpendicular to the surface, as represented in Fig. 4.1. In the near field regime (*i.e.* neglecting retardation effects), the resulting interaction potential for the two dipoles

[1] The case of a perfect reflector such as a metallic surface corresponds to $n_\mathrm{s} \to \infty$.

separated by a distance $2z$ can be written as:

$$V_{\mathrm{cl}} = -\frac{1}{2}\boldsymbol{d^I}\cdot\boldsymbol{E} = -\frac{1}{2}\boldsymbol{d^I}\cdot\frac{1}{4\pi\epsilon_0}\frac{\left[3\left(\boldsymbol{d}\cdot\hat{\mathbf{e}}_{\boldsymbol{z}}\right)\hat{\mathbf{e}}_{\boldsymbol{z}}-\boldsymbol{d}\right]}{(2z)^3}, \tag{4.3}$$

where $\boldsymbol{E}$ is the electrostatic field (see first part of Eq. (1.18)) radiated by the real dipole acting on its image. Using Eqs. (4.1) and (4.2), it gives:

$$V_{\mathrm{cl}} = -\frac{1}{4\pi\epsilon_0}\frac{n_{\mathrm{s}}^2-1}{n_{\mathrm{s}}^2+1}\left(\frac{d_x^2+d_y^2+2d_z^2}{16z^3}\right). \tag{4.4}$$

Quantum mechanical atom-surface potential In contrast to dipole-dipole interactions that we studied in the previous chapters, the vdW interaction is not a resonant process. In other words, it occurs between atoms in the same atomic state. Consequently, there is no light-induced dipole and the field $\boldsymbol{E}$ introduced previously is virtual: the vdW interaction can only be consistently described as a quantum-mechanical effect. It can be shown [Fichet *et al.*, 1995] that the corresponding atom-surface operator V_{AS} is still given by Eq. (4.4), where $\boldsymbol{d}$ is now the electric dipole moment operator. At first order perturbation in energy, the resulting shift of an atomic state $|a\rangle$ can be written as:

$$V(z) = \langle a|\, V_{\mathrm{AS}}\,|a\rangle = -\frac{C_3}{z^3}, \tag{4.5}$$

where the C_3 involved $\langle d_x^2\rangle$, $\langle d_y^2\rangle$ and $\langle d_z^2\rangle$ that are non-zero for an atom in a given atomic state while $\langle d_x\rangle{=}\langle d_y\rangle{=}\langle d_z\rangle = 0$. In order to calculate the C_3 coefficient, we need more details about the dielectric surface.

4.1.2 Calculation of the atom-surface C_3 coefficient for a Cs atom placed close to a dielectric surface

The quantum average given by Eq. (4.5) is a sum over all atomic levels $|m\rangle$ connected by electric dipole transition to $|a\rangle$. When these transitions do not lie close to plasmonic resonances of the medium, C_3 can be written as:

$$C_3^{|a\rangle} = -\frac{1}{4\pi\varepsilon_0}\sum_{\text{states}|m\rangle}\frac{n_{\mathrm{s}}(\omega_{\mathrm{am}})^2-1}{n_{\mathrm{s}}(\omega_{\mathrm{am}})^2+1}\left(\frac{|d_x^{\mathrm{am}}|^2+|d_y^{\mathrm{am}}|^2+2|d_z^{\mathrm{am}}|^2}{16z^3}\right). \tag{4.6}$$

The quantities $d_{x\ldots z}^{\mathrm{am}} = \langle a|\, d_{x\ldots z}\,|m\rangle$ are the dipole matrix elements along the x, y and z axis respectively, corresponding to optical transitions from states $|a\rangle$ to $|m\rangle$ of

frequency ω_{am}. The case including the plasmonic resonances of the material is more involved and is described theoretically in Ref. [Fichet *et al.*, 1995]. Experimental works have investigated this plasmonic coupling and found the existence of thermally excited surface modes [Laliotis *et al.*, 2014] or negative values for C_3 [Failache *et al.*, 1999]. This subject is beyond the scope of the present manuscript.

When measuring the shift on an optical transition, the effective C_3 results from the difference between the excited and ground states coefficients. Namely, if the optical transition couples the initial $|a\rangle$ and final states $|b\rangle$, the effective C_3 is given by:

$$C_3 = C_3^{|b\rangle} - C_3^{|a\rangle}. \tag{4.7}$$

In our experiment, we probe the Cs D_1 line. We therefore need the coefficients for the $6S_{1/2}$ and $6P_{1/2}$ states. Knowing the dipole matrix elements for the corresponding transitions and the refractive index of the surface for the appropriate range of frequencies allows one to calculate the effective strength of the vdW interaction. In Tabs. 4.1 and 4.2 we display the main contributions to these two coefficients in the case of a sapphire and borosilicate[2] surface respectively. The dipole matrix elements are theoretically calculated using Ref. [Safronova, Safronova, and Clark, 2016] and the Alkali Rydberg Calculator (ARC) Python package [Sibalic, Pritchard, and Weatherill, 2017]. The refractive index of sapphire (respectively borosilicate) is calculated from the data in Ref. [Weber, 1991] (respectively by the constructor Borofloat33).

The resulting C_3 coefficients for the D_1 line transition, calculated for the sapphire and borosilicate surface are:

$$C_{3,\mathrm{th}}^{\mathrm{Sa}} = 1.10 \pm 0.03 \text{ kHz} \cdot \mu\mathrm{m}^3, \tag{4.8}$$

$$C_{3,\mathrm{th}}^{\mathrm{Bo}} = 0.83 \pm 0.02 \text{ kHz} \cdot \mu\mathrm{m}^3. \tag{4.9}$$

The error bars associated with the theoretical values are due to the different models used by the authors [Safronova, Safronova, and Clark, 2016; Sibalic, Pritchard, and Weatherill, 2017] to calculate the dipole matrix elements.

In the next section, we will investigate the vdW interactions experimentally. Particularly, we will try to extract the C_3 coefficient for the D_1 line of Cs close to a sapphire surface.

[2] We will use the coefficient for the borosilicate surface in the next chapter.

Hyperfine transition	Contribution to $C_{3,\mathrm{th}}^{\mathrm{Sa}}$ (kHz·μm^3)	Reference
$6S_{1/2} \leftrightarrow 6P_{1/2}$	0.42	[Safronova, Safronova, and Clark, 2016]
$6S_{1/2} \leftrightarrow 6P_{3/2}$	0.83	[Safronova, Safronova, and Clark, 2016]
$6S_{1/2} \leftrightarrow 7P_{3/2}$	0.01	[Safronova, Safronova, and Clark, 2016]
Total $C_3^{6S_{1/2}} =$	1.258(2)	
$6P_{1/2} \leftrightarrow 6S_{1/2}$	0.42	[Safronova, Safronova, and Clark, 2016]
$6P_{1/2} \leftrightarrow 7S_{1/2}$	0.37	[Safronova, Safronova, and Clark, 2016]
$6P_{1/2} \leftrightarrow 8S_{1/2}$	0.02	[Sibalic, Pritchard, and Weatherill, 2017]
$6P_{1/2} \leftrightarrow 5D_{3/2}$	1.01	[Safronova, Safronova, and Clark, 2016]
$6P_{1/2} \leftrightarrow 6D_{3/2}$	0.37	[Safronova, Safronova, and Clark, 2016]
$6P_{1/2} \leftrightarrow 7D_{3/2}$	0.09	[Safronova, Safronova, and Clark, 2016]
$6P_{1/2} \leftrightarrow 8D_{3/2}$	0.04	[Sibalic, Pritchard, and Weatherill, 2017]
$6P_{1/2} \leftrightarrow 9D_{3/2}$	0.02	[Sibalic, Pritchard, and Weatherill, 2017]
$6P_{1/2} \leftrightarrow 10D_{3/2}$	0.01	[Sibalic, Pritchard, and Weatherill, 2017]
Total $C_3^{6P_{1/2}} =$	2.36(3)	

Table 4.1.: Dominant contributions to the cesium-sapphire vdW constant C_3 for $6S_{1/2}$ and $6P_{1/2}$ states.

Hyperfine transition	Contribution to $C_{3,\mathrm{th}}^{\mathrm{boro}}$ (kHz·μm^3)	Reference
$6S_{1/2} \leftrightarrow 6P_{1/2}$	0.32	[Safronova, Safronova, and Clark, 2016]
$6S_{1/2} \leftrightarrow 6P_{3/2}$	0.63	[Safronova, Safronova, and Clark, 2016]
$6S_{1/2} \leftrightarrow 7P_{3/2}$	0.01	[Safronova, Safronova, and Clark, 2016]
Total $C_3^{6S_{1/2}} =$	0.960(1)	
$6P_{1/2} \leftrightarrow 6S_{1/2}$	0.32	[Safronova, Safronova, and Clark, 2016]
$6P_{1/2} \leftrightarrow 7S_{1/2}$	0.28	[Safronova, Safronova, and Clark, 2016]
$6P_{1/2} \leftrightarrow 8S_{1/2}$	0.02	[Sibalic, Pritchard, and Weatherill, 2017]
$6P_{1/2} \leftrightarrow 5D_{3/2}$	0.76	[Safronova, Safronova, and Clark, 2016]
$6P_{1/2} \leftrightarrow 6D_{3/2}$	0.28	[Safronova, Safronova, and Clark, 2016]
$6P_{1/2} \leftrightarrow 7D_{3/2}$	0.07	[Safronova, Safronova, and Clark, 2016]
$6P_{1/2} \leftrightarrow 8D_{3/2}$	0.03	[Sibalic, Pritchard, and Weatherill, 2017]
$6P_{1/2} \leftrightarrow 9D_{3/2}$	0.01	[Sibalic, Pritchard, and Weatherill, 2017]
$6P_{1/2} \leftrightarrow 10D_{3/2}$	0.01	[Sibalic, Pritchard, and Weatherill, 2017]
Total $C_3^{6P_{1/2}} =$	1.79(1)	

Table 4.2.: Dominant contributions to the cesium-borosilicate vdW constant C_3 for $6S_{1/2}$ and $6P_{1/2}$ states.

4.2 Precise measurement of atom-wall vdW interaction

In this section, we present a method to measure precisely a C_3 coefficient using the wedged shape of the nano-cell. We illustrate it by a measurement of the vdW induced shift of the cesium $6S_{1/2} \rightarrow 6P_{1/2}$ transition in the presence of a sapphire surface.

4.2.1 An innovative method to extract precisely the vdW coefficient

In order to determine precisely the vdW atom-surface interaction, our new method is based on two ideas, building on the work of [Whittaker *et al.*, 2014] but using transmission spectroscopy:

1. It uses an atomic vapor confined in a nano-cell. As a consequence, the vdW shift is spatially inhomogeneous: the signal observed is integrated over atomic positions in the cell. Particularly, the position of the minimum of transmission is not related to the C_3 coefficient. Our method therefore relies on a full model of the optical response.

2. In any atomic vapor, Ref. [Laliotis *et al.*, 2008] pointed out that the "*interplay between the location of the resonance (i.e. frequency shift as possibly resulting from collisions) and the C_3 value [...] makes it very difficult to extract unambiguously the vdW interaction*". To circumvent this problem, we use the wedged shape of the nano-cell: this allows access both to the region where vdW interactions have strong effects on the total transmission signal, and the region where atoms in the bulk, not affected by the vdW induced shifts, dominantly contribute. Spectra from the thick region yield the collisional parameters for the bulk atomic vapor, thus allowing reliable fitting of thin-region spectra using our model.

Our method can be used with reflection, fluorescence or transmission signals from the atoms confined in the nano-cell. In this chapter, we perform transmission measurements to benefit from the knowledge in spectroscopy acquired in the previous chapters[3]. Particularly, the theoretical analysis of transmission spectra in nano-cells is significantly more complicated than for transmission through a bulk vapor. As we already saw, a number of effects starts to play a role with the reduction of the vapor thickness L (see Fig. 4.2(b)): (i) for micrometer thick layers, the cell walls act as a low-finesse

[3]We are also not aware of any measurement of low-lying atomic states vdW potential using transmission spectroscopy of thermal vapors.

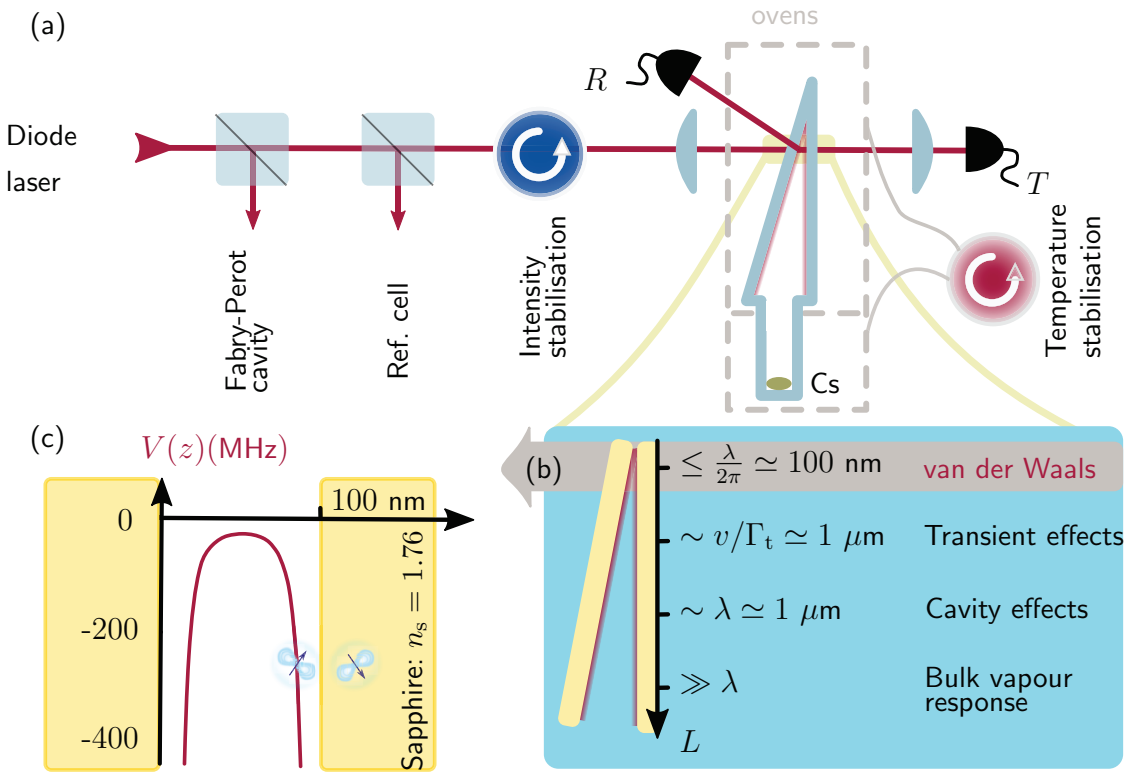

Figure 4.2: A method to extract vdW interactions (a) Optical set-up similar to the ones of previous chapters. The two photodiodes measure reflections R for thickness calibration and transmission T. The two ovens are PID-controlled by a system described in Fig. 4.3. (b) The wedged shape of the cell allows probing the transmission in thick cell regions, where the contribution of atoms close to surfaces is negligible compared to the contribution of the atoms in the bulk. It also allows going to sub-100 nm thick region where the atoms are strongly affected by the vdW potential, due to the interaction of their dipole with its image in the surface. (c) This gives rise to a position z dependent level shift $V(z)$, here calculated for the D_1 Cs transition.

cavity, resulting in level shifts, as studied in Chapter 3; (ii) the cell windows also cause dephasing of atoms upon direct collisions. Atoms flying off the walls experience transient dynamics during a time $1/\Gamma_t$, with Γ_t the collisionally broadened line-width. For a cell thickness below v/Γ_t (v is the average atom velocity), a significant number of probed atoms experience this transient regime, which significantly modifies the measured transmission, as seen in Chapter 2. For cesium atoms at a temperature $\Theta = 200°C$, this corresponds to a distance of ~ 1 µm. Finally, (iii) at atom-surface distances $z < \lambda/(2\pi)$ atomic energy levels experience a vdW shift from the two surfaces:

$$V(z) = -\frac{C_3}{z^3} - \frac{C_3}{(L-z)^3}, \tag{4.10}$$

as represented in Fig. 4.2(c). Equation (4.10) for $V(z)$ accounts only for the interaction of a dipole with its image in the sapphire. The interaction of a dipole image with its dipole images is neglected because it contributes for less than a few percent in the C_3, as shown in Refs. [Dutier, 2003] and [Hinds, 1991]. We now illustrate our method on a Cs vapor confined in a sapphire nano-cell.

4.2.2 Atoms flying in a spatially varying potential

Experimental details The experimental set-up (see Fig. 4.2(a)) is almost the same as the one presented in the two previous chapters. Here, the cell is filled with Cs instead of K. I have also added an active feedback system to control and stabilize the temperatures of both the reservoir and windows. The feedback loop, represented in Fig. 4.3(a), is operated by an Arduino controller. The controller is used to switch solid-state-relay from Crydom in order to turn on and off the reservoir and window ovens. As explained in the previous chapters, the exact value of the temperatures measured is not crucial[4]. However, thanks to this control, we ensure that the temperature remains constant within a few Celsius degree over the time of the experiment (see Fig. 4.3(b)). It prevents from large atomic density fluctuations that could impact the collisional processes that we try to estimate.

Using the wedged shape of the nano-cell, we obtain transmission spectra of the vapor represented in Fig. 4.4(a) for a range of cell thickness $L = 50 - 275$ nm and a temperature of 235°C (density $\mathcal{N} = 6 \times 10^{21}$ at·m^{-3}). The data result from an average over 100 realizations and we can measure in this way an absorption as low as 1%. The lowest signal-to-noise (SNR) ratio that we obtain is around 5, proving the excellent stability of the optical set-up. The SNR is limited by small oscillations on the base line (intensity collected on the photodiode without atoms) that are attributed to residual Fabry-Perot effects on lenses, cubes etc... The choice in the temperature therefore results from a compromise. On the one hand, broadening of the line due to collisions shortens the spatial response extension[5] ξ of the susceptibility. Broadening should therefore diminish the vdW effect due to the surface on the spectra. On the other hand, working with a reduced density would result in even smaller absorption rates,

[4] As long as the temperature of the reservoir remains 30°C colder than the one of the windows.
[5] $\xi = v/\Gamma_t$, as seen in Chapter 2.

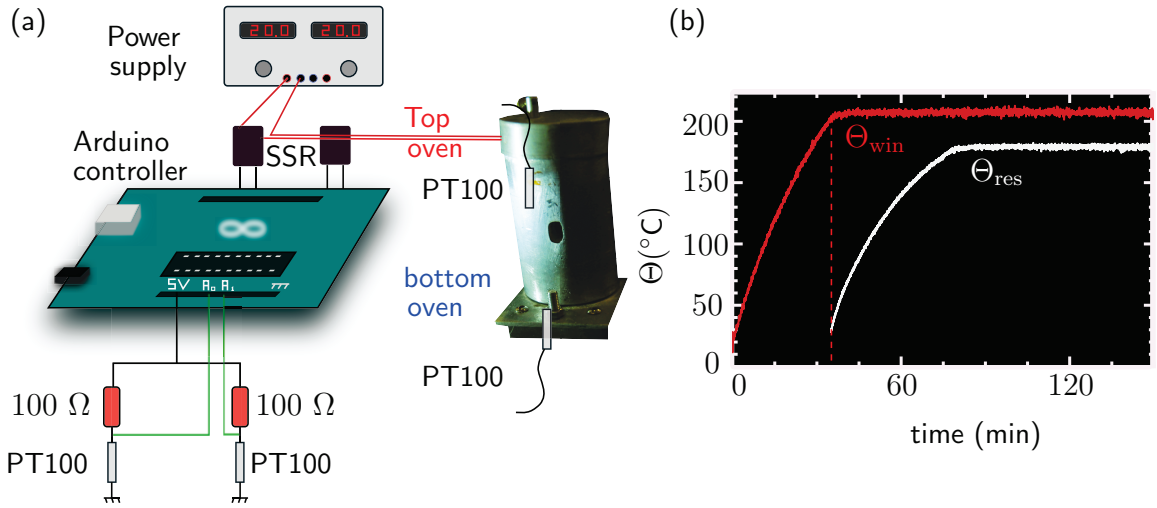

Figure 4.3: Control of temperatures (a) Two thermo-resistances PT100 are used to measure the temperature of the window (Θ_{win}) and the reservoir (Θ_{res}). A circuit consisting of two resistances in series powered in 5 V, produces a voltage compatible with the Arduino analog inputs (A_0, A_1). This voltage depends on the measured temperature. The micro-controller is programmed such as to provide an output current only if the measured temperature is below its set-point. In this case, a solid-state relay (SSR from Crydom) works as a closed switch and the power supply drives the thermo-heater associated with the oven. The circuit is similar for both window and reservoir ovens. (b) Example of controlled temperatures as a function of time.

hence affecting the SNR.

Fitting with Model 2 We recall that we developed a model in Chapter 2, called *Model 2*. This model worked up to 20% of absorption and included several effects: (i) the non-local correction due to atomic motion, (ii) the quenching collisions with the cell walls and (iii) the reflection of the fields induced by the cavity. We now use this model to fit our experimental data. It fits well the measured transmission spectra for cell thicknesses $L \geq 175$ nm (see for example Fig. 4.4(b)) where the signal is dominated by atoms far from the surface. In this region, fitting the temperature, level shift Δ_{p} and broadening Γ_{p} allows us to obtain the collisional self-broadening $\Gamma_{\mathrm{P0}}/(2\pi) = 830 \pm 10$ MHz (see Fig. 4.4(c)) and shift $\Delta_{\mathrm{P0}}/(2\pi) = -10 \pm 20$ MHz (see Fig. 4.4(d)) in the bulk vapor, arising solely from atom-atom collisions. The values and error bars are the mean and standard error of the fitted values for cell thicknesses $L \geq 175$ nm.

For cell thicknesses $L \leq 175$ nm, the contribution from atoms close to the surface

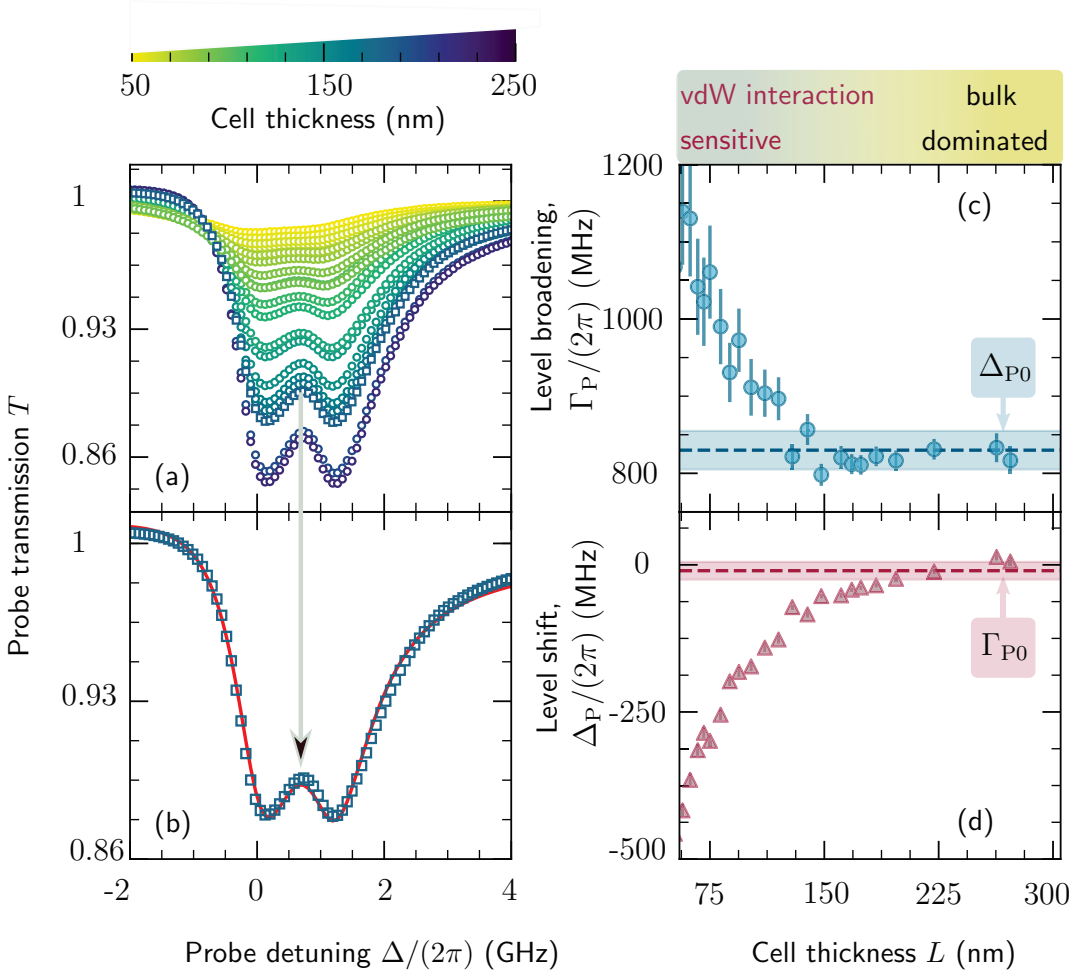

Figure 4.4: Bulk vapor properties (a) Measured transmission spectra at $235°$C, for cell thickness L in the range 50–225 nm. The left and right peaks correspond respectively to the $F = 4 \to 3$ and $F = 4 \to 4$ transitions of the Cs D_1 line. Model 2, not including atom-surface interactions, fits well spectra in the thick part of the cell (b), allowing the extraction of bulk properties of the vapor from values obtained for large L. (c-d): Determination of the collisional broadening Γ_{P0} and shift Δ_{P0} in the bulk vapor. For small L, the influence of the atom-surface interactions appears as an additional thickness-dependent line broadening and transition shift.

becomes significant. Model 2 captures this atom-surface interaction *phenomenologically* as a cell thickness dependent shift and broadening, as shown in Fig. 4.4(c-d). However, this phenomenological fit does not provide direct access to the C_3 vdW coefficient. In addition, Fig. 4.5 indicates that fine features of thin-cell spectra are not captured by Model 2. This motivated us to extend this model to explicitly include the spatially-varying vdW potential.

Atoms flying in a spatially varying potential Due to the divergences in $z = 0$ and $z = L$ of the potential (see Eq. (4.10)), the method adopted in Chapter 2 to solve the equation for coherences cannot be applied. Particularly, the Fourier transform used to derive Eq. (2.6) from Eq. (2.5) has no analytical solution in this case. We therefore find another way to derive the atomic polarization P. Namely, we start back with Eq. (2.5) recalled below:

$$v\frac{\partial\rho_{21}(z,v)}{\partial z} = -\left[\frac{\Gamma_t}{2} - i\Delta_{\mathrm{FF'}}(z)\right]\rho_{21}(z,v) + i\frac{d_{\mathrm{FF'}}E(z)}{2\hbar}\ ,$$

where the detuning $\Delta_{\mathrm{FF'}} = \omega_\ell - \omega_{\mathrm{FF'}}(z)$ is now spatially dependent. The resonant frequency is shifted as $\omega_{\mathrm{FF'}}(z) = \omega_{\mathrm{FF'}} + V(z)$ with $V(z)$ given by Eq. (4.10). We remind that in the nano-cell, the field $E(z)$ propagates forwards and backwards. For the general driving field

$$E(z) = E_+e^{ik_\ell z} + E_-e^{-ik_\ell z}, \tag{4.11}$$

consisting of the co-propagating E_+ and counter-propagating E_- fields along the z-axis, we write the coherences as:

$$\rho_{21}(z,v) = \rho_+(z,v)e^{ik_\ell z} + \rho_-(z,v)e^{-ik_\ell z}. \tag{4.12}$$

We thus obtain the two following equations from Eq. (2.5):

$$v\frac{\partial\rho_+}{\partial z} = -\left[\Gamma_t/2 - i(\Delta_{\mathrm{FF'}}(z) - k_\ell v)\right]\rho_+ + i\frac{d_{\mathrm{FF'}}E_+}{2\hbar}, \tag{4.13}$$

$$v\frac{\partial\rho_-}{\partial z} = -\left[\Gamma_t/2 - i(\Delta_{\mathrm{FF'}}(z) + k_\ell v)\right]\rho_- + i\frac{d_{\mathrm{FF'}}E_-}{2\hbar}. \tag{4.14}$$

Using the variation of constant method for differential equations, we find for $v \neq 0$:

$$\rho_+(z,v) = \rho_+(z_0,v)e^{-\Lambda_+/v} + i\frac{d_{\mathrm{FF'}}E_+}{2\hbar v}\int_{z_0}^{z}\mathrm{d}z'\ \exp\left[\frac{\Lambda_+(z')-\Lambda_+(z)}{v}\right], \quad (4.15)$$

$$\rho_-(z,v) = \rho_-(z_0,v)e^{-\Lambda_-/v} + i\frac{d_{\mathrm{FF'}}E_-}{2\hbar v}\int_{z_0}^{z}\mathrm{d}z'\ \exp\left[\frac{\Lambda_-(z')-\Lambda_-(z)}{v}\right], \quad (4.16)$$

where z_0 depends on the boundary conditions and the primitive

$$\Lambda_\pm(z) = \int \mathrm{d}u\frac{\Gamma_\mathrm{t}(u)}{2} - i\left[\Delta_{\mathrm{FF'}}(u) \mp k_\ell v\right]. \quad (4.17)$$

Had we ignored the vdW potential, we would have found:

$$\Lambda_\pm^{\mathrm{bulk}}(z) = \left[(\Gamma_{\mathrm{P}0}+\Gamma_0)/2 - i(\Delta_{\mathrm{FF'}} \mp k_\ell v)\right] z \quad (4.18)$$

and the reasoning that will follow would have exactly led to Model 2. If we now take into account the effect of the surface, the primitives are rather given by:

$$\Lambda_\pm(z) = \left\{\frac{\Gamma_0+\Gamma_{\mathrm{P}0}}{2} - i(\omega_\ell - \omega_{\mathrm{FF'}} - \Delta_{\mathrm{P}0} \mp k_\mathrm{l} v) + iC_3\left[\frac{1}{2z^3} - \frac{1}{2z(L-z)^2}\right]\right\} z. \quad (4.19)$$

In the above equation, we have assumed that the decay rate was not affected by the surface, which is justified as we are far from polaritonic resonances of the crystal surface [Failache *et al.*, 2002]. The first part of Eq. (4.19) describes the bulk properties of the medium (Eq. (4.18)), while the second line is due to the atom-surface vdW potential.

As in Chapter 2, we assume a loss of coherence at a collision of an atom with the cell walls (quenching collisions [Schuurmans, 1976]). It leads to the boundary conditions $\rho_\pm(v>0, z=0) = \rho_\pm(v<0, z=L) = 0$. Three cases can therefore been distinguished:

$$\rho_{\pm}(z, v>0) = i\frac{d_{\mathrm{FF'}}E_{\pm}}{2\hbar v}\int_0^z \mathrm{d}z' \exp\left[\frac{\Lambda_{\pm}(z')-\Lambda_{\pm}(z)}{v}\right], \tag{4.20}$$

$$\rho_{\pm}(z, v<0) = -i\frac{d_{\mathrm{FF'}}E_{\pm}}{2\hbar v}\int_z^L \mathrm{d}z' \exp\left[\frac{\Lambda_{\pm}(z')-\Lambda_{\pm}(z)}{v}\right], \tag{4.21}$$

$$\rho_{\pm}(z, v=0) = \frac{id_{\mathrm{F,F'}}E_{\pm}/2\hbar}{\Gamma_{\mathrm{t}} - i\Delta_{\mathrm{F,F'}}(z)}. \tag{4.22}$$

Knowing the coherences, we can compute the polarization:

$$P(z, \omega_l) = 2\mathcal{N}d_{\mathrm{F,F'}}C_{\mathrm{F,F'}}\langle\rho(z)\rangle, \tag{4.23}$$

where $\langle ... \rangle$ is the average over Maxwell Boltzmann velocity distribution. There are two underlying assumptions to write Eq. (4.23):

- We have assumed an homogeneous atomic density $\mathcal{N}$. This remains valid as long as $V(z) \ll k_{\mathrm{B}}\Theta$. In our case, the kinetic energy is in the THz range, much larger than the vdW potential (smaller than tenths of GHz for the vast majority of the atoms).

- Assuming a Maxwell Boltzmann velocity distribution for the velocity has also raised question [Todorov and Bloch, 2017], but no deviation from this distribution has been observed to date [Bloch *et al.*, 2019].

Now that we have expressed the polarization P, we can use Eqs. (2.20) and (2.21) to compute the transmitted field[6].

By using Eq. (4.19) in Eqs. (4.20-4.21) to obtain the coherence field for each velocity class at location z, we included the internal atomic dynamics as the atoms move relative to the surface, thus experiencing time-varying level shifts due to the vdW interaction $V(z)$. In previous works based on fluorescence measurement [Whittaker *et al.*, 2014], the motion was not accounted for [Bloch, 2015]. From now on we call this model *Model 3*.

[6]Note that in the simulations, we have to use a truncation of the spatial integration of $L_{\mathrm{cut}} = 0.1$ nm to avoid numerical divergences. We have checked that the results do not depend on the value of L_{cut} if $L_{\mathrm{cut}} \leq L/100$.

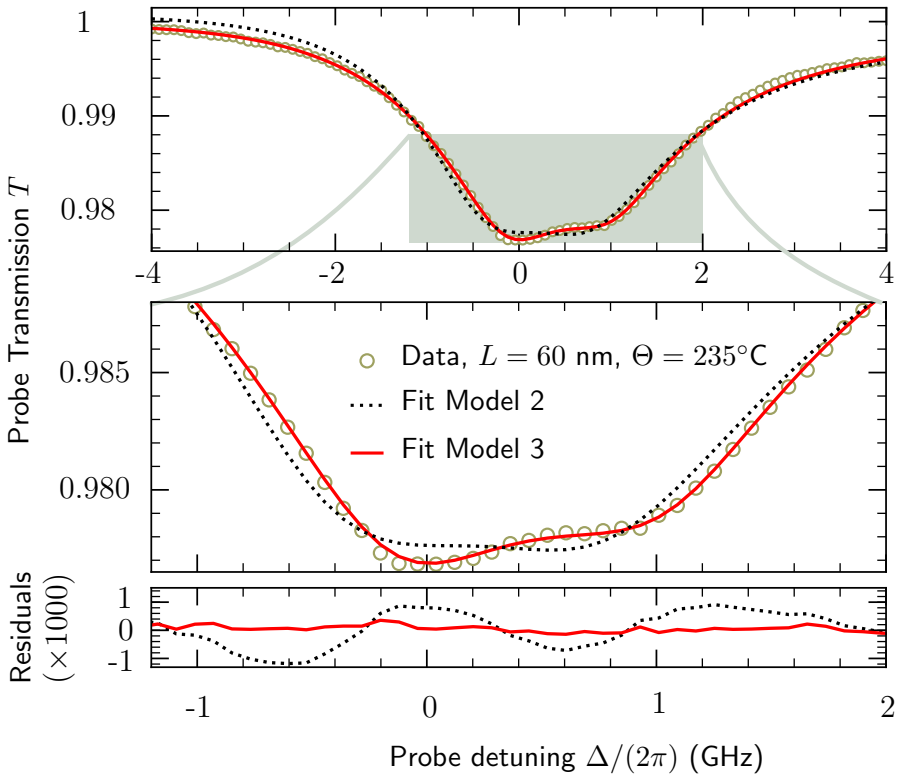

Figure 4.5: Comparison of Model 2 and Model 3 Model 2 (black dotted line), not including atom-surface interactions, misses line-shape features for spectra in the thin cell region (circles), as highlighted on the zoomed inset. This is despite the fact that in addition to temperature, we take the broadening Γ_P and shift Δ_P as free parameters to phenomenologically account for atom-surface interactions. Model 3 (red solid line) — that includes atom motion in the spatially dependent vdW potential explicitly — reproduces the asymmetric double-peak feature perfectly, with only the temperature and C_3 as free parameters when imposing bulk-determined line shift $\Delta_P = \Delta_{P0}$ and broadening $\Gamma_P = \Gamma_{P0}$.

4.2.3 Determination of the C_3 coefficient

We present the best fit of the data for a thin cell with $L = 60$ nm in Fig. 4.5. Model 3 has only two free parameters, the temperature (or equivalently the density $\mathcal{N}$) and C_3, as Δ_{P0} and Γ_{P0} are constrained to their bulk extracted values (see Eq. (4.19)). Yet, it shows outstanding agreement compared to Model 2 that only phenomenologically accounts for atom-surface vdW interactions. In particular, the red-side asymmetry cannot be retrieved without taking properly the vdW shift into account. The value for C_3 is extracted from fitting the spectra for each cell thickness L (main panel of Fig. 4.6). Thin cells yield a larger fraction of atoms close to the surface, where the

vdW potential induces large level shifts, and allow tighter constraints on the fitted parameters. This is visible on the map presented in the top insets of Fig. 4.6, where the region that minimizes the mean square error σ^2 is more tightly localized along the C_3-axis for thin cells.

Error bars assignment For each cell thickness, we extract a value of C_3 from the fit of the spectrum. The error bar for each C_3 is attributed as follows: we fix the thickness measured with an uncertainty of 5 nm. Collisional line-width and shift are also fixed to their bulk values Δ_{P0} and Γ_{P0} measured at large cell thicknesses. We perform an error propagation in the following way: we vary within their error intervals Δ_P, Γ_P and L and repeat the fitting procedure to find the C_3 that minimizes the sum of squared residuals. We thus obtain the systematic error on C_3 associated with the uncertainty in the determination of these fixed parameters. When applying this procedure, we find that the extracted C_3 is insensitive to the value of Γ_{P0}. On the contrary, it is very sensitive to the value of Δ_{P0} and L, which are by far the main contributors to the uncertainty of C_3. The error bars assigned for each thickness in Fig. 4.6 correspond to the variation of C_3 by changing Δ_{P0} (respectively L) within a range of ± 20 MHz (respectively ± 2.5 nm). We assume no statistical correlation between the errors due to L and Δ_{P0}. As a consequence, we take for the error bar on each C_3 (associated with one cell thickness) the quadratic sum of these two errors. Note that due to the good signal to noise ratio and to the averaging over many realizations, statistical error are negligible.

Final value for C_3 In order to give a final value for the extracted C_3, we make the final assumption that it does not vary with the cell thickness. This approximation assumes that retardation effects would not lead to an effective dependence of C_3 with L. The final value of the cesium-sapphire C_3 coefficient is then assigned, together with its error bar, as an average weighted by the individual error bar of each point. We obtain $C_{3,\mathrm{exp}}^{\mathrm{Sa}} = 1.26 \pm 0.10$ kHz·µm^3, in good agreement (see the side scale in Fig. 4.6) with the theoretical value $C_{3,\mathrm{th}}^{\mathrm{Sa}} = 1.10 \pm 0.03$ kHz·µm^3 obtained in the first section of this chapter [Peyrot *et al.*, 2019b]. In comparison to other similar measurements (See Refs. [Sargsyan *et al.*, 2017; Whittaker *et al.*, 2014]), our result is closer from the Lifshiftz theory of vdW interaction. Besides, the error bar reported in these two works are most likely underestimated. The reason is that they neither used a complete model describing the transient evolution of atoms in the spatially varying potential, nor assessed correctly the systematic errors such as collisional effects or cell thickness

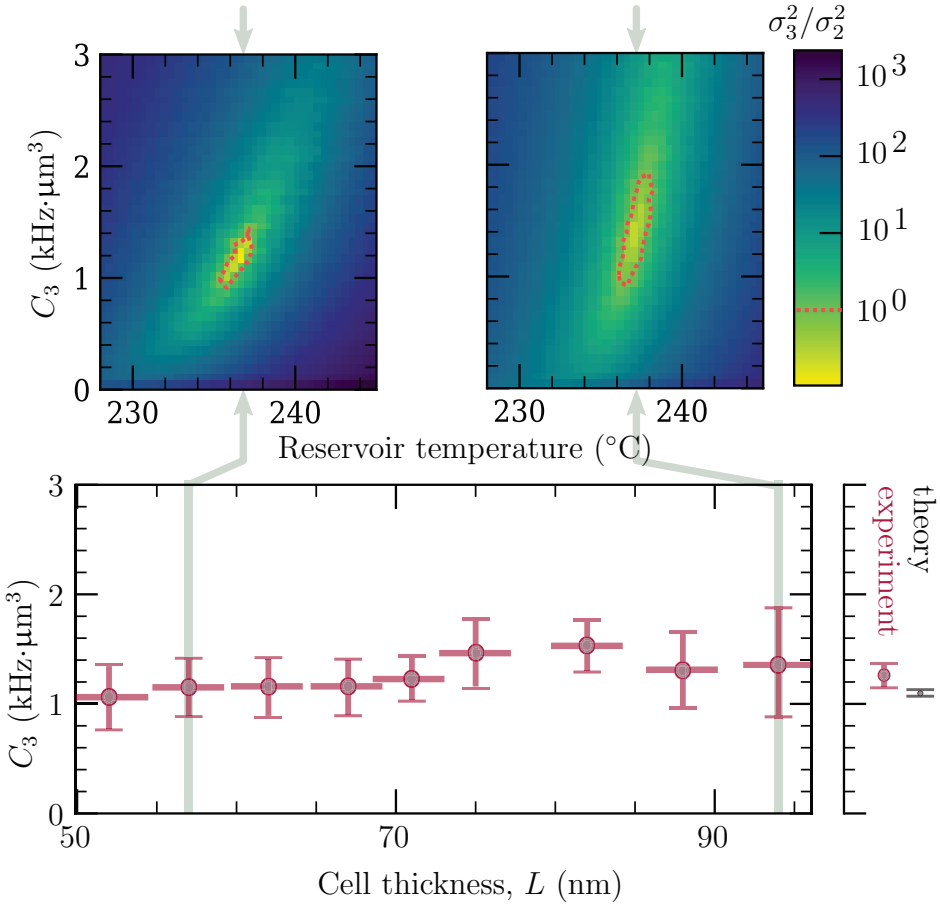

Figure 4.6: Determination of the C_3 coefficient for the D_1 line of Cs atoms close to a sapphire surface Main plot: C_3 (circles) obtained by fitting Model 3 to the transmission spectra for different cell thicknesses. Error bars are systematic. Top insets: temperature-C_3 maps of the sum of squared residuals σ^2 for Model 3 normalized by the best value found for Model 2, for two cell thicknesses indicated by vertical shaded bars on the main plot. The final value of C_3, obtained as a weighted average, is in excellent agreement with the theoretical prediction (side scale).

indetermination.

In the last short section, we show the limitations and perspectives of using vapor to study surfaces properties.

4.3 Long-range Casimir-Polder regime and short-range repulsive potential

As we have seen previously, transmission spectra of atomic vapor close to surfaces incorporate contributions of atoms at different distances from the surface. This was one of the main reason to build a model describing the complete line-shape to extract precisely the vdW C_3 coefficient. When the exact dependence of the interaction with the atom-surface distance is not already known, the advantages of our method largely vanish. We illustrate this point with a short discussion about the long-range Casimir-Polder interaction. Also, very close to a surface, a repulsive potential has been predicted together with an analytical form [Vargas and Mochn, 1996; Lima *et al.*, 2000]. In this case, our method can be used and we finally suggest the perspective to explore the effects that can have this repulsive potential on an experimental spectrum.

4.3.1 Retardation effects in the van der Waals potential

At the beginning of this chapter, the interaction of an atom with a surface has been understood as the interaction between a dipole $\boldsymbol{d}$ and its image $\boldsymbol{d_I}$ in the surface. If this atom is at an appreciable distance of the surface ($z > \lambda/(2\pi)$), the time taken for the electric field to travel from the dipole to its image and return can be larger than the period of fluctuations of the dipole itself. These fluctuations can only be understood within the quantum electrodynamics theory and are by far beyond the scope of this manuscript. However, an order of magnitude of the period of fluctuations can be given by the time corresponding to one oscillation of the dipole moment. This time is the inverse of the resonant frequency of the atom $1/\omega_0$. The distance travelled by light during this time is $c/\omega_0 \sim (3 \times 10^8 \mathrm{m{\cdot}s^{-1}})/(2 \times 10^{15} \mathrm{m{\cdot}s^{-1}}) \sim 150$ nm. If the atom-surface distance $z > 75$ nm, the field initially emitted by $\boldsymbol{d}$ and inducing $\boldsymbol{d_I}$ would return and find that the direction of $\boldsymbol{d}$ is now different from the original one. As a consequence, the attractive interaction is less favorable and retardation effects would lead to a dependence in $1/z^4$ of the interaction [Israelachvili, 2011].

References [Wylie and Sipe, 1984, 1985] show that the position-dependent atom-surface interaction potential is quite complicated to write down explicitly. Particularly, the general potential is not a sum of the short ($1/z^3$) and long ($1/z^4$) range contributions; otherwise it would scale as $1/z^3$ for large z, in contradiction with the Casimir-Polder regime. Our spectroscopic technique is not adapted to search experi-

mentally for the spatial form of the potential. The reason is that we need an analytical form of the potential to derive the primitives in Eq. (4.18) and fit the data with the model. Without this analytical form, the line-shape is not calculated correctly and the extracted parameters cannot be interpreted (as it was the case for Γ_P and Δ_P extracted at low L in Fig. 4.4(c-d)). Notably, had we found a spatial dependence of C_3 when L varies (originating for example from atoms experiencing an interaction with the surface in the Casimir-Polder regime) in Fig. 4.6, we could not have extracted any meaningful information about the underlying process.

4.3.2 Using the repulsive potential to trap atoms close to surfaces

Very close to a wall, the presence of a repulsive potential is also expected. The physical origin of this potential is that an atom moving toward the wall cannot penetrate the surface simply because the electronic shell of the projectile is repelled by the electronic density formed by the atoms belonging to the surface [Vargas and Mochn, 1996]. The complete atom-surface potential should therefore be the sum of the attractive and repulsive contributions. The simplest form possible for the repulsive potential is given by the hard-wall approximation [Israelachvili, 2011], consisting of an infinite potential barrier at the surface location. More realistic models, that allow for a finite deformation of the surface, rather suggest power law or exponential potentials. The latter can be written:

$$V_{\text{rep}}(z) = Ae^{-\alpha z}, \tag{4.24}$$

where A and α are two constants that depend on the properties of both the atom and the surface considered. The combination of a vdW attractive and exponential repulsive potential is represented in Fig. 4.7(a), where the full potential stands for:

$$V_{\text{tot}}(z) = -\frac{C_3}{z^3} + Ae^{-\alpha z}. \tag{4.25}$$

Searching for a signature of this full potential in the spectra was also an initial motivation of this Thesis. As pointed out in Ref. [Chang *et al.*, 2014], the combination of attractive and repulsive surface forces potentially allows guiding or trapping of atoms in close proximity to surfaces. The ability to trap atoms in controlled geometries (for example small channels etched on the surface) using the properties of the surface, could lead to hybrid nano-scale atom-surface meta-materials [Whittaker *et al.*, 2014]. As recently demonstrated using He scattering from LiF targets [Cantini and Tatarek,

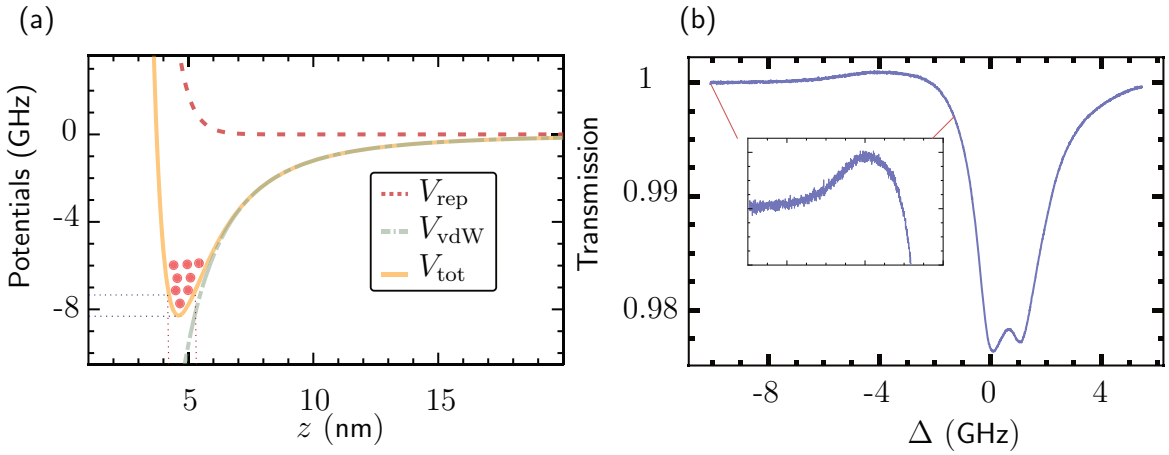

Figure 4.7: The repulsive potential (a) Sum of the repulsive and attractive potentials. The well-shape of the resulting total potential can be exploited to trap atoms at few nano-meters from the surface. With the value $C_3 = 1.2$ kHz·µm^3, $A = 4 \times 10^{13}$ Hz and $\alpha = 2 \times 10^9$ m^{-1}, the signature of the well should give rise to the presence of a small peak of absorption at a detuning of about 8 GHz. (b) Experimental spectrum for $L = 94$ nm, $\Theta = 235$°C. The laser is scanned up to 10 GHz on the red side of the resonance. The inset does not reveal any sign of the absorption peak around 8 GHz. The fact that the transmission is slightly above 1 around -3 GHz is discussed in Chapter 3.

1981; Debiossac *et al.*, 2014], atoms can be trapped in this full potential very close to a surface (see Fig. 4.7(a)). In these experiments, the authors investigate the diffracting pattern of an atomic beam scattered by the surface. They particularly show that the diffraction patterns allow to identify *so-called* bound-states of the atom-surface potential.

Surprisingly, there is to our knowledge no investigation of the full potential using spectroscopic methods. A previous work suggested that in the case of a Cs atom close to a sapphire surface, the coefficients of the repulsive potential should be $A = 4 \times 10^{13}$ Hz and $\alpha = 2 \times 10^9$ m^{-1} [Lima *et al.*, 2000]. If these figures are correct, we would expect to observe the signature of atoms trapped at about 5 nm from the surface corresponding to a detuning of 8 GHz. Indeed, as we can see in Fig. 4.7(a), the well-shaped of the potential should lead to a surplus of atoms in a slice of energy centred around 8 GHz. It would lead to a small peak of absorption at this detuning.

In Fig. 4.7(b), we scan the laser up to 10 GHz on the red side of the resonance to look experimentally for this surplus of atoms. As we can see, we could not find any sign of the presence of atoms in the well of this potential. The small variations in the intensity are mainly limitations of the SNR ratio due to unwanted interferences effects already discussed. There are several possibilities that can explain the absence of this

absorption peak:

- The SNR (about 5) is too small to observe it.
- As predicted in Ref. [Vargas and Mochn, 1996], the repulsive potential could possibly be highly dependent on the surface quality. No particular care of polishing have been taken for the sapphire cell used so far in this manuscript.
- A final possibility could be that the values given in Ref. [Lima *et al.*, 2000] for the repulsive potential constants are not correct.

All these assumptions will be tested further in the next chapter.

4.4 Conclusion

In this chapter, we have investigated the van der Waals interaction between a surface and an atomic vapor confined in a nano-cell. We have first recalled the Lifshitz theory of the non-retarded vdW interaction and calculated the C_3 coefficient characterizing the $1/z^3$ spatial dependence of the interaction. We have found that for an atom of cesium close to a sapphire surface, the coefficient corresponding to the D_1 line transition is $C_{3,\mathrm{th}}^{\mathrm{Sa}} = 1.10 \pm 0.03$ kHz $\cdot$ µm^3. This result uses the latest calculations of dipole matrix elements for low-lying cesium transitions and is therefore the most accurate prediction to date for this configuration. Subsequently, we have proposed an innovative method to measure precisely the value of C_3 using a vapor confined in a nano-cell. Up to now, the accuracy of the measured C_3 using atomic vapor was limited by the effect of collisions on the atomic spectra. Using the wedged shape of the nano-cell allows to access both the thick region where we can extract these collisional properties and the thin region where the vdW interaction is predominant. We have illustrated our method with a measurement of C_3 for the D_1 line for the cesium-sapphire configuration. In order to extract C_3, we have extended the model presented in Chapter 2 to account for the motion of the atoms in a spatially-varying potential. The final extracted value $C_{3,\mathrm{exp}}^{\mathrm{Sa}} = 1.26 \pm 0.10$ kHz$\cdot$µm^3 is in reasonable agreement with the theoretical prediction.

The presented method can be easily adopted for characterizing the interaction between any atom or molecule that can be produced in a vapor and any surface suitable for cell fabrication. However, it requires an analytical form of the atom-surface potential. We have seen that it is not particularly suited to determine an unknown

spatial dependence and have illustrated our purpose in the case where the retardation effects lead to the Casimir-Polder regime of vdW interaction. Finally we have also seen that at really short distances from the surfaces a repulsive potential originates from the fact that atoms cannot penetrate the surface. Based on earlier predictions, we have shown that it should lead to an absorption peak in the spectra lying at about 8 GHz from the natural resonance. We finally discussed the reasons which could explain the absence of this signature in the experimental spectrum.

In the next chapter of this manuscript, we will present a new generation of home-made nano-cells whose surface roughness rms is better than 2Å. We will do spectroscopic measurement on this cell to investigate further the presence of the repulsive potential.

Chapter 5

New super-polished borosilicate nano-cells

Contents

Introduction

As we have seen in the previous chapters, the interaction of light with an alkali vapor largely depends on the characteristics (size, refractive index,...) of the cell confining the atoms. Therefore, the possibility to change the nature of the cell is first a good opportunity for us to investigate how the spectral properties are modified when using a different system. Actually, the motivations for building new types of nano-cells are numerous. Indeed, miniaturization of devices confining atomic vapors has set the stage for the development of various compact light-matter interfaces [Petelski *et al.*, 2003; Wasilewski *et al.*, 2010]. In a near future, an attractive idea is to manufacture systems

based on the nano-cell technology, where the atoms can be confined in any conceivable geometry [Gmeiner *et al.*, 2016].

So far, we have used sapphire cells developed by our Armenian partners in the context of a scientific collaboration. However, the fabrication steps of these cells are confidential: it prevents us from modifying their properties (geometry, material, surface roughness, *etc...*). The ability to gain knowledge on the engineering processes required to build such nano-cells is a first step to develop more involved designs. At the nano-scale level, one of the first key points is the quality of the cell walls in terms of surface finish. Using the know-how of our optical workshop at the Institut d'Optique, we tackled this particular technical problem. Developing surfaces with ultra-low surface roughness is an asset to reduce stray light, which limits the signal-to-noise ratio of light-matter interaction with nano-metric atomic ensembles. Besides, super-polished surfaces can be ideal candidates for the fabrication of glass micro-cavities for quantum electrodynamics experiments [Roy and Barrett, 2011]. Finally, building cells with high-quality surfaces can be an advantage to study the presence of the atom-surface repulsive potential that we introduced in the previous chapter. Indeed, as the corrugation of the surface is expected to modulate the repulsive potential [Vargas and Mochn, 1996; Farias and Rieder, 1998], the position of an atom with respect to the surface would be ill-defined, complicating the spectroscopic investigation of this potential. Can we see the effect of the repulsive potential on spectral properties of atoms confined near super-polished surfaces? If not, what should be the appropriate experiment to observe it? We will attempt to give an answer to these questions at the end of the chapter.

Structure of the chapter In a first section, we report on the fabrication and characterization of a new super-polished wedged borosilicate nano-cell. Then we will present the first spectroscopic results we obtained with these cells. The cells have also been polished on the side and we have built a new optical set-up to observe the off-axis fluorescence from the vapor. We finally investigate in more details the repulsive potential problematic.

5.1 Fabrication and characterization of super-polished wedged borosilicate nano-cells

In this section, we report on the fabrication of glue-free all-glass nano-cells with a thickness varying between the optical contact (zero) and a maximum thickness of few hundred nano-meters. The surface of the cell has a root-mean-square (rms) roughness of about 2 Å. The cell has been designed by Yvan Sortais (Institut d'Optique), manufactured by Christian Beurthe (Institut d'Optique) and filled by Pierre Bonnay (Observatoire de Paris).

5.1.1 Origin of the project

Motivations and specifications Our goal was to produce a new cell with the following technical specifications:

- The thickness of the cell should vary linearly between 0 exactly and ~ 1 µm. We have seen in Chapter 4 that accessing extremely thin and thick regions provides the ability to measure more precisely the atom-surface interaction properties. The possibility to probe different system sizes is also an asset to study the dependence of spectral properties such as width and shift with the medium thickness as reported in Chapters 2 and 3.

- The cell assembling is done with optical bonding (see more details at the end of section 5.1.2) and makes no use of glue. This is a technological asset that prevents from any degasing when the temperature is raised. Indeed, most glues operate in a range of temperature that does not exceed a few hundreds of Celsius degrees. However, one may need to operate at much larger temperatures in the future to increase significantly the density of atoms [Peyrot *et al.*, 2018], or to study the dependence with temperature of the surface properties [Laliotis *et al.*, 2014].

- Finally, we require a low surface roughness of better quality than the one we currently use ($\sim$ nm). We therefore want to engineer surfaces with a rms roughness better than 1 nm.

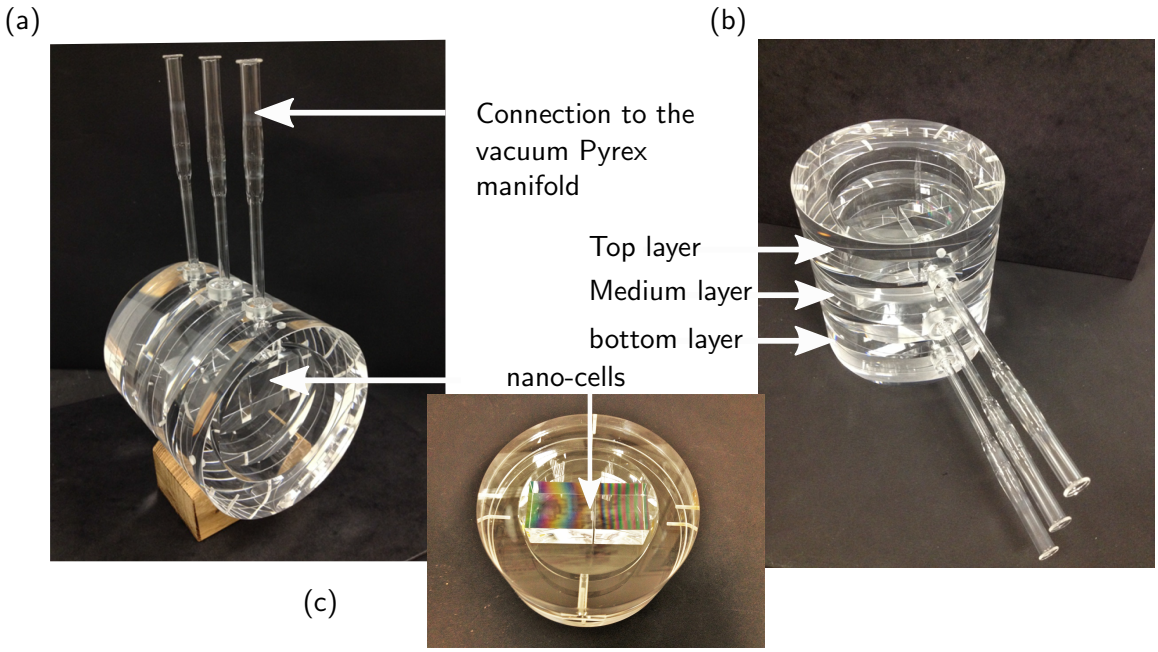

Figure 5.1: The Big-mac Photographs of the initial solution for the nano-cells project. The nano-cells are in the medium layer and the Newton colors (photograph (c)) indicate the varying in the cells thickness. The photographs are taken prior to filling with the alkali.

From the "Big-Mac" to "Mini-Macs" It is quite common in the French laboratories to attribute names to experiments. When I arrived to start this Thesis, I was supposed to work with the *so-called* Big-Mac cell which was expected to fulfil the above technical criteria. I am not going to give details for this choice of name. It is left to the reader's imagination. This masterpiece was realized at the Institut d'Optique and photographs of the design is presented in Fig. 5.1. The cell was made of silica and composed of three parts. The central part contained the nano-cell and the purpose of the bottom/top parts was to avoid the bending of the surfaces due to pressure forces when pumping[1]. Although the construction of the cell took a very long time, the system unfortunately never worked properly. Namely, we did not observe an interpretable spectroscopic signal in the cell. Besides, the massive dimension of the cell (diameter $\sim$ 12 cm, height $\sim$ 20 cm) was an obvious drawback to heat the system uniformly. It led to a new and more reasonable design, both in size and in material cost, that we called *Mini-Macs*, in the living memory of the *Big-Mac*.

[1]This was partly due to the diameter-to-thickness ratio of the *Big-Mac*. It is also one of the reasons to consider smaller geometries.

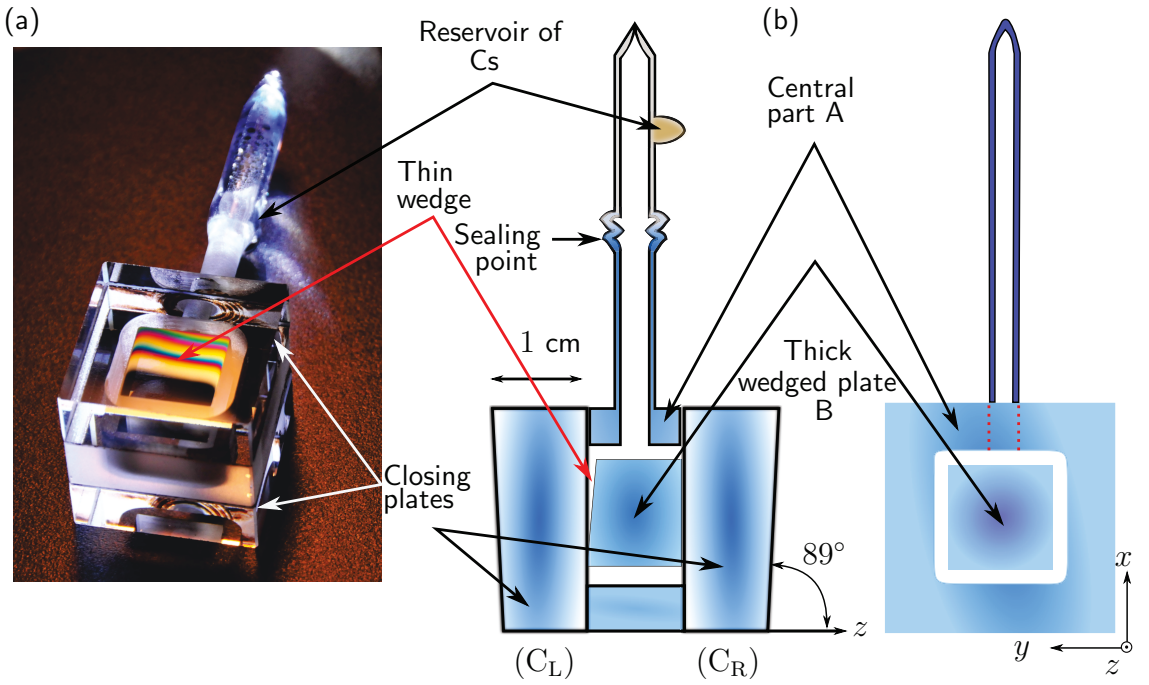

Figure 5.2: Cell assembling (a) Photograph of the cell. (b) Schematic of the cell (front view and side view).

5.1.2 Steps of fabrication

The Mini-Mac project The new generation of cells that we built is made of four parts that are optically bonded together, leading to a monolithic ensemble (see Fig. 5.2(a)). Using the same material for all parts avoids differential thermal expansion that could damage the optical bonding. Borofloat glass has been chosen for its good optical properties in the visible and near-infrared spectrum, and also because it is more easily super-polished than other materials used in previous cells (sapphire for instance). This glass was also chosen to facilitate the sealing to the Pyrex side arm that will contain the Cs reservoir, as the thermal expansion coefficients and the softening temperatures of both glasses are similar. However, unlike sapphire, and similar to fused silica, it reacts[2] with alkali at temperatures exceeding $\sim 250°C$ (see also Sec. 5.3.3). The central part (A) (see Fig. 5.2(b)) is machined using boring-bits so as to let a 6-mm external diameter, 4-mm internal diameter, and 25-mm long tube protrude from the front face to allow for connection to a Pyrex loading manifold containing the Cs reservoir. Glass is then removed from the inside of part (A) using milling-bits. In this hollow piece, a thick plate (B), carefully angled on one side, is introduced. The

[2]These reactions are not well documented. We have observed with large cells a brown cover on the surface at temperatures exceeding 250°C.

cell is closed by two thick plates (C_L) and (C_R) wedged by 1° to dismiss unwanted reflections. Plate (B) is optically contacted on one side on plate (C_R). On the other side, the gap formed by the angle between plate (B) and plate (C_L) constitutes the nano-enclosure and, therefore, its realization is crucial. The two main manufacturing difficulties that we will detail are: (i) the polishing of the different surfaces to reach excellent surface roughness and (ii) the control of the nano-gap thickness.

Surface roughness In order to realize surfaces with very low roughness such as those inside the thin wedge, we first grind them finely using alumina abrasives and a brass grinding wheel. The surfaces are then manually polished on a pitched wheel using an aqueous solution of rare earth oxide abrasives with a fine particle size ($\leq 1\mu m$). The final polish is performed with an increasingly diluted solution, leading to a super-polish. To the best of our knowledge, this procedure leads to better roughness on borosilicate glass compared to other polishing methods [Li *et al.*, 2008; Frost *et al.*, 2008]. Standard polish is obtained by using rougher abrasives and stopping the polishing procedure before the above-mentioned final dilution step.

Realization of the prism-shaped cell The thin wedge of plate (B) is realized by polishing iterations and controls of the wedge thickness and flatness between two polishing steps. This is done with an interferometric technique, using a Helium-Neon laser and a Fizeau interferometer. The wedge is realized so that four fringes appear in the interferogram, parallel to the y axis (see also Newton colors in Fig. 5.2(a)) with equal inter-fringe spacing. This corresponds to a thickness variation of 1.2 μm. In addition, the absolute thickness is controlled such that, along its thickest edge, the plate thickness exceeds the thickness of plate (A) by ~ 300 nm (see Fig. 5.3(a)), forming a ridge that will eventually be removed. This is controlled mechanically, using an electronic depth gauge with a resolution of 100 nm. Parts A and B are then optically contacted on a parallel plate (P_1) and polished simultaneously so as to remove the 300-nm thick ridge and bring parts (A) and (B) to equal height for closing purpose. This height equalization is controlled interferometrically using a flat etalon (P_2), as shown in Fig. 5.3(b). This procedure ensures that final assembly brings the closing plate (C_L) in optical contact with both parts (A) and (B). Therefore, the wedge thickness should vary between 0 exactly and about 900 nm.

All parts of the cell are cleaned with alcohol prior to final assembly by optical contact (no glue is used). The bonding of two surfaces is done at room temperature. It relies on the presence of hydroxyl molecules, which are bonded to the silicon atoms

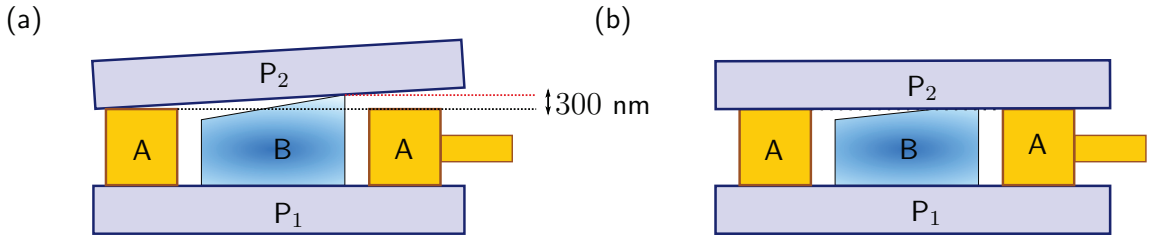

Figure 5.3: Realization of the edge Procedure to realize a thin wedge with thickness varying between 0 and 900 nm. Parts (A) and (B) are optically contacted on a parallel plate (P_1). (a) The thickness of part (B) first exceeds that of part (A) by 300 nm. The flat etalon (P_2) therefore sits on the ridge of part (B), leading to interference fringes (between part (A) and the flat etalon) with different white light colors on each side of the ridge. (b) After flattening the ridge and equalizing the heights of part (A) and (B), the flat etalon sits equally on parts (A) and (B), leading to equal color fringes.

of the glass and bring the two surfaces together by hydrogen bonding, mediated by the presence of water molecules [Cocheteau, 2014; Whittaker, 2017]. The bonding is obtained by pressing lightly onto the parts to be connected until white light color fringes disappear and are replaced by a uniform dark fringe where the two parts are in contact. The only requirements are the absence of dust and the complementarity of the two surfaces to be bonded: in our case, we found that a flatness difference of 30 nm rms or less was sufficient to achieve a stress-resistant and vacuum-tight optical bonding.

Once the cell is assembled we connected it to a turbo-molecular pumping stage via a Pyrex loading manifold, and baked the cell-manifold assembly at $350 - 400°C$ for four days while pumping. Although the pressure inside the cell cannot be evaluated precisely[3], this procedure proved to be necessary both to get rid of water vapor and residual contaminants inside the cell prior to filling the reservoir with Cs and to reinforce the optical bonding[4]. Cesium was then transferred, using a low temperature flame, from an ampoule with a breakable seal to the cell reservoir. The vapor filling step took place at the Laboratoire GEPI of the Observatoire de Paris.

[3] At the end of the pumping procedure, we measured at room temperature a pressure of 8×10^{-9} mbar at the pumping stage. The pressure inside the cell is certainly higher, due to the limited conductance of the Pyrex loading tube.

[4] It is likely that the temperature of this initial baking was too cold. It should rather be larger than 500°C (see also Ref. [Whittaker, 2017]) to make the optical bonding permanent. One of the cells we built lost the optical bonding, probably for this reason.

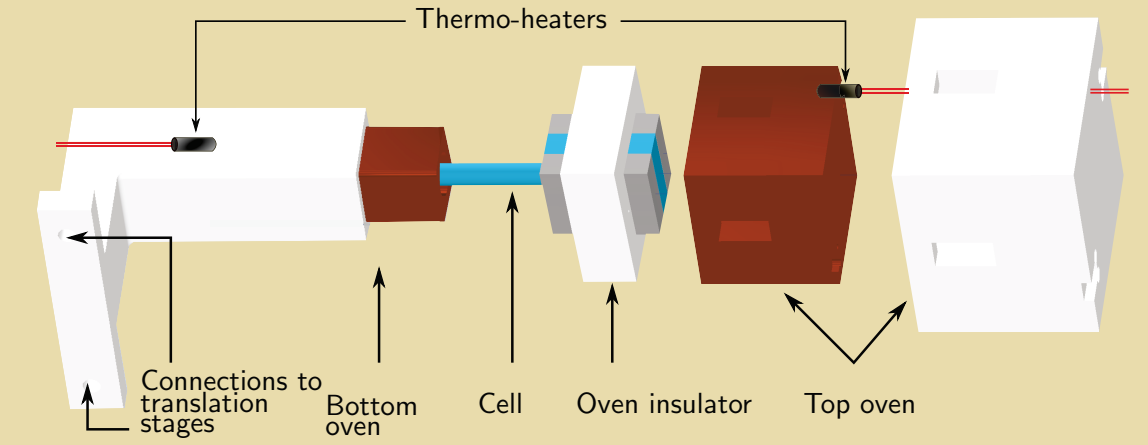

Figure 5.4: New oven design Thermo-heaters are introduced in copper via appropriated apertures in the Teflon parts. The two copper ovens are separated by a 1-cm PTFE piece. Connections to translation stages have been manufactured in order to have the possibility to move the cell with respect to the laser beam and hence probe different cell thicknesses.

New oven design The Armenian oven we have used so far is too small to contain the borosilicate cells. We have therefore built another oven in the mechanical workshop of Durham University. The oven is composed of two materials: (i) copper is used for its good thermal conductivity (~ 350 W·m^{-1}·K^{-1}) to ensure a quick and homogeneous heating of the cells with HT15W thermo-heaters from Thorlabs. (ii) It is surrounded by Teflon (PTFE) which has a very low thermal conductivity (~ 0.25 W·m^{-1}·K^{-1}) hence being an ideal candidate to insulate both the two ovens (reservoir and windows) from each other and from the exterior. The design, realized with the *Autodesk Inventor* software, is represented in Fig. 5.4.

In the following part, we will verify that the cell produced meets the initial technical specifications.

5.1.3 Characterization of the optical properties

Characterization of the surface roughness Figure 5.5(d) shows a typical roughness profile, measured using an optical heterodyne profiler (ZYGO 5500) with a sensitivity of 0.2 Å rms. The spatial resolution of the profiler is 1 µm, on the order of the distance travelled by the atomic dipoles of the vapor before they reach a steady state (limited by collisions inside the gas or radiative decay). To investigate atom-surface interactions over shorter travelling distances, and account for the transient response of the vapor to finer details of the surface [Peyrot *et al.*, 2019c], we characterize the surface on a

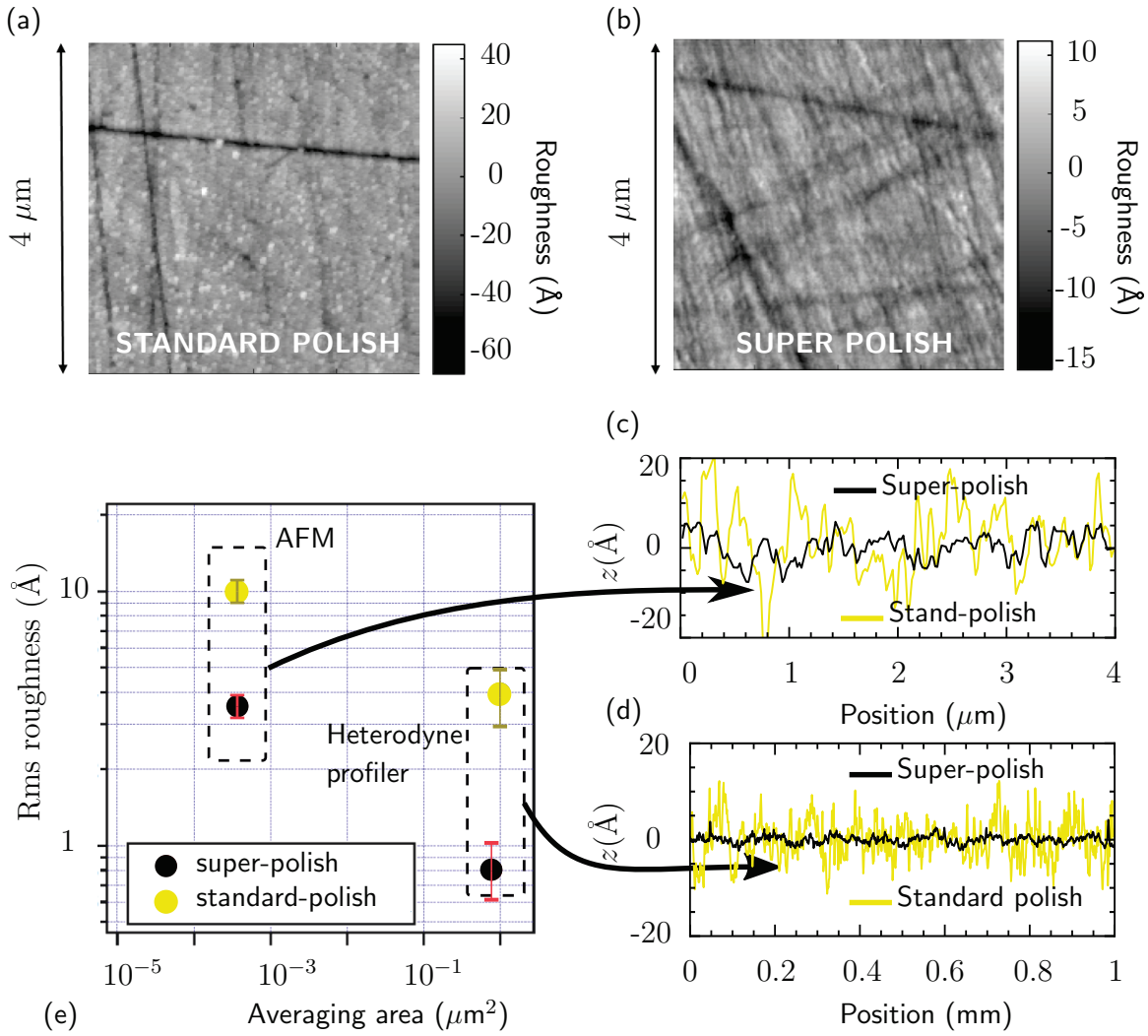

Figure 5.5: Roughness characterization Top: AFM imaging of (a) a standard polish and (b) a super-polished surface of our cell. Bottom: roughness profiles acquired with (c) the AFM and a spatial resolution of 20 nm and (d) the optical heterodyne profiler (spatial resolution: 1 µm). Red (blue) traces correspond, respectively, to the super-polish (standard polish) surfaces. (e) Rms roughness versus averaging area.

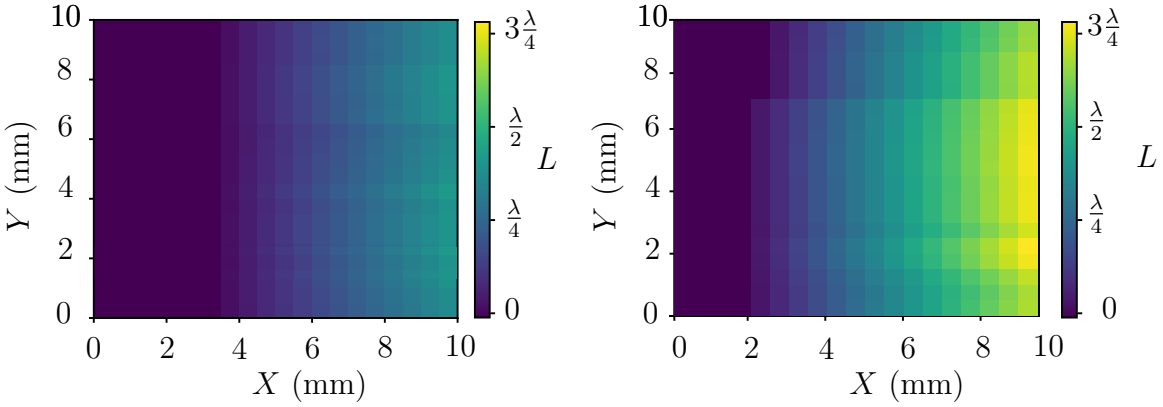

Figure 5.6: Wedge thickness characterization We have built two cells with different wedge angles. We represent the 2D mapping of the two wedges thickness (resolution of the prism along x and y axes: 0.5 mm)

smaller scale. To do so, we acquire images of the super-polished surfaces using an atomic force microscope (AFM 5500 from Keysight Technologies) in a tapping mode, equipped with a silicon tip (n-type). The spatial resolution of the AFM imaging is given by the radius of the tip ($\sim$ 10 nm or less). Typical images and roughness profiles acquired with the AFM are shown in Figs. 5.5(a-b-c) for a super-polish and a standard polish. As expected, the roughness is lower for a super-polish than a standard polish. In Fig. 5.5(e), we summarize the results obtain with the different techniques and show that we have been able to produce a surface with a rms surface roughness of about 2 Å (This value depends on the surface on which the roughness is averaged, as shown in Fig. 5.5 (e)).

Characterization of the prism size Using the method to measure the thickness that we presented in Chapter 2, we characterized the local thickness of the wedge. We represent a 2D map (x, y) of the local thickness in Fig. 5.6 for two cells that we have realized. We see on these figures that the thickness goes exactly to zero and increases linearly to about $\lambda/2$ and $3\lambda/4$ for the two different wedges. The larger wedge corresponds to the procedure to obtain a wedge with a thickness of 900 nm. The final thickness is slightly smaller than expected. This is probably due to van der Waals forces between plates C_{L} and B.

All things considered, we have fabricated and characterized a new generation of super-polished cells where a Cs vapor is confined in a nano-geometry [Peyrot *et al.*, 2019a]. In the following section we will produce the first spectroscopic results obtained with these cells.

5.2 First experimental observation using fluorescence spectroscopy

In this section we build a fluorescence optical set-up and optimize the signal-to-noise ratio of the detection system. We will also present the first spectroscopic results obtained with the cells presented in the first section. More quantitative fluorescence experiments will be investigated in the next (final) chapter.

5.2.1 A new experimental set-up

Fluorescence set-up The optical set-up is represented in Fig. 5.7. The oven is designed to observe off-axis fluorescence via a side-window. Thanks to a 3D translation stage, a lens with a 5 cm focal length is placed such that the atomic slab lies in its focal plane. We use a collimator to image this slab on a Thorlabs multi-mode fiber core. The fiber is connected to a single-photon counting-module (SPCM-AQRH-14-FC from Excelitas). The module detects single photons with a detection efficiency of about 40% at 894 nm and generates a transistor-transistor-logic (TTL) level pulse for each photon detected. Each pulse arrival time is recorded by the use of a high resolution counting module (HRM TDC from sensL). The time resolution of the SPCM and HRM are respectively 350 and 27 ps. The detection system is much faster than what we require to do fluorescence spectroscopy[5]. However, it would in principle be possible to investigate with this set-up ultra-fast atomic coherent dynamics [Keaveney, 2014; Ripka *et al.*, 2016; Whittaker, 2017], or measure intensity temporal correlations.

First experimental spectra To obtain a single spectrum, we record the arrival time of each photon during one laser scan. These times are referenced with respect to the laser trigger and we bin them to create a histogram (see Fig. 5.7). The bin size is chosen so as not to degrade the spectral resolution[6]. We can accumulate data by repeating this procedure over many laser scans to reduce the statistical noise. We present in Fig. 5.8(a) examples of spectra obtained for different cell thicknesses between 50 and 376 nm for a temperature of 220°C. We present fluorescence spectra normalized by the most significant bit value in the histogram. We see that without any particular care, we obtain very nice signal-to-noise ratios (SNR is about 5 for $L = 150$ nm). To

[5] The laser scans in 100 ms a 20 GHz frequency range. To be able to resolve a line-width as narrow as $\Gamma_0/(2\pi) = 6$ MHz, we would require a time resolution of 30 µs.

[6] Typically, if we scan the laser around 20 GHz and want to observe spectroscopic features as sharp as 6 MHz, we need at least 4000 bins. In practice, the line-width is larger than 50 MHz and 1000 bins is enough.

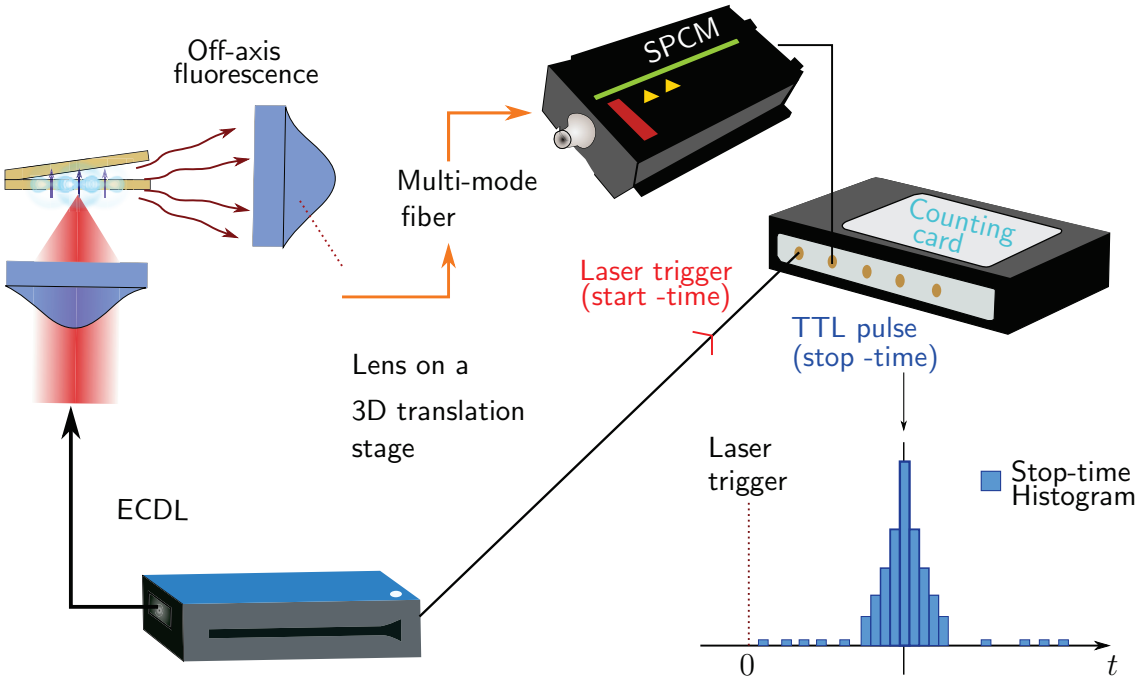

Figure 5.7: Fluorescence optical detection The laser diode is scanned around the vapor resonances. The set-up allows to measure 90° off-axis fluorescence. A 5-cm lens, placed on a 3D translation stage, images the atomic slab on the input of a multi-mode fiber. The fiber is connected to a single-photon counting module (SPCM) that produces a TTL pulse for each detected photon. A counting card is used to collect the arrival times of the photons with respect to the laser trigger time. A Python program is finally used to create a histogram of the arrival times.

observe thinner slab thickness, we need to improve this signal-to-noise ratio though.

5.2.2 Improving the signal-to-noise ratio

The predominant source of noise originates from photons generated in the laboratory which reach the detector (room-light, other electronic devices, *etc...*). To reduce as much as possible this noise we have combined the use of a home-made black chamber and a narrow bandpass filter FB900-40 (FWHM: 40 nm around 900 nm, transmission rate of about 70% at 894 nm) from Thorlabs. With this configuration, we reduced the parasite counting rate from more than a million count per second (saturation of the detector) to the dark-count limit (50 clicks per second) even with the room light on. When the laser drives the atoms, two types of photons can be collected by the detector: (i) fluorescence signal from the atoms, (ii) stray light of the laser radiation

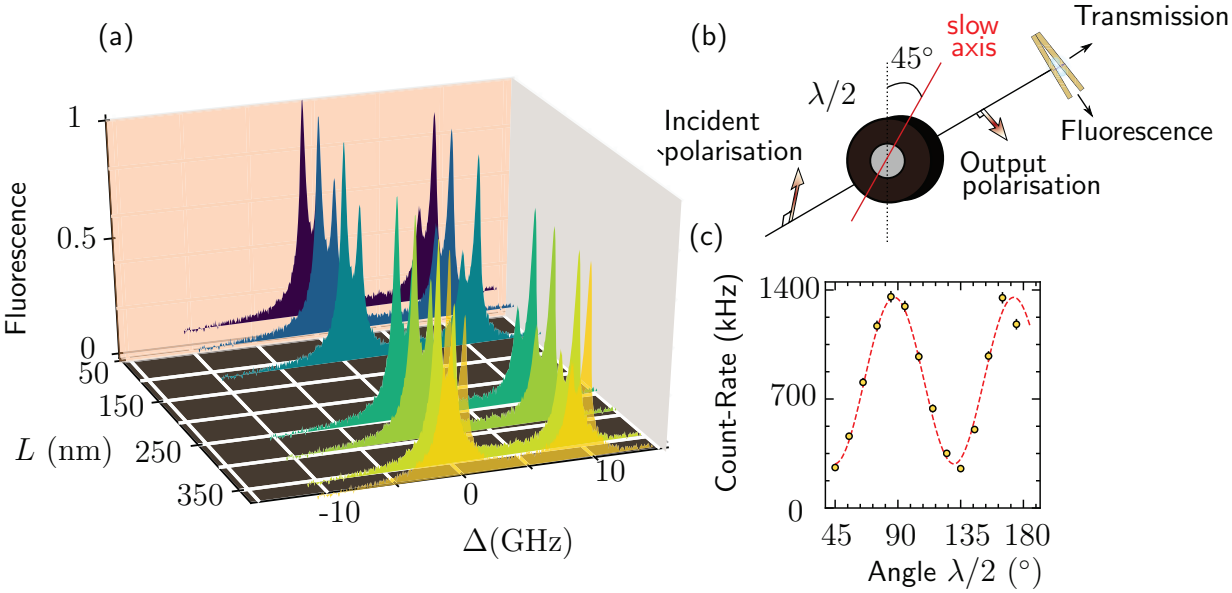

Figure 5.8: First fluorescence spectra (a) 90° off-axis fluorescence spectra obtained for $\Theta = 220°$C and a range of thickness going from 50 nm (purple) to 376 nm (yellow). (b) Optimal configuration to reduce the stray light on the detector. The linear polarization after the half-wave plate needs to be in the direction of the detection path. (c) Count-rate on the SPCM as a function of the wave-plate angle.

on the cell surfaces. The latter is now the main limitation for the signal-to-noise ratio (SNR) and there is no easy way to reduce it. We have noticed that the atomic signal does not depend on the incoming linear laser polarization while the noise does. We therefore used a half wave-plate to investigate the dependence of this noise with the incident laser polarization. We show in Fig. 5.8(c) the dependence of the photon count-rate on the SPCM as a function of the rotation angle of the wave-plate. We choose the horizontal orientation[7] (direction of the detection system, see Fig. 5.8(b)), that maximizes the SNR. In the next section we will show the experimental results with the best SNR obtained and study the presence (or not) of the repulsive atom-surface potential presented in the previous chapter in the spectral response of the vapor.

5.3 Atom-surface repulsive potential

We recall that an atom placed in the vicinity of a surface is subjected to an atom-surface potential and that this potential is expected to be the sum of an attractive long-range (vdW) and a repulsive short-range contributions. At the end of Chapter 4, we pointed

[7]Due to the angle-dependent emission pattern of a dipole, we observe a minimal scattering when the polarization is along the detection axis.

out three reasons that could prevent us from observing the signature of the repulsive potential close to a surface. In this section, we will try to address these three points: (i) we will look for the signature of the repulsive potential in the far-detuned wings of the spectra with the best SNR possible. (ii) We will provide simulations of the expected spectral signature and try to evaluate the effect of the surface roughness and temperature on these features. (iii) Finally, we will come back on the plausibility of the potential given in Ref. [Lima *et al.*, 2000].

5.3.1 Searching for the signature of the repulsive potential

We show in the main panel of Fig. 5.9 a spectrum obtained with the best SNR for $L = \lambda/8$ and a temperature of 215°C. To obtain this spectrum, we scanned the laser up to 25 GHz without mode-hop on the red side of the transition. Although the laser intensity is PID-controlled, as in the previous chapters, a small variation of the intensity during the scan remains. We have therefore normalized the spectra, *i.e* divide the signal by a ramp matching the variation of the laser intensity. This remains valid in the weak driving regime, where the number of emitted photons is proportional to the laser intensity. This is how we get the flat signal at very large detuning even in log scale[8]. If the values given by Ref. [Lima *et al.*, 2000] for the repulsive potential are correct, we are searching for a spectral peak[9] located around 8 GHz from the natural atomic resonance, as explained in the previous chapter. We report no sign of this peak neither at 8 GHz (see the inset in Fig. 5.9) nor up to 25 GHz.

5.3.2 Spectroscopy with a repulsive potential: simulations

To interpret the absence of spectral peaks at 8 GHz, we extend our model of transmission to include the repulsive potential. In a first approximation, we assume that the quantity $-\ln(T)$ is close enough to our fluorescence measurement to provide the spectral signatures that we expect[10]. We use the model developed in the previous chapter to simulate spectra with the repulsive potential. To this purpose, we need to compute again the primitives given in Eq. (4.17), accounting now for the full potential.

[8] We also note that the SNR obtained is not particularly better with respect to transmission techniques. We have a SNR of 20 for $L = \lambda/8$. In transmission, the corresponding absorption was about 5% for a residual oscillation on the base-line of 0.2 %.

[9] In fact, we expect two peaks corresponding to the two scanned transitions.

[10] We will investigate the actual differences between transmission and fluorescence spectra in the final chapter.

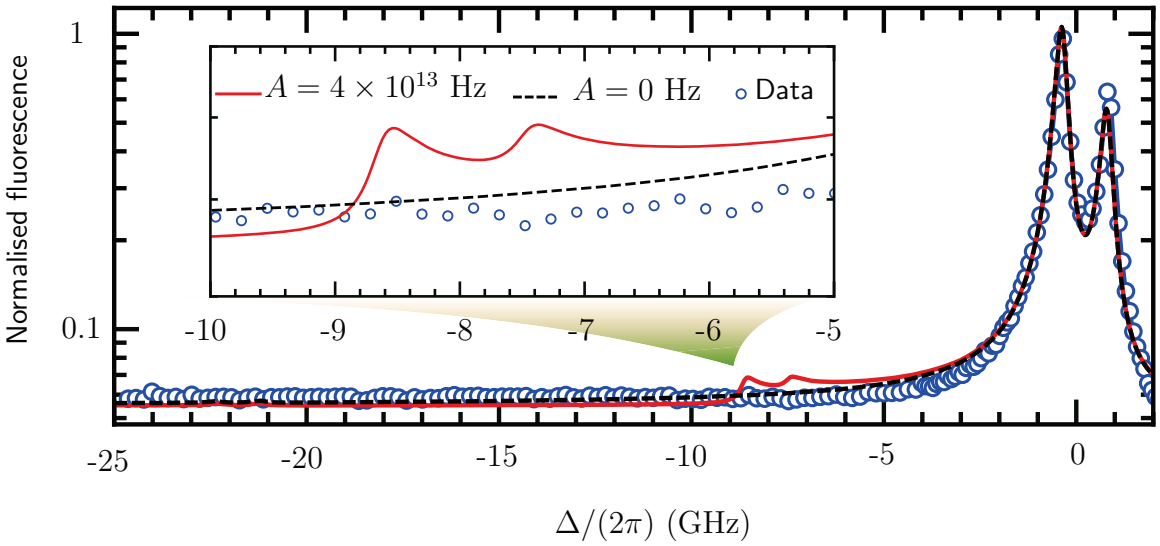

Figure 5.9: Searching for the repulsive potential Fluorescence spectrum for $L = \lambda/8 \sim 110$ nm and $\Theta = 215°$C. The laser is scanned without mode-hop up to 25 GHz on the red side of the transition. Blue dots: experimental data, red full (respectively black dashed) line: prediction of the model including the full atom-surface potential for $C_3 = 1.26$ kHz·µm^3, $\alpha = 2 \times 10^9$ m^{-1} and $A = 4 \times 10^{13}$ Hz (respectively 0 Hz). The plotted quantity is the optical density ($-\ln(T)$, where T is the transmission) normalized to its larger value. The parameters in the model used for the fit are $\Gamma_{P0} = 310$ MHz, $L = 110$ nm. We have added a relative and frequency independent noise of 5.4×10^{-2} to account for the conditions of the experiment. Inset: the presence of the two spectral features due to the full atom-surface potential appears on the theoretical curve with non vanishing A, but not on the data.

Adapting Eq. (4.25) to the case where the two walls of the cell act on the atoms, the full potential spatial dependence is:

$$V_{2-\text{walls}}(z) = \frac{C_3}{z^3} + Ae^{-\alpha z} + \frac{C_3}{(L-z)^3} + Ae^{-\alpha(L-z)}. \tag{5.1}$$

The primitives of Eq. (4.17) have the following analytical expressions:

$$\begin{aligned}\Lambda_\pm(z) \;=\; & \left\{ \frac{\Gamma_0 + \Gamma_{P0}}{2} - i(\omega_\ell - \omega_{FF'} - \Delta_{P0} \mp k_l v) \right. \\ & \left. + i\left[\frac{C_3}{2z^3} - \frac{C_3}{2z(L-z)^2} - \frac{Ae^{-\alpha z}}{\alpha z} + \frac{Ae^{-\alpha(L-z)}}{\alpha z} \right] \right\} z. \end{aligned} \tag{5.2}$$

We can now use the complete model to simulate the result we would expect for the

conditions of the experiment: ($\Theta \sim 215°C$, $\Gamma_{P0} = 310$ MHz, $L = \lambda/8 \sim 110$ nm). We also introduce a relative noise amplitude of 5.4×10^{-2} to best model the experimental situation[11]. We represent in Fig. 5.9 the result of the simulation. We observe the signature of the repulsive potential in the small increase in fluorescence that appears more clearly in the inset. In comparison, we have represented the same simulation for $A = 0$, where the peaks at 8 GHz are absent.

We have then investigated the influence of various parameters on the strength and location of the spectral features appearing in the inset of Fig. 5.9. First of all, we have remarked that increasing the broadening decreases the amplitude of the peaks. This confirms the fact that when the total homogeneous line-width Γ_t increases, the spatial relaxation distance $\xi = v/\Gamma_t$ decreases and atoms are more sensitive to the bulk than to surfaces. Then, we have tested the influence of the surface roughness. To this purpose, we have introduced a random fluctuation on the distance to the surface for all spatial integrations in the model[12]. We report that as long as the surface roughness is smaller than 2 nm, the prediction represented in Fig. 5.9 is not changed. Above this value, the peaks start to spread and finally disappear. The surface roughness that we use is smaller than 2 Å: it should therefore not affect the signal that we expect. Finally, we found that the parameters describing the potential (C_3, A and α) are decisive because they change drastically the form of the potential hence the location and depth of the well. In Chapter 4, we have determined experimentally the value of C_3. However, the figures for A and α for the repulsive potential have been taken from Ref. [Lima *et al.*, 2000]. We finally examine the plausibility of these numbers.

5.3.3 Adsorption of atoms on a surface

In the previous chapter, we suggested that the well formed by the attractive (van der Waals) and repulsive potentials originates from the adsorption of atoms on the surface. According to the type of interaction between the adsorbate (vapor) and the absorbent (surface), adsorption can be either physisorption or chemisorption [Stephens, Rhodes, and Wieman, 1994]. In the case of chemisorption, the bonding is usually covalent (strong) and the process is permanent. This is favored by high temperature and leads to a deterioration of the cells that we mentioned at the beginning of Sec. 5.1.2. When the bonding is due to van der Waals forces, one rather refers to physisorption.

[11] Without this noise, the signal obtained in the simulation would exactly go to zero far off resonance.
[12] Typically, we take $z \to z + \delta z$ in Eq. (5.2), with δz chosen randomly between 0 and the rms roughness.

Reference [Stephens, Rhodes, and Wieman, 1994] gives a comprehensive analysis of these different phenomena in the case of a Cs vapor close to various surfaces. In particular, the authors measured that the bonding energy related to the physisorption process is in the eV range. The order of magnitude is consistent with the ones used in the experiments using scattering of atomic beam on surfaces [Farias and Rieder, 1998; Debiossac *et al.*, 2014]. This information tells us that the figures given in Ref. [Lima *et al.*, 2000] cannot be realistic: they suggest a potential well depth of several GHz (typically ~ 0.03 meV for 8 GHz). After a more in-depth bibliographic review, we found that the same authors (Ref. [Lima *et al.*, 2000]) admitted that they had considered a very shallow surface well [Passerat de Silans *et al.*, 2006] and that atoms should be trapped much closer from the surface (few Å). In light of this information, it is not surprising that our experiment could not extract information about the repulsive potential.

Finally, we suggest more appropriate directions for a future investigation of adsorption phenomena based on Refs. [Stephens, Rhodes, and Wieman, 1994; Passerat de Silans *et al.*, 2006]. The physisorption process can be related to an adsorption energy E_a. In order to measure this adsorption energy, the authors of Ref. [Stephens, Rhodes, and Wieman, 1994] built a cell where the atomic chamber can be decoupled from the reservoir. In this case, the number of atoms n_0 in the closed volume is equal to the sum of atom number in the vapor n_vap and stuck on the wall n_wall:

$$n_0 = n_\mathrm{vap} + n_\mathrm{wall}. \tag{5.3}$$

The number of atoms stuck on the wall is $n_\mathrm{wall} = S\exp\left(E_\mathrm{a}/(k_b\Theta_\mathrm{s})\right)$ with Θ_s the temperature of the surface and S a proportionality constant that depends on the geometry of the cell. They performed absorption spectroscopy as a function[13] of Θ_s to find the value of E_a. A similar experiment could be used to measure the adsorption energy of Cs atoms close to sapphire or borosilicate surface.

A measurement of the adsorption energy would lead to the depth of the potential well. Knowing the attractive potential strength C_3 one could in principle construct a repulsive potential form (choosing the parameters A and α) that leads to a consistent value for the well depth. Ultimately, it should be in principle possible to load bound states of the full potential with photo-association techniques [Passerat de Silans *et al.*, 2006; Afanasiev, Melentiev, and Balykin, 2007]. This method consists in using two resonant lasers to induce a transfer of the atoms to the bound states of the potential

[13] The authors of Ref. [Stephens, Rhodes, and Wieman, 1994] pointed out that it is more appropriate to decrease rather than to increase temperature to avoid chemisorption.

by a Raman transition[14].

Conclusion

In conclusion, we have built a new generation of wedged and super-polished nano-cells. The fabrication makes no use of glue and the cells are assembled by optical bonding. They are filled with cesium and we have described the manufacturing steps to achieve the desired technical specifications. Namely, we have characterized the wedge of the cells in terms of local thickness and surface roughness:

- The cell thickness goes from exactly 0 (optical contact) to $\lambda/2$ and $3\lambda/4$ for the two cells respectively.
- The surface roughness of the super-polished parts is about 2 Å rms.

Concerning the atom-surface repulsive potential, we have realized that the constants describing the repulsive potential given in Ref. [Lima *et al.*, 2000] were not correctly assessed. We have suggested few directions to follow in order to carry on this investigation. We also want to point out that the work concerning the repulsive potential (*i.e.* model including the spatially varying potential) could nonetheless find applications using artificial repulsive potentials [Desbiolles and Dalibard, 1996; Hinds, Boshier, and Hughes, 1998]

Finally, we have built a new optical detection scheme in which we are able to collect off-axis fluorescence from the vapor confined in the cell. We have optimized the SNR and we will use this set-up in the last chapter to investigate more quantitatively the fluorescence signals.

[14] Due to atomic-motion, this experiment should probably be conducted with a cold atomic cloud rather than an atomic vapor.

Chapter 6

Off-axis fluorescence spectroscopy

Contents

Introduction

In this Thesis, we have mainly studied the transmission of light through a thermal atomic vapor. In this case – referred to as *on-axis* or *coherent* scattering – the field emitted by the atoms interferes with the driving field. At the end of the previous chapter, we also considered the possibility to observe the optical response of the vapor from a different point of view: when a medium consists of randomly positioned polarizable particles, light can be scattered in other directions than the one in which the laser propagates. Throughout this chapter, we will call this configuration *off-axis* scattering, *incoherent* scattering or *fluorescence* without distinction.

Fluorescence spectroscopy is interesting mainly because it allows for single photon detection on a laser-free background. For example, a four-wave mixing scheme has been used with rubidium vapors to create entangled photons pairs [Shu *et al.*, 2016] or to demonstrate the heralded generation of bichromatic single photons [Whiting *et al.*,

2017]. Reference [Mercadier *et al.*, 2013] studied the transport properties of photons in the vapor and evidenced the presence of long-lived scattering events (Lévy-flights). The ratio of single to multiple scattering has also been investigated [Dussaux *et al.*, 2016] by measuring the correlations between emitted photons. Finally, the manipulation of single photons led to the development of quantum hybrid platforms combining the advantages of both quantum dots and atomic vapor properties [Akopian *et al.*, 2011; Ulrich *et al.*, 2014].

Off-axis scattering of light in small thermal atomic vapors (thickness $L \leq \lambda$) has been less studied than coherent scattering. Historically, experiments in this regime have built on the seminal work of Dicke [Romer and Dicke, 1955]: in this vein, several works reported the observation of sub-Doppler spectroscopic signals [Cojan, J. L. , 1954; Schuurmans, 1976] and were followed by similar studies [Briaudeau *et al.*, 1998; Dutier *et al.*, 2003a] mainly using coherent techniques such as transmission or selective reflection. Only recently, atom-surface interactions have been investigated using vapors confined in nano-cells [Whittaker *et al.*, 2014; Fichet *et al.*, 2007]. Few works finally reported comparisons between transmission and fluorescence in such small systems (see for instance Ref. [Sarkisyan *et al.*, 2004]). In this chapter, we will study the off-axis light scattering from a thermal vapor confined in a nano-cell and investigate the differences with respect to a coherent detection technique such as transmission that we developed in the previous chapters. We note that the results in this chapter are preliminary and have not yet been the subject of a scientific publication.

Structure of this chapter In a first section, we investigate experimentally the differences between the optical response of a vapor observed in transmission and in fluorescence. Based on the observation, we will build a new model to describe the off-axis light scattering. We then show experimental fluorescence spectra in the very thin region, affected by the van der Waals interaction. Finally we shall study the effects of the resonant dipole-dipole interaction on the spectral widths and shifts of the fluorescence lines when the density of the vapor increases.

6.1 Fluorescence spectroscopy versus transmission spectroscopy

In this section we compare the spectral properties of the vapor confined in a nano-cell in two configurations: (i) light is collected on-axis (transmission), (ii) light is collected off-axis (fluorescence). We then study more in details a phenomenon called the *collapse and revival* of the Dicke narrowing [Dutier *et al.*, 2003b] with the two techniques.

Based on the differences that we observe, we finally derive a new model to study off-axis light scattering.

6.1.1 Comparison of spectroscopic properties

Using the set-up presented in Fig. 6.1(a), we can observe simultaneously the on-axis transmission with a photodiode and the off-axis fluorescence thanks to a detection system depicted in the previous chapter. We present in Fig. 6.1(b-c) a comparison of fluorescence and transmission spectra for a temperature of $\Theta = 210°\mathrm{C}$ at a thickness of $L = \lambda/4$ and $L = \lambda/2$ respectively. The first difference that we observe concerns the symmetry of the line-shape. In the case of transmission, we observe for $L = \lambda/4$ a strong asymmetry on the blue side[1] of the resonance in Fig. 6.1(b). We have seen in Chapter 3 that this asymmetry originates from the Fabry-Perot effect and that it is expected to appear for $L = \lambda/4 + \ell \cdot \lambda/2$ with $\ell \in \mathbb{N}$. Surprisingly, the line-shape is completely symmetric for the fluorescence spectrum. This first analysis shows that the Fabry-Perot nature of the cavity should play a minor role for light scattered off-axis.

We can also note that the optical response for $L = \lambda/2$ are really similar in both cases (see Fig. 6.1(c)). The authors of Ref. [Sarkisyan *et al.*, 2004] always found fluorescence spectra narrower than the transmission ones. We will show below that this holds as long as the collisional broadening remains negligible compared to the Doppler width. We therefore compare the two techniques at a lower temperature ($\Theta = 140°\mathrm{C}$), where the collisional broadening is very low. We display in Fig. 6.2(a) a line-shape comparison for $L = \lambda/2$ and we see that the fluorescence spectrum is indeed narrower. It confirms the observations of Ref. [Sarkisyan *et al.*, 2004]. The line-width gives us information on the role of the different velocity classes in the optical response. It has for example been predicted [Dutier *et al.*, 2003b] that the narrowing of the line-shape due to the motion of the atoms, should be maximal for $L = \lambda/2 + \ell\lambda$ with $\ell \in \mathbb{N}$. To observe this phenomenon, we perform a series of measurements at $\Theta = 140°\mathrm{C}$ and different cell thicknesses. We then fit the spectra in transmission and fluorescence with a model composed of Lorentzian functions to extract the width. As explained in the previous chapters, we do not expect this procedure to provide quantitative results. However we should extract a qualitative information concerning the dependence of the width with the cell thickness. We observe in Fig. 6.2(b) the dependence of the extracted widths as a function of the thickness around $L = \lambda/2$. For the fluorescence

[1] The difference between the line-shapes in transmission and fluorescence cannot be explained by a rescaling of the detuning axis. We note that we already observed such asymmetry in Fig. 3.4(b).

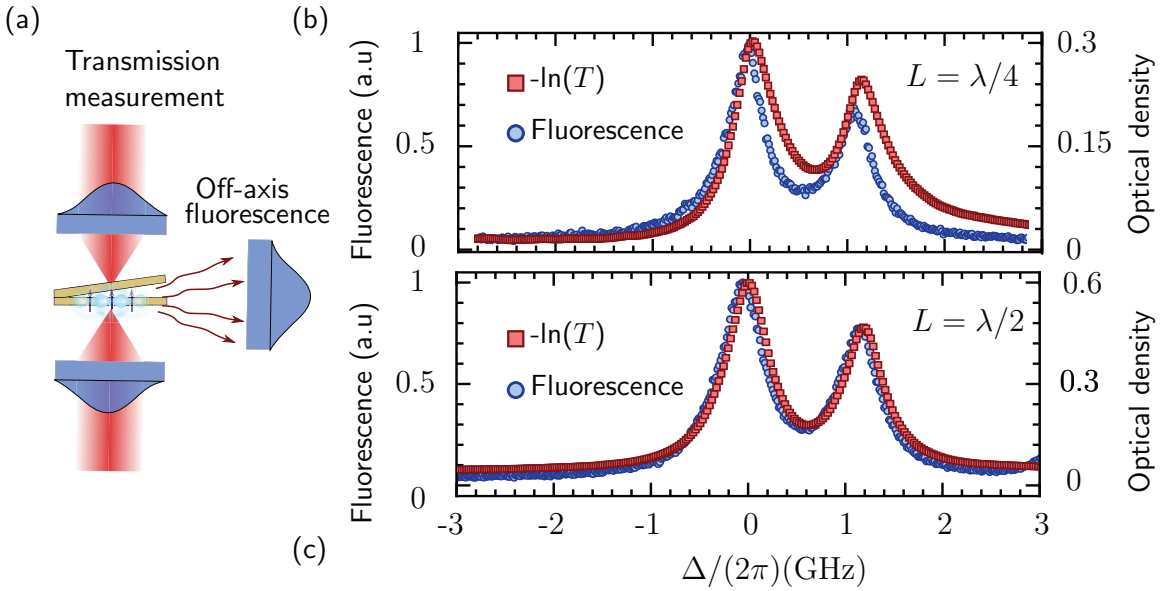

Figure 6.1: Optical set-up and cavity effects (a) Optical set-up similar to the one presented in the previous chapter. Here, we collect simultaneously the on-axis transmission on a photodiode and the off-axis fluorescence on the single photon counter module. (b, respectively c) Fluorescence in arbitrary units (a.u) and optical density ($-\ln(T)$) for $\Theta = 210°$C and $L = \lambda/4$ (respectively $L = \lambda/2$). Spectra obtained with the borosilicate cell.

spectra the width increases monotonically (in contradiction to the prediction for the oscillatory behavior mentioned above). On the contrary for the transmission spectra, the width decreases from $L = \lambda/4$ to $L = \lambda/2$ and increases afterwards[2].

This last observation is striking and agrees with one made in Ref. [Sarkisyan *et al.*, 2004]. In the next part, we try to understand more deeply the origin of this narrowing.

6.1.2 Collapse and revival of the Dicke narrowing

In his 1953 paper, Dicke showed that an emitter that experiences multiple collisions, with a mean free path much smaller than the wavelength of the emitted radiation, exhibits narrower line-shape compared to the standard Doppler width corresponding to its velocity [Dicke, 1953]. The result was derived under the condition that "*collisions should not influence the internal state of the radiator*". As we have seen in this manuscript and in many references cited before, a narrowing of optical spectra occurs

[2]For a more explicit observation of the collapse and revival of the Dicke narrowing one can refer to Refs. [Sarkisyan *et al.*, 2004; Dutier *et al.*, 2003b].

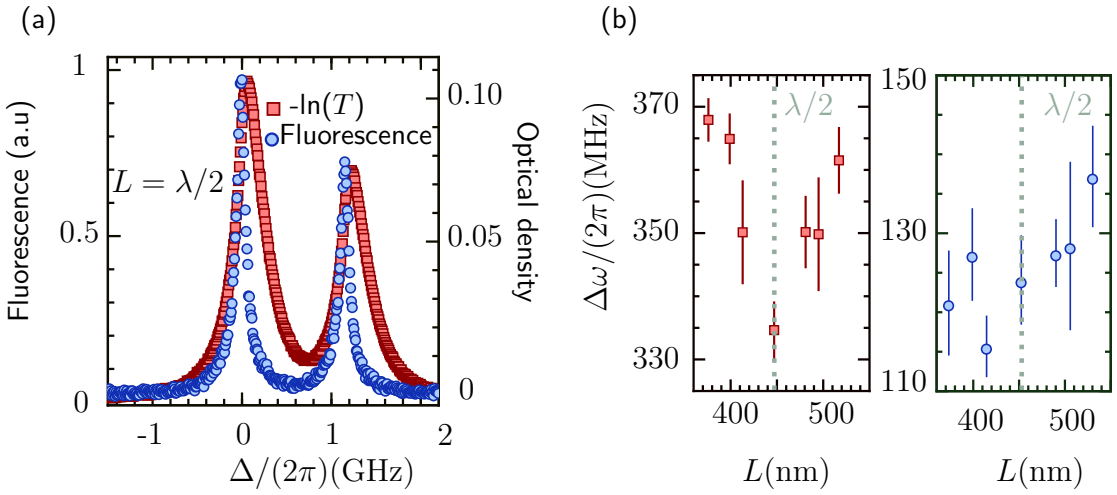

Figure 6.2: Transmission vs fluorescence: Dicke narrowing (a) Spectra for $L = \lambda/2$ and $\Theta = 140°$C. Blue dots: fluorescence. Red square: optical density ($-\ln(T)$). (b) Width extracted from the fit of the data with a model based on Lorentzian profiles. Red squares: transmission. Blue circles: fluorescence. Error bars are statistical. Spectra obtained with the borosilicate cell. We use the notation $\Delta\omega \neq \Gamma_t$ to recall that no quantitative meaning should be attributed to this quantity since the line-shape is not Lorentzian.

in thermal vapor cells of thickness $L \leq \lambda$. Although this effect was also termed Dicke narrowing, it is *a priori* not obvious that spectral line narrowing should occur, since atoms are completely depolarized when they collide with a cell wall (quenching collisions).

In the previous section, we saw that both transmission and fluorescence spectral lines were narrowed. However, the oscillatory behavior, named *Collapse and revival of the Dicke narrowing* has only been observed in transmission (or selective reflection) and has no equivalent in fluorescence [Dutier *et al.*, 2003b; Sarkisyan *et al.*, 2004]. In the following, we show that the narrowing of the lines originates from two distinct processes that are not immediately related to the initial work of Dicke.

Incoherent velocity selection A velocity selection of the atoms contributing to the signal (transmission or fluorescence) occurs because only dipoles flying parallel to the surface have enough time to reach steady-state. As we have already seen in Chapter 2, the dipole moment of an atom with non-zero velocity in a direction perpendicular to the surface is quenched by atom-wall collisions. The width of the line due to this velocity selection increases monotonically with the size of the cell. Indeed, for a given laser waist size, the larger the cell the less strict is the velocity selection (see Fig. 6.3(a-c)). This source of narrowing is not a coherent process (it does not depend

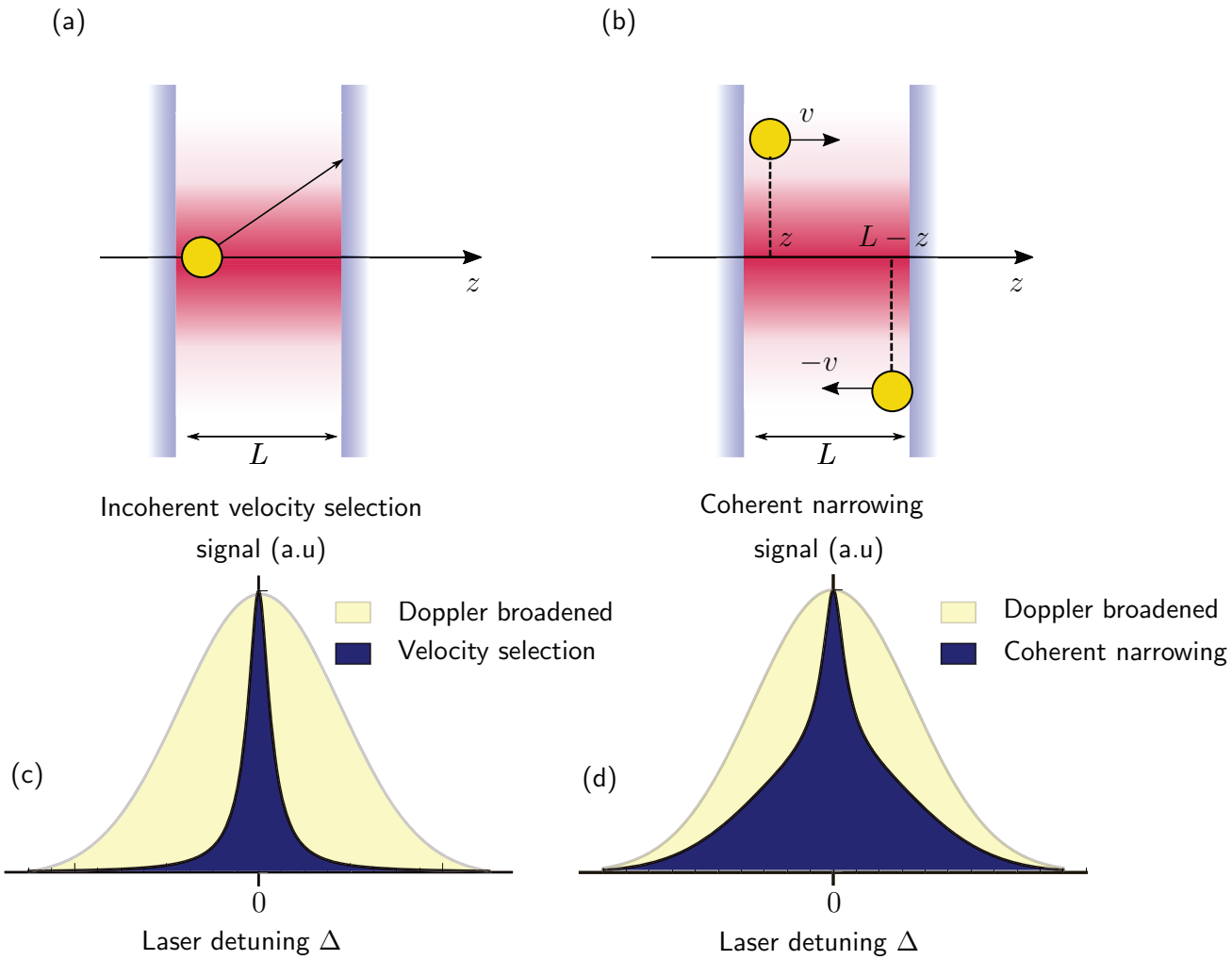

Figure 6.3: Coherent versus incoherent narrowing (a) Incoherent velocity selection. Single-atom process: a single emitter collides with a wall before reaching steady-state. (b) Coherent narrowing of the line. Two-body process: coherences from atoms at a position z in the cell propagating towards the other wall with a velocity v along z axis interfere with the coherences of atoms at position $L - z$ propagating in the other direction with a velocity $-v$. (c) Illustration of the incoherent velocity selection: only small velocities, with small Doppler shifts contribute to the signal. (d) Illustration of the coherent narrowing of the line: there is an increase of signal at $\Delta = 0$ due to constructive interferences.

on the phase of the dipole), and therefore does not produce periodic collapses and revivals. Besides, in contrast to the coherent narrowing that we discuss now, it can be understood simply as a single-atom process.

Coherent narrowing of the atomic lines The collapse and revival of the narrowing cannot be explained by the above velocity selection argument (see also Ref. [Sargsyan

et al., 2016]). In their observations, the authors of Refs. [Dutier *et al.*, 2003b; Sarkisyan *et al.*, 2004] reported the presence of a cell thickness periodic narrow contribution *on resonance* ($\Delta = \omega_\ell - \omega_0 = 0$). We now show that this periodic oscillation originates from interferences between pairs of velocity classes, v and $-v$ symmetrically positioned around the zero-velocity class (see Fig. 6.3(b)). To this purpose, we perform the following simulation: first, we ignore the cavity effects (*i.e.* we neglect the Fabry-Perot nature of the cell and take $\rho(z,v) = \rho_+(z,v)$ where ρ_+ is defined in Eq. (4.12)), which do not play any role in the narrowing. We use Eqs. (4.20) and (4.21) to compute the quantities:

$$M = |\rho(z,v) + \rho(L-z,-v)| \times M_\mathrm{b}(v), \tag{6.1}$$

$$\phi = \mathrm{Arg}\left[M_\mathrm{b}(v)\left(\rho(z,v) + \rho(L-z,-v)\right)\right], \tag{6.2}$$

where Arg is the argument of a complex number. Assuming first no decoherence (the total homogeneous line-width is $\Gamma_\mathrm{t} = 0$) and the laser on resonance ($\Delta = 0$), we see that M is $\lambda/2$ periodic with the distance z to the first surface (see Fig. 6.4(a)). The crucial point is the phase information: we see in Fig. 6.4(b) that the phase ϕ does not depend on the atomic velocity class for a given position z. Besides, we observe a π phase shift between the positions $z \in [\ell\lambda, \ell\lambda + \lambda/2],\ \ell \in \mathbb{N}$ and $z \in [(2\ell+1)\lambda/2, (l+1)\lambda],\ \ell \in \mathbb{N}$. The signal collected in the experiment is integrated over all positions z in the cell. We can now understand the increase of signal on resonance at $L = \lambda/2$ (see Fig. 6.3(d)). Integrating the coherences over $z = 0 \to \lambda/2$ includes only in-phase terms: the peak on resonance is maximal for this particular thickness. Now, if we consider $L = \lambda$, the phase opposition implies that the contributions of the coherence for $z = 0 \to \lambda/2$ are exactly cancelled by the contributions from $z = \lambda/2 \to \lambda$. The same argument can be extended for larger cell thicknesses. We now discuss what happens when the homogeneous linewidth increases and when the laser is not on resonance.

In presence of homogeneous broadening ($\Gamma_\mathrm{t} = \Gamma_0$, the natural line-width), the same argument as above holds (see the dependence of M and ϕ in Figs. 6.4(c-d)). However, the contrast is degraded and we have observed that the collapses of the narrowing vanish almost completely as soon as $\Gamma_\mathrm{t} = 5\Gamma_0$. This explains why the observation of the *Collapse and Revival of the Dicke narrowing* has been performed at very low temperature ($\Theta = 118°\mathrm{C}$ for Ref. [Dutier *et al.*, 2003b] and $\Theta = 120°\mathrm{C}$ in Ref. [Sarkisyan *et al.*, 2004], where the broadening due to collisions is smaller than Γ_0). Finally, we display M and ϕ in the case of $\Delta \gg \Gamma_\mathrm{t} = \Gamma_0$ in Figs. 6.4(e-f). We see

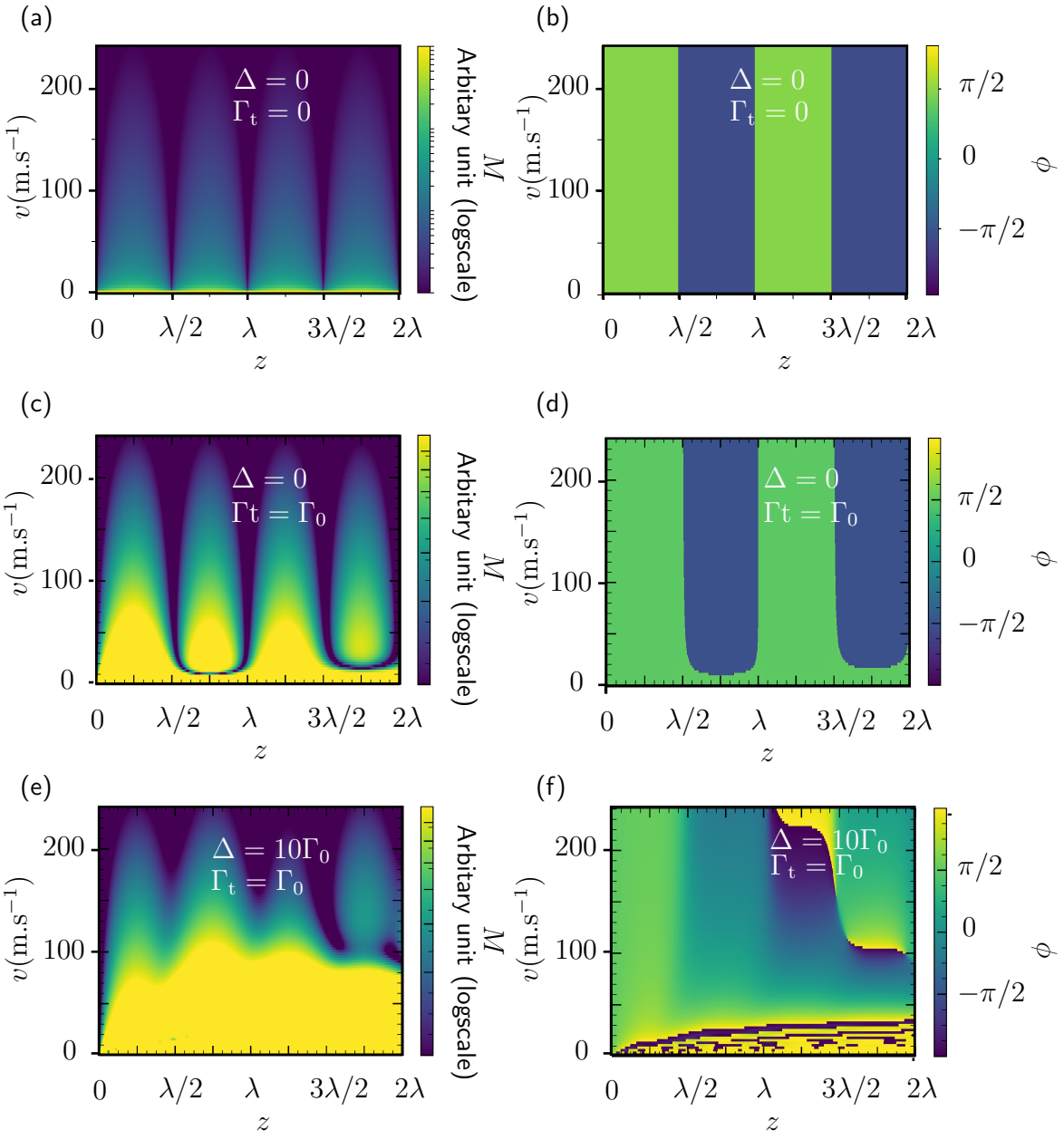

Figure 6.4: Collapse and revival of the Dicke Quantities M and ϕ (see main text) in the (v, z) plane. v is the projection of the velocity in the direction perpendicular to the surfaces. (a-b) the laser detuning is $\Delta = 0$ and the homogeneous line-width is $\Gamma_t = 0$. (c-d) $\Delta = 0$ and $\Gamma_t = \Gamma_0$, (e-f) $\Delta = 10\Gamma_0$ and $\Gamma_t = \Gamma_0$.

there that the summation over the atomic pairs $[(z, v),\ (L - z, -v)]$ has no particular structure in the (z, v) plane. This finally explains why the narrow feature only appears on resonance.

In conclusion, the coherent narrowing results from the interference of pairs of atoms with opposite velocity and located symmetrically with respect to the center of the cell. Besides, the resulting spectral feature is a contribution from all velocity classes on resonance in contrast to the incoherent narrowing which involved only low velocity classes. We also note that the signal resulting from the interferences is not only narrowed: it is periodically stronger in amplitude when $L = \lambda/2 + \ell\lambda,\ \ell \in \mathbb{N}$. Finally, this oscillation does not appear in fluorescence: we conclude that in some way, there is no interferences between the different pairs in this case.

6.1.3 A fluorescence model to study the interactions

Based on the observations we have made concerning the differences between transmission and fluorescence spectra, we now derive a model aiming at simulating the off-axis scattering from the atomic vapor confined in a nano-cell. The intensity collected by a detector placed at a point $\boldsymbol{r}$ in space is given by:

$$I \propto \langle |E_{\text{tot}}|^2 \rangle, \tag{6.3}$$

where $\langle ... \rangle$ denotes the ensemble average over different atomic spatial configurations and E_{tot} is the sum of the driving field E_ℓ and the field scattered by the laser-induced dipoles E_{sc}. Without loss of generality, we can write:

$$E_{\text{sc}} = \langle E_{\text{sc}} \rangle + \delta E_{\text{sc}}, \tag{6.4}$$

where $\langle \delta E_{\text{sc}} \rangle = 0$. The first and second terms in this equation are usually associated with the coherent and incoherent light scattering. On the one hand, the coherent part corresponds to the solution of the Helmoltz equation for the field scattered by a medium described by a dielectric constant. On the other hand, the incoherent part is related to the random positions of the atoms in the ensemble [Schilder *et al.*, 2016].

We can rewrite the intensity at any point in space as:

$$I \propto \langle |E_\ell + \langle E_{\text{sc}} \rangle + \delta E_{\text{sc}}|^2 \rangle. \tag{6.5}$$

We develop the modulus square:

$$I \propto \left\langle |E_\ell|^2 + (E_\ell \cdot \langle E_{\rm sc}\rangle + c.c.) + (E_\ell \cdot \delta E_{\rm sc} + c.c.) + |\langle E_{\rm sc}\rangle|^2 + |\delta E_{\rm sc}|^2 \right\rangle. \quad (6.6)$$

Because $\langle \delta E_{\rm sc}\rangle = 0$ we can rewrite this sum as:

$$I \propto \langle |E_\ell|^2\rangle + (E_\ell \cdot \langle E_{\rm sc}\rangle + c.c.) + |\langle E_{\rm sc}\rangle|^2 + \langle |\delta E_{\rm sc}|^2\rangle. \quad (6.7)$$

In the direction of propagation of the laser, as $|E_\ell| \gg |\langle E_{\rm sc}\rangle|$, the interference between the laser field and the coherent light scattering (two first terms on the right side of Eq. (6.7)) largely dominates over the two last terms of the equation. This explains why we neglected the incoherent light scattering term $|\delta E_{\rm sc}|^2$ in the previous chapters. In every other direction, the laser field is null because its distribution in the $\vec{k}$-space is a Dirac delta-function centred on $\vec{k_\ell}$. The off-axis intensity is therefore:

$$I(r) \propto |\langle E_{\rm sc}\rangle|^2 + \langle |\delta E_{\rm sc}|^2\rangle. \quad (6.8)$$

It can be shown that in a one-dimensional model, where the laser propagates in a direction z in a medium with finite extension along z and infinite extension along x and y, the coherent light scattering $\langle |\langle E_{\rm sc}\rangle|^2\rangle$ is also peaked around $\vec{k_\ell}$ [Schilder *et al.*, 2016]. If the system is not one-dimensional, the coherent scattered light is distributed in a cone around $\vec{k} = \vec{k_\ell}$ (see more details in Ref. [Schilder *et al.*, 2017]). In our case, the transverse direction is the laser waist ($w_0 \sim 100$ µm) that is much larger than the medium size ($L \sim \lambda$). We therefore neglect the term $|\langle E_{\rm sc}\rangle|^2$ for the intensity collected at almost normal incidence. We obtain:

$$I \propto \langle |\delta E_{sc}|^2\rangle = \langle \left| \sum_i E_{d_i}(\vec{k}, \vec{r}) \right|^2 \rangle, \quad (6.9)$$

where $E_{d_i}(\vec{k}, r)$ is the field radiated by a dipole d_i placed at a position r_i in the vapor, calculated at a position r corresponding to a direction $\vec{k} \neq \vec{k_\ell}$ in space. In the far field regime, it leads to:

$$I \propto \langle \left| \sum_i \frac{d_i e^{i\vec{k}\cdot(\vec{r}-\vec{r_i})}}{|\vec{r} - \vec{r_i}|} \right|^2 \rangle. \quad (6.10)$$

Because $|r| \gg |r_i|$ we can take the denominator out of the sum. Besides, we assume that the medium is dilute enough such that the dipoles are only induced by the laser

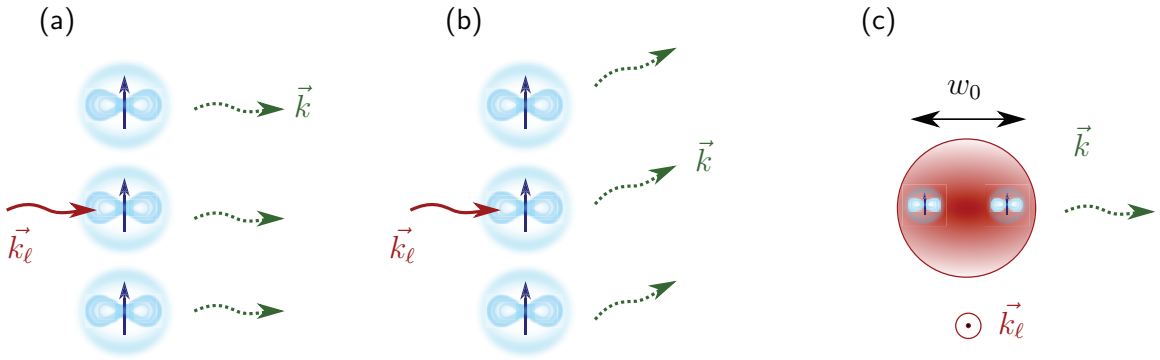

Figure 6.5: Phase matching condition (a) When light is collected on-axis, $\vec{k_\ell} - \vec{k} = 0$ and all fields emit in phase. There is phase matching. (b) When light is collected off-axis, $\vec{k_\ell} - \vec{k} \neq 0$ and the phases of the different fields calculated at a position r can be different. The phase matching condition is lost. (c) Illustration in the transverse plane. When the waist of the laser $w_0 \gg \lambda$, the phase of the fields collected off-axis are uniformly distributed in $[0, 2\pi]$.

field E_ℓ. Thus, $d_i = \alpha_i E_\ell$ with α_i the polarizability of the dipole d_i. The intensity becomes:

$$I \propto \langle \left| \sum_i \alpha_i E_\ell(r_i) e^{i\vec{k}\cdot(\vec{r}-\vec{r_i})} \right|^2 \rangle. \tag{6.11}$$

We then develop the modulus square

$$I \propto \langle \sum_i \alpha_i E_\ell(r_i) e^{i\vec{k}\cdot(\vec{r}-\vec{r_i})} \sum_j \alpha_j^* E_\ell^*(r_j) e^{-i\vec{k}\cdot(\vec{r}-\vec{r_j})} \rangle, \tag{6.12}$$

which can be separated into two terms:

$$I \propto \langle \sum_{i=j} |\alpha_i E_\ell(r_i)|^2 + \underbrace{\sum_{i\neq j} \alpha_i \alpha_j^* E_\ell(r_i) E_\ell^*(r_j) e^{i\vec{k}\cdot(\vec{r_j}-\vec{r_i})}}_{\propto e^{i(\vec{k}-\vec{k_\ell})\cdot(\vec{r_j}-\vec{r_i})}} \rangle. \tag{6.13}$$

When $\vec{k} \neq \vec{k_\ell}$, the average of the second term vanishes. This is because the summation is carried out over various phase terms $(\vec{k} - \vec{k_\ell}) \cdot (\vec{r_j} - \vec{r_i})$ uniformly distributed in $[0, 2\pi]$ (it happens when the size of the waist is much larger than the size of the cell, see also Fig. 6.5(c)). In Fig. 6.5(a-b), we illustrate the phase matching condition responsible for the cancellation of this term. As a result,

$$I \propto \langle \sum_{i=j} |\alpha_i E_\ell(r_i)|^2 \rangle. \tag{6.14}$$

Performing the average, we transform the sum in integral using $\rho(z) = \langle \alpha_i E_\ell(r_i) \rangle$ where $\langle \alpha_i E_\ell(r_i) \rangle$ is the configuration average for the coherences of all dipoles d_i located within the $(z,\, z + \delta z)$ slab. Thus[3]:

$$I \propto \int_0^L \mathrm{d}z' \, |\rho(z')|^2 \,. \tag{6.15}$$

We have observed in the spectra that the different velocity classes do not interfere. From this experimental observation, we can conclude that[4]

$$I \propto \int_0^L \mathrm{d}z' \int_{-\infty}^{\infty} \mathrm{d}v M_\mathrm{b}(v) \, |\rho(z', v)|^2 \,. \tag{6.16}$$

Finally, the coherence ρ is induced by the forward and backward cavity fields E_+ and E_- introduced in Chapter 4. We show that if the two associated coherences ρ_+ and ρ_- interfere, it leads to an oscillation of the width with a period $\lambda/2$ (see Fig. 6.6(a)). Without interference, this oscillation disappears (see Fig. 6.6(b)). The only solution that is in agreement with our experimental results presented in Fig. 6.6(c) is when these contributions do not interfere. We end up with the final formula[5]:

$$I \propto \int_0^L \mathrm{d}z' \int_{-\infty}^{\infty} \mathrm{d}v M_\mathrm{b}(v) \, |\rho_-(z', v)|^2 + |\rho_+(z', v)|^2 \,. \tag{6.17}$$

This result is preliminary and care should be taken when using it. We note however that it agrees with the formula given in Ref. [Andreeva *et al.*, 2007] in the limit of weak driving.

6.2 van der Waals interaction in fluorescence

In this section, we present a first attempt to extract the atom-surface C_3 coefficient from fluorescence spectra of the Cs D_1 line. We first show that we are able to see the influence of the surface phenomenologically with a model that does not include the spatially varying atom-surface potential. A model including this potential is under development.

[3] Note that in the regime of weak excitation, $|\rho|^2 = \rho_{22}$ as introduced in Chapter 1.

[4] We have dismissed the following situation: $I \propto \int_0^L \mathrm{d}z' \left| \int_{-\infty}^{\infty} \mathrm{d}v M_\mathrm{b}(v) \rho(z', v) \right|^2$, where the velocity classes interfere.

[5] We have dismissed the following situation: $I \propto \int_0^L \mathrm{d}z' \int_{-\infty}^{\infty} \mathrm{d}v M_\mathrm{b}(v) \, |\rho_-(z', v) + \rho_+(z', v)|^2$, where the coherences ρ_- and ρ_+ interfere.

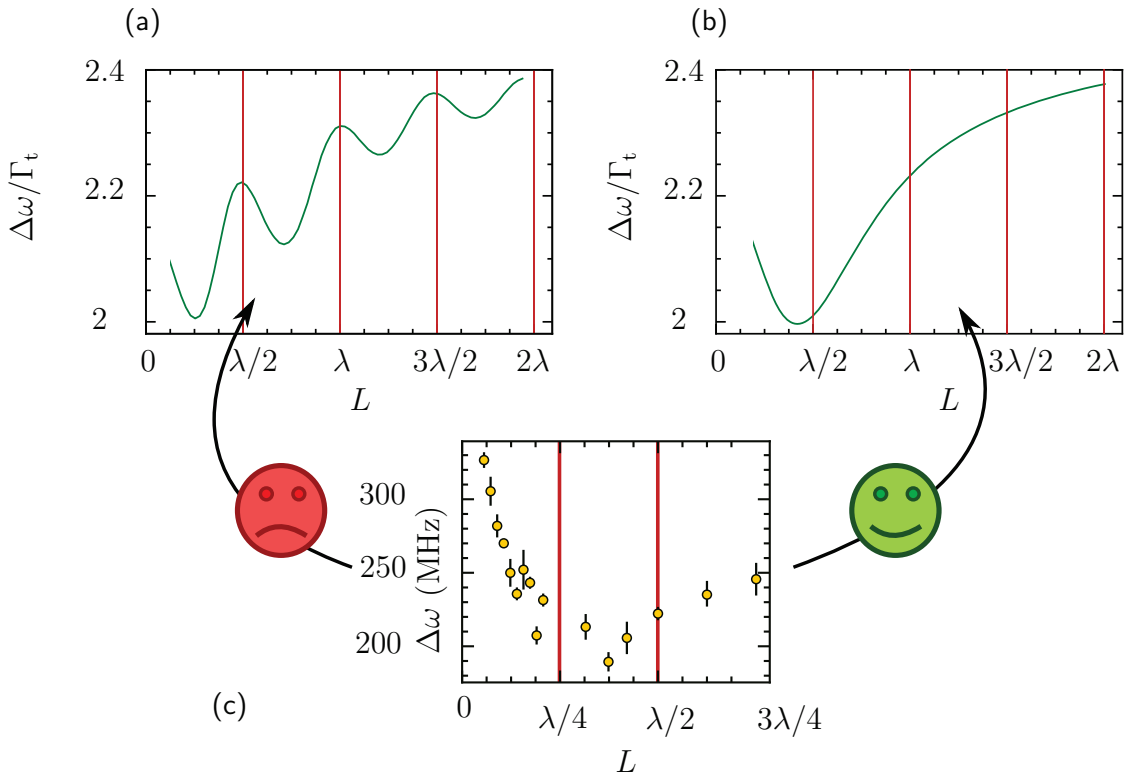

Figure 6.6: No cavity interferences (a) Width of spectra simulated with a model where we let the coherences ρ_- and ρ_+ interfere as a function of the cell thickness. The widths are extracted by Lorentzian fits and are normalized by the total homogeneous line-width Γ_t. The width features a $\lambda/2$ oscillation whose amplitude depends on Γ_t (b) Width of spectra assuming no interference (we use Eq. (6.17)). The oscillation is not present. The increase in the width for short thickness ($L < \lambda/2$) is due to transient broadening. (c) Experimental width $\Delta\omega$ as a function of the cell thickness for a temperature $\Theta = 175°C$. The experimental data do not feature the $\lambda/2$-periodic oscillation with the cell thickness. It seems to indicate that only a model with no cavity interference is appropriate.

6.2.1 Initial results: extraction of the bulk properties

Extraction of the bulk properties We follow the same experimental procedure as in Chapter 4 to extract the C_3 coefficient. We represent in Fig. 6.7(a-b-c) experimental spectra obtained for $\Theta = 210°C$. We first use Eq. (6.17) and Eqs. (4.20), (4.21) and (4.18) to model our data. We superimpose on these graphs the best fit to the data where we have adjusted Δ_P, Γ_P and an additional offset to account for the off-resonant noise. The model reproduces almost perfectly the line-shape: we have therefore managed to include the velocity selection at the origin of the incoherent

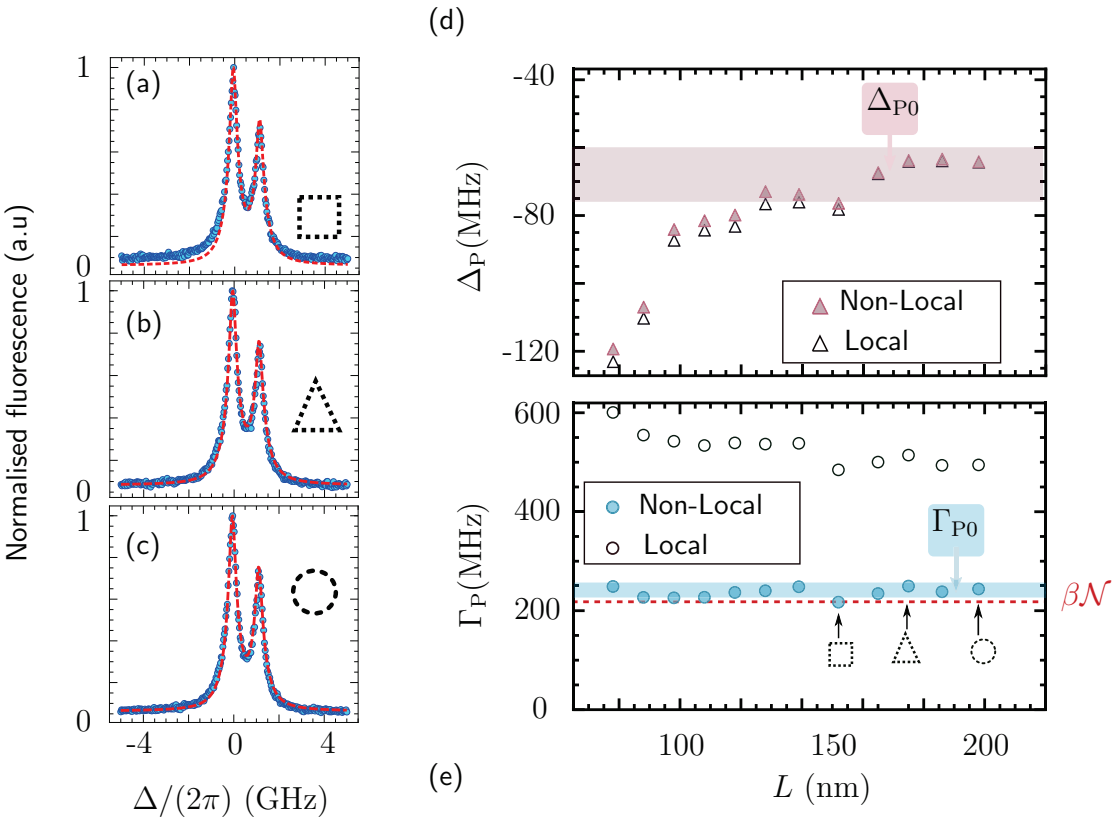

Figure 6.7: Bulk vapor properties Experimental fluorescence spectra. Temperature of the cesium reservoir of $\Theta = 210°\text{C}$ and cell thickness $L = 150,\ 170$ and 190 nm in (a), (b), (c) respectively. The square, triangle and circle are reported on the right panels to indicate the corresponding spectrum. The best fit using the non-local fluorescence model that does not include the atom-surface potential (see details in main text) is superimposed as a dashed red line. (d-e) Extracted Δ_P (triangles) and Γ_P (circles) as a function of the cell thickness L. Full symbols: non-local model. Empty symbols: local model. The bulk properties of the medium $\Delta_{\text{P}0}$ and $\Gamma_{\text{P}0}$ are extracted at large enough cell thickness.

narrowing. Indeed, despite the integration over Maxwell Boltzmann velocities, the theoretical line-shape is not Doppler broadened, in agreement with the experimental data.

We represent in Fig. 6.7(d-e) the extracted values for the parameters Δ_P and Γ_P as a function of the cell thickness. We first note that the value extracted for Γ_P is independent of the cell thickness and in excellent agreement with the collisional broadening predicted at this temperature for the D_1 line of cesium. As in Chapter 4, we report the phenomenological signature of the van der Waals potential in the red shift of Δ_P for $L \leq 150$ nm. We extract the bulk properties of the vapor $\Delta_{\text{P}0} = -65 \pm 12$ MHz and $\Gamma_{\text{P}0} = 237 \pm 8$ MHz taking the mean and the standard deviation of the

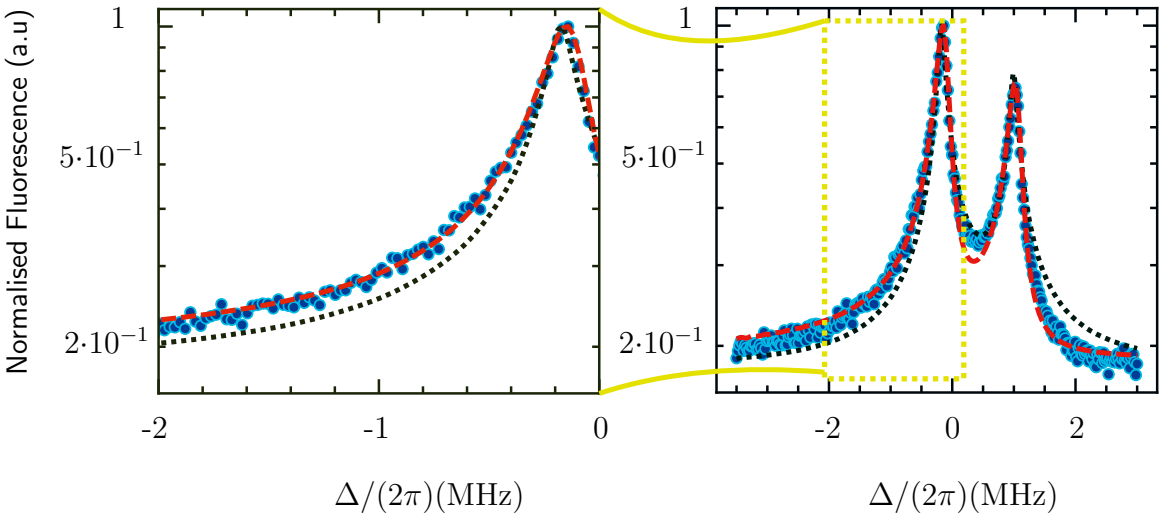

Figure 6.8: Red-side asymmetry Right panel: Blue circles, experimental spectrum for $L = 65$ nm and $\Theta = 210°$C. Black dotted line: best fit using Eq. (6.17) for the fluorescence not including the spatial dependence of the atom-surface potential (*i.e.* the coherences are calculated using Eqs. (4.20) and (4.21) together with Eq. (4.18)). Red dashed line: local model (see details in the main text) including the spatial dependent shift. (b) Zoom on the left of the $F = 4 \rightarrow F' = 3$ transition: only the model that accounts for the inhomogeneous line shift is able to reproduce the asymmetry.

parameters for $L \geq 150$ nm.

Observation of the asymmetry We show in Fig. 6.8 a spectrum in the thin region ($L = 65$ nm). The influence of the atom-surface interaction is more visible using the log-scale. The asymmetry on the red side of the transition originates from the spatially-dependent van der Waals shift. The model not including the atom-surface potential fails to reproduce this asymmetry. We have not developed yet a non-local model that include atom-surface interaction for fluorescence. As a preliminary result, we show that a local model for the fluorescence (*i.e.* we still use Eq. (6.17) but the coherences are calculated with Eq. (4.22), without integration over Maxwell Boltzmann distribution) is able to reproduce accurately the asymmetry. However, without taking into account the atomic motion, we cannot give a meaningful interpretation of the C_3 coefficient returned by the fit.

6.2.2 Work in progress

Effect of the temperature In the future, we could investigate the dependence of the atom-surface interaction with the temperature. The properties of the interaction are only affected by a change in the temperature of the cell windows while a change in the temperature of the reservoir (*i.e.* a different vapor density) should not affect the interaction [Laliotis *et al.*, 2008]. The influence of the temperature on the interaction originates from temperature dependent polaritonic surface modes [Passerat de Silans *et al.*, 2009]. Reference [Laliotis *et al.*, 2014] indicates that a change in the temperature of several hundreds of degrees is required to see a modification of the C_3 coefficient. The borosilicate cells, that cannot be used above 250°C are therefore not good candidates for this experiment. Due to the glue used to build the sapphire cells, the maximum allowed operation temperature is 400°C. As a consequence, we should develop another design for both cell and oven to perform this experiment.

Effect of the material In principle, we have all the tools (experimental and theoretical) to compare the van der Waals interaction for cesium atoms close to sapphire and borosilicate using transmission spectroscopy. However, we have not been able to obtain satisfactory agreement between theory and experiment when adjusting our transmission model to the spectra obtained with the home-made borosilicate cell built in the previous chapter. We attribute the above discrepancy to a still not well understood additional Fabry-Perot effect. Fluorescence spectra are more promising since we have obtained very good agreement between theory and experiment for spectra in the thick regions (see Figs. 6.7(a-b-c)). Due to the lack of a full model in the thin region we cannot yet extract the C_3 coefficients with these spectra. We have finally already seen differences between the two cells when we compare the phenomenological influence of the surface on the parameters Δ_{P} extracted with the non-local model. We have compared the value of Δ_{P} as a function of the cell thickness for the two cells heated at equivalent windows temperatures ($\Theta_{\mathrm{win}} = 220$°C). We have observed that the shift is larger in the case of a sapphire window than a borosilicate window. This is in qualitative agreement with the Lifshitz theory on van der Waals interaction because the C_3 is expected to be larger in the case of sapphire (see Eqs. (4.8) and (4.9)).

6.3 Resonant dipole-dipole interactions

To conclude this chapter, we revisit the resonant dipole-dipole interaction using fluorescence spectroscopy. In particular, we investigate the dependence with L and $\mathcal{N}$ of the shifts (and widths) modified by the resonant dipole-dipole interaction.

6.3.1 Collective Lamb Shift in fluorescence

In Chapter 2, we demonstrated that for a dilute enough atomic slab placed in vacuum, the minimum of transmission should be shifted by a quantity called the Collective Lamb Shift (CLS). We represent in Fig. 6.9(a) theoretical simulations to compare the dependence of the line peak in the case of transmission and fluorescence. Using Eq. (6.17), we see that in a regime where $\mathcal{N}/k_\ell^3(\Gamma_0/\Gamma_t) \ll 1$, the fluorescence peak is not shifted. We superimpose for comparison the results we obtained in Chapter 3 in transmission. The absence of CLS in the case of fluorescence was expected for at least two reasons:

- Fluorescence is not a coherent process described by the Helmoltz equation for the propagation of light in a medium of index n. Therefore, it does not verify the conditions under which we derived the CLS.
- We note that in Eq. (6.16), the different terms in the summation are symmetric around zero-detuning. As a result, the signal resulting from the integration cannot be shifted.

Subsequently, we have led an experiment where we compare simultaneously the positions of the peaks in fluorescence and transmission. The temperature of the reservoir in the borosilicate cell is $\Theta = 210°C$ and the medium thickness varies between 70 and 550 nm. We display the results in Fig. 6.9(b). The experiment clearly confirms the simulations: out of the range where the van der Waals interaction displaces the energy levels in the two cases, only the transmission peak position is thickness-dependent[6]. We therefore demonstrate here that cavity effects, responsible for the CLS in the transmission of atomic lines has no equivalent in fluorescence. Besides, even when the medium surrounding the atoms is not vacuum, the line-shape remains symmetrical out of the range where the van der Waals interaction plays a significant role ($L \geq \lambda/(2\pi)$).

[6]Note that due to the asymmetry of the line-shape in the case of transmission, this thickness dependence is not the Cooperative Lamb shift which is only valid when the medium is surrounded by vacuum, as we showed in Chapter 2.

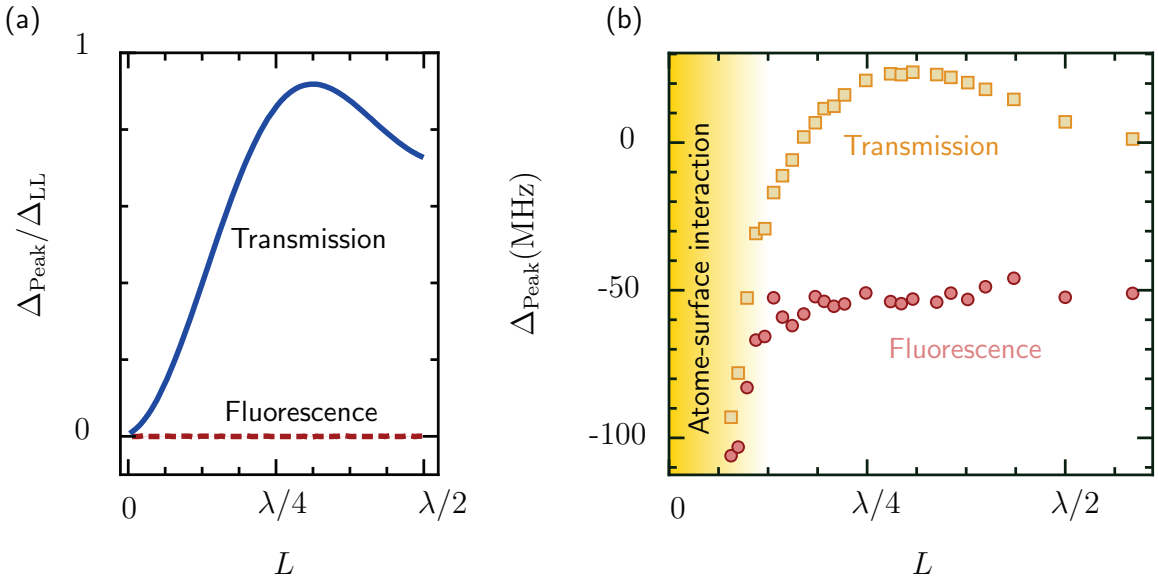

Figure 6.9: Revisiting the CLS in fluorescence (a) Simulations. Positions of the peak (minimum for transmission, maximum for fluorescence) of the resonance as a function of the cell thickness for $N/k_\ell^3(\Gamma_0/\Gamma_t) = 10^{-4}$. (b) Experiment. Position of the $F = 4 \rightarrow\ F' = 3$ resonant feature for transmission and fluorescence spectra collected in a borosilicate cell at a reservoir temperature of $\Theta = 210°\mathrm{C}$. Error bars are smaller than the markers.

This is an important result of this chapter: the Fabry-Perot nature of the cavity does not induce shift or any modification of the off-axis optical response. In other word, the off-axis optical response seems to be directly related to the bulk vapor properties.

6.3.2 Dependence of shifts and widths with density

To investigate the modification of the bulk vapor properties when the density increases, we have collected fluorescence spectra for different temperatures of the reservoir. We display in Fig. 6.10 these spectra at a fixed cell thickness as a function of the density in the borosilicate (panel (a)) and sapphire cells (panel (b)). We see that as the density increases, the line becomes very broad. We have fitted the spectra with the non-local model and extracted the parameters Δ_P and Γ_P as a function of the density for different cell thicknesses. We observe a linear dependence of the shifts and the widths with respect to the density (see Fig. 6.11(a-b)).

As in the case of transmission (see Figs. 3.5(c-d)), we represent in Fig. 6.11(c-d) the slopes $\partial\Delta_P/\partial\mathcal{N}$ and $\partial\Delta_P/\partial\mathcal{N}$ as a function of the cell thickness. For the broadening, we observe that at very low thickness, the extracted slope is in excellent agreement with

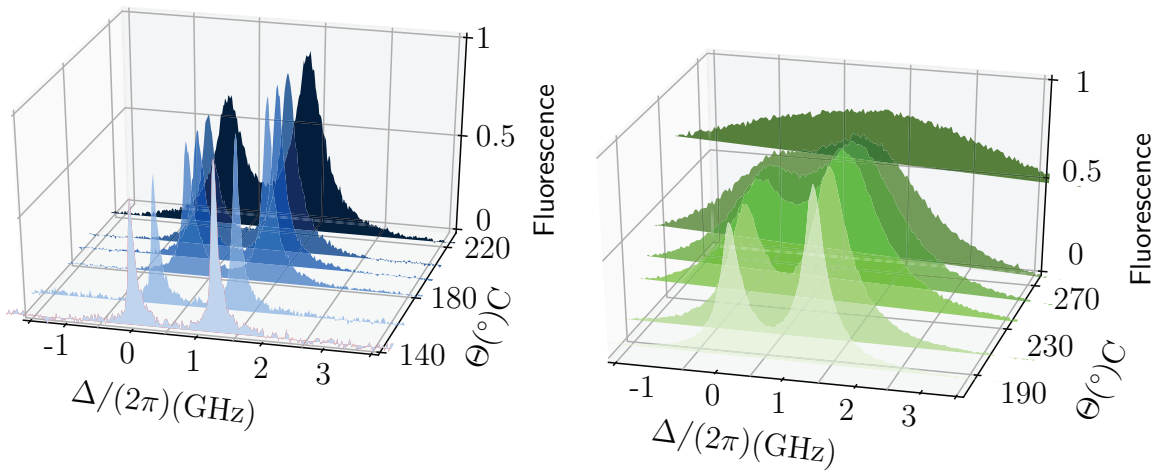

Figure 6.10: Fluorescence versus density (a) Fluorescence spectra in the borosilicate cell as a function of the temperature for $L = 330$ nm. (b) Same quantity for the sapphire cell and a cell thickness of $L = 300$ nm.

the theoretical prediction for the collisional broadening coefficient β (0.75 Hz·cm^3). However, the collisional broadening coefficient seems to increase with the cell thickness. This result is unexpected. One possible explanation of this phenomenon could be that when we collect light at $\sim 90°$ from the optical axis, light initially scattered by the atoms could excite other atoms (multiple scattering) in the direction in which light is collected. To verify this last hypothesis, one could lead an experiment where the statistical properties of the collected photons would be measured, as in Ref. [Dussaux *et al.*, 2016]. We have observed the same dependence (agreement with the collisional broadening at low L and increase for large L) when we realized the experiment with the sapphire cell. For the shift, we observe a similar behavior. The slope clearly increases with the cell thickness.

Conclusion

In this chapter, we have analysed quantitatively the off-axis light scattering by a thermal vapor confined in a nano-cell. To this purpose, we have first performed a systematic comparison between fluorescence and transmission spectra for identical parameters of thickness and density. We have particularly observed that a maximal narrowing only occurs in transmission for the particular thickness of $L = \lambda/2$. This

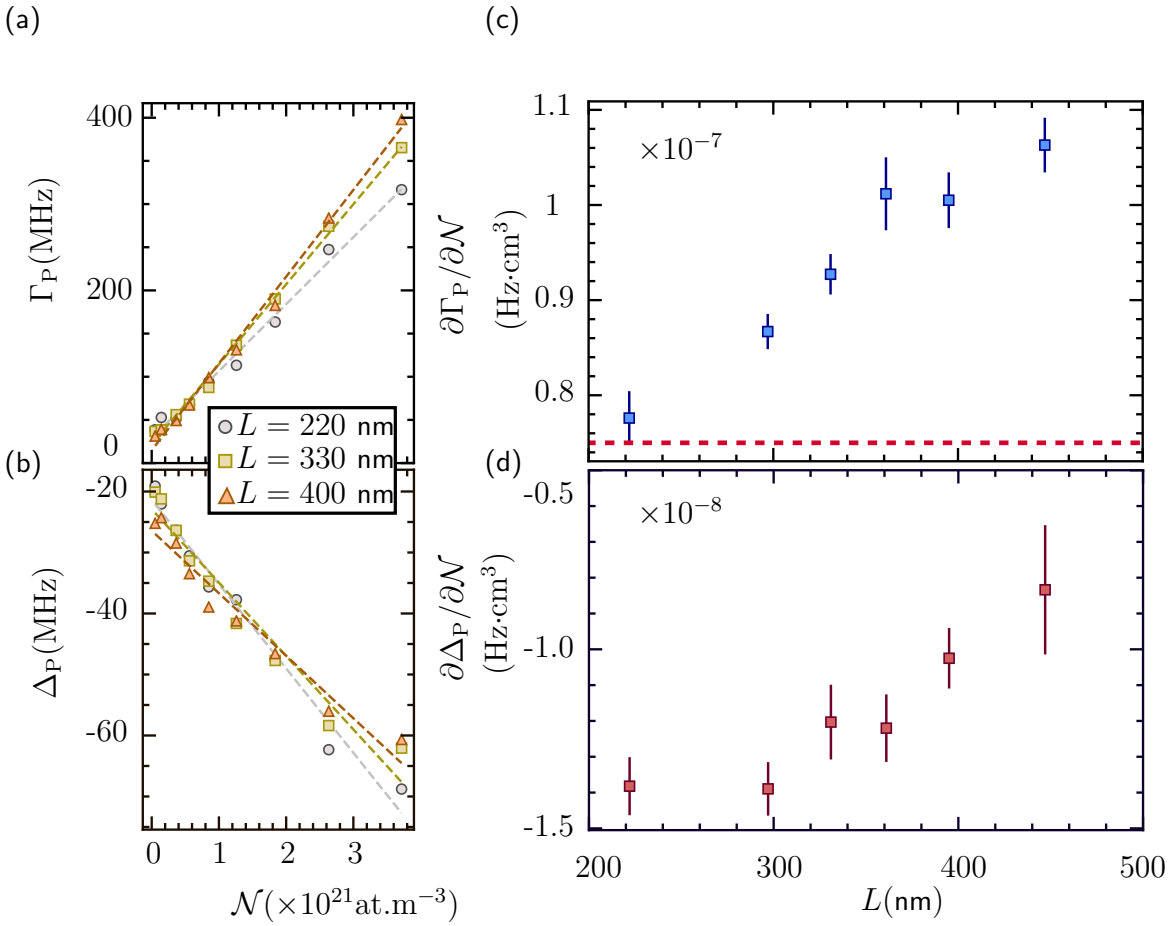

Figure 6.11: Density shifts and widths in fluorescence Left pannels: Extracted width Γ_P (a) and shift Δ_P(b) as a function of the atomic density for different cell thicknesses. Spectra obtained with the borosilicate cell. Dashed lines are linear fit to the experimental points. (c) and (d): slopes of the linear fit for the widths and shifts respectively as a function of the cell thickness. The dashed red line indicates the theoretical prediction for the collisional broadening.

phenomenon is actually λ-periodic with the cell thickness[7], and originates from the mesoscopic character of the vapor that we already encountered in Chapter 2. We have analysed in more depth the physical origin of the periodic behavior and showed that it corresponds to interferences between opposite velocity classes of the atomic ensemble confined in the cell.

We have used this observation to make assumptions in order to derive a new theoretical model for studying the off-axis light scattering from the vapor. Using this model, we have started the analysis of the van der Waals atom-surface interaction

[7]This period particularly indicates that this are not cavity effects which are $\lambda/2$-periodic with the cell thickness.

based on the method outlined in Chapter 4. We have also suggested several experiments that could be done in the future regarding interesting applications using atoms in the vicinity of a surface.

Finally we revisited experimentally the resonant dipole-dipole interaction with an off-axis detection technique. We first confirmed experimentally and theoretically that the Collective Lamb Shift is a quantity that can only be measured in transmission. It is therefore a quantity related to the coherent response of the vapor. Due to the absence of asymmetry caused by cavity effects, the line-shape is easier to model in fluorescence by comparison to transmission spectra. The access to the bulk properties is hence facilitated. We therefore conclude this chapter highlighting the fact that off-axis fluorescence detection is an alternative method to transmission to gain information on the optical response of a vapor confined in a nano-cell. On the one hand, all coherent effects resulting from the phase imprinted by the laser are lost and the method should not be used if such effects are of interest. On the other hand, if the goal is to suppress unwanted and complex line-shape modifications to extract the response of the bulk vapor, the fluorescence technique is possibly more appropriated.

Conclusion

Let us recall the main results presented in this manuscript. Although some of the outlooks for this project have already been mentioned throughout the different chapters, we will also suggest some final tracks that would be interested to explore in the future.

In the first chapter of this manuscript, we recalled the equations governing the interaction of a resonant light with an ensemble of atoms in interaction. In particular, we show that, as soon as there are more than several atoms in the ensemble, computational times to describe the exact optical response quickly diverge. Consequently, we considered another theoretical approach to interpret the experimental results obtained in this manuscript: we have adopted a mean-field theory in which the atomic ensemble is considered as a continuous polarizable medium. In this framework, we have derived *ab initio* the transmission of light through a motionless, thick and dilute atomic ensemble. We explained that in order to study the resonant dipole-dipole interaction in dense ensembles, thin systems were appropriate to reduce the optical density. It led us to anticipate the modifications of the spectral transmission properties that could occur working with a dense thermal vapor confined in a nano-cell. At the end of this chapter, we have formulated a series of question that we tried to answer in the following chapters and that we now summarize.

First of all, we had to deal with atomic motion. Inspired by several works of the community, we have highlighted explicitly that atomic motion induces a non-local response of the vapor to the incident electromagnetic field. The important quantity is the distance over which they relax: $\xi = v/\Gamma_t$, with v the atomic velocity and Γ_t the total homogeneous line-width. In large cells of thickness $L \gg \xi$, where atoms can reach steady-state, non-locality gives rise to the well-known Doppler-broadened spectra. In short cells ($L < \xi$), collisions with the cell walls quench atomic dipoles and the optical response depends on the size of the system: this is the *mesoscopic regime*. In this regime, the modification of the line-shape is drastic: spectra can be very narrow and we explained in Chapter 6, the different origins of what is commonly called *Dicke narrowing*. When the density of the medium increases, atom-atom collisions understood as a dynamic resonant dipole-dipole interaction become predominant. As a consequence, the total homogeneous broadening increases. The optical response of the medium becomes local again and this is in this framework that we investigated the effects of density on the atomic resonant frequency ω_0.

The first motivation for this Thesis was to understand the origin of the so-called *Cooperative Lamb Shift* (CLS). We have first shown that the origin of this shift was due to dipole-dipole interaction included in the propagation of light in a thin slab acting as a Fabry-Perot cavity. We have then related the CLS to an observable quantity: this is the displacement of the minimum of transmission of an atomic slab surrounded by vacuum. Finally, we refined the condition to observe it (optical response $\chi \ll 1$) and pointed out that in a real cavity such as a nano-cell, this quantity was not measurable. To account for the physical environment around the atoms we have developed a full model of transmission through the nano-cell system with which we have extracted the bulk atomic properties (shifts, widths) deconvolved from the cavity effects.

Our second motivation was to characterize the effects of the miniaturization of the cell on the spectral properties of the vapor. In addition to the growing influence of collisions with the wall, atoms close to surfaces are subjected to the van der Waals atom-surface interaction. We have developed a new method to determine precisely the influence of this interaction. Particularly, we have measured a C_3 coefficient in very good agreement with the theoretical prediction, hence validating a versatile method that could be used in a variety of situations including different atoms and cell materials. In the last chapter, we investigated the properties of light scattered off-axis by the vapor. We saw that due to the incoherent nature of this light, the line-shapes were easier to interpret. Particularly, we report no measurable modification of the optical response attributed to the cavity in this configuration. For future applications that would not require the coherent nature of the light scattering, this method is therefore perhaps more appropriated. Finally, we presented the fabrication and characterization of a new generation of all-glass super-polished nano-cells, with a surface roughness of about 1 Å rms. We conclude this manuscript with several perspectives made possible with this technological development.

1. We have seen that cavity effects can play a significant role in the transmission of light through the cell. In the future, we can imagine applying dielectric coatings on the cell walls as for increasing or decreasing the reflectivity of the surfaces. On the one hand, we could make a better-finesse cavity to favor cavity-induced dipole-dipole interactions. On the other end, we could make this effect completely negligible. In a more exotic way, we could even apply different coatings for each wall to mimic a situation where the cell would be composed of different materials. Similarly, we could imagine to apply on the surfaces an anti-relaxation coating, to change the boundary conditions of the light-matter interaction as in Ref. [Seltzer and Romalis, 2009]. In this situation, it is not sure whether or

not we could reach the mesoscopic regime induced by the non-local response of the atoms. In the nano-geometry, this is a technological challenge to apply these coatings. First, care should be taken to leave free areas for the molecular bonding. Second, calculations of the dielectric coating layer thickness have to be accounted for in the realization of the wedge geometry.

2. We have not studied in this manuscript the effect of the surface roughness on the spectral properties of the vapor. However, the quality of the surface is predicted to play a significant role in the way atoms are adsorbed on the surface walls. It would be really enlightening to measure the adsorption energy as a function of the surface roughness. In the longer term, we could consider manufacturing surfaces with a roughness down to the atomic level using for example lithographic techniques.

3. Finally, it would be very interesting to investigate the multiple scattering events. We have seen in the last chapter that it could depend on the cell thickness. We could also investigate the dependence of such events as a function of the angle with which we collect the signal. To this purpose, we should investigate the statistical properties of light collected on the side of the cell.

As a final statement, as dipole-dipole interaction in miniaturised geometries are a promising tool for future several applications, I hope that this manuscript contributed to a certain extent to characterise some of the effects that could bias the way light interacts with matter in these devices.

Appendix A: Calculation of various integrals

Contents

In this appendix, we compute several integrals that we mentioned throughout the manuscript.

A.1 Calculation of the dipole field integral

Integral to compute The purpose of this Appendix is to derive Eq. (1.36):

$$E_{\mathrm{d}}(z) = \frac{ik_\ell \mathcal{N}\alpha(\omega_\ell)}{2}\int_0^L \mathrm{d}z' E_{\mathrm{loc}}(z') e^{ik_\ell|z-z'|},$$

starting from Eq. (1.35) projected on $\boldsymbol{e_x}$:

$$\begin{aligned} E_{\mathrm{d}}(r) =& \frac{\mathcal{N}\alpha(\omega_\ell)k_\ell^3}{4\pi}\int_{-\infty}^{\infty}\mathrm{d}x'\int_{-\infty}^{\infty}\mathrm{d}y'\int_0^L \mathrm{d}z' \\ & \left\{\left[3(\boldsymbol{e_x}.\hat{\mathbf{n}})^2-1\right]\left(\frac{1}{(k_\ell R)^3}-\frac{i}{(k_\ell R)^2}\right)-\left[(\boldsymbol{e_x}.\hat{\mathbf{n}})^2-1\right]\frac{1}{k_\ell R}\right\} \\ & \times e^{ik_\ell R}E_{\mathrm{loc}}(r'). \end{aligned} \tag{A.1}$$

Demonstration The demonstration closely follows the work made in Ref. [Fearn, James, and W Milonni, 1996] that includes both near and far-field contributions. We start to note that $\boldsymbol{e}_{\mathrm{x}}\cdot\hat{\boldsymbol{n}} = (x-x')/R$ and that the local field only depends on z' such that we obtain:

$$E_{\mathrm{d}}(r) = \frac{\mathcal{N}\alpha(\omega_\ell)k_\ell^3}{4\pi}\int_{-\infty}^{\infty}\mathrm{d}x'\int_{-\infty}^{\infty}\mathrm{d}y'\int_0^L\mathrm{d}z' \left\{\left[3\frac{(x-x')^2}{R^2}-1\right]\left(\frac{1}{(k_\ell R)^3}-\frac{i}{(k_\ell R)^2}\right)-\left[\frac{(x-x')^2}{R^2}-1\right]\frac{1}{k_\ell R}\right\} \times e^{ik_\ell R}E_{\mathrm{loc}}(z'). \tag{A.2}$$

We now use polar coordinates: $(x-x') = \mathcal{R}\cos\phi$ and $\mathcal{R}^2 = R^2-(z-z')^2$ which leads to:

$$E_{\mathrm{d}}(r) = \frac{\mathcal{N}\alpha(\omega_\ell)k_\ell^3}{4\pi}\int_0^{\infty}\mathcal{R}\;\mathrm{d}\mathcal{R}\int_0^{2\pi}\mathrm{d}\phi\int_0^L\mathrm{d}z' \left\{\left[3\frac{\mathcal{R}^2\cos\phi^2}{R^2}-1\right]\left(\frac{1}{(k_\ell R)^3}-\frac{i}{(k_\ell R)^2}\right)-\left[\frac{\mathcal{R}^2\cos\phi^2}{R^2}-R^2\right]\frac{1}{k_\ell R^3}\right\} \times e^{ik_\ell R}E_{\mathrm{loc}}(z'). \tag{A.3}$$

Performing the integration over ϕ and using $\mathcal{R}\;\mathrm{d}\mathcal{R} = R\;\mathrm{d}R$, the integral is rewritten as:

$$E_{\mathrm{d}}(r) = \frac{\mathcal{N}\alpha(\omega_\ell)}{4}\int_{|z-z'|}^{\infty}\mathrm{d}R\int_0^L\mathrm{d}z' \left\{(1-ik_\ell R)\cdot\left(\frac{1}{R^2}-3\frac{|z-z'|^2}{R^4}\right)+\left(R^2+|z-z'|^2\right)\frac{k_\ell^2}{R^2}\right\}\times e^{ik_\ell R}E_{\mathrm{loc}}(z'). \tag{A.4}$$

We now need to introduce the special integral:

$$F_n = \int_{|z-z'|}^{\infty}\mathrm{d}z'\frac{e^{ik_\ell R}}{R^n},\;\; n = 0,\;1,\;2,\;3,\;4. \tag{A.5}$$

A simple variable change $R' = R-|z-z'|$ and applying the residue theorem allows to derive:

$$F_0 = -\frac{1}{ik_\ell}e^{ik_\ell|z-z'|}. \tag{A.6}$$

Using integration by parts, we find the following recurrence relation:

$$F_n(z,z') = \frac{1}{ik_\ell}\left[nF_{n+1} - \frac{e^{ik_\ell|z-z'|}}{|z-z'|^n}\right]. \tag{A.7}$$

As we can write the dipole field under the form:

$$\begin{aligned} E_{\mathrm{d}}(r) =& \frac{\mathcal{N}\alpha(\omega_\ell)}{4}\int_0^z \mathrm{d}z' F_2(z,z') - ik_\ell F_1(z,z') - 3|z-z'|^2 F_4(z,z') \\ &+ 3ik_\ell|z-z'|^2 F_3(z,z') + k_\ell F_0(z,z') + k_\ell^2|z-z'|^2 F_2(z,z') \end{aligned} \tag{A.8}$$

and applying the relation (A.7) leads to Eq. (1.36).

A.2 Calculation of the transmission through an atomic slab surrounded by vacuum

The purpose of this Appendix is to derive Eq. (2.18) starting from Eqs. (2.15), (2.16) and (2.17). We start to derive the two intergrals I_1 and I_2. . Because the driving fields propagates in the medium without any reflection, we can write it as $E(z'') = E_0 e^{ik_\ell z''}$. As in the manuscript, we also introduce $\Lambda_+ = \Gamma_{\mathrm{t}}/2 - i\left(\Delta_{\mathrm{FF'}} - k_\ell v\right)$ for the sake of readability. Starting from Eqs. (2.16) and (2.17) we obtain:

$$I_1 = \frac{iE_0\mathcal{N}\epsilon_0 C_{\mathrm{FF'}}^2 d^2}{\hbar}\int_0^{+\infty}\mathrm{d}v\frac{M_{\mathrm{b}}(v)}{v}\exp\left(\frac{-z'(\Gamma_{\mathrm{t}}/2 - i\Delta_{\mathrm{FF'}})}{v}\right)\int_0^{z'}\mathrm{d}z''\exp\left(\frac{z''\Lambda_+}{v}\right), \tag{A.9}$$

$$I_2 = -\frac{iE_0\mathcal{N}\epsilon_0 C_{\mathrm{FF'}}^2 d^2}{\hbar}\int_{-\infty}^{0}\mathrm{d}v\frac{M_{\mathrm{b}}(v)}{v}\exp\left(\frac{-z'(\Gamma_{\mathrm{t}}/2 - i\Delta_{\mathrm{FF'}})}{v}\right)\int_{z'}^{L}\mathrm{d}z''\exp\left(\frac{z''\Lambda_+}{v}\right). \tag{A.10}$$

Performing the spatial integral we have:

$$I_1 = \frac{iE_0\mathcal{N}\epsilon_0 C^2_{\mathrm{FF'}} d^2}{\hbar} \int_0^{+\infty} \mathrm{d}v M_\mathrm{b}(v) \exp\left(\frac{-z'(\Gamma_\mathrm{t}/2 - i\Delta_{\mathrm{FF'}})}{v}\right) \left[\frac{\exp\left(\frac{z'\Lambda_+}{v}\right) - 1}{\Lambda_+}\right], \tag{A.11}$$

$$I_2 = -\frac{iE_0\mathcal{N}\epsilon_0 C^2_{\mathrm{FF'}} d^2}{\hbar} \int_0^{+\infty} \mathrm{d}v M_\mathrm{b}(v) \exp\left(\frac{-z'(\Gamma_\mathrm{t}/2 - i\Delta_{\mathrm{FF'}})}{v}\right) \left[\frac{\exp\left(\frac{L\Lambda_+}{v}\right) - \exp\left(\frac{z'\Lambda_+}{v}\right)}{\Lambda_+}\right]. \tag{A.12}$$

We now rewrite Eq. (2.15) as:

$$E_\mathrm{t} = E_0 e^{ik_\ell z} + \sum_{F,F'} \frac{ik_\ell}{2\epsilon_0} \int_0^L \mathrm{d}z' e^{ik_\ell(z-z')} \left(I_1 + I_2\right), \tag{A.13}$$

that can be expressed as:

$$E_\mathrm{t} = E_0 e^{ik_\ell z} - \sum_{F,F'} \frac{\mathcal{E}_0\mathcal{N} C^2_{\mathrm{FF'}} d^2 k_\ell}{2\hbar} e^{ik_\ell z} \times \tag{A.14}$$

$$\int_0^L \mathrm{d}z' \left\{ \int_0^\infty \mathrm{d}v M_\mathrm{b}(v) \left[\frac{1 - \exp\left(\frac{-z'\Lambda_+}{v}\right)}{\Lambda_+}\right] - \int_{-\infty}^0 \mathrm{d}v M_\mathrm{b}(v) \left[\frac{\exp\left(\frac{(L-z')\Lambda_+}{v}\right) - 1}{\Lambda_+}\right] \right\}. \tag{A.15}$$

We perform the second spatial integration:

$$E_\mathrm{t} = E_0 e^{ik_\ell z} - \sum_{F,F'} \frac{\mathcal{E}_0\mathcal{N} C^2_{\mathrm{FF'}} d^2 k_\ell}{2\hbar} e^{ik_\ell z} \times \tag{A.16}$$

$$\left\{ \int_0^\infty \mathrm{d}v M_\mathrm{b}(v) \left[\frac{L}{\Lambda_+} + v\frac{\exp\left(-\frac{L\Lambda_+}{v}\right) - 1}{\Lambda_+^2}\right] + \int_{-\infty}^0 \left[\frac{L}{\Lambda_+} - v\frac{\exp\left(\frac{L\Lambda_+}{v}\right) - 1}{\Lambda_+^2}\right] \right\}. \tag{A.17}$$

A final variable change $v \to |v|$ leads to Eq. (2.18) and concludes this demonstration.

A.3 Calculation of the transmission through an atomic slab in a Fabry-Perot cavity

In this Appendix, we provide semi-analytical[1] results for the field transmitted to a non-local slab of atoms placed in a Fabry-Perot cavity. Although the derivation is painful, we provide semi-analytical results because a fully-numerical model is way too slow for fitting procedures. In contrast to the above Appendix A.2, the driving field and emitted fields are multiply reflected in the cavity. In this case, the field transmitted by the cavity is:

$$E_{\mathrm{t}} = E_{\mathrm{t}0} + E_{A_+} + E_{A_-}, \tag{A.18}$$

where E_{A_+} and E_{A_-} are defined in Eqs. (2.20) and (2.21). Our work here is to compute E_{A_+} and then E_{A_-}. For the sake of simplicity, we use the reduced notation $A = t_{20}/(1 - r_{20}^2 \exp 2ik_\ell L)$. Starting from Eq. (2.20), and using Eq. (2.14):

$$E_{A_+} = F \exp(ik_\ell z) \sum_{F,F'} \frac{ik_\ell}{2\epsilon_0} \int_0^L \mathrm{d}z' \exp(-ik_\ell z') \int_{-\infty}^{\infty} \mathrm{d}z'' \epsilon_0 \chi_L(z', z'', \omega_\ell) E(z''). \tag{A.19}$$

Using Eqs. (2.11), (2.9) and (2.10) we can express the field E_{A+} by the means of two integrals involving positive and negative velocities on a reduced spatial domain[2]:

$$E_{A_+} = -AB \sum_{F,F'} \left(I_{A1} - I_{A2} \right), \tag{A.20}$$

where $B = (k_\ell \mathcal{N} C_{\mathrm{FF'}}^2 d^2)/(2\hbar)$,

$$I_{A1} = \int_0^\infty \mathrm{d}v \frac{M_{\mathrm{b}}(v)}{v} \int_0^L \mathrm{d}z' \exp\left(-ik_\ell z'\right) \int_0^{z'} \mathrm{d}z'' \exp\left(\frac{(z' - z'')(-\frac{\Gamma_{\mathrm{t}}}{2} + i\Delta_{\mathrm{FF'}})}{v} \right) E(z''), \tag{A.21}$$

$$I_{A2} = \int_{-\infty}^0 \mathrm{d}v \frac{M_{\mathrm{b}}(v)}{v} \int_0^L \mathrm{d}z' \exp\left(-ik_\ell z'\right) \int_{z'}^{L} \mathrm{d}z'' \exp\left(\frac{(z' - z'')(-\frac{\Gamma_{\mathrm{t}}}{2} + i\Delta_{\mathrm{FF'}})}{v} \right) E(z''). \tag{A.22}$$

[1] We perform the spatial integrations and leave the velocity integration that has no analytical solution.

[2] We recall that the main argument to calculate separately the contributions from positive and negative velocity is that the coherence is quenched at a wall collision

In the dilute regime, the field that excites the atoms is the one of an empty cavity:

$$E(z'') = E_0 \underbrace{\frac{t_{10}}{1 - r_{20} \exp 2ik_\ell L}}_{C} \left(e^{ik_\ell z''} + r_{20} \exp\left(ik_\ell (2L - z'')\right) \right). \tag{A.23}$$

There is no particular difficulties in the integration steps: it mainly involves primitives of exponentials such that in Appendix A.2. We provide the results of the cumbersome successive integrations:

$$I_{A1} = E_0 C \int_0^\infty \mathrm{d}v M_\mathrm{b}(v) \Bigg\{ \frac{L}{\Lambda_+} + \frac{v}{\Lambda_+^2} \left(\exp(-\frac{\Lambda_+ L}{v}) - 1 \right) \tag{A.24}$$

$$+ \frac{r_{20} e^{2ik_\ell L}}{\Lambda_-} \left[\frac{(1 - e^{2ik_\ell L})}{2ik_\ell} + \frac{v}{\Lambda_+} \left(\exp(-\frac{\Lambda_+ L}{v}) - 1 \right) \right] \Bigg\} \tag{A.25}$$

and

$$I_{A2} = E_0 C \int_{-\infty}^0 \mathrm{d}v M_\mathrm{b}(v) \Bigg\{ \frac{-L}{\Lambda_+} + \frac{v}{\Lambda_+^2} \left(\exp(\frac{\Lambda_+ L}{v}) - 1 \right) \tag{A.26}$$

$$+ \frac{r_{20} e^{2ik_\ell L}}{\Lambda_-} \left[\frac{(e^{2ik_\ell L} - 1)}{2ik_\ell} + \frac{v}{\Lambda_+} \exp(\frac{\Lambda_- L}{v}) \left(1 - \exp(-\frac{\Lambda_+ L}{v}) \right) \right] \Bigg\}. \tag{A.27}$$

We now compute E_{A_-}:

$$E_{A_-} = r_{20} F \exp(ik_\ell z) \sum_{F,F'} \frac{ik_\ell}{2\epsilon_0} \int_0^L \mathrm{d}z' \exp(+ik_\ell z') \int_{-\infty}^\infty \mathrm{d}z'' \epsilon_0 \chi_L(z', z'', \omega_\ell) E(z''). \tag{A.28}$$

As before, we can rewrite E_{A_-} as:

$$E_{A_+} = -AB \sum_{F,F'} \left(I_{A3} - I_{A4} \right), \tag{A.29}$$

where:

$$I_{A3} = \int_0^\infty \mathrm{d}v \frac{M_\mathrm{b}(v)}{v} \int_0^L \mathrm{d}z' \exp\left(+ik_\ell z'\right) \int_0^{z'} \mathrm{d}z'' \exp\left(\frac{(z'-z'')(-\frac{\Gamma_\mathrm{t}}{2}+i\Delta_{\mathrm{FF'}})}{v}\right) E(z''), \tag{A.30}$$

$$I_{A4} = \int_{-\infty}^0 \mathrm{d}v \frac{M_\mathrm{b}(v)}{v} \int_0^L \mathrm{d}z' \exp\left(+ik_\ell z'\right) \int_{z'}^L \mathrm{d}z'' \exp\left(\frac{(z'-z'')(-\frac{\Gamma_\mathrm{t}}{2}+i\Delta_{\mathrm{FF'}})}{v}\right) E(z''). \tag{A.31}$$

We finally give the results of the integrations:

$$I_{A3} = E_0 C \int_0^\infty \mathrm{d}v M_\mathrm{b}(v) \Bigg\{ \frac{1}{\Lambda_+}\left[\frac{v}{\Lambda_-}\left(\exp(-\frac{\Lambda_- L}{v})-1\right)+\frac{\exp(2ik_\ell)-1}{2ik_\ell}\right] \tag{A.32}$$

$$+\frac{r_{20}e^{2ik_\ell L}}{\Lambda_-}\left[L+\frac{v}{\Lambda_-}\left(\exp(-\frac{\Lambda_- L}{v})-1\right)\right]\Bigg\}, \tag{A.33}$$

$$I_{A4} = E_0 C \int_{-\infty}^0 \mathrm{d}v M_\mathrm{b}(v) \Bigg\{ \frac{1}{\Lambda_+}\left[\frac{v}{\Lambda_-}\left(\exp(\frac{\Lambda_+ L}{v})-\exp(2ik_\ell L)\right)+\frac{1-\exp(2ik_\ell)}{2ik_\ell}\right] \tag{A.34}$$

$$+\frac{r_{20}e^{2ik_\ell L}}{\Lambda_-}\left[-L+\frac{v}{\Lambda_-}\left(\exp(\frac{\Lambda_- L}{v})-1\right)\right]\Bigg\}. \tag{A.35}$$

We have derived the expression that allows to compute E_{A_+} and E_{A_-} in a reasonnable computing time. Ultimately, having the field transmitted by the Fabry-Perot cavity without atoms:

$$E_t = \frac{t_{10}t_{20}\exp(ik_\ell z)}{1-r_{20}\exp(2ik_\ell L)}, \tag{A.36}$$

we can compute the transmission factor:

$$T = \left|\frac{E_t}{E_{t0}}\right|^2, \tag{A.37}$$

which is used for fitting the data.

A.4 Collective Lamb shift

A.4.1 Taylor-expansion of the field transmitted by a dense atomic slab

In this Appendix we provide the calculation steps to derive the Collective Lamb shift. Particularly, we detail the Taylor expansion to go from Eq. (3.12) to Eq. (3.15). We first make the calculation without the Lorentz field correction and we show that the latter only introduces an additional shift offset Δ_{LL}.

We start from Eq. (3.12) recalled below:

$$E_{\mathrm{t}}(z) = E_0 e^{ik_\ell z} + \frac{ik_\ell \chi}{2} \int_0^L dz' \left(E_{\mathrm{tr1}} e^{ink_\ell z'} + E_{\mathrm{tr2}} e^{-ink_\ell z'} \right) e^{ik_\ell (z-z')}. \tag{A.38}$$

We do a Taylor-expansion of E_{t} at second order in χ. Therefore we expand the term in the integral at first order in χ. We have particularly:

$$n = 1 + \frac{\chi}{2} + o(\chi^2), \tag{A.39}$$

$$t_1 = \frac{2}{1+n} = \frac{1}{1 + \frac{\chi}{4} + o(\chi^2)} = 1 - \frac{\chi}{4} + o(\chi^2), \tag{A.40}$$

$$r_2 = \frac{n-1}{n+1} = \frac{\frac{\chi}{2} + o(\chi^2)}{2 + \frac{\chi}{2} + o(\chi^2)} = \frac{\chi}{4} + o(\chi^2). \tag{A.41}$$

With $\exp(2ink_\ell L) = (1 + ik_\ell \chi L + o(\chi^2)) \exp(2ik_\ell L)$, we can neglect the terms in the denominator of E_1 and E_2 :

$$E_{\mathrm{tr1}} = \frac{t_1 E_0}{1 - r_2^2 \exp(2ink_\ell) L} = \left(1 - \frac{\chi}{4} + o(\chi^2)\right) E_0, \tag{A.42}$$

$$E_{\mathrm{tr2}} = \frac{t_1 r_2 \exp(2ink_\ell L) E_0}{1 - r_2^2 \exp(2ink_\ell) L} = \left(\frac{\chi}{4} + o(\chi^2)\right) E_0. \tag{A.43}$$

Using Eqs. (A.42), (A.43) and $\exp(2ink_\ell z') = (1 + ik_\ell \chi z' + o(\chi)) \exp(2ik_\ell z')$ in Eq. (3.12):

$$E_{\mathrm{t}}(z) = E_0 e^{ik_\ell z} + \frac{ik_\ell \chi E_0}{2} \int_0^L \mathrm{d}z' \Bigg\{ \left((1 - \frac{\chi}{4} + o(\chi^2) \right) \left(1 + ik_\ell \chi z' + o(\chi^2) \right) e^{ik_\ell z'} \tag{A.44}$$

$$+ \left(\frac{\chi}{4} + o(\chi^2) \right) e^{ik_\ell (2L - z')} \Bigg\} e^{ik_\ell (z - z')}. \tag{A.45}$$

Performing the integral over z', it leads to Eq. (3.14) that is recalled below:

$$E_{\mathrm{t}} \simeq E_0 e^{ik_\ell z} \left[1 + i\frac{\chi k_\ell L}{2} \left(1 + \frac{i\chi k_\ell L}{4} - \frac{\chi}{4} + \frac{\chi}{4} \frac{e^{2ik_\ell L} - 1}{2ik_\ell L} \right) + o(\chi^2) \right]. \tag{A.46}$$

Finally, using $1 + x \sim 1/(1 - x)$ in the parenthesis[3], the transmitted field can be written as:

$$E_{\mathrm{t}} \simeq E_0 e^{ik_\ell z} \left[1 + \frac{i\frac{\chi k_\ell L}{2}}{1 - \frac{i\chi k_\ell L}{4} + \frac{\chi}{4} - \frac{\chi}{4}\frac{e^{2ik_\ell L} - 1}{2ik_\ell L}} + o(\chi^2) \right]. \tag{A.47}$$

In order to proceed further, we need a more explicit expression for the optical response χ.

A.4.2 Calculation without Lorentz field correction

Ignoring the local field corrections (*i.e.* the polarisation field in Eq. (1.30)), the relation between χ and the polarisability (the response from a single emitter) α is $\chi = \mathcal{N}\alpha$. Using $\alpha = (6i\pi/k_\ell^3)/(\Gamma_{\mathrm{t}} - 2i\Delta)$, introducing $\Delta_{\mathrm{LL}} = -\pi\Gamma_0\mathcal{N}/k_\ell^3$ and multiplying numerator and denominator of Eq. (A.50) by $(\Gamma_{\mathrm{t}} - 2i\Delta)$, we have:

$$T = \left| \frac{E_{\mathrm{t}}}{E_0} \right|^2 = \left| 1 - \frac{3\pi\mathcal{N}\Gamma_0 L/k_\ell^2}{\Gamma_{\mathrm{t}} - 2i\Delta - 3/2k_\ell L\Delta_{\mathrm{LL}} + 3/2i\Delta_{\mathrm{LL}} \left((\exp(2ik_\ell L) - 1)/(2ik_\ell L) - 1 \right)} + o(\chi^2) \right|^2. \tag{A.48}$$

Regrouping real and imaginary parts in the denominator leads to:

[3] We point out that this transformation is only valid at first order in χ. Particularly, to find higher density orders for the shift, one should include all the relevant terms at the beginning of this demonstration.

$$T = \left|\frac{E_\mathrm{t}}{E_0}\right|^2 = \left|1 - \frac{3\pi\mathcal{N}\Gamma_0 L/k_\ell^2}{\left[\Gamma_\mathrm{t} - \frac{3}{2}\Delta_\mathrm{LL}(k_\ell L + \frac{\sin^2(k_\ell L)}{k_\ell L}\right] - 2i\left[\Delta + \frac{3}{4}\Delta_\mathrm{LL}\left(1 - \frac{\sin(k_\ell L)\cos(k_\ell L)}{k_\ell L}\right)\right]} + o(\chi^2)\right|^2 . \tag{A.49}$$

We finally retrieve Eq. (3.15).

A.4.3 Calculation with Lorentz field correction

Ultimately, we show that the effect of the Lorentz local field is to shift the resonance by exactly $|\Delta_\mathrm{LL}|$. We now use the Clausius-Mossoti relation to relate the susceptibility and the polarizability: $\chi = \mathcal{N}\alpha/(1 - \mathcal{N}\alpha/3)$. Starting from Eq. (A.50), we can easily derive:

$$\left|\frac{E_\mathrm{t}}{E_0}\right|^2 = \left|1 + \frac{i\frac{\mathcal{N}\alpha k_\ell L}{2}}{1 - \frac{\mathcal{N}\alpha}{3} - \frac{i\mathcal{N}\alpha k_\ell L}{4} + \frac{\mathcal{N}\alpha}{4} - \frac{\mathcal{N}\alpha}{4}\frac{e^{2ik_\ell L}-1}{2ik_\ell L}} + o(\chi^2)\right|^2 . \tag{A.50}$$

The only difference caused by the Lorentz correction is the term $\mathcal{N}\alpha/3$ at denominator. Applying the same transormation that the one to obtain Eq. (A.48), we see that the only effect is to shift the resonance by a quantity $|\Delta_\mathrm{LL}|$. We thus retrieve the full formula for the Collective Lamb shift of Eq. (3.2).

Appendix B: Weak-probe approximation

Contents

B.1 Testing the limits of the weak-driving regime

In this Appendix, we show the dependence of the absorption in the nano-cell as a function of the power of the laser. The experiment is carried out at $\Theta = 170°\text{C}$ and $L = 220$ nm. In Fig. B.1(a), we observe that for increasing laser power P_ℓ, the quantity of absorption decreases. This is due to a power broadening which appears when the linear response of the dipole is no longer valid [Grynberg *et al.*, 2010]. We can also note that for high laser powers, a structure appears at the center of each hyperfine transition. This effect is similar to a pump-probe effect. Indeed, due to the thin nature of the cell, the laser reflected on the second interface can induce saturated absorption.

In the case of a Cs atom, the saturation intensity for a linearly polarized light is $I_{\text{sat}} \simeq 2\ \text{mW}\cdot\text{cm}^{-2}$ [Steck]. In Fig. B.1(b), we represent the evolution of the transmission at resonance as a function of I/I_{sat}. The waist is about $w_0 \simeq 500$ µm and we use $I = P_\ell/(\pi w_0^2)$. We observe that as long as $I/I_{\text{sat}} < 100$, the experiment can be considered in the weak driving regime. For experiments with thermal vapors, we therefore do not require that $I/I_{\text{sat}} < 1$, as would be the case for cold dilute gases.

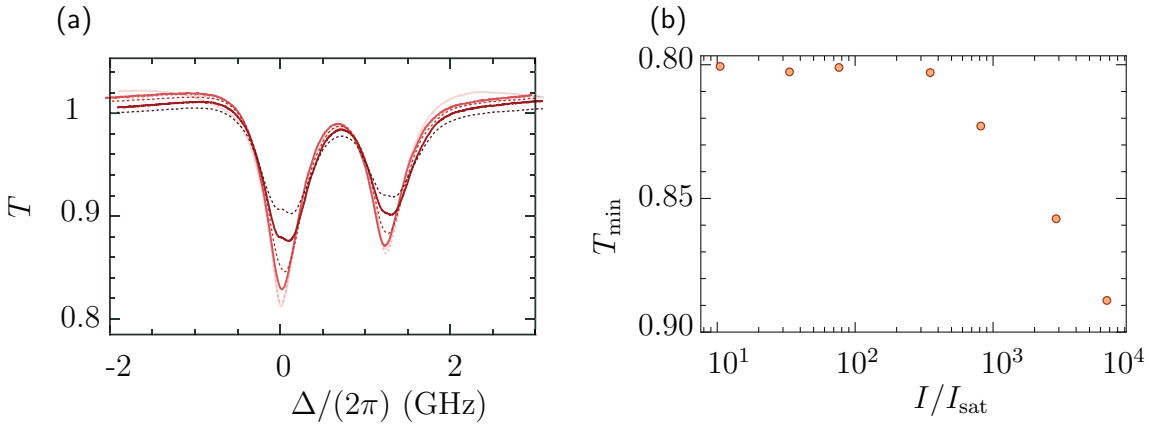

Figure B.1: Saturation of optical transitions due to power effects (a) Transmission spectra for different laser powers. The power goes from $P_\ell = 3$ µW in pink full line to $P_\ell = 4$ mW in dashed brown line. (b) Transmission at resonance with respect to the saturation parameter I/I_{sat}.

We have not led a quantitative analysis in the strong driving regime, which is much more involved. However our findings are not surprising: to observe the effect of the saturation, the broadening should be larger than the Doppler width and the broadening due to collisions. In our case we see that the full width at half maximum is about 500 MHz. The power induced broadening can be written as [Grynberg *et al.*, 2010]:

$$\Gamma_0 \sqrt{1 + I/I_{\text{sat}}} \tag{B.1}$$

This explains qualitatively why we observe the saturation of $I/I_{\text{sat}} > 10^2$. We refer to Ref. [Sargsyan *et al.*, 2016] for a more complete study of the strong driving regime.

Resumé en Francais

Chapter C

French summary

Introduction

Les vapeurs atomiques confinées dans des cellules nanométriques constituent une plateforme intéressante pour la réalisation de senseurs atomiques. Dans cette thèse, nous étudions l'interaction entre la lumière et un ensemble d'atomes d'alcalins dans une telle cellule. Nous nous concentrons sur les phénomènes qui pourraient modifier la réponse optique du système et ainsi affecter la précision du senseur.

Chapitre 1

Dans le premier chapitre, les prérequis théoriques pour décrire l'interaction de la lumière avec la matière sont introduits. En particulier, le champ rayonné par un dipôle à l'origine de l'interaction dipôle-dipôle est explicité. En augmentant progressivement le nombre d'atomes, nous soulevons le problème fondamental des systèmes composés de nombreuses particules en interaction. En synthétisant la littérature concernant les réalisations expérimentales reliées à cette problématique, la nano-cellule de vapeur utilisée dans cette thèse est remise dans son contexte. En utilisant des vapeurs chaudes d'alcalins confinées en nano-cellules, il est clairement établi que de nombreuses modifications de la réponse optique des atomes à une excitation lumineuse sont attendues. Nous développons finalement un modèle simpliste décrivant la transmission de la lumière à travers la cellule. Ce modèle sera raffiné tout au long des chapitres suivants.

Chapitre 2

Premièrement, le mouvement des atomes dans la vapeur induit une réponse non-locale à la lumière. La non-localité est caractérisée par la distance parcourue par les atomes pour atteindre leur régime stationnaire. Cette distance, aussi appelée distance de relaxation, s'écrit $\xi = v/\Gamma_t$, où v est la vitesse de l'atome et Γ_t la largeur spectrale homogène totale. Quand la distance de relaxation des atomes excède la taille de la cellule, la réponse optique dépend de la taille du système. Cette réponse non-locale

est à l'origine du rétrécissement spectral observé dans de nombreuses références. Le mouvement des atomes est introduit dans notre modèle de transmission et le modèle théorique reproduit parfaitement les données expérimentales. En transmission, nous avons montré que cela entraine une modification des propriétés de la vapeur avec une période égale à la longueur d'onde de la transition optique.

Chapitre 3

La largeur spectrale homogène augmente avec la densité atomique. Ainsi, dans les systèmes atomiques denses, la réponse redevient locale. Dans ce régime cependant, l'interaction dipôle-dipôle résonnante engendre des déplacements de fréquence collectifs pour des ensembles dont la taille est sub-longueur d'onde : le *Collective Lamb Shift* (CLS). Nous avons démontré que ces shifts sont induits par la cavité formée par la cellule, clarifiant ainsi un débat de plus de 40 ans. En particulier, nous avons montré que l'origine de ces shifts ne provient pas d'un déplacement de la fréquence de résonnance des atomes mais plutôt d'un déplacement du minimum du spectre de transmission. Ensuite, nous avons mis en évidence que le CLS ne peut pas être mesuré dans une expérience de vapeur confinée dans une nano-cellule car le milieu confinant les atomes possède un indice différent de l'unité. Pour extraire les déplacements énergétiques dans les milieux denses, un modèle de transmission à travers la cellule est utilisé pour déconvoluer les effets de cavité des propriétés intrinsèques aux atomes.

Chapitre 4

Proche des surfaces, la réponse optique des atomes est aussi impactée par l'interaction de van der Waals (vdW). Cette interaction est importante lorsque les atomes se situent à une distance plus petite que $\lambda/(2\pi)$ des parois de la cellule. A cause de la compétition entre différents déplacements énergétiques (interaction dipôle-dipôle, interaction atome-surface...), l'extraction des paramètres caractérisant l'interaction atome-surface est compliquée. Particulièrement dans le cas des états faiblement excités où l'influence de la surface est limité, extraire avec précision la force de l'interaction est une tâche délicate. Nous avons introduit une nouvelle méthode pour extraire avec précision la force de cette interaction. Pour cela, nous avons utilisé la forme en coin de la cellule pour déterminer les effets de densités dans les parties épaisses, où les atomes sont peu sensibles à l'interaction de vdW. Puis, après avoir fixé les propriétés

atomiques correspondantes, le mouvement des atomes dans un potentiel dépendant de la distance atome-surface est utilisé pour extraire le coefficient C_3 caractérisant l'effet de la surface en régime non retardé.

Chapitre 5

L'interaction d'un atome avec la surface peut dépendre de la rugosité de celle-ci mais aussi de son matériau. De plus, il pourrait être possible d'exploiter les propriétés d'un potentiel répulsif proche de surface pour piéger des atomes à quelques nanomètres de la surface et ainsi réaliser de nouvelles interfaces ou la lumière pourrait interagir fortement avec les atomes. Pour répondre à cet enjeu, nous avons réalisé à l'atelier d'optique de l'Institut d'Optique une nouvelle génération de nano-cellules en Borosilicate. Ces cellules ont deux caractéristiques inédites. Premièrement, elles sont réalisés d'un bloc : les différents éléments de la cellules sont adhérés moléculairement et l'assemblement ne fait usage d'aucune colle qui pourrait être source de biais supplémentaire pour la réponse optique. Deuxièmement, l'enceinte confinant les atomes est polie afin d'atteindre une rugosité de surface de quelques Å. Nous avons obtenus de premiers résultats spectroscopiques, présentés à la fin du chapitre.

Chapitre 6

Dans un ultime chapitre, nous avons observé les propriétés de la réponse optique des atomes en fluorescence. La technique de fluorescence consiste à collecter la lumière hors-d'axe. Nous avons premièrement comparé les différences spectrales entre la spectroscopie de fluorescence (processus incohérent) et de transmission (processus cohérent). Nous avons à la fois constaté l'absence de shift de cavité ainsi que la disparition de l'oscillation du rétrécissement spectral de période λ observé dans le Chapitre 2. En se basant sur ces observations expérimentales, nous avons construit un modèle classique pour décrire la réponse des atomes collectée hors-axe.

Conclusion

En conclusion, nous avons étudié les propriétés de la réponse atomique dans une vapeur chaude d'alcalin confinée dans une cellule nanométrique. En particulier nous avons clarifié le rôle du mouvement des atomes, de la cavité formée par la cavité ainsi

que l'effet de la surface.

Bibliography

Afanasiev, A. E., Melentiev, P. N., and Balykin, V. I., *"Laser-induced quantum adsorption of atoms on a surface,"* JETP Letters **86**, 172 (2007) [cited in page 123].

Agrat, N., Yeyati, A. L., and van Ruitenbeek, J. M., *"Quantum properties of atomic-sized conductors,"* Physics Reports **377**, 81 (2003) [cited in page 40].

Akopian, N., Wang, L., Rastelli, A., Schmidt, O., and Zwiller, V., *"Hybrid semiconductor-atomic interface: Slowing down single photons from a quantum dot,"* Nature Photonics **5**, 230 (2011) [cited in page 126].

Andreeva, C., Cartaleva, S., Petrov, L., Saltiel, S. M., Sarkisyan, D., Varzhapetyan, T., Bloch, D., and Ducloy, M., *"Saturation effects in the sub-doppler spectroscopy of cesium vapor confined in an extremely thin cell,"* Phys. Rev. A **76**, 013837 (2007) [cited in page 136].

Aspect, A., Arimondo, E., Kaiser, R., Vansteenkiste, N., and Cohen-Tannoudji, C., *"Laser cooling below the one-photon recoil energy by velocity-selective coherent population trapping,"* Phys. Rev. Lett. **61**, 826 (1988) [cited in page 29].

Awschalom, D., Loss, D., and Samarth, N., Semiconductor Spintronics and Quantum Computation, 1st ed. (Springer-Verlag Berlin Heidelberg, 2002) [cited in page 12].

Balik, S., Win, A. L., Havey, M. D., Sokolov, I. M., and Kupriyanov, D. V., *"Near-resonance light scattering from a high-density ultracold atomic ^{87}rb gas,"* Phys. Rev. A **87**, 053817 (2013) [cited in page 29].

Bender, H., Stehle, C., Slama, S., Kaiser, R., Piovella, N., Zimmermann, C., and Courteille, P. W., *"Observation of cooperative mie scattering from an ultracold atomic cloud,"* Phys. Rev. A **82**, 011404 (2010) [cited in page 29].

Bettles, R. J., Gardiner, S. A., and Adams, C. S., *"Cooperative ordering in lattices of interacting two-level dipoles,"* Phys. Rev. A **92**, 063822 (2015) [cited in page 12].

Bettles, R. J., Gardiner, S. A., and Adams, C. S., *"Enhanced optical cross section via collective coupling of atomic dipoles in a 2d array,"* Phys. Rev. Lett. **116**, 103602 (2016) [cited in pages 12 and 25].

Bienaimé, T., Bux, S., Lucioni, E., Courteille, P. W., Piovella, N., and Kaiser, R., *"Observation of a cooperative radiation force in the presence of disorder,"* Phys. Rev. Lett. **104**, 183602 (2010) [cited in page 29].

Bloch, D., *"Comment on "optical response of gas-phase atoms at less than $\lambda/80$ from a dielectric surface","* Phys. Rev. Lett. **114**, 049301 (2015) [cited in pages 85 and 97].

Bloch, D. and Ducloy, M., *"Atom-wall interaction,"* Advances In Atomic, Molecular, and Optical Physics, **50**, 91 (2005) [cited in page 59].

Bloch, D., Todorov, P., Carlos de Aquino Carvalho, J., Maurin, I., and Laliotis, A., *"Search for deviations from the ideal maxwell-boltzmann distribution for a gas at an interface,"* (2019) p. 60 [cited in page 97].

Boyd, R., Non-Linear Optics (Academic Press, 2009) [cited in page 40].

Briaudeau, S., Saltiel, S., Nienhuis, G., Bloch, D., and Ducloy, M., *"Coherent doppler narrowing in a thin vapor cell: Observation of the dicke regime in the optical domain,"* Phys. Rev. A **57**, R3169 (1998) [cited in pages 40, 51, 54, 57, 58, and 126].

Bromley, S. L., Zhu, B., Bishof, M., Zhang, X., Bothwell, T., Schachenmayer, J., Nicholson, T. L., Kaiser, R., Yelin, S. F., Lukin, M. D., Rey, A. M., and Ye, J., *"Collective atomic scattering and motional effects in a dense coherent medium,"* Nature Communications **7** (2016), 10.1038/ncomms11039 [cited in pages 12 and 35].

Browaeys, A., Barredo, D., and Lahaye, T., *"Experimental investigations of dipole–dipole interactions between a few rydberg atoms,"* Journal of Physics B: Atomic, Molecular and Optical Physics **49**, 152001 (2016) [cited in page 14].

Burgmans, A. L. J., Schuurmans, M. F. H., and Bölger, B., *"Transient behavior of optically excited vapor atoms near a solid interface as observed in evanescent wave emission,"* Phys. Rev. A **16**, 2002 (1977) [cited in page 40].

Busche, H., Huillery, P., Ball, S., Ilieva, T., Jones, M., and Adams, C., *"Contactless nonlinear optics mediated by long-range rydberg interactions,"* Nat. Phys **13**, 655 (2006) [cited in pages 13 and 40].

C. Rotschild, B. Alfassi, O. C. and Segev, M., *"Long-range interactions between optical solitons,"* Nat. Phys **2**, 769 (2006) [cited in page 40].

Campbell, S. L., Hutson, R. B., Marti, G. E., Goban, A., Darkwah Oppong, N., McNally, R. L., Sonderhouse, L., Robinson, J. M., Zhang, W., Bloom, B. J., and Ye, J., *"A fermi-degenerate three-dimensional optical lattice clock,"* Science **358**, 90 (2017) [cited in page 12].

Cantini, P. and Tatarek, R., *"Selective-adsorption structures in the inelastic scattering of he-graphite (0001),"* Phys. Rev. B **23**, 3030 (1981) [cited in page 102].

Chalony, M., Pierrat, R., Delande, D., and Wilkowski, D., *"Coherent flash of light emitted by a cold atomic cloud,"* Phys. Rev. A **84**, 011401 (2011) [cited in page 29].

Chang, D. E., Sinha, K., Taylor, J. M., and Kimble, H. J., *"Trapping atoms using nanoscale quantum vacuum forces,"* Nature Communications **5**, 4343 EP (2014), article [cited in page 102].

Chang, D. E., Ye, J., and Lukin, M. D., *"Controlling dipole-dipole frequency shifts in a lattice-based optical atomic clock,"* Phys. Rev. A **69**, 023810 (2004) [cited in page 12].

Cherroret, N., Hemmerling, M., Nador, V., Walraven, J. T. M., and Kaiser, R., *"Robust coherent transport of light in multilevel hot atomic vapors,"* Phys. Rev. Lett. **122**, 183203 (2019) [cited in page 14].

Churchill, R. J. and Philbin, T. G., *"Electromagnetic reflection, transmission, and energy density at boundaries of nonlocal media,"* Phys. Rev. B **94**, 235422 (2016) [cited in page 61].

Cocheteau, N., Caractrisation et modlisation dune adhrence molculaire renforce, Ph.D. thesis (2014) [cited in page 113].

Cocoletzi, G. H. and Mochn, W. L., *"Excitons: from excitations at surfaces to confinement in nanostructures,"* Surface Science Reports **57**, 1 (2005) [cited in page 61].

Cohen-Tannoudji, C., Diu, B., and Laloe, F., Mcanique quantique, 2nd ed. (EDP science, 2018) [cited in page 23].

Cojan, J. L. ,, *"Contribution à l'étude de la réflexion sélective sur les vapeurs de mercure de la radiation de résonance du mercure,"* Ann. Phys. **12**, 385 (1954) [cited in pages 40 and 126].

Corman, L., Ville, J. L., Saint-Jalm, R., Aidelsburger, M., Bienaimé, T., Nascimbène, S., Dalibard, J., and Beugnon, J., *"Transmission of near-resonant light through a dense slab of cold atoms,"* Phys. Rev. A **96**, 053629 (2017) [cited in pages 29, 36, 65, and 71].

Davis, K. B., Mewes, M. O., Andrews, M. R., van Druten, N. J., Durfee, D. S., Kurn, D. M., and Ketterle, W., *"Bose-einstein condensation in a gas of sodium atoms,"* Phys. Rev. Lett. **75**, 3969 (1995) [cited in page 28].

Debiossac, M., Zugarramurdi, A., Lunca-Popa, P., Momeni, A., Khemliche, H., Borisov, A. G., and Roncin, P., *"Transient quantum trapping of fast atoms at surfaces,"* Phys. Rev. Lett. **112**, 023203 (2014) [cited in pages 103 and 123].

Desbiolles, P. and Dalibard, J., *"Loading atoms in a bi-dimensional light trap,"* Optics Communications **132**, 540 (1996) [cited in page 124].

Dicke, R., *"The effect of collisions upon the doppler width of spectral lines,"* Phys. Rev. **89** (1953), 10.1103/PhysRev.89.472 [cited in pages 57 and 128].

Dobbertin, H., Not released, Ph.D. thesis (2020) [cited in pages 79 and 82].

Dussaux, A., Passerat de Silans, T., Guerin, W., Alibart, O., Tanzilli, S., Vakili, F., and Kaiser, R., *"Temporal intensity correlation of light scattered by a hot atomic vapor,"* Phys. Rev. A **93**, 043826 (2016) [cited in pages 126 and 143].

Dutier, G., Cavite nanometrique de vapeur de Cesium: spectroscopie a haute resolution et interaction de surface de type van der Waals, Ph.D. thesis (2003) [cited in pages 51 and 92].

Dutier, G., Saltiel, S., Bloch, D., and Ducloy, M., *"Revisiting optical spectroscopy in a thin vapor cell: mixing of reflection and transmission as a fabry–perot microcavity effect,"* J. Opt. Soc. Am. B **20**, 793 (2003a) [cited in pages 51, 55, 72, and 126].

Dutier, G., Yarovitski, A., Saltiel, S., Papoyan, A., Sarkisyan, D., Bloch, D., and Ducloy, M., *"Collapse and revival of a dicke-type coherent narrowing in a sub-micron thick vapor cell transmission spectroscopy,"* Europhysics Letters (EPL) **63**, 35 (2003b) [cited in pages 41, 53, 57, 61, 126, 127, 128, 129, and 131].

Eagen, C., Weber, W., McCarthy, S., and Terhune, R., *"Time-dependent decay of surface-plasmon-coupled molecular fluorescence,"* Chemical Physics Letters **75**, 274 (1980) [cited in pages 40 and 61].

Failache, H., Saltiel, S., Fichet, M., Bloch, D., and Ducloy, M., *"Resonant van der waals repulsion between excited cs atoms and sapphire surface,"* Phys. Rev. Lett. **83**, 5467 (1999) [cited in pages 84 and 88].

Failache, H., Saltiel, S., Fischer, A., Bloch, D., and Ducloy, M., *"Resonant quenching of gas-phase cs atoms induced by surface polaritons,"* Phys. Rev. Lett. **88**, 243603 (2002) [cited in page 96].

Farias, D. and Rieder, K.-H., *"Atomic beam diffraction from solid surfaces,"* Reports on Progress in Physics **61**, 1575 (1998) [cited in pages 108 and 123].

Fearn, H., James, D., and Milonni, P., *"Microscopic approach to reflection, transmission and the ewald-osen extinction theorem,"* Am. J. Phys. **64**, 986 (1996) [cited in page 53].

Fearn, H., James, D., and W Milonni, P., *"Microscopic approach to reflection, transmission, and the ewaldoseen extinction theorem,"* American Journal of Physics **64** (1996), 10.1119/1.18315 [cited in pages 32, 66, and 151].

Feynman, R., The Feynman Lectures on Physics: Vol. II, 33, u vol. (American Journal of Physics, 1965) p. 750 [cited in pages 11 and 23].

Fichet, M., Dutier, G., Yarovitsky, A., Todorov, P., Hamdi, I., Maurin, I., Saltiel, S., Sarkisyan, D., Gorza, M.-P., Bloch, D., and Ducloy, M., *"Exploring the van der waals atom-surface attraction in the nanometric range,"* Europhysics Letters (EPL) **77**, 54001 (2007) [cited in pages 84 and 126].

Fichet, M., Schuller, F., Bloch, D., and Ducloy, M., *"van der waals interactions between excited-state atoms and dispersive dielectric surfaces,"* Phys. Rev. A **51**, 1553 (1995) [cited in pages 86, 87, and 88].

Ford, G. and Weber, W., *"Electromagnetic interactions of molecules with metal surfaces,"* Physics Reports **113**, 195 (1984) [cited in pages 40 and 61].

Friedberg, R., Hartmann, S., and Manassah, J., *"Frequency shifts in emission and absorption by resonant systems ot two-level atoms,"* Physics Reports **7**, 101 (1973) [cited in pages 18, 36, 64, 65, 69, and 81].

Friedberg, R. and Manassah, J. T., *"Cooperative lamb shift in an ellipsoid,"* Phys. Rev. A **81**, 063822 (2010) [cited in pages 36 and 65].

Friedberg, R. and T. Manassah, J., *"The dynamical cooperative lamb shift in a system of two-level atoms in a slab-geometry,"* Physics Letters A **373**, 3423 (2009) [cited in page 36].

Frost, F., Ziberi, B., Schindler, A., and Rauschenbach, B., *"Surface engineering with ion beams: From self-organized nanostructures to ultra-smooth surfaces,"* Applied Physics A **91**, 551 (2008) [cited in page 112].

Frucci, G., Huppert, S., Vasanelli, A., Dailly, B., Todorov, Y., Beaudoin, G., Sagnes, I., and Sirtori, C., *"Cooperative lamb shift and superradiance in an optoelectronic device,"* New Journal of Physics **19**, 043006 (2017) [cited in page 64].

Gardiner, C. and Zoller, P., The Quantum World of Ultra-Cold Atoms and Light - Book 1: Foundations of Quantum Optics, 1st ed. (World Scientific Publishing Co, 2014) [cited in page 20].

Gilberd, P. W., *"The anomalous skin effect and the optical properties of metals,"* Journal of Physics F: Metal Physics **12**, 1845 (1982) [cited in page 40].

Gmeiner, B., Maser, A., Utikal, T., Gotzinger, S., and Sandoghdar, V., *"Spectroscopy and microscopy of single molecules in nanoscopic channels: spectral behavior vs. confinement depth,"* Physical Chemistry Chemical Physics **18**, 19588 (2016) [cited in page 108].

Griffith, W. C., Jimenez-Martinez, R., Shah, V., Knappe, S., and Kitching, J., *"Miniature atomic magnetometer integrated with flux concentrators,"* Applied Physics Letters **94**, 023502 (2009) [cited in page 14].

Gross, M. and Haroche, S., *"Superradiance: An essay on the theory of collective spontaneous emission,"* Physics Reports **93**, 301 (1982) [cited in page 11].

Grynberg, G., Aspect, A., Fabre, C., and Cohen-Tannoudji, C., Introduction to Quantum Optics: From the Semi-classical Approach to Quantized Light (Cambridge University Press, 2010) [cited in pages 20, 161, and 162].

Hinds, E. A., Advances In Atomic, Molecular, and Optical Physics, Vol. 28, p 237, 1st ed. (Yale University, 1991) [cited in pages 85 and 92].

Hinds, E. A., Boshier, M. G., and Hughes, I. G., *"Magnetic waveguide for trapping cold atom gases in two dimensions,"* Phys. Rev. Lett. **80**, 645 (1998) [cited in page 124].

Huang, J.-S., Kern, J., Geisler, P., Weinmann, P., Kamp, M., Forchel, A., Biagioni, P., and Hecht, B., *"Mode imaging and selection in strongly coupled nanoantennas,"* Nano Letters **10**, 2105 (2010) [cited in page 12].

Hughes, I. G. and Hase, T. P. A., Measurements and their Uncertainties: A Practical Guide to Modern Error Analysis (OUP, Oxford, 2010) [cited in page 58].

Israelachvili, J. N., Intermolecular and Surface forces, 3rd ed. (Academic Press, 2011) [cited in pages 101 and 102].

J. Alton, D., Stern, N., Aoki, T., Lee, H., Ostby, E., Vahala, K., and J. Kimble, H., *"Strong interactions of single atoms and photons near a dielectric boundary,"* Nat. Phys. **7** (2010), 10.1038/nphys1837 [cited in page 84].

Jackson, J. D., Classical electrodynamics, 3rd ed. (Wiley, 1999) [cited in pages 11, 23, and 68].

Jahier, E., Guna, J., Jacquier, P., Lintz, M., Papoyan, A., and Bouchiat, M., *"Temperature-tunable sapphire windows for reflection loss-free operation of vapor cells,"* Appl. Phys. B **71**, 561565 (2000) [cited in page 46].

Javanainen, J. and Ruostekoski, J., *"Light propagation beyond the mean-field theory of standard optics,"* Opt. Express **24**, 993 (2016) [cited in pages 64, 65, 69, and 73].

Javanainen, J., Ruostekoski, J., Li, Y., and Yoo, S.-M., *"Shifts of a resonance line in a dense atomic sample,"* Phys. Rev. Lett. **112**, 113603 (2014) [cited in pages 27, 35, 36, 65, 80, and 82].

Javanainen, J., Ruostekoski, J., Li, Y., and Yoo, S.-M., *"Exact electrodynamics versus standard optics for a slab of cold dense gas,"* Phys. Rev. A **96**, 033835 (2017) [cited in pages 65 and 69].

Javanainen, J., Ruostekoski, J., Vestergaard, B., and Francis, M. R., *"One-dimensional modeling of light propagation in dense and degenerate samples,"* Phys. Rev. A **59**, 649 (1999) [cited in page 26].

Jennewein, S., Besbes, M., Schilder, N. J., Jenkins, S. D., Sauvan, C., Ruostekoski, J., Greffet, J.-J., Sortais, Y. R. P., and Browaeys, A., *"Coherent scattering of near-resonant light by a dense microscopic cold atomic cloud,"* Phys. Rev. Lett. **116**, 233601 (2016) [cited in pages 13, 29, and 36].

Katz, O. and Firstenberg, O., *"Light storage for one second in room-temperature alkali vapor,"* Nature Communications **9**, 2074 (2018) [cited in page 14].

Keaveney, J., Collective AtomLight Interactions in Dense Atomic Vapours, Ph.D. thesis, Durham University (2014) [cited in pages 13, 48, and 117].

Keaveney, J., Hughes, I. G., Sargsyan, A., Sarkisyan, D., and Adams, C. S., *"Maximal refraction and superluminal propagation in a gaseous nanolayer,"* Phys. Rev. Lett. **109**, 233001 (2012a) [cited in page 80].

Keaveney, J., Sargsyan, A., Krohn, U., Hughes, I. G., Sarkisyan, D., and Adams, C. S., *"Cooperative lamb shift in an atomic vapor layer of nanometer thickness,"* Phys. Rev. Lett. **108**, 173601 (2012b) [cited in pages 13, 31, 36, 65, 70, and 71].

Kitching, J., Knappe, S., and Hollberg, L., *"Miniature vapor-cell atomic-frequency references,"* Applied Physics Letters **81**, 553 (2002) [cited in page 14].

Knappe, S., Schwindt, P., Shah, V., Hollberg, L., Kitching, J., Liew, L., and Moreland, J., *"A chip-scale atomic clock based on 87rb with improved frequency stability,"* Opt. Express **13**, 1249 (2005) [cited in pages 14 and 84].

Kreibig, U. and Genzel, L., *"Optical absorption of small metallic particles,"* Surface Science **156**, 678 (1985) [cited in page 40].

Laliotis, A., Maurin, I., Fichet, M., Bloch, D., Ducloy, M., Balasanyan, N., Sarkisyan, A., and Sarkisyan, D., *"Selective reflection spectroscopy at the interface between a calcium fluoride window and cs vapour,"* Applied Physics B **90**, 415 (2008) [cited in pages 84, 90, and 140].

Laliotis, A., Passerat De Silans, T., Maurin, I., Ducloy, M., and Bloch, D., *"Casimir-Polder interactions in the presence of thermally excited surface modes,"* Nature Communications , /ncomms5364 (2014) [cited in pages 88, 109, and 140].

Landau, L. and Lifshitz, E., Non-Linear Optics (Pergamon Press, 1960) [cited in page 40].

Landau, L., Pitaevskii, L., and Lifshitz, E., *"Electrodynamics of continuous media, second edition,"* Pergamon Press. (1960) [cited in page 43].

Landragin, A., Courtois, J.-Y., Labeyrie, G., Vansteenkiste, N., Westbrook, C. I., and Aspect, A., *"Measurement of the van der waals force in an atomic mirror,"* Phys. Rev. Lett. **77**, 1464 (1996) [cited in page 84].

Le Kien, F., Balykin, V. I., and Hakuta, K., *"Atom trap and waveguide using a two-color evanescent light field around a subwavelength-diameter optical fiber,"* Phys. Rev. A **70**, 063403 (2004) [cited in page 84].

de Léséleuc, S., Barredo, D., Lienhard, V., Browaeys, A., and Lahaye, T., *"Optical control of the resonant dipole-dipole interaction between rydberg atoms,"* Phys. Rev. Lett. **119**, 053202 (2017) [cited in page 13].

Lewis, E., *"Collisional relaxation of atomic excited states, line broadening and interatomic interactions,"* Physics Reports **58**, 1 (1980) [cited in pages 35, 79, and 80].

Li, Y., Hou, J., Xu, Q., Wang, J., Yang, W., and Guo, Y., *"The characteristics of optics polished with a polyurethane pad,"* Opt. Express **16**, 10285 (2008) [cited in page 112].

Lima, E. G., Chevrollier, M., Di Lorenzo, O., Segundo, P. C., and Oriá, M., *"Long-range atom-surface bound states,"* Phys. Rev. A **62**, 013410 (2000) [cited in pages 85, 101, 103, 104, 120, 122, 123, and 124].

Lodahl, P., Mahmoodian, S., Stobbe, S., Rauschenbeutel, A., Schneeweiss, P., Volz, J., Pichler, H., and Zoller, P., *"Chiral quantum optics,"* Nature **541**, 473 (2017) [cited in page 84].

Lorentz, H. A., The Theory of Electrons: and Its Applications to the Phenomena of Light and Radiant Heat, 2nd ed. (Dover, 2011) [cited in page 27].

M. Ducloy, and M. Fichet,, *"General theory of frequency modulated selective reflection. influence of atom surface interactions,"* J. Phys. II France **1**, 1429 (1991) [cited in pages 19, 31, and 84].

Maki, J. J., Malcuit, M. S., Sipe, J. E., and Boyd, R. W., *"Linear and nonlinear optical measurements of the lorentz local field,"* Phys. Rev. Lett. **67**, 972 (1991) [cited in pages 31, 36, and 79].

Maurin, I., Todorov, P., Hamdi, I., Yarovitski, A., Dutier, G., Sarkisyan, D., Saltiel, S., Gorza, M.-P., Fichet, M., Bloch, D., and Ducloy, M., *"Probing an atomic gas confined in a nanocell,"* Journal of Physics: Conference Series **19**, 20 (2005) [cited in page 71].

Mercadier, N., Chevrollier, M., Guerin, W., and Kaiser, R., *"Microscopic characterization of lévy flights of light in atomic vapors,"* Phys. Rev. A **87**, 063837 (2013) [cited in page 126].

Mitsch, R., Sayrin, C., Albrecht, B., Schneeweiss, P., and Rauschenbeutel, A., *"Quantum state-controlled directional spontaneous emission of photons into a nanophotonic waveguide,"* Nature Communications **5**, 5713 (2014) [cited in pages 83 and 84].

Mohapatra, A. K. and Unnikrishnan, C. S., *"Measurement of the van der waals force using reflection of cold atoms from magnetic thin-film atom mirrors,"* Europhysics Letters (EPL) **73**, 839 (2006) [cited in page 84].

Nienhuis, G., Schuller, F., and Ducloy, M., *"Nonlinear selective reflection from an atomic vapor at arbitrary incidence angle,"* Phys. Rev. A **38**, 5197 (1988) [cited in pages 40 and 41].

Patterson, B. D., Solano, P., Julienne, P. S., Orozco, L. A., and Rolston, S. L., *"Spectral asymmetry of atoms in the van der waals potential of an optical nanofiber,"* Phys. Rev. A **97**, 032509 (2018) [cited in page 84].

Pellegrino, J., Bourgain, R., Jennewein, S., Sortais, Y. R. P., Browaeys, A., Jenkins, S. D., and Ruostekoski, J., *"Observation of suppression of light scattering induced by dipole-dipole interactions in a cold-atom ensemble,"* Phys. Rev. Lett. **113**, 133602 (2014) [cited in pages 13 and 29].

Perczel, J., Borregaard, J., Chang, D. E., Pichler, H., Yelin, S. F., Zoller, P., and Lukin, M. D., *"Topological quantum optics in two-dimensional atomic arrays,"* Phys. Rev. Lett. **119**, 023603 (2017) [cited in page 12].

Petelski, T., Fattori, M., Lamporesi, G., Stuhler, J., and Tino, G., *"Doppler-free spectroscopy using magnetically induced dichroism of atomic vapor: A new scheme for laser frequency locking,"* The European Physical Journal D **22**, 279 (2003) [cited in page 107].

Peyrot, T., Beurthe, C., Coumar, S., Roulliay, M., Perronet, K., Bonnay, P., Adams, C. S., Browaeys, A., and Sortais, Y. R. P., *"Fabrication and characterization of super-polished wedged borosilicate nano-cells,"* Opt. Lett. **44**, 1940 (2019a) [cited in page 116].

Peyrot, T., N., S., Sortais, Y. R. P., Browaeys, A., Sargsyan, A., D., S., Hughes, I. G., and Adams, C. S., *"Measurement of the atom-surface van der waals interaction by transmission spectroscopy in a wedged nano-cell,"* To Appear in Phys. Rev. A. (2019b) [cited in page 99].

Peyrot, T., Sortais, Y. R. P., Browaeys, A., Sargsyan, A., Sarkisyan, D., Keaveney, J., Hughes, I. G., and Adams, C. S., *"Collective lamb shift of a nanoscale atomic vapor layer within a sapphire cavity,"* Phys. Rev. Lett. **120**, 243401 (2018) [cited in pages 71, 73, and 109].

Peyrot, T., Sortais, Y. R. P., Greffet, J.-J., Browaeys, A., Sargsyan, A., Keaveney, J., Hughes, I. G., and Adams, C. S., *"Optical transmission of an atomic vapor in the mesoscopic regime,"* Phys. Rev. Lett. **122**, 113401 (2019c) [cited in pages 60 and 114].

Pippard, A. B. and Bragg, W. L., *"The surface impedance of superconductors and normal metals at high frequencies ii. the anomalous skin effect in normal metals,"* Proceedings of the Royal Society of London. Series A. Mathematical and Physical Sciences **191**, 385 (1947) [cited in page 40].

Riehle, F., *"Optical clock networks,"* Nature Photonics **11**, 25 EP (2017), review Article [cited in page 12].

Ripka, F., Chen, Y.-H., Löw, R., and Pfau, T., *"Rydberg polaritons in a thermal vapor,"* Phys. Rev. A **93**, 053429 (2016) [cited in page 117].

Ripka, F., Kübler, H., Löw, R., and Pfau, T., *"A room-temperature single-photon source based on strongly interacting rydberg atoms,"* Science **362**, 446 (2018) [cited in page 14].

Ritter, R., Gruhler, N., Dobbertin, H., Kübler, H., Scheel, S., Pernice, W., Pfau, T., and Löw, R., *"Coupling thermal atomic vapor to slot waveguides,"* Phys. Rev. X **8**, 021032 (2018) [cited in pages 40 and 84].

Röhlsberger, R., Schlage, K., Sahoo, B., Couet, S., and Rüffer, R., *"Collective lamb shift in single-photon superradiance,"* Science **328**, 1248 (2010) [cited in page 65].

Romer, R. and Dicke, R., *"New technique for high-resolution microwave spectroscopy,"* Phys. Rev. **99** (1955), 10.1103/PhysRev.99.532 [cited in pages 57 and 126].

Roof, S. J., Kemp, K. J., Havey, M. D., and Sokolov, I. M., *"Observation of single-photon superradiance and the cooperative lamb shift in an extended sample of cold atoms,"* Phys. Rev. Lett. **117**, 073003 (2016) [cited in pages 36 and 65].

Roy, A. and Barrett, M. D., *"Fabrication of glass micro-cavities for cavity quantum electrodynamics experiments,"* Applied Physics Letters **99**, 171112 (2011) [cited in page 108].

Safronova, M. S., Safronova, U. I., and Clark, C. W., *"Magic wavelengths, matrix elements, polarizabilities, and lifetimes of cs,"* Phys. Rev. A **94**, 012505 (2016) [cited in pages 88 and 89].

Sander, T. H., Preusser, J., Mhaskar, R., Kitching, J., Trahms, L., and Knappe, S., *"Magnetoencephalography with a chip-scale atomic magnetometer,"* Biomed. Opt. Express **3**, 981 (2012) [cited in page 14].

Sangouard, N., Simon, C., de Riedmatten, H., and Gisin, N., *"Quantum repeaters based on atomic ensembles and linear optics,"* Rev. Mod. Phys. **83**, 33 (2011) [cited in page 14].

Sargsyan, A., Papoyan, A., Hughes, I. G., Adams, C. S., and Sarkisyan, D., *"Selective reflection from an rb layer with a thickness below lambda over 12 and applications,"* Opt. Lett. **42**, 1476 (2017) [cited in page 99].

Sargsyan, A., Pashayan-Leroy, Y., Leroy, C., and Sarkisyan, D., *"Collapse and revival of a dicke-type coherent narrowing in potassium vapor confined in a nanometric thin cell,"* Journal of Physics B: Atomic, Molecular and Optical Physics **49**, 075001 (2016) [cited in pages 57, 130, and 162].

Sarkisyan, D., Bloch, D., Papoyan, A., and Ducloy, M., *"Sub-doppler spectroscopy by sub-micron thin cs vapour layer,"* Optics Communications **200**, 201 (2001) [cited in pages 31, 46, and 84].

Sarkisyan, D., Varzhapetyan, T., Sarkisyan, A., Malakyan, Y., Papoyan, A., Lezama, A., Bloch, D., and Ducloy, M., *"Spectroscopy in an extremely thin vapor cell: Comparing the cell-length dependence in fluorescence and in absorption techniques,"* Phys. Rev. A **69**, 065802 (2004) [cited in pages 126, 127, 128, 129, and 131].

Schilder, N. J., Sauvan, C., Hugonin, J.-P., Jennewein, S., Sortais, Y. R. P., Browaeys, A., and Greffet, J.-J., *"Polaritonic modes in a dense cloud of cold atoms,"* Phys. Rev. A **93**, 063835 (2016) [cited in pages 133 and 134].

Schilder, N. J., Sauvan, C., Sortais, Y. R. P., Browaeys, A., and Greffet, J.-J., *"Homogenization of an ensemble of interacting resonant scatterers,"* Phys. Rev. A **96**, 013825 (2017) [cited in pages 37 and 134].

Schuurmans, M., *"Spectral narrowing of selective reflection,"* Journal de Physique **37**, 469 (1976) [cited in pages 19, 40, 41, 45, 72, 96, and 126].

Schwab, K., Henriksen, E., Worlock, J., and Roukes, M., *"Measurement of the quantum of thermal conductance,"* Nature (2000), 10.1038/35010065 [cited in page 40].

Sedlacek, J. A., Schwettmann, A., Kübler, H., Löw, R., Pfau, T., and Shaffer, J. P., *"Microwave electrometry with rydberg atoms in a vapour cell using bright atomic resonances,"* Nature Physics **8**, 819 EP (2012), article [cited in page 14].

Seltzer, S. J. and Romalis, M. V., *"High-temperature alkali vapor cells with antirelaxation surface coatings,"* Journal of Applied Physics **106**, 114905 (2009) [cited in page 148].

Shahmoon, E., Wild, D. S., Lukin, M. D., and Yelin, S. F., *"Cooperative resonances in light scattering from two-dimensional atomic arrays,"* Phys. Rev. Lett. **118**, 113601 (2017) [cited in page 12].

Sheng, D., Li, S., Dural, N., and Romalis, M. V., *"Subfemtotesla scalar atomic magnetometry using multipass cells,"* Phys. Rev. Lett. **110**, 160802 (2013) [cited in page 14].

Shu, C., Chen, P., Kiu Aaron Chow, T., Zhu, L., Xiao, Y., Loy, M., and Du, S., *"Subnatural-linewidth biphotons from a doppler-broadened hot atomic vapor cell,"* Nature Communications **7**, 12783 (2016) [cited in page 125].

Sibalic, N., Pritchard, J. D, A. C. S., and Weatherill, K. J., *"Arc: An open-source library for calculating properties of alkali rydberg atoms,"* Computer Physics Communications **220**, 319 (2017) [cited in pages 88 and 89].

Siddons, P., Adams, C. S., Ge, C., and Hughes, I. G., *"Absolute absorption on rubidium d lines: comparison between theory and experiment,"* Journal of Physics B: Atomic, Molecular and Optical Physics **41**, 155004 (2008) [cited in pages 13 and 42].

Passerat de Silans, T., Farias, B., Oria, M., and Chevrollier, M., *"Laser-induced quantum adsorption of neutral atoms in dielectric surfaces,"* Applied Physics B: Lasers and Optics **82**, 367 (2006) [cited in page 123].

Passerat de Silans, T., Maurin, I., Segundo, P., Saltiel, S., marie pascale, G., Ducloy, M., Bloch, D., Meneses, D., and Echegut, P., *"Temperature dependence of the dielectric permittivity of caf2, baf2 and al2o3: Application to the prediction of a temperature-dependent van der waals surface interaction exerted onto a neighbouring cs(8p3/2) atom,"* Journal of physics. Condensed matter : an Institute of Physics journal **21**, 255902 (2009) [cited in page 140].

Solomon, G. S., Pelton, M., and Yamamoto, Y., *"Single-mode spontaneous emission from a single quantum dot in a three-dimensional microcavity,"* Phys. Rev. Lett. **86**, 3903 (2001) [cited in page 12].

Steck, D. A., *"Cesiumd line data,"* [cited in pages 48, 49, and 161].

Stephens, M., Rhodes, R., and Wieman, C., *"Study of wall coatings for vaporcell laser traps,"* Journal of Applied Physics **76**, 3479 (1994) [cited in pages 122 and 123].

Svidzinsky, A. A., Chang, J.-T., and Scully, M. O., *"Cooperative spontaneous emission of n atoms: Many-body eigenstates, the effect of virtual lamb shift processes, and analogy with radiation of n classical oscillators,"* Phys. Rev. A **81**, 053821 (2010) [cited in page 26].

Thijssen, R., Verhagen, E., Kippenberg, T. J., and Polman, A., *"Plasmon nanomechanical coupling for nanoscale transduction,"* Nano Letters **13**, 3293 (2013) [cited in page 12].

Todorov, P. and Bloch, d., *"Testing the limits of the maxwell distribution of velocities for atoms flying nearly parallel to the walls of a thin cell,"* The Journal of Chemical Physics **147** (2017), 10.1063/1.4997566 [cited in page 97].

Tserkezis, C., Mortensen, N. A., and Wubs, M., *"How nonlocal damping reduces plasmon-enhanced fluorescence in ultranarrow gaps,"* Phys. Rev. B **96**, 085413 (2017) [cited in page 61].

Ulrich, S. M., Weiler, S., Oster, M., Jetter, M., Urvoy, A., Löw, R., and Michler, P., *"Spectroscopy of the D_1 transition of cesium by dressed-state resonance fluorescence from a single (in,ga)as/gaas quantum dot,"* Phys. Rev. B **90**, 125310 (2014) [cited in page 126].

Vargas, M. and Mochn, W., *"Bound state spectroscopy of he adsorbed on nacl(001): band structure effects,"* Surface Science **355**, 115 (1996) [cited in pages 101, 102, 104, and 108].

Vartanyan, T. and Lin, D., *"Enhanced selective reflection from a thin layer of a dilute gaseous medium,"* Phys. Rev. A **51**, 1959 (1995) [cited in pages 40, 41, 54, and 72].

Vartanyan, T. and Trger, F., *"Line shape of resonances recorded in selective reflection: influence of an antireflection coating,"* Optics Communications **110**, 315 (1994) [cited in page 40].

Vetsch, E., Reitz, D., Sagué, G., Schmidt, R., Dawkins, S. T., and Rauschenbeutel, A., *"Optical interface created by laser-cooled atoms trapped in the evanescent field surrounding an optical nanofiber,"* Phys. Rev. Lett. **104**, 203603 (2010) [cited in page 84].

Voisin, C., Fatti, N. D., Christofilos, D., and Valléel, F., *"Ultrafast electron dynamics and optical nonlinearities in metal nanoparticles,"* J. Phys. Chem. B **105**, 2264 (2001) [cited in page 40].

Wade, C. G., Sibalic, N., De Melo, N. R., Kondo, J. M., Adams, C. S., and Weatherill, K. J., *"Real-time near-field terahertz imaging with atomic optical fluorescence,"* Nature Photonics **11**, 40 (2017) [cited in page 84].

Wade, C. G., Sibalic, N., de Melo, N. R., Kondo, J. M., Adams, C. S., and Weatherill, K. J., *"Real-time near-field terahertz imaging with atomic optical fluorescence,"* Nature Photonics **11**, 40 EP (2016) [cited in page 14].

Wasilewski, W., Jensen, K., Krauter, H., Renema, J. J., Balabas, M. V., and Polzik, E. S., *"Quantum noise limited and entanglement-assisted magnetometry,"* Phys. Rev. Lett. **104**, 133601 (2010) [cited in page 107].

Weber, M. J., Handbook of optical materials, 1st ed. (CRC PRESS, 1991) [cited in page 88].

Weller, L., Bettles, R., Siddons, P., Adams, C., and Hughes, I., *"Absolute absorption on rubidium d1 line: including resonant dipole-dipole interactions,"* J. Phys. B **44** (2011), 10.1088/0953-4075/44/19/195006 [cited in pages 31, 59, 60, 76, and 80].

Whiting, D. J., Šibalić, N., Keaveney, J., Adams, C. S., and Hughes, I. G., *"Single-photon interference due to motion in an atomic collective excitation,"* Phys. Rev. Lett. **118**, 253601 (2017) [cited in page 125].

Whittaker, K., Construction and characterisation of ultra-thin alkali-metal vapour cells, Ph.D. thesis (2017) [cited in pages 70, 113, and 117].

Whittaker, K. A., Keaveney, J., Hughes, I. G., Sargsyan, A., Sarkisyan, D., and Adams, C. S., *"Optical response of gas-phase atoms at less than $\lambda/80$ from a dielectric surface,"* Phys. Rev. Lett. **112**, 253201 (2014) [cited in pages 59, 85, 90, 97, 99, 102, and 126].

Wooten, F., ed., Optical Properties of Solids (Academic Press, 1972) [cited in page 40].

Wylie, J. M. and Sipe, J. E., *"Quantum electrodynamics near an interface,"* Phys. Rev. A **30**, 1185 (1984) [cited in page 101].

Wylie, J. M. and Sipe, J. E., *"Quantum electrodynamics near an interface. ii,"* Phys. Rev. A **32**, 2030 (1985) [cited in page 101].

Zambon, B. and Nienhuis, G., *"Reflection and transmission of light by thin vapor layers,"* Optics Communications **143**, 308 (1997) [cited in page 72].

Zentile, M., Keaveney, J., Weller, L., Whiting, D., Adams, C., and Hughes, I., *"Elecsus: A program to calculate the electric susceptibility of an atomic ensemble,"* Comp. Phys. Comm. **189**, 162 (2015a) [cited in pages 13 and 46].

Zentile, M. A., Whiting, D. J., Keaveney, J., Adams, C. S., and Hughes, I. G., *"Atomic faraday filter with equivalent noise bandwidth less than 1 ghz,"* Opt. Lett. **40**, 2000 (2015b) [cited in page 14].

Zhu, B., Cooper, J., Ye, J., and Rey, A. M., *"Light scattering from dense cold atomic media,"* Phys. Rev. A **94**, 023612 (2016) [cited in page 35].

université PARIS-SACLAY | ÉCOLE DOCTORALE Ondes et Matière (EDOM)

Titre : Interaction dipôle-dipôle dans des vapeurs denses d'alcalins confinées en cellules nanométriques

Mots clés : Interaction dipôle-dipôle résonnante, nano-cellule, cavité Fabry-Pérot, déplacement énergétique, transmission, van der Waals, surface, senseur atomique

Résumé : Les vapeurs atomiques confinées dans des cellules nanométriques constituent une plateforme intéressante pour la réalisation de senseurs atomiques. Dans cette thèse, nous étudions l'interaction entre la lumière et un ensemble d'atomes d'alcalins dans une telle cellule. Nous nous concentrons sur les phénomènes qui pourraient modifier la réponse optique du système et ainsi affecter la sensibilité du senseur. Premièrement, nous étudions la réponse non locale à la lumière induite par le mouvement des atomes dans la vapeur thermique. Quand la distance de relaxation des atomes excède la taille de la cellule, la réponse optique dépend de la taille du système. En transmission, nous avons montré que cela entraine une modification des propriétés de la vapeur avec une période égale à la longueur d'onde de la transition optique. Nous avons ensuite montré que lorsque la densité augmente, la réponse redevient locale. De plus, dans ce régime dense, l'interaction dipôle-dipôle résonnante engendre des déplacements de fréquences collectifs pour des ensembles sub-longueur d'onde. Nous avons démontré que ces shifts sont induits par la cavité formée par la cellule, clarifiant ainsi un débat de plus de 40 ans. Pour ce faire, nous avons développé un modèle pour extraire les effets de la densité déconvolués de ceux de la cavité. Proche des surfaces, la réponse optique des atomes est aussi impactée par l'interaction de van der Waals. Nous avons introduit une nouvelle méthode pour extraire avec précision la force de cette interaction. Nous avons également construit une nouvelle génération de nano-cellules super-polies en verre et enfin comparé les propriétés spectrales en transmission et spectroscopie hors d'axe.

Title : Dipole-dipole interaction in dense atomic alkali vapors confined in nano-scale cells

Keywords : Resonant dipole-dipole interaction, nano-cell, Fabry-Pérot cavity, energy shift, transmission, van der Waals, surface, atomic sensor

Abstract : Alkali vapors confined in nano-scale cells are promising tools for future integrated atom-based sensor. In this thesis, we investigate the interaction between light and an ensemble of atoms confined in a nano-geometry. We focus on the different processes that can modify the optical response of the atomic ensemble and possibly affect the sensitivity of a sensor based on that technology. First, we study the non-local response of atoms to a light excitation due the atomic motion in thermal vapors. When the distance over which the atoms relaxes is larger than the size of the cell, the optical response depends on the size of the system. We have observed that for transmission spectroscopy, this leads to a periodic modification of the optical response with a period equal to the wavelength of the optical transition. Subsequently we showed that when the density of atom increases, the atomic response becomes local again. In this dense regime, the resonant dipole-dipole interaction in a sub-wavelength geometry leads to collective frequency shifts of the spectral lines. We demonstrate that these shifts were induced by the cavity formed by the cell walls, hence clarifying a long-standing issue. We developed a model to extract the density shifts deconvolved from the cavity effects. Close to a surface, the optical response is also affected by the van der Waals atom-surface interaction. We introduced a new method to extract precisely the strength of this interaction. We also developed a new generation of super-polished glass nano-cells and we presented promising spectroscopic signals. Finally, using these cells, we have compared transmission and off-axis spectroscopic techniques.

Université Paris-Saclay
Espace Technologique / Immeuble Discovery
Route de l'Orme aux Merisiers RD 128 / 91190 Saint-Aubin, France